Chem Soc Rev

REVIEW ARTICLE

View Article Online
View Journal | View Issue

Cite this: *Chem. Soc. Rev.*, 2023, **52**, 3098

Received 29th July 2022

DOI: 10.1039/d2cs00481j

rsc.li/chem-soc-rev

Mechanical properties and peculiarities of molecular crystals

Wegood M. Awad,[a] Daniel W. Davies,[b] Daichi Kitagawa,[c] Jad Mahmoud Halabi,[a] Marieh B. Al-Handawi,[a] Ibrahim Tahir,[a] Fei Tong,[d] Gonzalo Campillo-Alvarado,[b] Alexander G. Shtukenberg,[e] Tamador Alkhidir,[fp] Yuki Hagiwara,[o] Mubarak Almehairbi,[fp] Linfeng Lan,[h] Shodai Hasebe,[o] Durga Prasad Karothu,[am] Sharmarke Mohamed,[*fp] Hideko Koshima,[*g] Seiya Kobatake,[*c] Ying Diao,[*b] Rajadurai Chandrasekar,[*i] Hongyu Zhang,[*h] Changquan Calvin Sun,[*j] Christopher Bardeen,[*k] Rabih O. Al-Kaysi,[*l] Bart Kahr[*e] and Panče Naumov[*aemn]

In the last century, molecular crystals functioned predominantly as a means for determining the molecular structures *via* X-ray diffraction, albeit as the century came to a close the response of molecular crystals to electric, magnetic, and light fields revealed that the physical properties of molecular crystals were as rich as the diversity of molecules themselves. In this century, the mechanical properties of molecular crystals have continued to enhance our understanding of the colligative responses of weakly bound molecules to internal frustration and applied forces. Here, the authors review the main themes of research that have developed in recent decades, prefaced by an overview of the particular considerations that distinguish molecular crystals from traditional materials such as metals and ceramics. Many molecular crystals will deform themselves as they grow under some conditions. Whether they respond to intrinsic stress or external forces or interactions among the fields of growing crystals remains an open question. Photoreactivity in single crystals has been a leading theme in organic solid-state chemistry; however, the focus of research has been traditionally on reaction stereo- and regio-specificity. However, as light-induced chemistry builds stress in crystals anisotropically, all types of motions can be actuated. The correlation between photochemistry and the responses of single crystals—jumping, twisting, fracturing, delaminating, rocking, and rolling—has become a well-defined field of research in its own right: photomechanics. The advancement of our understanding requires theoretical and high-performance computations. Computational crystallography not only supports interpretations of mechanical responses, but predicts the responses itself. This requires the engagement of classical force-field based molecular dynamics simulations, density functional theory-based approaches, and

[a] *Smart Materials Lab, New York University Abu Dhabi, PO Box 129188, Abu Dhabi, United Arab Emirates. E-mail: pn21@nyu.edu*
[b] *Department of Chemical and Biomolecular Engineering, University of Illinois at Urbana-Champaign, 600 S. Mathews Ave., Urbana, IL 61801, USA*
[c] *Department of Chemistry and Bioengineering, Graduate School of Engineering, Osaka Metropolitan University, 3-3-138 Sugimoto, Sumiyoshi-ku, Osaka, 558-8585, Japan*
[d] *Key Laboratory for Advanced Materials and Joint International Research Laboratory of Precision Chemistry and Molecular Engineering, Feringa Nobel Prize Scientist Joint Research Center, Frontiers Science Center for Materiobiology and Dynamic Chemistry, Institute of Fine Chemicals, School of Chemistry and Molecular Engineering, East China University of Science and Technology, Shanghai, China*
[e] *Department of Chemistry/Molecular Design Institute, New York University, New York, USA*
[f] *Department of Chemistry, Green Chemistry & Materials Modelling Laboratory, Khalifa University of Science and Technology, Abu Dhabi, United Arab Emirates*
[g] *Research Organization for Nano and Life Innovation, Waseda University, Tokyo, Japan*
[h] *State Key Laboratory of Supramolecular Structure and Materials, Jilin University, 2699 Qianjin Street, Changchun 130012, China*
[i] *Advanced Organic Photonic Materials and Technology Laboratory at School of Chemistry, University of Hyderabad, Hyderabad, India*
[j] *Pharmaceutical Materials Science and Engineering Laboratory, Department of Pharmaceutics, College of Pharmacy, University of Minnesota, Minneapolis, Minnesota, USA*
[k] *Department of Chemistry, University of California Riverside, 501 Big Springs Road, Riverside, CA, USA*
[l] *College of Science and Health Professions, King Saud Bin Abdulaziz University for Health Sciences (KSAU-HS) & King Abdullah International Medical Research Center (KAIMRC), Ministry of National Guard Health Affairs, Riyadh, Kingdom of Saudi Arabia*
[m] *Center for Smart Engineering Materials, New York University Abu Dhabi, PO Box 129188, Abu Dhabi, United Arab Emirates*
[n] *Research Center for Environment and Materials, Macedonian Academy of Sciences and Arts, Bul. Krste Misirkov 2, MK–1000 Skopje, Macedonia*
[o] *Graduate School of Advanced Science and Engineering, Waseda University, Tokyo, Japan*
[p] *Advanced Materials Chemistry Center (AMCC), Khalifa University of Science and Technology, PO Box 127788, Abu Dhabi, United Arab Emirates*

the use of machine learning to divine patterns to which algorithms can be better suited than people. The integration of mechanics with the transport of electrons and photons is considered for practical applications in flexible organic electronics and photonics. Dynamic crystals that respond rapidly and reversibly to heat and light can function as switches and actuators. Progress in identifying efficient shape-shifting crystals is also discussed. Finally, the importance of mechanical properties to milling and tableting of pharmaceuticals in an industry still dominated by active ingredients composed of small molecule crystals is reviewed. A dearth of data on the strength, hardness, Young's modulus, and fracture toughness of molecular crystals underscores the need for refinement of measurement techniques and conceptual tools. The need for benchmark data is emphasized throughout.

1. Introduction to mechanical properties and effects in molecular crystals

1.1. General introduction to mechanical properties

1.1.1. Basic mechanical properties. For long, Nature has inspired engineering and industrial designs that are often drawn from elements of complex biogenic architectures, nano- and micro-structures, and naturally occurring materials with unique combinations of mechanical properties. Mechanical properties are the physical properties exhibited by a material as it undergoes deformation in response to an applied force or pressure. The most common and important examples of mechanical properties are elastic modulus, hardness, strength, toughness, and fatigue. Engineers typically use tensile testing

Wegood M. Awad

Wegood Awad graduated with a BSc in chemical engineering and is now a global PhD fellow in chemistry at NYU and NYUAD. She has received numerous awards and funds for multidisciplinary projects throughout her education. Currently, she is focusing on integrating nanomaterials into biological systems to tackle challenges faced in drug delivery and creating bioinspired materials. Her interests are biomimetics, bioinspired material engineering, 3D printing, and nanocrystals.

Daniel W. Davies

Daniel Davies studied chemical engineering at the University of Iowa, receiving his BS in 2016. He also studied chemical engineering at the University of Illinois, Urbana-Champaign, and graduated with a PhD in 2023. His work investigated polymorphic phase transitions in organic semiconductors for switching electronic properties. He is currently a postdoc fellow at the University of Texas at Austin, where he is working on dynamic tuning of the optical and electronic properties of nanocrystals via electrochemical doping.

Daichi Kitagawa

Daichi Kitagawa received his PhD degree from Osaka City University in 2014. In 2014–2015, he was engaged as a postdoctoral researcher at JSPS. In 2015, he was promoted to an assistant professor at Osaka City University, and he was promoted to a senior professor in 2019. His current research focuses on the fabrication of novel photochromic molecules, photomechanical crystalline materials, and photoreaction dynamics in crystalline states.

Jad Mahmoud Halabi

Jad Mahmoud Halabi earned a BSc in mechanical engineering from New York University Abu Dhabi in 2016. Having developed strong interest in the potential of materials research to drive technological advancement across different sectors, Jad pursued his PhD in chemistry with a focus on materials science at New York University. His research at the Smart Materials Lab focused on characterizing dynamic organic crystals as energy-harvesting materials and their implementation as actuating elements in technological applications.

under controlled conditions to determine how a material responds to forces in tension. The main output of a tensile test is a load *versus* elongation curve that translates into a stress–strain diagram and is used to determine many primary mechanical properties such as the Young's modulus, strength, yield point, toughness, and fatigue when the loading is performed in a cyclic mode. *Stress* reflects the changes of internal forces within a material that react to balance the exerted external load, while *strain* is the deformation of the material compared to its original length. These two properties and the relationship between them capture well the mechanical responses of materials under loading. For example, Young's modulus—also referred to as the modulus of elasticity or elastic modulus—is a measure of a material's reversible deformation, that is, deformations that fully recover upon removal of the driving force. This is characterized by the linear relationship between stress and strain and is governed by Hooke's law. While elasticity and stiffness are often used interchangeably, engineers make a distinction between them in that elasticity is an intrinsic property while stiffness is extrinsic. Stiffness depends on the Young's modulus and the geometry of the material, meaning that two structures with equal Young's moduli can still have different stiffness values.

Conventionally, there are two types of strength: yield strength and ultimate strength. Yield strength is the maximum

Marieh B. Al-Handawi

Marieh Al-Handawi earned her PhD in chemistry and materials science from New York University's Graduate School of Arts and Sciences in 2022. She is currently working as a postdoctoral associate in Naumov's Smart Materials Lab at New York University Abu Dhabi, where she is involved in various interdisciplinary projects related to the design, fabrication, and characterization of materials. Her main research interest is focused on the intersection between materials science and biology, where she investigates natural phenomena with possible applications to materials science, such as biomineralization, water harvesting technologies, and bioluminescence, and applies the underlying principles to bioinspired artificial materials.

Ibrahim Tahir

Ibrahim Tahir obtained his BSc in pure chemistry from the United Arab Emirates University in the UAE, graduating in 2019. Under the supervision of Professor Panče Naumov, Ibrahim is focused on bridging fundamental sciences with practical applications by studying the mechanical properties of dynamic materials with photoactuating or semiconducting properties. His research aims to advance the field of soft robotics, a rapidly growing area with a wide range of applications in various industries. Conducting this research requires collaboration from multiple disciplines, including chemistry, physics, and engineering, which presents both challenges and exciting opportunities for Ibrahim.

Fei Tong

Fei Tong obtained his BS from the Renmin University of China in 2012 and received his PhD in chemistry in 2017 from the University of California, Riverside, under the supervision of Prof. Christopher J. Bardeen. He continued to work as an assistant research scientist and a postdoctoral fellow in the same group from January 2018 to August 2020. After that, he joined the East China University of Science and Technology (ECUST) and has worked as a distinguished research fellow since November 2020. His current research focuses on responsive molecular crystals, crystal engineering, and photochemistry.

Gonzalo Campillo-Alvarado

Gonzalo Campillo-Alvarado is an assistant professor of chemistry at Reed College in Portland, OR, USA. His research focuses on designing dynamic crystalline materials with an emphasis on boron for applications in chemical separations, pharmaceutics, and electronics. Before joining Reed, he was an Illinois Distinguished Postdoctoral Research Associate at the University of Illinois at Urbana-Champaign, mentored by Prof. Ying Diao. He received his PhD in chemistry from the University of Iowa (advisor: Prof. Leonard R. MacGillivray), his MSc in chemistry at Universidad Autónoma del Estado de Morelos, and his BSc in biopharmaceutical chemistry at Universidad Veracruzana.

stress at the yielding point after which a material will start to deform plastically. Typically, however, strength is used to refer to the maximum stress a material can sustain before weakening and eventually failing. If the stress continues to increase beyond the ultimate strength, the material will reach the breaking point. The energy per unit volume absorbed by the material up until that point is the *toughness*, commonly referred to as fracture toughness. While materials that are strong and tough—withstanding damage or fracturing—are generally sought after, the two properties are mutually exclusive.[1] To achieve high toughness, a material must be able to undergo a controlled deformation to enable the dissipation of high stresses. Otherwise, these stresses will contribute to crack initiation and propagation, causing the material to fracture. This consideration explains why strong and rigid materials such as glass and ceramics are brittle while more ductile materials that deform more easily might not be as strong but tend to be tougher. Therefore, plasticity plays an important role in characterizing high-toughness materials where the plastic zone is extended making it resistant to cracking and bond breakage.[1] Molecular crystals, for example, are generally characterized as brittle, meaning that they often fail through cleavage along crystallographic planes instead of allowing for dislocations to flow. When the movement of these dislocations is blocked, they pile up and create microcavities that then lead to crack growth.[2] Recently, more examples of plasticity in molecular crystals have been reported, introducing new possibilities of investigating and optimizing higher toughness in these crystalline solids.[3–6]

Nascent examples of more compliant and soft molecular crystals provide an opportunity to utilize these conventionally

Alexander G. Shtukenberg

Alexander G. Shtukenberg received a specialist degree in 1993 from the Geological Faculty of Saint Petersburg State University, Russia. Under the supervision of Yuri Punin, he received a Candidate of Science degree in 1997 and continued to work at the Geological Faculty as a researcher and faculty member. In 2009, he earned the Doctor of Science degree, and in 2010, he became a professor at the same university. Since 2010, he has been associated with the Molecular Design Institute in the Department of Chemistry at New York University and is currently a research professor.

Tamador Alkhidir

Tamador Alkhidir is a visiting researcher in the Advanced Materials Chemistry Center (AMCC) at Khalifa University and also works as a curriculum specialist in the UAE Ministry of Education. She received her PhD from Khalifa University in 2020. Her research interests are focused on the applications of computational materials modelling for gaining a better understanding of structure–property correlations. She is an expert in the simulation of the electrical and mechanical properties of organic and inorganic materials using DFT methods.

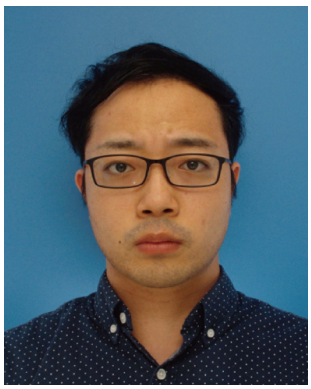

Yuki Hagiwara

Yuki Hagiwara obtained his BSc degree from Waseda University in 2019. He is currently a graduate student in the research group of Dr Hideko Koshima at Waseda University. He is studying mechanically responsive molecular crystals with light and heat, with a focus on the photothermal effect.

Mubarak Almehairbi

Mubarak Almehairbi is an MSc student in the Applied Chemistry program at Khalifa University. He completed his BSc chemistry capstone project under the supervision of Prof. Sharmarke Mohamed. During this capstone project, he was successful in developing a code to better understand and predict the mechanical properties of organic molecular crystals using DFT methods. In his current role as an MSc student, his research is focused on the computational prediction of the vibrational–rotational spectra of diatomic radicals found in the Martian atmosphere. Mubarak has an ongoing passion for code development and in the application of machine learning methods to better understand and predict materials properties.

fragile structures and complement the soft and predominantly amorphous organic polymers and elastomers. The more mechanically robust properties of molecular crystals also promise to resolve the issues of defect and fracture formation when subjected to moderate abrasion, compromising the advantageous long-range order and jeopardizing their unique optical, electrical, and magnetic properties. Low resistance to fatigue and wear is also commonly associated with poor cyclability, and may further pose difficulties in processing and integration in technological devices. For this reason, crystalline organic solids have largely remained in the purview of solid-state chemists, crystallographers, and crystal engineers. However, the recent burgeoning research into the responsive properties of adaptive organic molecular crystals has started to unveil hitherto unexplored and potentially useful dynamic aspects. New reports of unconventional mechanical compliance have prompted a comprehensive revalidation of molecular crystals as technologically applicable smart-material candidates.

Mechanical hardness is desirable in robust and sophisticated devices and machines. While definitions vary, *hardness* can be defined as a surface property in that it measures a material's resistance to permanent surface deformation, and is a highly characteristic property of a solid. The hardness reflects a materials' resistance to wear and tear, which is essential in dynamic mechanical parts and in material design for mechanical actuators where positional accuracy that is otherwise lost in plastic deformation becomes relevant. It is no exaggeration to say that without the advances in hard and strong materials, the 19th century would not have witnessed an industrial revolution.[7] More recently, soft materials such as polymers and elastomers have also gained attention in many technological applications, particularly in biotechnology, stimuli-responsive materials, nanotechnology, and robotics.[8] For example, their low hardness and ease of deformation turn them into great candidates for safe robot–human interfaces.

Routine hardness tests are typically the simplest way to produce and measure irreversible deformation in a material.[9]

Linfeng Lan

Mr Linfeng Lan received his BS degree in chemistry from Jilin University in 2019. Currently, he is a PhD student at Jilin University under the supervision of Prof. Dr Hongyu Zhang. His research interests focus on the optical and mechanical properties of organic crystals and the application of organic crystalline materials in combination with polymers.

Shodai Hasebe

Shodai Hasebe obtained his BSc degree from Waseda University in 2020. He is currently a graduate student in the research group of Dr Hideko Koshima at Waseda University. His research focuses on mechanically responsive molecular crystals and the application of mechanical crystals to actuators and soft robots.

Durga Prasad Karothu

Durga Prasad Karothu obtained his PhD with T. N. Guru Row from the Indian Institute of Science, Bangalore. He has been a visiting researcher with P. Coppens at the University of Buffalo (USA) and with R. E. Dinnebier at the Max Planck Institute for Solid State Research in Stuttgart (Germany). He was the recipient of the Rising Star Award from the Asian Crystallographic Association (AsCA) for the year 2022. He is currently a senior research scientist in the Naumov Group at New York University Abu Dhabi. His research focuses on the development of organic-based smart materials, organic solid-state chemistry, photocrystallography, and electron diffraction.

Sharmarke Mohamed

Sharmarke Mohamed is an Associate Professor of Chemistry, theme leader in the Advanced Materials Chemistry Center (AMCC), and PI of the Green Chemistry and Materials Modelling Laboratory at Khalifa University. In 2011, he received his PhD from UCL. His PhD research focused on small molecule X-ray crystallography and computational methods of crystal structure prediction. He has worked in the pharmaceutical industry as an experimental drug development chemist and is an inventor on a number of patents. Since joining the faculty at Khalifa University in 2014, he has widened his research interests to cover mechanochemistry, multiscale materials modeling and green chemistry.

Hard indenter tips with predefined geometries and shapes are driven at a constant loading or displacement rate into a specimen surface.[10] The shape of the tip can vary among different methods from a rhombohedron (Knoop) to a sphere (Brinell and Rockwell B or C), a square pyramid (Vickers), or a trigonal pyramid (Berkovich).[7] The ratio of the applied force to the size of the indentation projection is the hardness number which is typically obtained on different scales depending on the indenter shape. This oftentimes makes it difficult to compare hardness tests obtained through different methods. Despite hardness often being considered as a measure of resistance to plastic deformation, it is rather a complex property. Hardness is usually treated as a measure of a material's resistance to penetration, spreading, or scratching which respectively yields quantitative information on elastic, plastic, or fracture properties.[7] Evidently, the underlying mechanisms for these deformations are different and involve reversible and irreversible components.

1.1.2. Indentation hardness and modulus. In contrast to tensile testing, hardness tests are performed non-destructively and *in situ* which does not adversely impact or damage the surface given that the indentations are small.[11,12] Additionally, tensile testing requires standard specimens, while hardness tests (particularly small-scale indentations) can be localized. This allows for multicomponent testing of heterogenous materials such as biological materials and is ideal for many new materials that are only produced on a small scale, such as molecular crystals. For organic solids, insufficient material to

Hideko Koshima

Dr Hideko Koshima was a professor at Ehime University, and in 2014, she moved to Waseda University. Her research interests are in solid-state organic photochemistry, chiral chemistry, and microwave chemistry. Over the last decade, her research had focused on mechanical molecular crystals that are actuated by light and heat. In 2001, she received the Japanese Woman Scientists Association Award, and in 2014, she received the Japanese Photochemistry Association Award for Distinguished Contribution to Photochemistry.

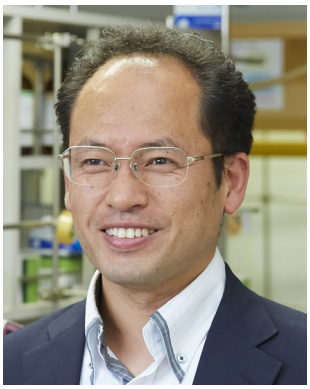

Seiya Kobatake

Seiya Kobatake is professor of materials chemistry at Osaka Metropolitan University in Japan. He received his PhD degree from Osaka City University in 1996, and continued as a postdoctoral researcher. From 2000–2004, he was a research associate at Kyushu University. He moved to Osaka City University as an associate professor in 2004 and was promoted to professor in 2011. He has been in his current position since April 2022. Concurrently, he worked as a PRESTO researcher, JST, from 2006–2010. His current research interests include solid-state photochromic reactions, photomechanical materials, and the application of photochromic materials.

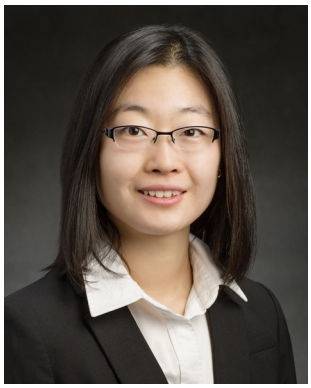

Ying Diao

Ying Diao is an associate professor, I. C. Gunsalus Scholar and Dow Chemical Company Faculty Scholar at the University of Illinois at Urbana-Champaign. She received PhD from MIT in 2011, and pursued postdoctoral training at Stanford University from 2011 to 2014. Her research group, started in 2015 at Illinois, focuses on understanding the assembly of organic functional materials and innovating printing approaches that enable structural control down to a molecular and nanoscale. She was named an MIT Technology Review Innovators Under 35, a recipient of the NSF CAREER Award, NASA Early Career Faculty Award, and Sloan Fellowship in Chemistry.

Rajadurai Chandrasekar

Rajadurai Chandrasekar is a professor of chemistry and associated with the Center for Nanotechnology at the University of Hyderabad, India. He earned a PhD from the Max Planck Institute for Polymer Research at Mainz. He worked as a postdoctoral researcher in the Institute of Nanotechnology at the Karlsruhe Institute of Technology. His research currently focuses on organic- and polymer-based optically linear and nonlinear photonic components and their integrated circuits. His recent research interests include the micromanipulation of photonic structures using atomic force microscopy (mechanophotonics).

perform tensile testing leaves the microindentation and nanoindentation as the only option. Nanoindentation has recently become more popular for determining the mechanical properties of molecular crystals, and has inspired design synthesis and property optimization through crystal engineering.[2,13] The method was developed to measure the hardness and Young's modulus of materials through load–displacement (P–h) diagrams obtained from one cycle of loading and unloading.[14] Unlike previous indentation methods, nanoindentation does not depend on imaging of the indentation mark. The maximum load (P_{max}), the maximum displacement (h_{max}), the permanent penetration depth after unloading, and the contact stiffness (elastic unloading stiffness or the initial slope of the unloading curve) are essential parameters in the measurement, limiting accuracy.[14] Advances in dynamic property measurement as a function of indentation depth,[15] calibration of indenter area functions,[16] and determination of the load–frame compliance (effect of the applied force on the testing machine)[17] have been made to improve the accuracy of these mechanical property measurements. Following the Oliver and Pharr framework,[18] the indentation hardness H of a material can then be calculated as:

$$H = \frac{P_{max}}{A(h_c)} \quad (1)$$

where A is the area function and h_c is the contact depth computed using the contact stiffness. To compute the Young's modulus E, the indentation modulus or the reduced modulus

Hongyu Zhang

Prof. Dr Hongyu Zhang received his PhD in 2006 at Jilin University, majoring in organic chemistry. He joined Prof. Shigehiro Yamaguchi's group at Nagoya University as a JSPS postdoctoral fellow (2006–2008). In 2008, he joined the faculty of Jilin University as an associate professor of chemistry and was promoted to full professor in 2014. His main research interests focus on the design and synthesis of organic functional materials and their applications in optoelectronics. He received a number of awards and honors, including the NSFC outstanding Young Scholar Award (2017) and the CCS Lectureship Award for Creative Young Supramolecular Chemists (2020).

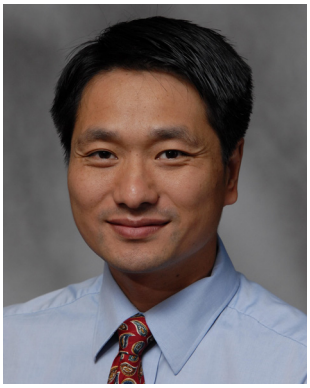

Changquan Calvin Sun

Changquan Calvin Sun is a professor of pharmaceutics at the University of Minnesota, USA. Professor Sun's research focuses on the efficient formulation and design of high-quality tablet products through the appropriate application of materials science and engineering principles. Two main areas of his current research are: (1) crystal and particle engineering for superior pharmaceutical properties; and (2) fundamental understanding of pharmaceutical processes, including powder compaction. He is a Fellow of the American Association for the Advancement of Science (AAAS), the American Association of Pharmaceutical Scientists (AAPS), and the Royal Society of Chemistry (RSC).

Christopher Bardeen

Christopher J. Bardeen received his PhD degree from UC Berkeley in 1995. After a postdoctoral fellowship at University of California, San Diego, he became an assistant professor at the University of Illinois, Urbana-Champaign, in 1998. In 2005, he moved to the University of California, Riverside. His current research interest focuses on spectroscopy, photochemistry, and mechanical dynamics in organic materials.

Rabih O. Al-Kaysi

Rabih Al-Kaysi was born in Beirut, Lebanon. He received his BSc in chemistry (1995) from the American University of Beirut. He obtained his PhD in chemistry (2002) from the University of Southern Mississippi. His postdoctoral research was completed at the University of Rochester (2002–2004) and the University of California, Riverside (2004–2007) with C. J. Bardeen. In 2007, he joined King Saud bin Abdulaziz University for Health Sciences and the Ministry of National Guard Health Affairs in Riyadh, Kingdom of Saudi Arabia, where he is currently a full professor of chemistry at the College of Science and Health Professions as well as an adjunct senior research scientist for the King Abdullah International Medical Research Center.

E_r is first determined, and it is related to the Young's modulus of the sample according to the following equation:

$$\frac{1}{E_r} = \frac{(1-\nu_s^2)}{E} + \frac{(1-\nu_t^2)}{E_t} \quad (2)$$

where ν_s is the sample's Poisson's ratio (often assumed at 0.3 for molecular solids) and E_t and ν_t are respectively the Young's modulus and Poisson's ratio of the indenter tip. However, this relation is most frequently used to evaluate Young's modulus of isotropic materials. Indentation of anisotropic materials such as molecular crystals poses many challenges and further complicates this relationship. Usually, the anisotropy of elastic properties is investigated through indentations along different orientations.[10,19–21] This is particularly difficult for small crystals where certain faces are inaccessible. Moreover, indentations on small scales are also subject to boundary effects.[22] Additionally, 3D analysis would be required to properly determine the anisotropic character of mechanical properties, which can be costly.

1.1.3. Anisotropy and plasticity. Indentation measurements on anisotropic single crystals can be influenced by the indenter shape. Additionally, despite indentation being conducted on specific planes or along certain axes, stress develops in all directions during indentation. The result is a measured indentation modulus that is an average of the elastic constants in all other directions.[23] The measured indentation modulus is however weighted along the indentation direction and can still vary considerably depending on the crystal face. However, given that the indenter is not just pushing in one direction, the resulting modulus is often greater than the real Young's modulus of the specific crystal face. Therefore, since there is no way to directly compute Young's modulus from the indentation modulus for anisotropic materials, different iterative approaches and numerical methods such as finite element analysis have been explored to assess a material's elastic anisotropy.[10] On the other hand, some studies suggest that hardness does not vary much with the orientation of the indentation plane. This is explained by the fact that the plastic strain field induced by indentation is complicated by accommodation of the deformation by the activation of multiple slip planes concurrently.[10] Therefore, the same slip planes might contribute to differently oriented hardness measurements where the resulting measurement is the average over all the activated slip systems. Other studies have suggested the contrary, claiming that hardness is indeed dependent on the crystal face and can vary greatly. For example, crystals with polar structures (for example, zinc blende) can have different degrees of hardness even on opposite sides of the same Miller plane.[7]

Hardness is indeed a complex property. Although a number of studies have been reported on the topic, it is still not very well understood, particularly for anisotropic molecular single crystals. Thus, it is hard to evaluate such crystalline solids with single hardness values. Additionally, even though hardness is used to assess plasticity of materials, there is a great discrepancy between the observed hardness values and those simulated or postulated for non-metallic materials. The indentation patterns induced by the plastic deformation are not in line with the slip-line fields proposed by the continuum theory.[24] Plastic deformation by definition is a discontinuous, time-dependent flow process in which the matter is irreversibly displaced on applying a shear stress and is translated into movement of dislocations, slip, twinning, and kinking motions. Such structural changes do not always explain hardness values for molecular crystals. Given that hardness is not independent of the indentation modulus but it is rather a hybrid property determined from both reversible and irreversible deformation, a new elasticity index (I), defined as the ratio of indentation hardness to indentation modulus, $I = \frac{H_I}{E_I}$, was introduced recently.[25]

Bart Kahr

Bart Kahr was born in New York City in 1961. He studied chemistry with I. D. Reingold at Middlebury College, Kurt Mislow at Princeton University (PhD, 1988), and J. M. McBride at Yale University. He was a faculty member at Purdue University from 1990 to 1996 and at the University of Washington, Seattle, from 1997 to 2009. After which, he returned to his hometown, where he is currently professor of chemistry at the Molecular Design Institute at New York University. His research group studies the growth, structure, and physical properties of complex organized media.

Panče Naumov

Panče Naumov is a tenured professor at New York University Abu Dhabi, with a cross-appointment at NYU's Molecular Design Institute, and a director of the Center for Smart Engineering Materials. He is a native of Macedonia, where he got a BSc degree from Ss. Cyril and Methodius University. After acquiring his PhD in chemistry and materials science from the Tokyo Institute of Technology in 2004, Dr Naumov continued his research at the National Institute for Materials Science, Osaka University and Kyoto University. The research in his group is related to materials science, focusing on smart materials, crystallography, bioluminescence, and petroleomics.

The elasticity index is derived from the expression for an irreversible deformation character, R_{ID}:

$$R_{ID} = \frac{H}{\left(1 - \sqrt{\frac{H_I}{E_I}}\sqrt{\frac{2}{\tan\beta}}\right)^2} \quad (3)$$

where H_I and E_I are the indentation hardness and indentation modulus, respectively, and β is the equivalent cone angle of the indenter. The expression proves the hybridity of indentation hardness by combining constitutive relationships for rigid-perfectly-plastic and purely elastic conical indentation. As $\frac{H_I}{E_I}$ approaches 0, the indentation hardness becomes more reflective of irreversible deformation or plasticity. This is the case in ductile materials such as some metals with $I \approx 10^{-3}$ for which indentation tests were developed and are best understood. The elastic index for brittle ceramics (elastic materials) is around 0.4. It is 0.05 for biological materials, and approximately 0.04 for organic single crystals.[25–27] When comparing two materials, it does not always follow that a material with a higher hardness value has higher resistance to plastic deformation. Even if indentation hardness values are high, they can still be dominated by a large indentation modulus such that R_{ID} is not necessarily high. An elasticity index is then useful for deducing the functional relevance of indentation measurements, for example, for practical classification of materials in categories such as ductile or brittle. It also allows for a better comparison between different materials. Molecular crystals in their range of mechanical properties and anisotropy are similar to biological materials and require similar care. Indentation hardness values for molecular crystals can also be treated as an estimation of the elastoplastic work required to cause indentation of a unit volume. The elasticity index ratio is then useful for categorizing molecular crystals by the dominance of reversible or irreversible deformation reflected by high or low values of I, respectively. From a more application-focused approach, Ashby *et al.* have proposed a new property to characterize the softness of different materials.[28] They used a geometric mean of hardness and Young's modulus to more practically compare different materials through a metric that accounts for the elastic rigidity due to a high Young's modulus that contributes to a material's true hardness.

1.2. Mechanical effects

1.2.1. Categorization. Over the past decade, efforts to categorize the mechanical effects of molecular crystals have resulted in a holistic understanding of the dynamic processes converging at the interface of macroscopic and molecular levels (Fig. 1). Earlier attempts to conceptualize the mechanical effects were based on the experimentally observed outcome of introducing stress from chemistry, heat, light, or mechanical forces to a single crystal specimen. Common effects (*i.e.*, deformation, motion, and disintegration) can be broadly categorized into *disintegrative* (*i.e.*, a single crystal breaks as a result of the stress) and *restorative* (*i.e.*, the integrity of a single crystal is maintained at the expense of internal transformations).[29–31] The complexity and diversity of experimental mechanical effects have motivated groups to produce detailed general,[13,29–32] and topical reviews that focus on crystal adaptronics,[33] martensitic transitions,[34] plastic crystals,[35,36] thermally induced and photo-induced mechanical effects,[37] growth-induced bending/twisting,[38] and dynamic crystals with switchable properties.[39]

Here, we present the main types of mechanical effects emphasizing recent research at the time of writing related to martensitic transitions (*i.e.*, thermoelasticity, superelasticity, and ferroelasticity),[34] which have been documented for organic/organometallic molecular crystals (Fig. 2). In addition, we briefly touch on categories of complex motion that typically arise from a combination of two or more independent effects.[30] We note that given a rapidly evolving field, the categories presented here, rather than being definitive, serve only as a general guideline and nomenclature, and are subject to change to accommodate new discoveries and modes in crystalline transformations.

1.2.2. Disintegrative mechanical effects. Disintegrative mechanical effects in single crystals occur after an induction period that precedes relaxation from stress, thus causing a leaping or so-called ''salient'' response. The effects can be considered photosalient, thermosalient or mechanosalient, when the source of stress is light, heat, or pressure, respectively. In the following subsections, we describe and discuss specific effects caused by rapid deformation or disintegration along with some representative examples.

1.2.2.1. Jumping. Jumping or hopping single crystals were first documented by Etter and Siedle (1983) in (phenylazophenyl)palladium hexafluoroacetylacetonate.[55] Upon heating one facet of the crystal, the mechanical strain triggered the crystals to ''fly off'' the hot stage. The underlying molecular mechanisms indicate that on heating or cooling, rapid and anisotropic phase transitions allowed the crystals to jump upon stress release.[56–59] Light and pressure have also triggered jumping in molecular crystals.[60–62] Jumping results from several factors (*e.g.*, amount of accumulated strain and the time scale of disintegration) caused by minuscule perturbations at a molecular level expressed by a sudden release of accumulated energy. In many cases, crystals may jump to dissipate energy through continued fragmentation concurrent with the jumping.[60]

1.2.2.2. Fragmentation. Photosalient derivatives of diarylethenes have shown rapid single crystal fragmentation upon irradiation with UV light.[40] Fragmentation of single crystals was accompanied by a color change from colorless to blue. The photochromic fragmentations were rationalized by strain caused by disturbance of intermolecular hydrogen bonding in the single crystals upon ring opening of diarylethenes. Photosalient fragmentation has also been observed in [2+2]-photocycloaddition of discrete styrylpyridine Cu complexes forming 1D cyclobutane-based coordination polymers,[63] and in [2+2]-photocycloaddition of diolefinic derivatives.[64]

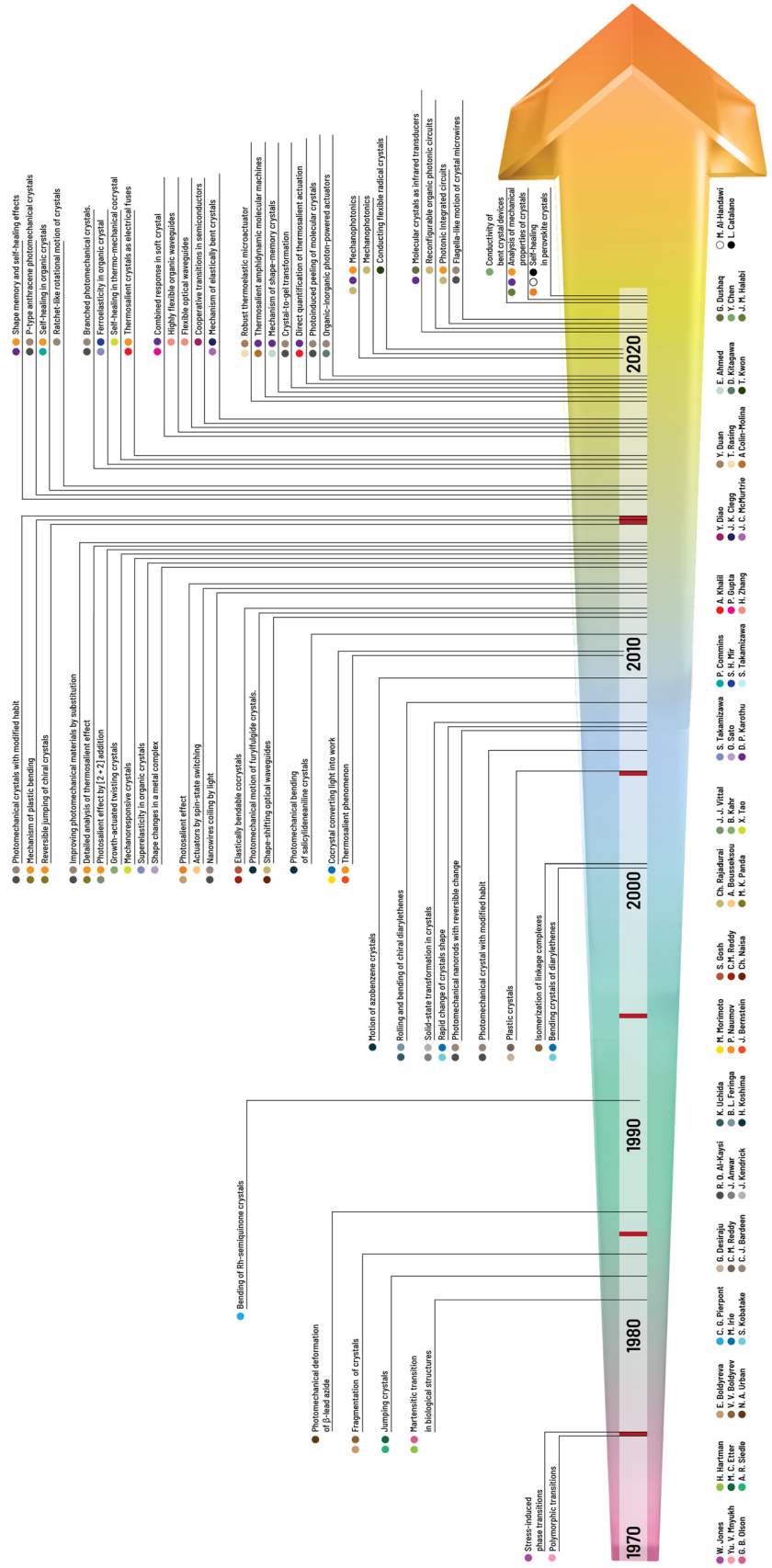

Fig. 1 Chronology of the milestones in research on mechanical properties and effects of molecular crystals with the names of the main contributors to the research field of crystal adaptronics.

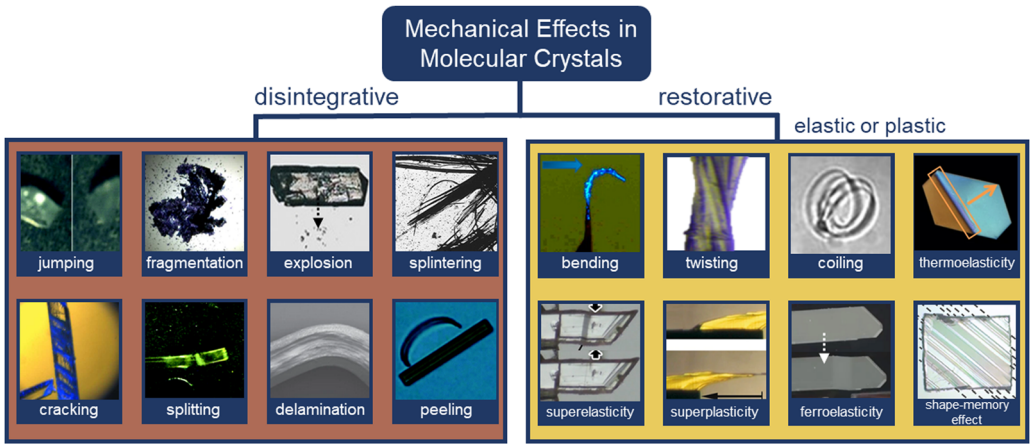

Fig. 2 Categories of mechanical effects in molecular crystals. Disintegrative mechanical effects: jumping,[37] fragmentation,[40] explosion,[41] splintering,[42] cracking,[43] splitting,[44] delamination,[45] and peeling.[46] Restorative mechanical effects: bending,[47] twisting,[46] coiling,[48] thermoelasticity,[50] superelasticity,[51] superplasticity,[52] ferroelasticity,[53] and shape memory effects.[75] All images have been reproduced or adapted with permission from ref. 37 Copyright 2014, The Royal Society of Chemistry, ref. 40 Copyright 2016, American Chemical Society, ref. 41 Copyright 2018, Wiley-VCH, ref. 42 Copyright 1996, American Chemical Society, ref. 43 Copyright 2015, International Union of Crystallography, ref. 44 Copyright 2019, The Royal Society of Chemistry, ref. 45 Copyright 2015, Springer Nature, ref. 46 Copyright 2019, The Royal Society of Chemistry, ref. 47 Copyright 2013, American Chemical Society, ref. 48 Copyright 2017, The Royal Society of Chemistry, ref. 49 Copyright 2013, Wiley-VCH, ref. 50 Copyright 2018, Springer Nature, ref. 51 Copyright 2019, American Chemical Society, ref. 52 Copyright 2018, Springer Nature, ref. 75 Copyright 2019, Springer Nature, and ref. 54 Copyright 2019, American Chemical Society.

1.2.2.3. Explosion. Strain/kinetic energy can be stored in crystals to harvest explosive mechanical responses. A representative case involves polymeric crystals derived from topochemical azide–alkyne reactions, in which humidity plays a critical role in modulating explosion (*i.e.*, dehydration was used to trigger crystal explosion).[41] Cocrystallization strategies have also been used to modulate the explosive response of materials (*i.e.*, energetic cocrystals). For instance, common explosives 3,5,7-tetranitro-1,3,5,7-tetraazacyclooctane (HMX)[65] and 2,4,6-trinitrotoluene (TNT) were cocrystallized with hexanitrohexaazaisowurtzitane (CL-20) to produce more powerful energetic materials that detonate upon mechanical stress.[66] Modulation of explosive properties through cocrystallization relies on modifying packing coefficients, density, and thermal properties.[66] Polymorphism also affects energy release from explosive crystals.[67]

1.2.2.4. Splintering. Splintering in single crystals has been typically observed as a needle-like fragmentation parallel to the long axis of the crystal. Splintering in single crystals is a common effect in enzymatic degradation of biomolecules and bacterial products, often causing the "splinters" to bend into curved loops.[42,68] Studies revealed molecular self-assembly into a tubular packing to be of fundamental importance to the splintering of single crystals through degradation.[69] Splintering in molecular crystals has also been documented during thermosalient transitions of *N*′-2-propylidene-4-hydroxybenzohydrazide[56] and photosalient effects of 4-chlorocinnamic acid.[70]

1.2.2.5. Cracking. Cracks in single crystals have been observed as a result of strain release and often precede additional mechanical effects (*e.g.*, jumping). They are commonly observed before actual disintegration occurs, but occasionally crystals crack without motion. A representative example involves a [2+2]-photodimerization reaction of 3,4-dimethoxycinnamic acid crystallized as blocks.[43] Cracks perpendicular to the main elongation axis and double-bond plane quickly developed on exposure to UV light. It was rationalized that the built-up strain is released on cleaving the molecular planes, facilitated by the presence of slip planes in the crystal. Cracking was also observed when single crystals of disilanyl macrocycles were heated along crystallographic planes with relatively weak supramolecular contacts, followed by jumping.[71]

1.2.2.6. Splitting. Single crystals can often break into two or more parts. In the case of a triphenylethenyl gold isocyanide complex, splitting occurred perpendicular to the longest crystal axis with additional thermosalient responses (*i.e.*, motion and bending).[44] Here, a thermally induced phase transition caused expansion of the crystal length (*i.e.*, major axis) and contraction of the thickness (*i.e.*, shortest axis) resulting in an anisotropic strain release. Splitting has also been observed along the major axis of single crystals when they are subjected to localized heating. Twinned crystals of 1,2,4,5-tetrabromobenzene exhibited smooth splitting along their twinning interface when one of the components was heated.[72]

1.2.2.7. Delamination. Visible delamination of single crystals has been achieved through the application of mechanical stress (*i.e.*, shearing) approximately parallel to the layers. The sliding of molecular layers resulted in a molecular rearrangement that accommodated the applied stress.[13,73] For instance, partial delamination of single crystals facilitated plastic bending by enabling sliding of layers on top of each other.[45,74,75] In another study, reversible photodelamination of crystalline

microribbons of asymmetric perylene diimide was achieved by irradiation with a laser, which caused lateral sliding of stacked layers.[76] Similarly, delamination of vinyl azides was caused by phototriggered gas release with UV light.[77]

1.2.2.8. Peeling. The capacity of crystals to undergo photoinduced peeling of surface layers has been observed in *cis*-olefins as a result of olefinic *cis*-to-*trans* and η^1-SO_2 to η^1-OSO linkage photoisomerization effects.[46,78] In the former case, UV light irradiation of *cis*-dimethyl-2(3-(anthracen-9-yl)allylidene)malonate (*cis*-DMAAM) block-like microcrystals resulted in delamination and curling in the longitudinal section of a single crystal. It should be noted that peeling occurred after the UV-light was turned off, suggesting it to be a result of molecular rearrangement. In the latter case, SO_2 photoisomerization in a $[Ru(NH_3)_4(SO_2)(3\text{-phenylpyridine})]Cl_2{\cdot}H_2O$ complex caused the peeling effect to emanate from one end of the main crystal face, halting midway due to the presence of accumulated crystal strain from curling.

1.2.3. Restorative mechanical effects. Restorative mechanical effects arise when single crystals relax upon removal of external stimuli by mechanical reconfiguration (*i.e.*, reshaping) without showing appreciable disintegration or delamination.[29] Restorative effects in single crystals can be broadly categorized into *elastic* (*i.e.*, reversible) or *plastic* (*i.e.*, irreversible), depending upon the spontaneity of shape recovery. Elastic single crystals regain their initial shapes after the applied stimulus due to the restoration of their supramolecular architectures. In contrast, plastic crystals permanently deform due to dislocations and defects generated upon applying an external stimuli.[30,79] Compliance in restorative mechanical crystals is generally facilitated by non-covalent interactions that are relatively weaker compared to covalent, ionic, or metallic bonds.[80,81] It is important to note that mechanical effects may change from elastic to plastic, following the regimes in a typical stress–strain curve, and also adhere to "supermechanical" deformations (*e.g.*, superelastic and ferroelastic) in some cases.[30] Mechanical deformation modes resulting from martensitic transitions and thermomechanical stress (*i.e.*, thermoelasticity, superelasticity, ferroelasticity, and shape memory effects) are also considered in this section.

1.2.3.1. Bending. The bending of crystals, one of the most basic restorative mechanical effects of single crystals, has been widely documented since the early 19th century.[38] Bending can arise predominantly during crystallization and phase transitions, photochemical transformations (*e.g.*, cycloaddition and *trans–cis* isomerization), and from thermally or mechanically induced effects.[29] Molecular underpinnings for crystals that bend elastically suggest an expansion of the crystal on the outer side and immediate restoration of the initial shape after the stimulus has been removed.[75] Plastic bending (*i.e.*, bending beyond the elastic limit) involves the slippage of molecular layers in the single crystals, causing the evolution of defects on partial delamination.[13] In the case of *N*-(4-ethynylphenyl)-3-fluoro-4-(trifluoromethyl)benzamide, cooperative reconfigurations of $CF_3\cdots CF_3$ interactions between adjacent molecular layers contribute to the mechanical bending of single crystals.[74] In the context of photoinduced bending, permanent photomechanical *trans–cis* isomerization of *cis*-azobenzene compounds were performed by subjecting single crystal needles to UV irradiation.[47] Upon irradiation, single crystals underwent irreversible bending to the opposite direction from the light source. Reversible photomechanical bending of *trans*-4-aminoazobenzene and oxazole crystals has also been observed,[82,83] the latter resulting from a topochemical [2+2]-photodimerization. Cocrystals of desolvated perylene and 1,2,4,5-tetracyanobezene displayed a rare case of solvomechanical bending on exposure to tetrahydrofuran (THF) vapors.[84]

Our understanding of the reasons behind the elasticity, which is commonly observed with slender molecular crystals has particularly evolved over the past years. Even materials that have been traditionally considered very hard display elastic properties when they are small with high aspect ratios. Detailed X-ray diffraction studies of the copper(II) acetylacetonate complex[85] have clearly shown that the bending of a crystal is accompanied by (or, occurs as a result of) rotation of the molecules, with a slight decrease in the distance between the neighboring molecules on the inner (concave) side and a slight increase in the distance on the outer (convex) side of the crystal. This work discredits an earlier hypothesis of molecular interlocking being the necessary condition for the elastic behavior. At the present state of knowledge, it appears that there is no single mechanism or structural feature that is a necessary condition for elasticity. Clearly, in the future, systematic and accurate studies will be needed to discern such features or a specific combination thereof, if they exist.

1.2.3.2. Twisting. Helical or twisted crystals may be considered bent in more than one direction. Although naturally occurring twisted crystals have been known for some time,[86] the molecular mechanistic details have remained elusive. It has been established that a common requirement is the existence of at least two bending faces in a crystal.[87] This observation has facilitated the bottom-up design of twisted helical crystals through mechanical deformation.[48] Twisting has been achieved as a result of photochemical reactions in micro- and nano-sized crystals due to their increased ability to withstand exposure to UV radiation without polycrystalline fragmentation *vs.* macro-sized crystals (the higher surface-to-volume ratio dissipating the interfacial stress between unreacted/reacted phases/domains at surfaces).[64,70,88] For instance, crystalline microribbons based on anthracene derivatives underwent twisting on exposure to UV light as a result of [4+4] photodimerization.[70,89] Thermosalient twisting as a result of topochemical polymerization of azide and alkyne monomers,[90] and molecular rearrangement of cocrystals has also been observed.[91]

1.2.3.3. Coiling. Crystals that wind or curl into coils or spirals due to twisting and bending have also gained attention due to their potential to be used as actuators. Molecular crystals containing boronate esters[92] and 1,4-bis[2-(4-methylthienyl)]-2,3,5,6-tetrafluorobenzene[93] coil around objects through

mechanical manipulation. This effect is facilitated by a combination of bending (*i.e.*, plastic deformation) and twisting (*i.e.*, elastic deformation).[29] Photoinduced coiling has been observed in straight nanowires of an anthracene derivative, dimethyl-2-(3-(anthracen-9-yl)allylidene)malonate,[46] as a result of *E*-to-*Z* isomerization, where exposure to pulses of visible light triggered the nanowires to curl into bundles. The effect persists even after the light stimulus has been removed, while microwires made from 3-(anthracen-9-yl)acrylic acid[94] curl into a closed loop upon continuous exposure to visible light.

1.2.3.4. Thermoelasticity. Thermoelasticity in single crystals originates in martensitic or other transitions occurring between high-temperature (HT) and low-temperature (LT) polymorphs that are related enantiotropically. Macroscopically, thermoelasticity in single crystals is accompanied by anisotropic changes in crystal shape and size that are reversible (*i.e.*, elastic) due to cooperative molecular motion, thus facilitating shape recovery. Compared to elasticity alone, where recovery of the crystal shape is enabled by the capacity of molecules to resist deformation, thermoelasticity is enabled by cooperative polymorph transitions driven by thermal energy. Examples of molecular mechanisms in thermoelastic crystals include cooperative interlayer gliding of planes,[95] conformational changes enabled by flexible molecules/motifs,[50] and molecular rotation.[96,97] It should be noted that thermoelasticity is a prerequisite for superelasticity and shape memory effects.[98]

1.2.3.5. Superelasticity. Superelasticity in single crystals is observed when a thermoelastic transition is triggered by a mechanical stimulus. It can be considered the mechanical analog of thermoelasticity. The mechanism of action involves the mechanical deformation of a single crystal through shear loading under isothermal conditions accomplished by altering the Gibbs free energy change of HT-to-LT phase transitions. In other words, the mechanical stress applied to thermoelastic crystals alters the thermodynamic equilibrium and facilitates cooperative elasticity through structural transitions, which is fundamentally different from intrinsic elasticity (*i.e.*, resistance to change). After shear unloading, crystals exhibit shape recovery. An important characteristic of superelastic crystals is frictional work, which acts as a kinetic barrier resulting from structural defects.[34] Superelasticity, albeit rare, has been found in molecular solids such as 6,13-bis(triiso-propylsilylethynyl)pentacene[97] and terephthalamide[99] crystals. Alternative molecular mechanisms for superelasticity exist that deviate from the conventional thermoelastic transitions. These include twinning transitions[51,100] and transitions between monotropic phases.[101]

1.2.3.6. "Superplasticity". "Superplastic" deformability in organic crystals has been reported for single crystals of *N*,*N*-dimethyl-4-nitroaniline.[52] In this example, "superplasticity" is based on a multi-layer slipping mechanism that enables deformation of over 500% when shearing is along the tilt direction of the major axis. The difference between the "superplasticity" and regular plasticity, however, remains elusive because it is not clear to what extent a crystal needs to be plastic in order to be "superplastic". The rationale for the "superplasticity" suggested that the highly anisotropic multilayer slipping is regulated by interlayer hydrogen bonding.[52]

1.2.3.7. Ferroelasticity. In a ferroelastic molecular crystal, a twinned deformed state is maintained when mechanical stress is applied, resulting in domains of two or more orientations. In addition, the domains are mechanically interconvertible when a reverse mechanical stress is applied. In a ferroelastic single crystal, the twinning domains are equally stable and do not recover spontaneously (*i.e.*, detwinning) as in the case of superelasticity.[34] Therefore, deformational twinning acts as the main molecular basis for ferroelastic transformations.[53,97,102]

1.2.3.8. Shape-memory effects. The discovery of the shape memory effect in molecular crystals is a milestone for the development of molecular crystals due to its resemblance to that of some metal alloys and polymers exhibiting multiple (thermo)mechanical transitions.[30,33] It was first reported for a crystal of terephthalic acid, and later on, the details of the mechanism were explained.[62,75] To engineer molecular crystals with shape memory, the common starting point is the ferroelastic twinning of a molecular crystal upon shear loading. Thermal treatment of the twinned structure restores the original shape by cooperative rearrangement during thermoelastic transitions. Cooling can either restore the original shape[54,103] or induce twinning.[75] Shape-memory has typically been discovered by serendipity. Further studies are needed to understand the full spectrum and applications of this mechanical effect.

1.2.4. Complex motility. Complex motility or locomotion effects in single crystals induce two or more restorative mechanical effects.[30] Crystals that exhibit complex motility are of increased interest for the fields of soft robotics due to their adaptability for accomplishing tasks or specific functions.[104] Current examples of complex motility mechanisms in molecular crystals include rolling,[105] walking,[106] swimming,[107] crawling[108] and ratcheting,[109] and the list continues to expand rapidly.

2. Spontaneous growth-induced deformations

2.1. Ubiquity

A force applied to a crystal with forceps, or a light-field that can induce chemical changes, may cause bending and/or twisting, as amply illustrated herein. However, many crystals can deform themselves in the absence of apparent external forces. A large proportion (up to one-third) of molecular crystals can be made to twist as they grow.[38,110–113] In some families of crystals, such as binary charge transfer complexes, the proportion can be greater than one-half.[114] This group includes many common materials that have been studied for decades or more.[115–119] Below we focus on twisting, the most spectacular and easily detected deformation, however spontaneous growth-induced deformations also include varieties of bending and scrolling.[38]

However, the great number of materials in this class raises a question: what kind of molecular objects deserve to be called *crystals*? Semi-infinite translational symmetry associated with a set of basis vectors remains a part of many serviceable definitions of a crystal, and helicoidal crystals choose to give this up.[5]

2.2. Evidence

Helicoidal crystals have two constants of the second-rank curvature tensor $\kappa_1 = -\kappa_2$, at an angle of $\pm\pi/4$ between the orthogonal, tangential tensor components. Twisting is characterized by a pitch (length) associated with a 180° rotation of a crystal, $P = \pi/\varphi$, inversely proportional to φ, the twist per unit length. When twisted crystals are grown as discrete objects, from solution,[120] vapor,[121] and even from melts in some cases,[119] their dimensions can be effectively determined by scanning electron microscopy (Fig. 3A and B). In many other instances, fine fibrils are packed in spherulites.[122] In such cases, optical microscopy[123] is the most incisive method of analysis (Fig. 3C–E). Polarization modulation techniques[124] can be used to investigate the details of mesoscale stereochemistry and the organization of polycrystalline structures. (Fig. 3F and G).[125–131]

2.3. Symmetry

Helicoids are chiral; however, crystals of almost any symmetry can twist as they grow.[133,134] No direct relationship between molecular or crystallographic chirality and sense of twisting is expected, which can be a counterintuitive fact to many chemists for whom chirality begets chirality. Nevertheless, enantiomorphous helices are correlated with stereogenic building components or the stereochemistry of twist-inducing additives (albeit growth conditions can affect the sense of twist in some materials).[135] Heterochiral helices should be likewise correlated with enantiomorphous space groups and/or enantiopolar growth directions.[136] Sometimes banded spherulites grow along polar directions, and then it becomes important to distinguish non-equivalent positive/negative growth directions. This can be achieved by monitoring growth with tailor-made additives.[137,138]

2.4. Mechanisms

Even though the problems associated with crystal twisting have been brought forward in successive generations for more than a century, there is no consensus as to why so many crystals twist themselves as they grow. Given the diversity of simple structures that will form twisted crystals, it is likely that there is more than one reason for morphologies that deviate from lattices with long-range translational symmetry.[38,132,139] The most important of them are briefly outlined below (Fig. 4).

2.4.1. Fields. Thermal (temperature gradients), mechanical (density variations), and compositional (variations in impurity concentrations) fields formed around crystallizing materials can generate forces on a growing crystal which produce a twist.[140,141] This mechanism, however, has mainly been applied to polymer crystals composed of very thin lamellae.[142–144]

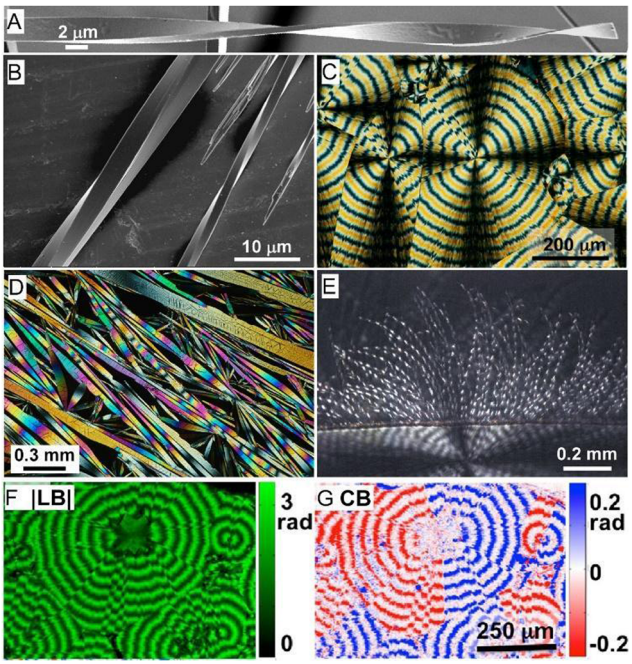

Fig. 3 (A) SEM of twisted *N*-(2-thienylcarbonyl)glycine crystals grown from vapor.[121] Adapted with permission from ref. 121 Copyright 2015, The Royal Society of Chemistry. (B) Cryo-SEM of several twisted benzamide (form II) needles with different cross-section sizes and pitches grown from aqueous solution.[120] Adapted with permission from ref. 120 Copyright 2020, Wiley-VCH. (C) Polarized light optical micrograph of aspirin spherulite grown in the presence of salicylic acid. Concentric banding is a tell-tale feature of in-concert twisting of radial crystallites. (D) Assortment of hippuric acid needles grown from the melt between crossed polarizers. Most needles are twisted as indicated by the modulation of the interference colors. However, some large crystals show much more homogeneous retardance, indicating that the process of untwisting is mostly completed in these crystals. Adapted with permission from ref. 134 Copyright 2010, American Chemical Society. (E) Polarized light optical micrograph of a compact banded δ-mannitol spherulite growing from the melt in the presence of poly(vinylpyrrolidone) (lower part of the image). The compact spherulite opens into isolated twisted fibers when the material penetrates a vapor bubble (upper part of the image).[132] Adapted with permission from ref. 132 Copyright 2012, American Chemical Society. (F) and (G) Micrographs of the absolute value of linear retardance (|LB|) and circular retardance (CB), respectively, of aspirin spherulites grown in the presence of salicylic acid and obtained using Mueller matrix polarimetry. Different signs of CB correspond to different senses of twisting in antipodal parts of the same spherulite. Panels (C), (F) and (G) have been adapted with permission from ref. 119 Copyright 2013, American Chemical Society.

2.4.2. Dislocations. Crystals may respond to disturbances during growth by sometimes encoding linear defects such as screw dislocations in their structure. To relieve the stress around dislocation lines, crystals can respond by showing linear (far from the core) and non-linear (in the core) elastic distortions. This is most vivid in whisker-like crystals in which one screw dislocation parallel to the growth axis can result in baroque nanocrystalline screws—Eshelby twisting (Fig. 4A).[145] Simulations of screw dislocations under the constraints of a force field are illustrative of the mechanical relaxation.[146–148] Alternatively, a helix of a given sense can be viewed as a helix

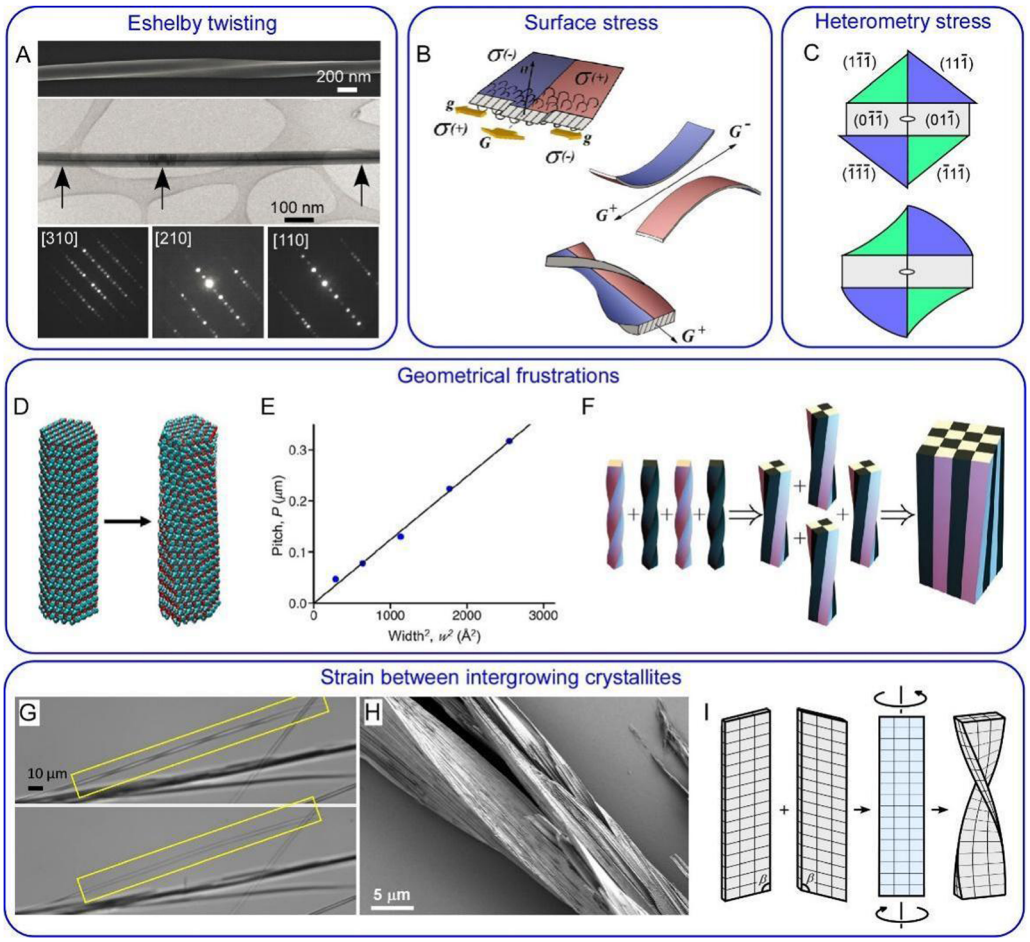

Fig. 4 Twisting mechanisms. (A) Eshelby twisting in GeS nanowires. Upper part: SEM image of a twisted nanowire. Middle part: TEM image of a nanowire with Eshelby twist. The dark line in the middle of the wire is in contrast to an axial screw dislocation. Lower part: convergent beam electron diffraction patterns taken from the locations marked by black arrows. They demonstrate the change of the crystal orientation along the wire from [110] to [210] and then to [310] with respect to the incident electron beam. Adapted with permission from ref. 158 Copyright 2019, Springer Nature. (B) Surface stress in thin crystals illustrated for polymer lamellae. Due to the difference in the polymer chain folding with respect to the growth front orientation (*G* and *g* indicate growth in the direction of lamella elongation and in the perpendicular direction, respectively) different parts of the lamella develop different signs of surface stress, σ, depicted in red and blue. If these two parts are separated, they would bend in opposite directions. But when bound together they decrease their elastic energy by twisting. Adapted with permission from ref. 152 Copyright 2016, Springer International Publishing. (C) Schematic diagram of heterometry stress in resorcinol crystals grown in the presence of tartaric acid. Enantiomorphous {11$\bar{1}$} blue and {1$\bar{1}\bar{1}$} green faces adsorb and overgrow tartaric acid differentially. This can result in a change in lattice constants in corresponding growth sectors followed by the formation of sector specific strain and stress. Stress relaxation produces a twist moment at the crystal tip and twists the crystal. Adapted with permission from ref. 133 Copyright 2011, American Chemical Society. (D) Trigonal benzil nanocrystalline rod before (left) and after geometry optimization (right). Twisting is due to the intrinsic tendency of a comparatively small number of molecules decoupling themselves from a lattice characteristic of a large periodic crystal. (E) Pitch of an optimized benzil nanorod as a function of its cross-sectional area. Panels (D) and (E) are adapted with permission from ref. 154 Copyright 2020, American Chemical Society. (F) Untwisting during assembly of smaller components with a geometrical frustration. At each step, four identical twisted silicone rods are glued together in full contact, and the resulting structure is relaxed to its elastic energy minimum. Adapted with permission from ref. 156 Copyright 2019, The Royal Society of Chemistry. In both cases, panel (E) and (F), the pitch is proportional to the area of the rod cross-section as predicted by the theory.[156] (G) Dissolution of one of two layers served to transform a twisted pair of benzamide (form II) crystals (upper image) into a single straight crystal (lower image). (H) Partial sublimation of benzamide in vacuum reveals a complex intergrowth of fine lamellae. (I) Schematic diagrams illustrating creation of misfit stress, twist moment, and twisting at the interface of (010) benzamide contact twin. Panels (G–I) are adapted with permission from ref. 120 Copyrights 2020, Wiley-VCH.

of the opposite sense from an orthogonal direction. Many dislocations orthogonal to the growth direction could lead to an overall twist in the direction perpendicular to the cores.[149]

2.4.3. Surface stress. Surface stress associated with desymmetrization at interfaces remains a credible mechanism for mechanical deformations, especially for thin lamellae of chain folded polymers (Fig. 4B). The story of how this hypothesis was developed and demonstrated at Bell Laboratories was vividly told recently.[150] New evidence for this mechanism in polyethylene, among other polymers,[151] comes from focused X-ray scattering.[152]

2.4.4. Heterometry. Many twisted crystals display their nonclassical morphologies in the absence of impurities (in evidence), while in other cases, additives appear to be crucial to the process of twisted crystal growth. Impurities

contained within mixed crystals from stereoregular mechanisms may give rise to sub-volumes of crystals with different metric constants, sub-volumes nevertheless smoothly connected. The strain, and associated stress, may lead to twist moments in suitably dissymmetric crystals.[153] Resorcinol crystals of the β phase will twist in opposite directions when grown in the presence of D- and L-tartaric acid (Fig. 4C).[133] This demonstrates that additives can not only drive twisting but determine the twist sense. Even though tartaric acid is not an obvious impurity in non-isomorphous resorcinol, in crystals growing from supercooled melts, diffusivity is diminished and chemical entities may be entrapped that would be excluded during solution growth closer to equilibrium conditions. Salicylic acid is a powerful "twisting agent" for aspirin.[119] Nevertheless, measuring small differences in additive concentration in sub-volumes of micron-size crystals challenges the limits of chemical analysis at present.

2.4.5. Geometrical frustration. Geometrical frustration has recently emerged as an explanation for twisting in some cases. A cornerstone of the science of crystallography that has redounded since the 19th century is the crystallographic restriction, the notion that only certain rotational symmetries are compatible with three-dimensional lattices. This principle did not survive the discovery of quasi-periodic lattices; nevertheless, it remains a guide for the vast majority of materials characterized using the 230 Schönflies–Federov space groups. However, it is a strange idea from the point of view of local interactions between molecules. During association, molecules may organize with whatever point symmetries that they should choose, given the inexhaustibly large number of possible molecular structures. Molecules follow local forces. They cannot be aware of the crystallographic restriction until they are part of a crystal. This is a process, the process of growth. Simulations of nanocrystals show that some materials are intrinsically twisted (Fig. 4D and E).[154] Atomistic simulations of nanocrystals show that even in the absence of dislocations, aggregates of *ca.* 1000 molecules or more (comparable to the size of nuclei), resist conforming to allowed rotational symmetries by twisting. Local, non-crystallographic interactions lead to geometrical frustration[155] that cannot be realized globally and is manifested as a twist deformation, a compromise between the local interactions and the rules of crystallography that govern semi-infinite constructions. This was demonstrated with intrinsically twisted entities made from silicone rubber, forced to "grow" by untwisting individual helicoids and gluing them into larger ensembles (Fig. 4F).[156] On a nanoscale, many crystals made from dissymmetric molecules may forgo translational symmetry. Sometime later, in order to take advantage of the thermodynamic driving force of growth, larger crystals may untwist because now the energy penalty for maintaining a lattice-less structure is increasingly burdensome. This work has helped us to reframe the question "Why are so many crystals twisted?" to "Why are so many crystals straight? "[146]

2.4.6. Strain between intergrowing crystallites. Strain between intergrowing crystallites is another mechanism recently brought into consideration.[120] Benzamide, the first polymorphic crystalline compound, crystallizes from supercooled solutions as fine needles (Fig. 3B). Micrographs show crystalline bilayers in which one needle growing on top of another causes the underlying layer to twist (Fig. 4G). At higher temperatures, when the overlayer dissolves and retreats, the underlayer straightens. Here, twisting is vividly manifested in the assembling of independent lamellae. A complex lamellar organization of benzamide crystals was also observed by electron microscopy (Fig. 4H).[120] Orientationally mismatched ribbons will have an associated strain at the interface. This results in a helical structure with a pitch $P = 2\pi h/\sin(2\beta - \pi)$, where β is the angle between the lattice planes, and h is the bilayer thickness (Fig. 4I).[157] The observed linear $P(h)$ dependence supports this mechanism.

2.5. Mechanics

Twisted crystals are known for all types of materials with a wide range of cross-sections with diameters from nanometers to a few centimeters. A majority of them, however, are molecular crystals growing at high homologous temperatures, T/T_m = 0.6–0.98, with small cross-section sizes, h = 50 nm–5 μm. Keeping in mind that the elastic modulus of molecular crystals was shown to decrease linearly as T/T_m increases,[159] the force required to twist such a crystal will be small, thereby providing a rationale for the ubiquity of the phenomenon.

The dependence of pitch, P, on cross-section size, h, typically obeys a power law $P \propto h^n$ with the exponent n close to 1 (Fig. 5).[38,121,132] This suggests that the twist is determined from the rigidity of a cross-section and the crystal untwists as it thickens. Indeed, the process of untwisting was experimentally observed for hippuric acid[134] and mannitol.[132] The closeness of

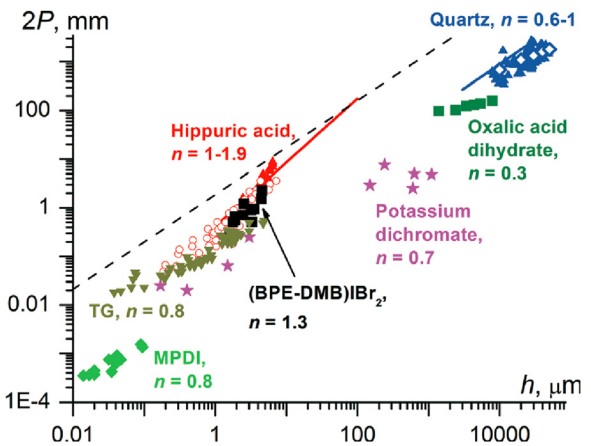

Fig. 5 Correlation between the full twisting period ($2P$, 2π rotation, mm) and the smallest crystal size in a cross-section (h, μm). Blue symbols: quartz (up triangles, open diamonds, and the line corresponds to different sources of data); olive squares: oxalic acid dihydrate; magenta stars: potassium dichromate; black squares: (1,4-bis[2-(pyrene-1-yl) vinyl]-2,5-dimethylbenzene)IBr_2, (BPE-DMB)Ibr_2; red symbols: hippuric acid (up triangles = melt grown crystals); open circles = vapor grown crystals; line = melt and solution grown crystals; dark yellow down triangles: *N*-(2-thienylcarbonyl)glycine, TG; green diamonds: poly(*m*-phenylene isophthalamide), MPDI. The values of n are exponents in the fit $P = kh^n$. In the region below the dashed line, $2P < 10^3\pi h$, elastic stress in twisted crystals should relax, at least partially.[121] Adapted with permission from ref. 121 Copyright 2015, The Royal Society of Chemistry.

the exponent to unity means that stress can remain elastic only if the twist is induced by stress between comparably sized domains located parallel to the crystal elongation direction (mechanisms in Sections 2.4.4 and 2.4.6). In all other cases, partial or full relaxation of elastic stress is expected. It is commonly observed that twisted morphologies are preserved upon crystal fragmentation, supporting the plastic nature of the deformation.

For most crystals, shear strain on the crystal surface is higher than $\gamma = \pi h/(2P) > 0.001$ (Fig. 5). On deformation mechanism maps,[160] crystallization at homologous temperatures T/T_m = 0.6–0.98 corresponds to diffusional flow, dislocation creep, or conventional plastic flow. Nanoscale molecular crystals (h = 50 nm–5 μm) typically contain no or very few dislocations,[121] meaning that plasticity cannot be dislocation mediated. However, it can be easily mediated by the flow of vacancies.

3. Photomechanical molecular crystals

3.1. Advantages of using photomechanical molecular crystals

3.1.1. Using photons to control motion. Machines powered by photons instead of electrons could be fueled with lightweight optical fibers or operated in free space without physical attachment to a power source. The development of such light-powered machines requires materials that directly convert light energy into mechanical work. Historically, such photoresponsive solids were composed of macromolecular soft materials like polymers or gels that incorporate a photoisomerizable active unit, usually an azobenzene moiety that undergoes a light-driven *cis–trans* isomerization reaction. Early on, it was realized that some degree of order was necessary to align the molecular subunits, and currently, liquid crystalline polymers and elastomers are the most common photomechanical materials.[161] An alternative way to order the photoreactive molecules is to simply allow them to crystallize in the absence of a polymer backbone. Over the last twenty years, crystals composed of photoreactive molecules have emerged as a new frontier in the development of photomechanical materials, prompting several reviews on photomechanical, photodeformable, or photoresponsive molecular crystals.[29,162–168]

3.1.2. Molecular tunability. Small molecule chemistry allows a designer to harness the full potential of synthetic chemistry to make a wide variety of molecules with desired properties. In addition to varying the core photoisomerization functionality, it is also possible to use different substituents to affect the strength and directionality of intermolecular interactions (within the realm of crystal engineering) and the electronic state structure that governs the photophysics (absorption wavelength, photochemical quantum yield, *etc.*). The chemical compatibility of a photochrome with a polymer scaffold is no longer a concern.

3.1.3. Unambiguous structure–function correlation. While polymers typically suffer from chain length variations (polydispersity) and the presence of chemical defects, small molecules can be purified to a high level (>99%). Furthermore, it is usually possible to grow single crystals of both reactant and product molecules that are suitable for structure determination *via* single-crystal X-ray diffraction analysis. The ability to map out a structure at an atomic level provides a unique window into the dynamics and makes these systems amenable to classical or quantum mechanical calculations.

3.1.4. High elastic modulus. Organic or coordination compound molecular crystals typically have an elastic modulus E in the range of 1–40 GPa,[169] which is much higher than that of elastomers (<10 MPa) or gels (<1 MPa) and comparable to that of glassy polymers. The importance of E can be seen if we consider the simple one-dimensional expansion of a rod, in which the mechanical work (elastic energy) generated by a photochemical force F, that expands the rod from length L_0 to $L_0 + \Delta L$, is given as

$$W = \int_0^{\Delta L} F\,\mathrm{d}x = \frac{AE\Delta L^2}{2L_0} \tag{4}$$

where W is the work and A is the cross-sectional area of the expanding rod. In this simple limit, the amount of work for a given strain (ΔL) is linearly proportional to the modulus E.

3.1.5. Ultrafast response time. A polymer-based material is limited by the viscoelastic response time of the host, while a mechanical perturbation in a crystal can propagate much faster. Previous work on impulsive temperature jumps has shown that the ultrafast deformation of a crystal is limited by the speed of sound, so rapid (<1 ns) photochemical reactions should generate motions on similar timescales. The initial reports of crystals responding on a microsecond scale[170] are probably due to photothermal effects.[29,30] Naumov and co-workers recorded acoustic soundwaves emanating from exploding thermosalient crystals.[171]

3.1.6. High work density. The absence of a host material or polymer backbone means that a molecular crystal contains the highest possible density of photochromic molecules. Assuming that the packing geometry allows the molecular photoisomerization events to add constructively, the work density should be proportional to the photochrome density and thus it should be highest for molecular crystals.

3.1.7. Challenges. Given the potential advantages of molecular crystals listed above, it may be surprising that they are relative latecomers in the photomechanical research field. However, there remain both practical and fundamental challenges in converting crystals into useful engineering materials. At a molecular level, there are the usual challenges of designing photochromes that can be reversibly cycled, are resistant to side reactions that degrade performance, and crystallize in favorable orientations. At the level of the material, one has to manage the tendency of crystals to shatter due to the internal stress that accompanies a photochemical reaction. The second major issue is the processing of crystals into usable materials on a macroscopic scale. A further challenge is the solubility of most of these organic crystals in aqueous or organic solvents, which could lead to degradation of the material or incompatibility

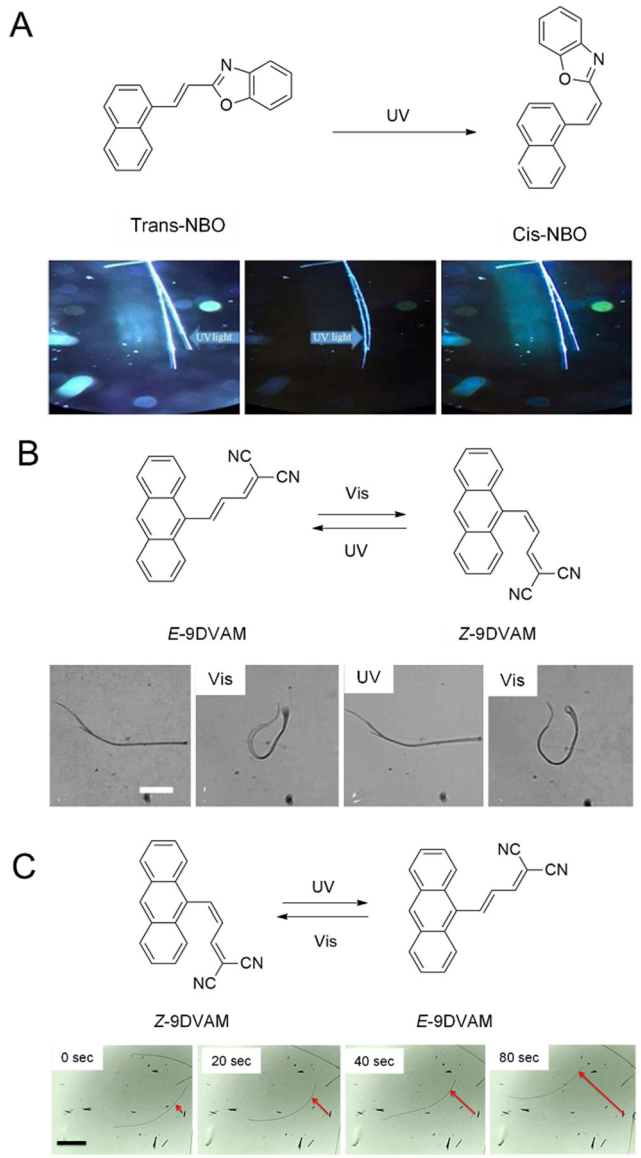

Fig. 6 Optical micrographs of (A) *trans*-NBO needle-like microcrystals bending towards UV (365 nm).[186] Adapted with permission from ref. 186 Copyright 2018, Wiley-VCH (B) E-9DVAM nanowires *ca.* 230 nm in diameter actuated during alternating exposure to UV and visible light. The scale bar is 10 μm.[187] Adapted with permission from ref. 187 Copyright 2016, The Royal Society of Chemistry (C) Z-9DVAM microwire irradiated simultaneously with UV and visible light. The microwire propagates on the surface after 20, 40, and 80 s, as indicated by the red arrow. The scale bar is 230 μm.[190] Adapted with permission from ref. 190 Copyright 2021, Wiley-VCH.

with applications that use solvents. This problem has been partially addressed by using protective coatings, for example, a poly(vinyl alcohol) layer,[172,173] thin silica sheath,[174] or crystalline ceramic shell.[175] Recently, a number of hybrid materials composed of crystals and polymers have been reported, and many of them have superior properties relative to the organic crystals alone.[173] Finally, questions concerning photon-to-work efficiency and incorporation into actual devices are yet to be fully addressed. In the following sections, we attempt to give an overview of this relatively new field of material research, which focuses on how molecular crystals can give rise to novel and possibly useful mechanics.

3.2. Types of photochemical reactions in photomechanical crystals

3.2.1. Categorization based on the photochemical process. A crystal is composed of ordered photochromes that can photochemically react to produce work. The photochemistry can be intramolecular, such as unimolecular photoisomerizations, or intermolecular, such as [2+2] or [4+4] photodimerizations. In the following section, we summarize most of the relevant photochemical reactions in photomechanical crystals.

3.2.2. *Trans–cis* photoisomerization. Photomechanical crystals formed by *trans–cis* photoisomerization of azobenzene and azobenzene derivatives are widely studied.[82,107,176–178] Although unsubstituted azobenzene is not reactive in bulk crystalline form due to packing constraints, appropriate substitution on the phenyl rings can open up room in the crystal for photoisomerization. The earliest example of photoinduced bending of an azobenzene crystal was reported by Koshima *et al.* in 2009.[179] The diversity of synthetic procedures that can lead to the formation of azobenzene derivatives helped researchers design azobenzenes with different photophysical properties. The majority of azobenzene derivatives are synthesized *via* the azo coupling of a diazonium salt with an electron-rich aromatic nucleophile. Other synthetic procedures have been surveyed in a review by Merino.[180] UV irradiation of *trans*-azobenzene photomechanical crystals induces a phase change, allowing them to bend with the concurrent generation of a thermally unstable *cis* isomer that reverts to the *trans* form on the order of seconds to days. The *cis* isomer reset rate and wavelength of light absorbed by the *trans* isomer can be modulated by attaching different electron-donating or withdrawing groups to the phenyl rings. Besides the ability of these crystals to be actuated in response to light, chiral azobenzene derivatives can bend and twist in a specific direction depending on the crystal face being irradiated.[181] While most *trans*-azobenzene derivatives absorb in the UV, co-crystal engineering incorporating halogenated azobenzenes produced photomechanical crystals that can absorb visible light (532 nm) to deform with a slow reset time.[47,182,183] Pseudorotaxane crystals composed of axial azobenzene molecules showed subtle bending when exposed to UV light, paving the way for designing derivatives with different ring elements.[184] While azobenzenes were mainly incorporated in liquid crystalline polymers to induce photomechanical motion,[185] some authors opted to investigate the photomechanics of perhalogenated azobenzene derivatives and the effect of halogen bonds on their photomechanical performance.[47]

Photomechanical crystals that rely on the *trans–cis* photoisomerization of olefins are less common due to the tight packing of the crystals, which restricts motion. However, there are a few exceptions. Needle-like crystals of naphthylvinylbenzoxazole[186] show directional photoinduced bending upon exposure to UV light (Fig. 6A). Single crystals or nanowires of (*E*)-2-(3-(anthracen-9-yl)allylidene)malononitrile (*E*-9DVAM)

show bending towards light when irradiated with visible radiation and can be reset by exposure to UV light (365 nm)[187] (Fig. 6B). Ultra-long microwires of (*Z*)-2-(3-(anthracen-9-yl)allylidene)malononitrile (*Z*-9DVAM) can twist and propagate autonomously when exposed simultaneously to visible and UV light (Fig. 6C). Similar anthracene derivatives show unique photoisomerization-induced coiling and solvent incorporation that is facilitated by the presence of surfactants such as cetyltrimethylammonium bromide (CTAB) and sodium dodecyl sulfate (SDS).[49,188,189]

3.2.3. [2+2] photodimerization. Photocycloaddition in crystalline olefins has been studied for decades. A systematic analysis of [2+2] photocycloaddition outcomes *vs.* crystal packing was pioneered by Schmidt and Ginsburg,[191] which revealed the highly demanding topochemistry of this reaction. Most of the solid-state [2+2] photodimerization reactions occur between olefin carbons attached to an aromatic ring such as in cinnamates and chalcones.[192,193] However, small-molecule derivatives of benzylidenedihydrofuranes (*E*-BDHF), reported by Naumov, also show photomechanical bending and photosalience upon continuous UV irradiation[182] (Fig. 7A). Lu and co-workers observed the bending, curling, rolling, and photosalience of a styrylbenzoxazole derivative upon UV light exposure.[105] In a later study, they investigated a series of molecular crystal photomechanical actuators with fluorine substitution. The intermolecular F···H–C interaction inside the flat crystals modulated the photomechanical response, which led to positive/negative phototropism of the crystal actuators.[186,195] Photomechanical actuators made from halogen-substituted naphthalene acrylic acids were also investigated[196] and most recently 3,5-dichlorophenyl-containing chalcone polymorphic crystals showed both thermal and photomechanical bending.[197] Vittal and co-workers showed that [2+2] photodimerization leads to photosalience in a coordination polymer of divalent lead.[198] Thin ribbon-like crystals of 4-chlorocinnamic acid can twist and bend upon exposure to UV light, while thicker crystals (5–10 microns) of the same material do not show any response[70] (Fig. 7B). Extreme photosalience of (*E*)-4-fluorocinnamaldehyde malononitrile (4FCM) was observed upon exposure to UV or visible light.[199] (Fig. 7C). Photomechanical bending of macroscopic-scale crystals of 1,2-bis(4-pyridyl)-ethylene-based pyridinium salt was observed upon exposure to UV light. The [2+2] photodimerization of the olefin bond leads to increase in the fluorescence of the bent crystal, offering a visual cue of the photomechanical work.[200]

3.2.4. [4+4] photodimerization. [4+4] photodimerization between aromatic groups can also lead to a photomechanical response, with anthracene derivatives being the most commonly used class of photochromes. Many anthracene derivatives are photochemically reactive in the solid state since their molecules can pack parallel in planes and are close enough to satisfy Schmidt's conditions.[191] Fig. 8 shows some anthracene derivatives that can be obtained as photomechanical crystals. Like the [2+2] photodimerization, this reaction reduces conjugation and the photoproduct absorption is strongly blue-shifted. This negative photochromic reaction[201] can theoretically result in 100% conversion[202] even in optically thick crystals. Some of the earliest anthracene photomechanical crystals studied were

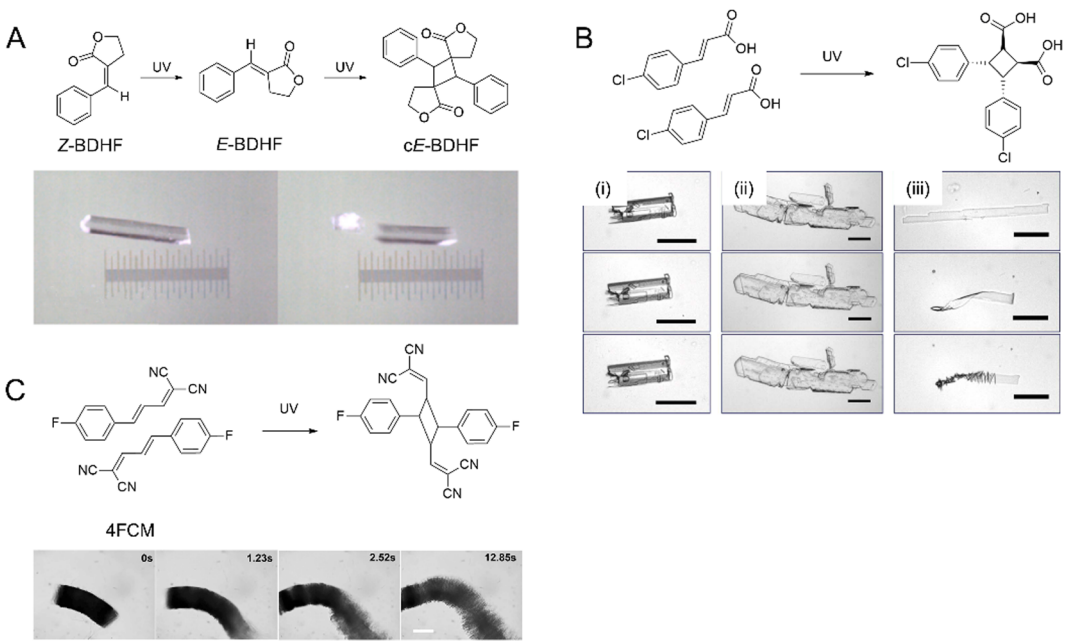

Fig. 7 (A) Snapshots of photosalinet *Z*-BDHF crystals splitting into fragments after UV exposure and [2+2] photodimerization.[194] Adapted with permission from ref. 194 Copyright 2015, American Chemical. Society (B) [2+2] photodimerization of 4Cl-CA. Optical images of three crystal shapes of 4Cl-CA (i) rectangular prism crystal, (ii) plate crystal, and (iii) microribbons. Top images were taken before UV (365 nm) exposure, the middle images were taken after 5 min exposure, and the bottom images were taken 1 h after exposure.. Scale bars: 50 μm.[70] Adapted with permission from ref. 70 Copyright 2012, The Royal Society of Chemistry. (C) Optical micrograph of a crystalline 4FCM nanowire bundle undergoing [2+2] photocycloaddition when exposed to 405 nm.[199] The scale bar is 50 μm. Adapted with permission from ref. 199 Copyright 2020, The Royal Society of Chemistry.

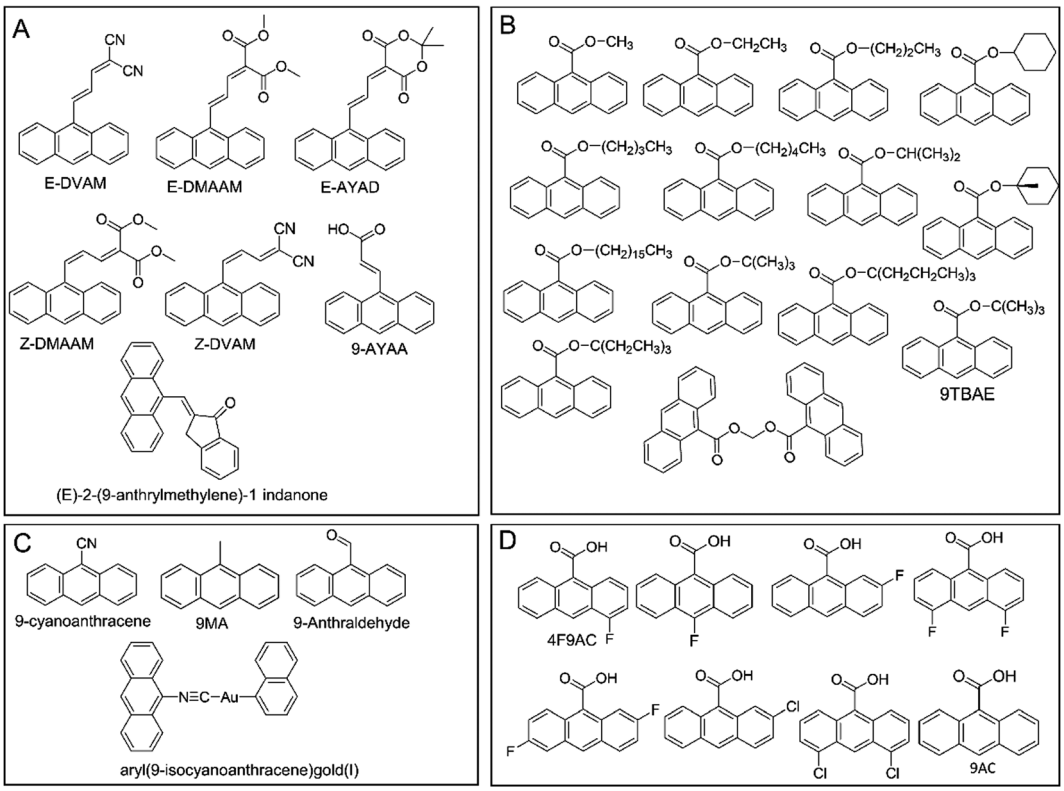

Fig. 8 Chemical structures of anthracene derivatives that can be made into photomechanical crystals: (A) conjugated anthracene derivatives, (B) 9-anthracene carboxylate esters, (C) miscellaneous anthracene derivatives, and (D) 9-anthracene carboxylic acid and its halogenated derivatives.

derivatives of 9-anthracene carboxylate esters. Nanowires made from these derivatives expand anisotropically along the long axis by as much as 15% after irradiation with 365 nm light.[203–206] The ability of simple anthracene derivatives such as 9-methylanthracene (9MA) to form different crystal shapes helped clarify the mechanism involved.[207,208] Other solid-state photodimerization reactions that have been studied include 9-cyanoanthracene[209,210] and 9-anthraldehyde.[94,211] Thin plate-like microcrystals of an indanone-substituted anthracene, (*E*)-2-(9-anthrylmethylene)-1-indanone, gradually bent away from UV light (365 nm) due to a [4+4] photodimerization reaction between the anthracene units stacked parallel in a head-to-tail manner[212] (Fig. 9A).

The [2+2] and [4+4] photodimerization reactions tend to have limited reversibility. Anthracene photodimers can, in principle, be reverted to monomer units by heating or irradiation at 254 nm. In practice, thermal ''unzipping'' at elevated temperature is detrimental to the crystal structure, and 254 nm irradiation cannot achieve 100% back reaction due to the formation of a photostationary state and secondary photoreactions. However, thermal reversibility can be achieved when substituted anthracenes crystallize in a head-to-head ''syn'' arrangement,[213] rather than a head-to-tail ''anti'' arrangement common for most 9-substituted anthracenes. This reversible photochemistry offers the potential to use photomechanical crystals of 9-anthracene carboxylic acid (9AC) and its derivatives as thermally reversible (T-type) photoactuators[213–215] (Fig. 9B).

3.2.5. Photoresponsive coordination/organometallic complexes. The first observation of photomechanical motion in a molecular crystal was reported by Abakumov and Pierpont in 1992 in a rhodium organometallic complex.[216] Boldyreva, Naumov *et al.* studied the photosalient behavior of microcrystals made from the cobalt coordination compound $[Co(NH_3)_5(NO_2)]Cl(NO_3)$.[60] When irradiated with UV light, crystals of this compound undergo sudden jumps and leap over distances 100 times their size. Needle-like crystals of the compound were used to study the photomechanical bending in crystals, and resulted in a plausible mathematical model.[217] The model comes with several requirements such as a homogeneous photoreaction, a needle-like crystal habit, bending as the sole photomechanical effect, and a reversible photochemical reaction. From such a point of view, this organometallic complex was suitable since exposure to blue light causes the nitro group in the ''nitro form'' to switch its coordination atom from nitrogen to oxygen to afford a linkage isomer, the ''nitrito form''. The process is thermally reversible, and thus the photomechanical reaction is of T type. Ito and Seki reported the synthesis of the novel derivative aryl(9-isocyanoanthracene)gold(I) complex. Crystals made from this complex exhibit photosalience upon UV irradiation and thermosalience upon cooling, providing a rare example of a dynamic crystal powered by multiple stimuli[218] (Fig. 10).

3.2.6. Photocyclization of diarylethenes and furylfulgides. Many of the photomechanical crystals studied are composed of thermally reversible (T-type) photochromes that reset over a

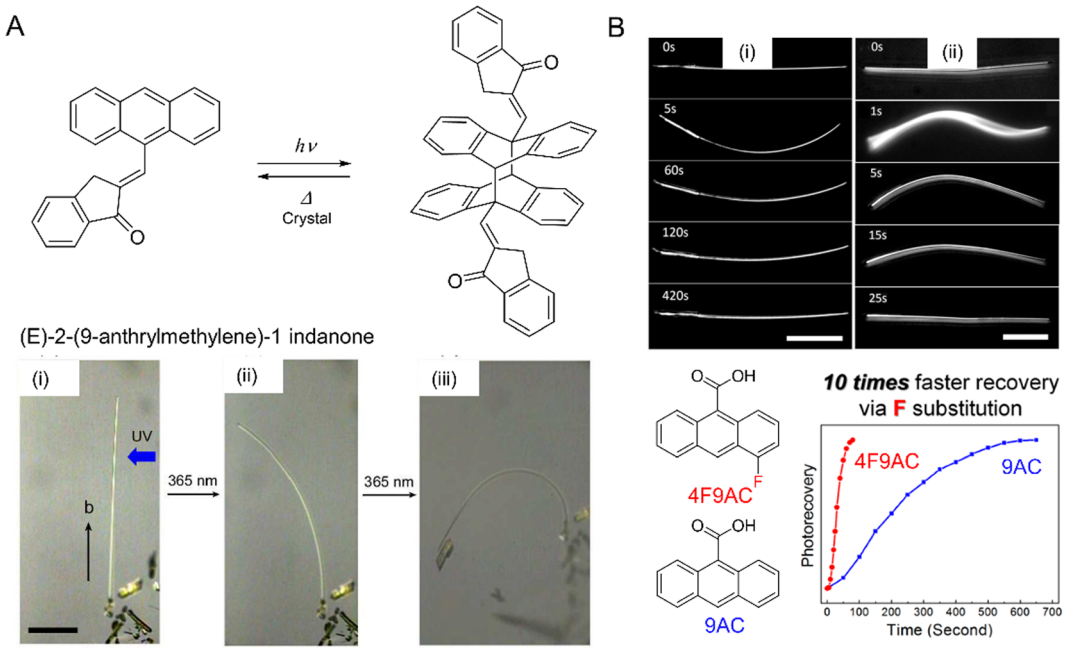

Fig. 9 (A) Chemical structures and photochemical reaction. Pictures of narrow plate-like microcrystals of (*E*)-2-(9-anthrylmethylene)-1-indanone irradiated with UV (365 nm) leading to [4+4] photodimerization and bending of the crystal (i) before and after UV irradiation from the right for (ii) 4 and (iii) 13 min. The scale bar is 100 μm.[212] Adapted with permission from ref. 212 Copyright 2016, The Royal Society of Chemistry. (B) Optical micrographs of (i) 9-anthracene carboxylic acid (9AC) and (ii) 4-fluoro-9-anthracene carboxylic acid (4F-9AC). The 4F-9AC crystal completely untwists in 25 s, while the 9AC crystal requires 420 s to unbend. Both scale bars are 50 μm. Plot: Photorecovery *vs.* time plot for 4F-9AC *vs.* 9AC.[214] Adapted with permission from ref. 214 Copyright 2014, American Chemical Society.

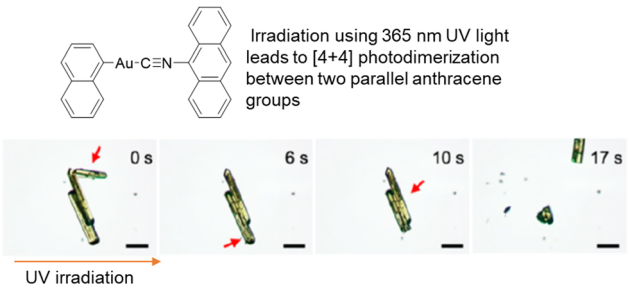

Fig. 10 Optical micrographs of microcrystals of an aryl(9-isocyanoanthracene)gold(I) complex exhibiting photosalient effects when irradiated with UV light (365 nm). The thick red arrows indicate the position of the crystals that jumped. Scale bars represent 50 μm.[218] Adapted with permission from ref. 218 Copyright 2021, American Chemical Society.

period of seconds to days. Highly stable photochromes whose isomerization can only be reversed by absorption of a second photon are referred to as P-type. Diarylethenes[219] are a promising class of molecules for optical memory with excellent thermal stability. The photochemistry of diarylethenes involves photoinduced ring-opening upon exposure to visible light and ring closure after irradiation with UV light. The small structural changes of diarylethene derivatives during photoreaction facilitate their photochromism in the crystalline state. The accompanying change in crystal shape was the basis for the design of P-type photomechanical actuators. The first photomechanical diarylethene crystal was reported by Irie *et al.* in 2007[220] (Fig. 11A). Diarylethene photomechanical crystals are known for their photochemical durability, recycling frequency, and fast response time. Photomechanical cocrystals containing diarylethenes can be actuated over 1000 times without showing signs of fatigue or photodegradation. A detailed investigation into the reversible photomechanical twisting of ribbon-like crystals of 1,2-bis(2-methyl-5-phenyl-3-thienyl)perfluorocyclopentene showed a unique behavior that depends on the illumination direction. A helicoid-to-cylindrical twisting mode was obtained by simply varying the direction of UV illumination with respect to the crystal facets. This method provides a convenient way to generate a variety of photomechanical motions of a single crystal.[221] Uchida and Morimoto reported the synthesis of a diarylethene containing a perfluorocyclohexene ring. Crystals grown by sublimation had a hollow rectangular morphology and were loaded with fluorescent microbeads. These crystals show violent photosalient photomechanical action when irradiated with UV light, exploding and releasing the loaded microbeads.[222] Furylfulgides are a close relative of the diarylethenes with limited application as photomechanical actuators due to their inferior photomechanical properties. However, plate-like microcrystals made from a furylfulgide showed reversible photomechanical bending accompanied by a color change from yellow to orange when irradiated with UV light[223] (Fig. 11B).

3.2.7. Intramolecular hydrogen transfer. Phenylhydrazones are a class of photochromes that rely on excited-state intramolecular proton transfer and are photochemically active

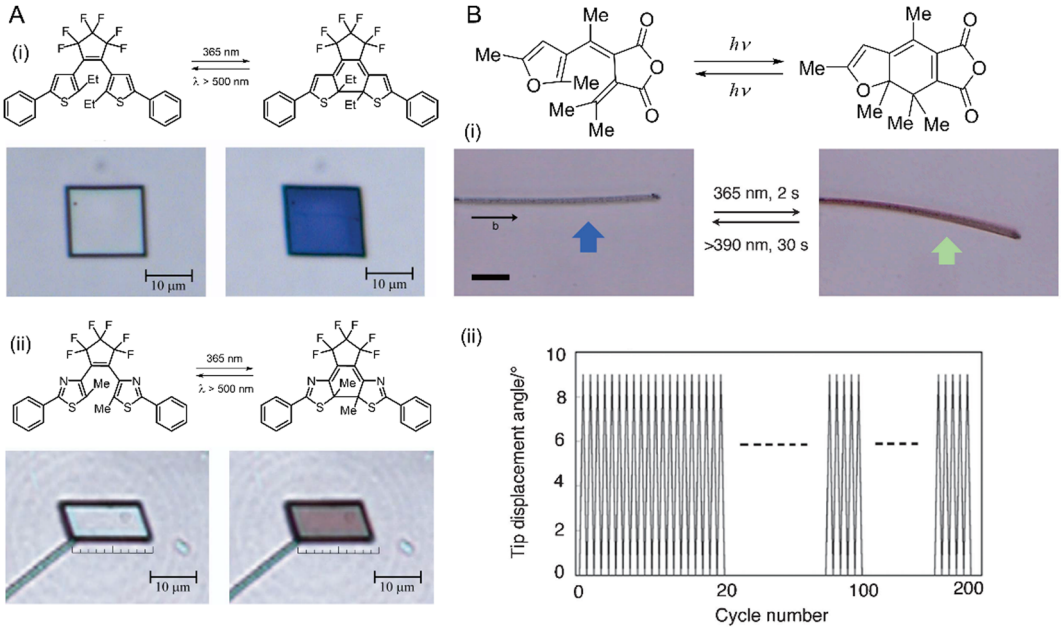

Fig. 11 Photomechanical effects of diarylethene crystals. (A) Chemical structures and optical microscopic images of the photomechanical deformation of two diarylethene compounds (i) and (ii) upon irradiation with ultraviolet (365 nm, left) and visible (500 nm, right) light leading to a reversible contraction by 7%. Crystal thickness ≈ 330 nm.[220] Adapted with permission from ref. 220 Copyright 2007, Springer Nature. (B) Chemical structures and photoreaction of a furylfulgide derivative. (i) Images of the reversible bending (blue arrow, 365 nm; green arrow, >395 nm) of a narrow, plate-like crystal of furylfulgide by as many as 200 cycles (ii). Scale bars are 20 μm.[223] Adapted with permission from ref. 223 Copyright 2012, The Chemical Society of Japan.

in polymers, liquid crystals, and as neat crystals.[224–226] To our knowledge, the crystals have not been utilized for photomechanical applications. Photoinduced intramolecular hydrogen transfer occurs between a phenolic hydrogen atom and a nitrogen atom in salicylidenes *via* a triplet state.[227] This class of molecules can be used as molecular switches.[228] Asahi, Koshima *et al.* studied the photochromic properties of the salicylidenephenylethylamine *N*-3,5-di-*tert*-butylsalicylidene-1-phenylethylamine. Plate-like crystals of the enol-(*S*)-1 and enol-(*R*)-1 enantiomers can twist upon irradiation with UV light, with helicity that depends on the enantiomer used.[229]

3.2.8. Photoinduced production of gas. Photochemical decomposition of some molecules can lead to the formation of gas molecules. Photodecarbonylation of 1,3-dithiophenylpropanone microcrystals under UV light leads to the formation of carbon monoxide with complete disintegration of the crystal.[230–232] Organic azides are prone to photodecomposition with the formation of nitrogen gas and reactive nitrene intermediates that can either polymerize or lead to the formation of rearrangement products.[233] Single crystals of vinyl azides such as 3-azido-1-phenylpropenone, 3-azido-1-(4-methoxyphenyl)-propenone, and 3-azido-1-(4-chlorophenyl)propenone were irradiated with UV light causing the crystals to crack or bend with slight expansion due to the buildup of internal pressure, pushing on the crystalline matrix, and eventually release dinitrogen gas with formation of a reactive vinylnitrene intermediate and disintegration of the crystal[77] (Fig. 12A).

3.3. Examples of crystals as energy transducers

3.3.1. Crystals convert energy to work. A photomechanical crystal can convert absorbed photon energy and transform it to work. By definition, work is equal to the product of force generated multiplied with the displacement. In almost all cases, the force arises from internal stress generated from the simultaneous presence of reactant and product phases. The deformations generated by photomechanical crystals can adopt different modes depending on the size, shape, and orientation of the crystal, and the direction of incident radiation. All of these factors affect the photoinduced stress tensor inside the crystal, which in turn drives the crystal deformation.[29] In the following section, we summarize the different types of photomechanical crystal motions.

3.3.2. Photosalient crystals. When some crystals are taken over a phase transition by heating or cooling internal strain can build up in their interior that is suddenly released, resulting in rapid fracture or deformation. This phenomenon is known as the thermosalient effect.[60,96,234] In a photosalient crystal, the absorbed photons generate crystal strain due to the formation of a photoproduct layer on the surface of the crystal.[192,198,222,235–240] The gradual strain buildup is suddenly released causing the crystal to jump and oftetimes balistically disintegrate. It is thought that photosalient crystals have the potential to generate work.[235] The mechanism of the photosalient effect was studied thoroughly by Naumov and Boldyreva on $[Co(NH_3)_5(NO_2)]Cl(NO_3)$ and 4-hydroxy-2-(2-pyridinylmethylene)-hydrazide.[217,241] An extreme case of explosive photosalience was

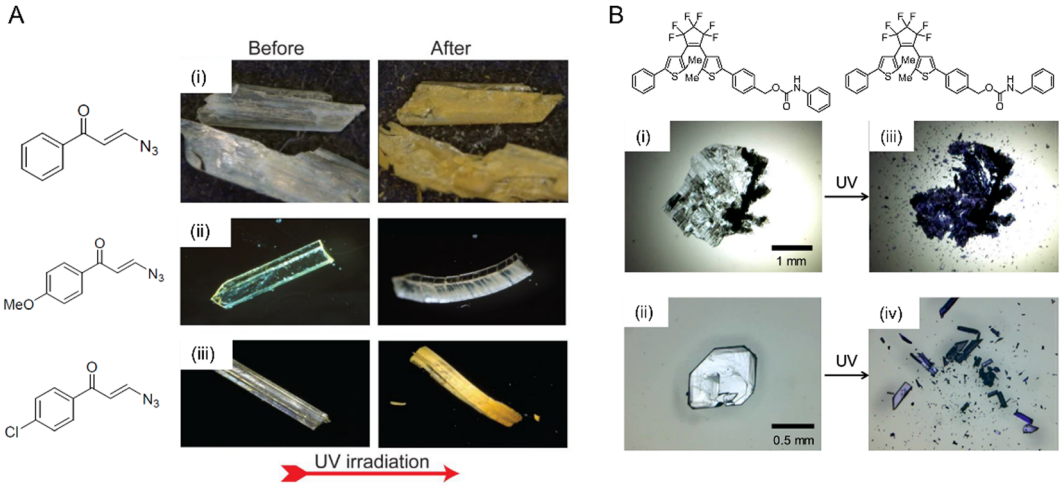

Fig. 12 Mechanical effects due to the evolution of the photosalient effect. (A) Optical micrographs of microcrystals made from (i) 3-azido-1-phenylpropenone with a crystal size of ~1.6 × 0.5 × 0.1 mm, (ii) 3-azido-1-(4-methoxyphenyl)propanone with a crystal size of ~1.5 × 0.3 × 0.1 mm, and (iii) 3-azido-1-(4-chlorophenyl)propanone with a crystal size of ~2 × 0.5 × 0.2 mm undergoing a photomechanical effect with the release of dinitrogen gas upon UV irradiation.[77] Adapted with permission from ref. 77 Copyright 2020, American Chemical Society. (B) Optical micrographs of two diarylethene derivatives undergoing a violent photosalient effect upon UV light exposure. (i) and (ii) Before UV exposure and (iii) and (iv) after UV exposure.[40] Adapted with permission from ref. 40 Copyright 2016, American Chemical Society.

reported by Kobatake and Kitagawa.[40] Diarylethene crystals with urethane bonding can be explosively photosalient producing fragments that can fly as fast as a few meters per second (Fig. 12B).[40] The photosalient effect provides a dramatic illustration of the power that can be generated by photochemistry, but its violently random nature leaves open the question of whether it can be harnessed to generate useful work.

3.3.3. Photomechanical bending of crystals. Bending in response to absorbed light is another commonly observed mode of crystal motion. Photomechanical crystal bending is often observed for systems that do not exhibit photosalience. In photomechanical crystals, the formation of photoproducts on the surface is accompanied by generation of a nonuniform strain due to structural incompatibility between the photoproducts and the reactants, leading to bending away from or towards the light source. The bending motion can be analyzed using mechanochemical models. Kitagawa and co-workers have used the bimetal model described by Timoshenko to address the photomechanical bending speed in relation to the amount of light absorbed and crystal thickness in diarylethene crystals.[242,243] Bardeen and Naumov/Chizhik/Boldyreva, independently from each other, have used models that assume an exponential profile of photoproducts to describe photomechanical bending in other crystals.[207,244]

Long crystals of diarylethene derivatives have been shown to bend reversibly in response to a specific wavelength of light. In some cases, the bending speed was fast enough to impart a momentum and, in some cases, to lift heavy objects.[245] Azobenzene derivatives were extensively studied since they exhibit thermally reversible bending (T-type) with reset times that can be tuned by modifying the chemical structure of the azobenzene derivative. A study of the photomechanical response of halogenated cinnamic acid derivatives, such as 4-chlorocinnamic acid, showed that the thickness of the crystal plays a significant role in determining the photomechanical motion.[70] The degree of bending can be very small; nanowires made from diarylethene[246] (Fig. 13A) or 9AC[247] (Fig. 13B) can bend reversibly following a P- and T-type mechanism, respectively. Highly branched microcrystals of 4-fluoro-9-anthracene carboxylic acid (4F-9AC) can have multiple arms that bend in unison[248] (Fig. 13C) upon exposure to UV light.

3.3.4. Photomechanical twisting. Photomechanical microcrystals with ribbon-like morphologies often twist along the long axis instead of bending, as seen for microneedle-like crystals of 9MA.[207] Microribbons of 9AC can be grown *via* slow evaporation of 9AC solution in ethyl acetate floating on top of water, known as the ''floating drop method''. Irradiation of the surface of the 9AC microribbons with UV light generates a photodimer/monomer interface leading to a reversible isotropic twist[89] (Fig. 14A). 9MA microribbons grown by the floating-drop method can also twist but in a non-reversible fashion.[207] Other examples of twisting photomechanical crystals have been reported for diarylethene derivatives.[221,249] Kobatake *et al.* reported how illumination direction affects the reversible photomechanical twisting of ribbon-like crystals of 1,2-bis(2-methyl-5-phenyl-3-thienyl)perfluorocyclopentene prepared by sublimation[221] (Fig. 14B). Crystalline microribbons made from perylenediimide derivatives have been shown to undergo a continuous twisting under scanning laser irradiation, but the chemical origin of this motion is still unclear[250] (Fig. 14C). pH-Driven reprecipitation of 4F-9AC from aqueous solution led to the formation of branched microcrystals with chiral shape. UV irradiation followed by thermal relaxation of the crystals induced a twist in the arms, causing an overall ratchet-like rotation[109] (Fig. 14D).

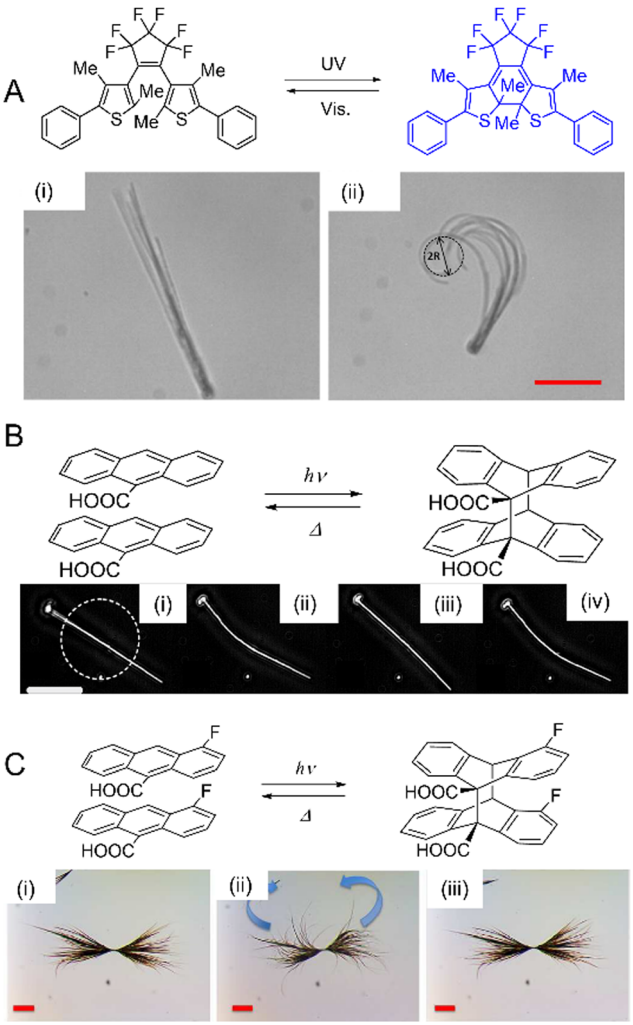

Fig. 13 Examples of crystal bending. (A) Diarylethene derivative nanowires before (i) and after (ii) 365 nm UV light irradiation. R = bend radius. Scale bar = 20 μm.[246] Adapted with permission from ref. 246 Copyright 2018, The Royal Society of Chemistry. (B) Dark field optical micrographs of the nanowire, made from 9AC, with a diameter of *ca.* 230 nm, (i) before UV exposure, (ii) bending after brief exposure to 365, (iii) reversible or resetting after 10 minutes at room temperature, and (iv) bending after brief exposure to 365 nm. Scale bar = 20 μm.[247] Adapted with permission from ref. 247 Copyright 2007, Wiley-VCH. (C) Optical micrographs of highly branched microcrystals of 4F-9AC. (i) Before exposure to UV (365 nm), (ii) during UV exposure with curling branches, and (iii) 10 s after thermal relaxation at room temperature, the arms reset. Scale bar = 25 μm.[248] Adapted with permission from ref. 248 Copyright 2017, The Royal Society of Chemistry.

3.3.5. Photomechanical curling and rolling. Curling crystals show extreme bending with multiple loops. Photomechanical crystals rarely show extreme curling while maintaining their integrity, failing instead by fracture or amorphization. An exception is the photoinduced curling seen in nanowires made from *cis*- or *trans*-dimethyl-2(3-(anthracen-9-yl)allylidene)malonate (*trans*- or *cis*-DMAAM). The photoinduced curling occurs after a brief pulse of visible light initiates the formation of amorphous layer on the nanowire surface[49] (Fig. 15A). The presence of a surfactant speeds up the curling process, and the coiled product loses crystallinity and eventually dissolves.[188] Thin plates of 9MA provide an example of a curling crystal that maintains crystallinity throughout the process. Flat 9MA plates can coil into cylinders during the [4+4] photodimerization reaction, and then uncoil back to flat plates after the reaction was completed and the internal reactant-product strain disappeared.[208] Long microwires of (*E*)-3-(anthracen-9-yl) acrylic acid (9-AYAA) showed a strong photoinduced coiling–uncoiling transition when irradiated with visible light[94] (Fig. 15B).

3.3.6. Photomechanical peeling or delamination. Photoinduced peeling of the photoreactive layer in a crystal was observed for block-like microcrystals composed of *cis*-DMAAM. Special growth conditions lead to the formation of uniform tetragonal microcrystals from aqueous surfactant solutions that are several micrometers thick. A pulse of UV light (405 nm) converts a fraction of molecules on the surface of the crystal to the *trans* isomer, creating an amorphous mixed layer that peels off the parent crystal. This photoinduced delamination can be repeated multiple times on the same block until it is converted into thin slices[46] (Fig. 16A). Kobatake and Kitagawa found that lateral UV irradiation of crystals of a photochromic diarylethene derivative leads to fast peeling of the exposed surface (Fig. 16B), while the same crystal exhibits photosalience when it is irradiated with UV light on one of its wider faces.[251] A similar peeling was observed by Cole and co-workers in a completely different crystal based on linkage isomerization.[78] A related phenomenon has been observed in microribbons made from perylene diimide derivatives. Visible light causes lateral or longitudinal light-induced morphological change between the layers. This morphological change originates from the directional sliding of the stacked layers with respect to one another between their polar surfaces. Upon exposure to an electron beam, the laterally displaced layers slide back to their original positions[76] (Fig. 16C).

3.3.7. Photomechanical autonomous motion. The ability to harness light energy and transform it into rapid, autonomous motion has been shown to occur in some photoresponsive liquid crystal elastomers.[252–255] However, autonomous motion tends to be slow and perpetuated by a self-shadowing mechanism or intermittent irradiation from a light source.[256] Long crystalline microwires composed of (*Z*)-2-(3-(anthracen-9-yl)allylidene)malononitrile (*Z*-9DVAM) can be continuously actuated when exposed to a combination of ultraviolet and visible light. The photoinduced motion mimics the oscillations of biological flagella and enables the propagation of microwires across a surface and through liquids[190] (Fig. 6C). Che and co-workers exploited the energy released from light-driven crystal phase change to induce slow crawling of a molecular crystal. Scanning laser irradiation has been used to actuate different phases of molecular crystals to generate phase-dependent transient elastic lattice deformation. The generated force is sufficient to move the crystal anisotropically at a velocity of about 60 μm min^{-1} (Fig. 17A).[257]

3.3.8. Photoinduced loss of crystallinity. In general, reversible photomechanical crystals (P or T type) rely on crystal-to-crystal transformations. However, the large morphology changes associated with loss of crystallinity (*e.g.*, melting or

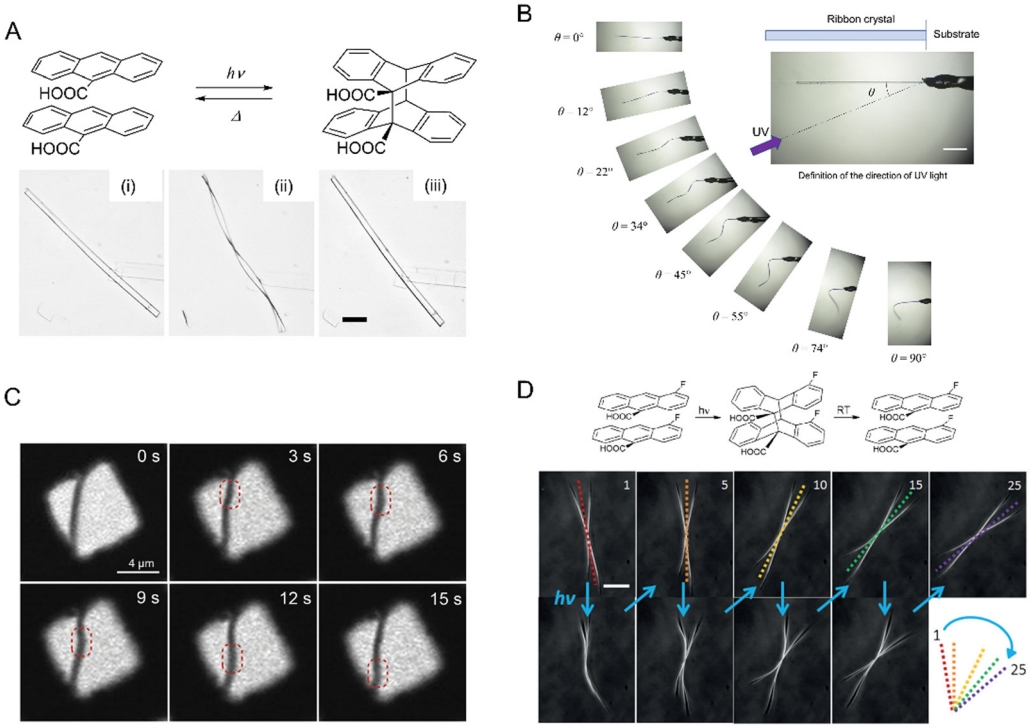

Fig. 14 Examples of crystal twisting. (A) Reversible twisting of 9AC microribbon: (i) before irradiation; (ii) immediately after irradiation with 365 nm light; and (iii) untwisting after 9 min in the dark at room temperature. Scale bar = 20 μm.[89] Adapted with permission from ref. 89 Copyright 2011, American Chemical Society. (B) Sequence of images of a flat microcrystal of 1,2-bis(2-methyl-5-phenyl-3-thienyl)perfluorocyclopentene exhibiting diverse twisting motions depending on the angle of the incident UV light. The scale bar is 300 μm.[221] Adapted with permission from ref. 221 Copyright 2018, American Chemical Society. (C) Confocal scanning laser micrograph of twist propagation along a typical microribbon of perylenediimide derivatives bridged on a copper grid.[250] Adapted with permission from ref. 250 Copyright 2019, Wiley-VCH. (D) Dark-field optical micrograph of an X-shaped microcrystal of 4F-9AC that rotates clockwise after brief irradiation with UV light with five cycles being shown.[109] Scale bar: 20 μm. Adapted with permission from ref. 109 Copyright 2016, Wiley-VCH.

solvent swelling) underlies the photomechanics of crystals of anthracene derivative (*E*)-5-(3-anthracen-9-yl-allylidene)-2,2-dimethyl-[1,3] dioxane-4,6-dione (*E*-AYAD). When these crystals are suspended in aqueous surfactant solutions, a photoinduced crystal-to-gel transition occurs accompanied by a large volume expansion (>10 times) that enables the crystal to engulf surrounding nanoparticles. The degree of gelation can be controlled by adjusting the irradiation intensity and duration[189] (Fig. 17B). Photoinduced loss of crystallinity followed by crystallization was demonstrated by Norikane *et al.* to induce directional motion of 3,3-dimethylazobenzene crystals on a glass surface using light irradiation at two different wavelengths (365 and 465 nm) to sequentially melt and recrystallize different regions of the crystal[108,258] (Fig. 17C). Dramatic light-induced changes in adhesion have also been observed in this class of compounds.[259–261]

3.3.9. Photomechanical expansion. In all the examples given above, the crystal deformation relies on partial photoconversion. 100% conversion of a crystal will not generate an internal strain, however, the dimensions of the product crystals will be different. In principle, this expansion/contraction can also produce work, analogous to a material that undergoes a phase transition. In practice, a negative photochromic reaction is needed so that the excitation light can penetrate the entire crystal. 9-Anthracene carboxylate ester monomers undergo [4+4] photodimerization, providing a convenient negative photochromic reaction.[203,204] Typically, this photoreaction leads to the disintegration of bulk crystals, and in many cases, a photosalient effect. The photosalience can be tamed by turning these crystals into nanowires with cross-sections on the order of 230 nm.[262,263] The nanowires show anisotropic expansion along the long axis without any fragmentation or disintegration. This photomechanical expansion was extensively studied on nanowires made from 9-*tert*-butylanthracene carboxylates (9TBAE) and modeled using different techniques such as wide-angle X-ray scattering (WAXS) and solid-state NMR crystallography. Considering the changes in both molecular geometry and orientation makes it possible to obtain quantitative agreement between the theoretical and experimental expansion factors[205,264] (Fig. 18A). A seeded-growth method from aqueous surfactants was used to precipitate highly crystalline thin microplates of 9MA. These microplates show uniform photomechanically induced expansion along the long axis of up to 7% when irradiated at 405 nm[265] (Fig. 18B).

3.4. Preparation of photomechanical crystals

3.4.1. Classical methods: solvent crystallization and sublimation. The morphology of a photomechanical molecular

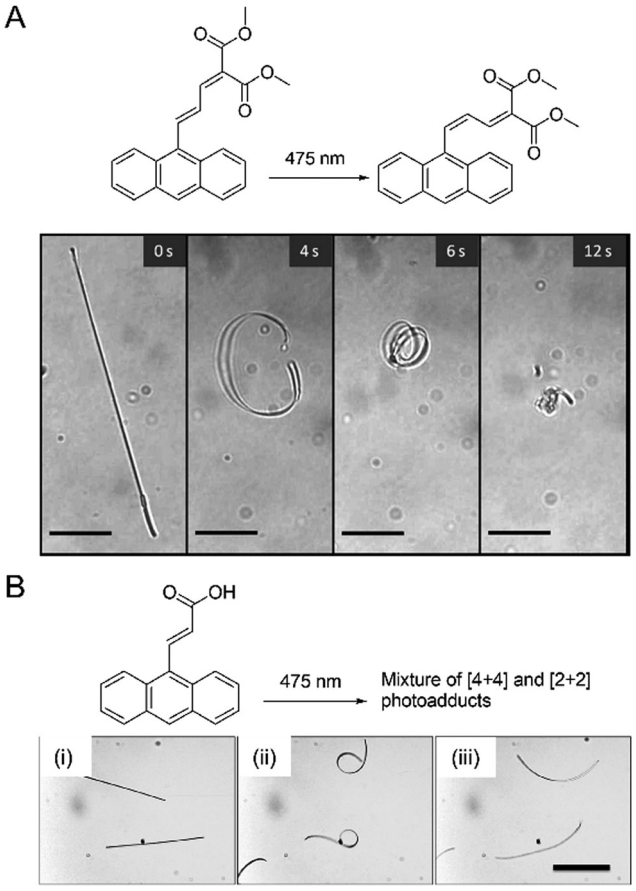

Fig. 15 Examples of crystal coiling. (A) Molecular structure and photoisomerization of *E*-DMAAM. Crystalline nanowires made from *E*-DMAAM with *ca.* 230 nm diameter suspended in an aqueous surfactant coil after exposure to 1 s pulse of 475 nm light. Coiling continues even after the light is switched off. Scale bar, 10 μm.[49] Adapted with permission from ref. 49 Copyright 2013, Wiley-VCH. (B) 9-AYAA microwires suspended in water coil and uncoil with continuous exposure to 475 nm light, (i) before exposure, (ii) halfway, (iii) total exposure. Scale bar, 30 μm.[94] Adapted with permission from ref. 94 Copyright 2015, The Royal Society of Chemistry.

crystal is pivotal in determining the mode of work output. For example, the stress due to a thin layer of photoproduct may be unable to bend a very thick crystal plate but may induce curling in a thinner sheet. The need to generate crystal shapes that are favorable for the observation of photomechanical motion motivates this section, in which we survey protocols and strategies used to prepare photomechanical molecular crystals with controllable size and shape. Classical methods for growing photomechanical molecular crystals can be generalized as crystallization from solution or deposition from a vapor phase. Recrystallization *via* slow evaporation of an organic solvent or slow diffusion of an antisolvent (sometimes referred to as ''bad'' or ''poor'' solvent) is the widely used method. Parameters such as growth temperature, pressure, and solvent diffusion rates can be adjusted to control the seed formation rate. This method gives large single-crystal samples; unfortunately, it is usually time-consuming.[221,266,267] Deposition of crystals *via* sublimation of thermally stable samples by heating at temperatures typically 10–20 °C higher than the melting point of the solid[179,220,268] is another growth method. This method provides faster way to harvest large single crystals. Sublimation of thermally unstable or air-sensitive samples is performed under reduced pressure or in an inert atmosphere, respectively. Large crystals can also be prepared *via* the vapor-phase method using a suitable solvent.[269–271] In most cases, these classical methods lead to the formation of larger crystals with a wide distribution of shapes and sizes.[272]

3.4.2. Hard template-directed crystal growth. One of the main challenges for organic molecular crystal growth is controlling the size and shape of the growing crystal. A convenient way to grow molecular crystals with a specific shape and size is to take advantage of templates with uniform tubular channels that force the organic molecules to assemble in a well-defined space. Inorganic filters from commercially available anodic aluminum oxide (AAO) have nanochannels with uniform diameter and length that can be tuned by applying specific anodization conditions.[263,273–275] Organic solvents such as *N*,*N*-dimethylformamide (DMF), or tetrahydrofuran (THF) are typically chosen to dissolve organic molecules to form a highly concentrated solution that is dropped onto a suspended AAO template and placed in a confined glass jar for slow solvent annealing. A fine stream of inert gas can be slowly mixed with the solvent vapors during the annealing process.[204] Soaking the AAO template in a melted organic sample is another method of loading the AAO template. However, without solvent annealing, the crystals tend to grow as polycrystalline tubes. After evaporation of the solvent, the filled AAO template surface can be gently polished and the alumina template is dissolved in a dilute phosphoric acid or sodium hydroxide solution[49,203,246,247] to release the crystalline nanowires. Solvent annealing inside the AAO template provides a reliable way to fabricate uniform and highly crystalline nanowires with diameters as small as 18 nm and as large as 250 nm[276–278] (Fig. 19A).

3.4.3. Solvent exchange method and floating drop method. Heterogeneous nucleation induced by the vessel walls and perturbations in the solution can cause high defect density in crystals and lead to low-quality samples. One way to circumvent this problem is to gently add the solution of the organic molecules in a ''good'' solvent on top of a ''poor'' solvent (antisolvent), in which the molecule has limited solubility. The solvents slowly diffuse together, reducing the solubility of the organic solute and leading to slow growth of crystals.[279–281] In the floating drop method for crystal formation, a solution of the compound in a volatile low-density solvent (*e.g.*, ethyl acetate, diethyl ether, or hexanes) is deposited on the surface of water. Slow evaporation of the more volatile solvent, coupled with the smooth surface of water, allow seed crystals at the interface to form floating ribbons or needle-like microcrystals, and the process is aided by the surface tension of the water.[282–284] By adjusting the solution concentration, good control of the thickness and specific aspect ratio of the crystals can be achieved.[70,207] Photomechanical microribbons and microneedles made from anthracene derivatives were grown[89,213,214]

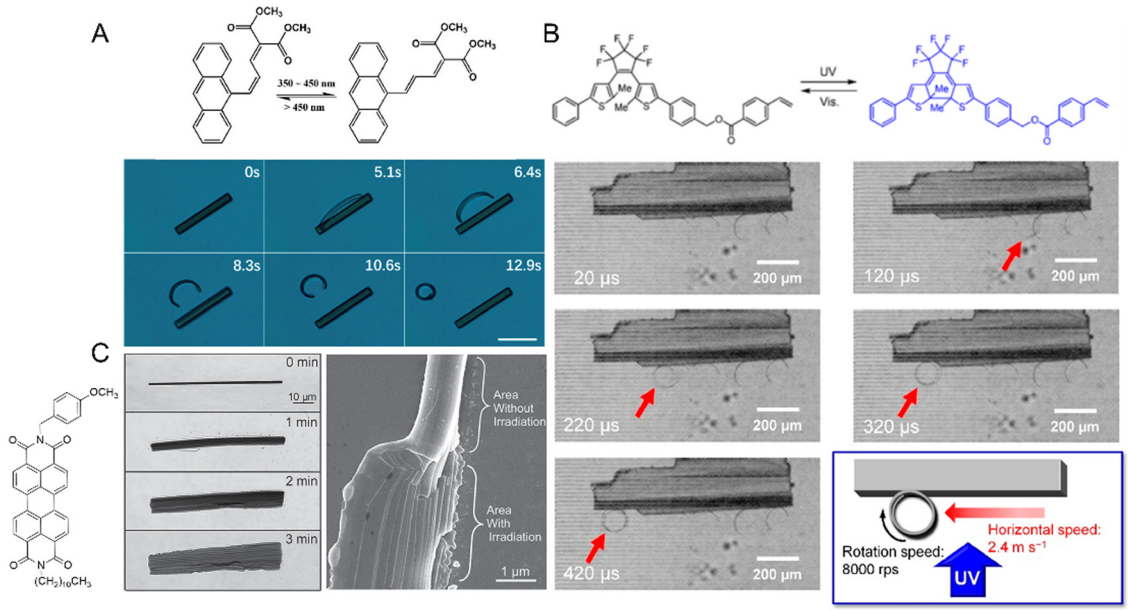

Fig. 16 Crystal delamination and peeling. (A) Structure and optical micrograph of a *cis*-DMAAM microcrystal photoinduced peeling after exposure to a 1 s pulse from 405 nm light. Scale bar, 5 μm.[46] Adapted with permission from ref. 46 Copyright 2019, The Royal Society of Chemistry. (B) Photoinduced fast peeling and curling of a diarylethene derivative. The red arrow indicates the position and direction of the peel.[251] Adapted with permission from ref. 251 Copyright 2021, American Chemical Society. (C) Optical micrograph (left) and scanning electron micrograph (right) of a microribbon made from the corresponding perylene diimide derivative laterally expanding upon exposure to 488 nm.[76] Adapted with permission from ref. 76 Copyright 2015, Wiley-VCH.

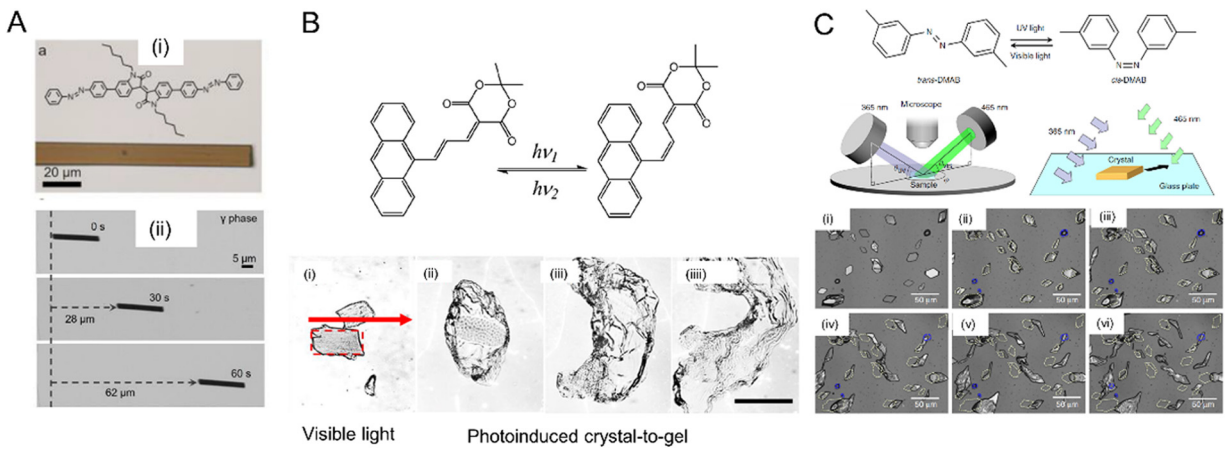

Fig. 17 Photoinduced crawling of crystals. (A) Molecular structure of the perylene derivative (i), and optical micrographs (ii) of a microcrystal (length 20 μm and width 2 μm) traveling across a glass slide while being irradiated with a 405 nm laser.[257] Adapted with permission from ref. 257 Copyright 2020, Wiley-VCH. (B) Optical micrographs of (*E*)-AYAD microcrystals suspended in an aqueous surfactant solution under visible light irradiation, (i) original crystal shape outlined by a red rectangle, (ii)–(iiii) expansion of the crystal forming a gel after several minutes of continuous light exposure. Scale bar, 50 μm.[189] Adapted with permission from ref. 189 Copyright 2019, Wiley-VCH. (C) Chemical structure of the photoisomerization reaction 3,3′-dimethylazobenzene. A schematic diagram of the experimental setup. Optical micrographs of microcrystal motion after irradiation for t = 0 (i), 3 (ii), 6 (iii), 10 (iv), 15 (v) and 20 min (vi). Scale bar, 50 μm.[108] Adapted with permission from ref. 108 Copyright 2015, Springer Nature.

that can photomechanically bent or twisted, depending on their habit.

3.4.4. Surfactant-mediated growth methods. Solvent annealing inside AAO templates and the floating drop method produce one-dimensional wires, needles, or two-dimensional ribbons. Other shapes may expand the types of photomechanical motion that crystals can generate and enable further applications. Controlling the rate of crystal growth is necessary to obtain uniform distribution of crystal sizes. One way to gradually introduce molecules into a growth medium is to rely on a chemical reaction to allow transfer between an aqueous and organic phase. Acid-catalyzed hydrolysis of acid-sensitive functional groups such as

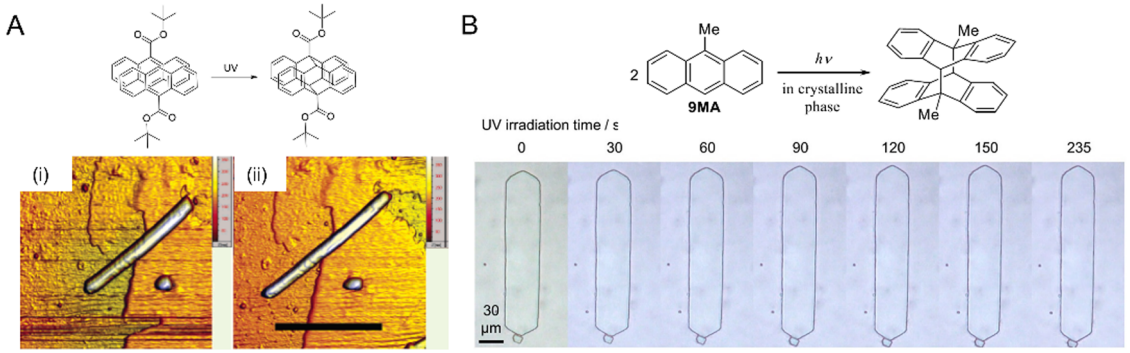

Fig. 18 Photoinduced crystal expansion. (A) Atomic micrographs of a 9-TBAE nanowire, *ca.* 230 nm diameter (i) before illumination and (ii) after illumination at 365 nm showing lateral expansion by 15%. Scale bar, 6 μm.[204] Adapted with permission from ref. 204 Copyright 2006, American Chemical Society. (B) Optical micrographs of plate-like microcrystals of 9MA upon UV (405 nm) irradiation. The crystal expands along the long axis over a period of *ca.* 8 min (left to right panel).[265] Adapted with permission from ref. 265 Copyright 2022, Wiley-VCH.

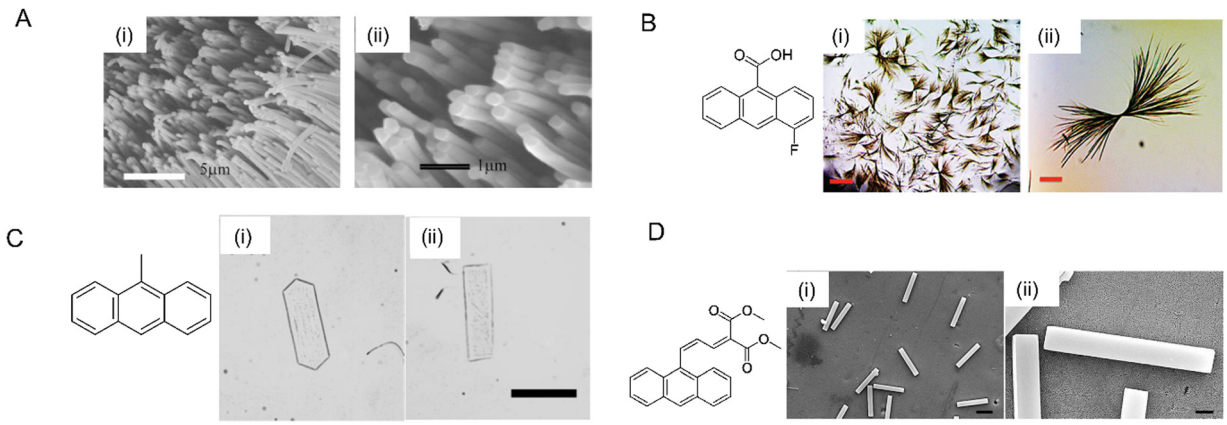

Fig. 19 Photomechanical crystals prepared by using different methods. (A) Scanning electron microscopy image of molecular crystal nanowires of a perylene derivative (molecular structure on the left) grown *via* solvent annealing inside AAO templates, (i) zoomed-out image, and (ii) zoomed-in image revealing the solid cores of the nanowires.[263] Adapted with permission from ref. 263 Copyright 2006, The Royal Society of Chemistry. (B) Optical micrographs of 4F-9AC highly branched microcrystals, (i) scale bar 400 μm and (ii) scale bar 50 μm.[248] Adapted with permission from ref. 248 Copyright 2017, The Royal Society of Chemistry. (C) Optical microscopy image of two types of 9MA thin microplate crystals, (i) hexagonal and (ii) rectangular; scale bar 50 μm.[208] Adapted with permission from ref. 208 Copyright 2018, Wiley-VCH. (D) Scanning electron micrographs of Z-DMAAM microblocks and (D) scanning electron micrographs of Z-DMAAM microblocks; (i) scale bar 100 μm, (ii) scale bar 10 μm.[46] Adapted with permission from ref. 46 Copyright 2019, The Royal Society of Chemistry.

acylals or *tert*-butyl esters can produce microcrystals of free aldehyde or carboxylic acid, respectively, with good control of size and shape if the hydrolysis is performed in an aqueous surfactant under gentle agitation. This chemical reaction-driven method was used to prepare highly branched microcrystals from 4F-9AC with T-type photomechanical properties[94,248] (Fig. 19B).

Ionic, neutral, and copolymer surfactants can be used to control the shapes and sizes of organic crystals precipitated from aqueous solutions containing a surfactant above its critical micelle concentration. A variety of different crystal habits have been obtained, including fibers, cubes, octahedra, microblocks, wires, *etc.*[46,208,285–287] A surfactant-mediated two-step reprecipitation method was used to grow single-crystal platelets composed of 9MA with two different molecular orientations[208] (Fig. 19C). Similar approaches were used to grow microblocks of DMAAM crystals (Fig. 19D)[46] and ultralong *Z*-9DVAM microwires.[190] Although this method often requires considerable trial and error to find a suitable solvent/surfactant combination, it can afford to novel crystal shapes.

3.4.5. Fabrication of photomechanical cocrystals. Cocrystallization of two or more different organic molecules with specific stoichiometric ratio provides another opportunity to tune the material properties and functionalities. Synergy may be achieved in cocrystals by combining components with different physical and chemical properties.[288–291] Naumov *et al.* provided a rare example of multifunctional thermally, twistable photobendable, elastically deformable, and self-healable cocrystals.[91] Self-healing materials are particularly important for their ability to spontaneously recover their integrity over time, a property that could significantly increase the lifetime of organic devices.[92] Irie *et al*. reported a two-component cocrystal composed of 1,2-bis(2-methyl-5-(1-naphthyl)-3-thienyl)-perfluorocyclopentene and perfluoronaphthalene. The cocrystals exhibited fast reversible bending over a broad temperature

range (4.7 K to 295 K) under alternating UV and visible light irradiation.[245] Barrett, Friščić *et al.* used a halogen bond-driven crystallization strategy to prepare azo-based crystalline materials with different photomechanical properties. The isomerization and photomechanical bending motion of cocrystals were qualitatively characterized using *in situ* single-crystal X-ray diffraction.[183] Noncovalent intermolecular interactions (hydrogen bonding, halogen bonding, π–π stacking interactions, van der Waals forces) offer opportunities to engineer crystals with complex shapes and uniform sizes for diverse functionalities in the future.[292–294]

3.5. Current status and applications of photomechanical molecular crystals

3.5.1. Lifting objects. As described above, there are many interesting and potentially useful aspects of the photomechanical molecular crystals and the current efforts of many researchers are focused on discovering new compounds and new types of motion. Although the research field is clearly in a developmental stage, there are already examples of photomechanical molecular crystals with applications as actuators and switches. Typically, the size of photomechanical molecular crystals must be on a sub-millimeter scale to avoid stress-related crystal fracture. An exception are millimeter-size acicular cocrystals of 1,2-bis(2-methyl-5-(1-naphthyl)-3-thienyl)perfluorocyclopentene and perfluoronaphthalene, that exhibit photoreversible bending upon alternate irradiation with UV and visible light with excellent fatigue resistance over 250 cycles of bending and unbending.[245] A needle-shaped cocrystal can lift a weight 275 times heavier than itself (Fig. 20A). The maximum stress generated by UV irradiation was estimated to be 44 MPa, which is 100 times larger than that of muscles (~0.3 MPa). Thus, the crystal operates as a cantilever having a powerful force and large mechanical work. An alternative to growing large single crystals is to create ordered arrays of nanocrystals in a matrix. Diarylethene nanowires grown in a porous AAO template were shown to generate substantial bending forces in composite membranes.[199,295,296] The advantage of the nanocrystal composite approach is that it is scalable, and the porous host can be prepared using a variety of materials and in different shapes (Fig. 20B).

3.5.2. Gearwheel rotation. Another key element for practical application is the high durability of the crystals. Mixed crystals composed of two different diarylethenes, 1-(5-methyl-2-phenyl-4-thiazolyl)-2-(5-methyl-2-*p*-tolyl-4-thiazolyl)perfluorocyclopentene and 1,2-bis(5-methyl-2-*p*-tolyl-4-thiazolyl)perfluorocyclopentene can survive over 1000 photomechanical bending cycles without any damage. Weakened intermolecular interactions in the mixed crystals bring about greater flexibility and improved durability. The photoinduced bending crystal motion could be used to operate a gearwheel as shown in Fig. 20C.[170] The flexible crystal bending enabled it to perform actual photomechanical work.[297]

3.5.3. ON/OFF switching of an electrical circuit. A simple and convenient way to add a new functionality to photomechanical crystals is to coat the crystal surface with a different material. P-Type rod-like crystals of 1,2-bis(5-methyl-2-phenyl-4-thiazolyl)perfluorocyclopentene were coated with a thin gold layer on the surface; the rod-like crystals retained their photomechanical response.[298] ON/OFF switching of an electric circuit was demonstrated by utilizing the gold-coated rod-like crystals as shown in Fig. 20D. Before UV irradiation, the gold layer was attached to a wire and the current was able to flow stably even when the current value was over 30 mA. Upon UV exposure, the rod-like crystals bent upward and the gold layer was detached from the wire, resulting in switching off the current. This current ON/OFF switching could be repeated over 10 cycles.

3.5.4. Manipulating micro- and nano-particles. Most photomechanical molecular crystals have solid structures, but some have a hollow or tubular morphology. Hollow structures can be utilized to encapsulate materials for a controlled release.[222] In the case of a diarylethene, 1,2-bis(5-phenyl-2-methyl-4-thiazolyl)perfluorocyclohexene, both solid and hollow crystals can be obtained. The crystals without holes showed photomechanical bending, while the hollow crystals showed remarkable photosalience, scattering crystal shards with a speed of up to 2.67 m s^{-1}. Upon UV irradiation, plastic microbeads that have been incorporated inside the crystal cavity scatter in a way that resembles the opening of the seeds of plants called impatiens (Fig. 20E).

Another example of particle manipulation was accomplished by highly branched sheaf-like microcrystals of 4F-9AC.[248] The branched microcrystals were obtained by slow acid hydrolysis of a *tert*-butyl ester of 4F-9AC in aqueous phosphoric acid/SDS/1-dodecanol at 35 °C. Upon exposure to 405 nm light the microcrystal branches twisted in unison, sweeping away more than 75% of silica microspheres in their vicinity. This photomechanical actuation can be repeated indefinitely after the branches return to their original shape within seconds (Fig. 20F). More precise manipulation of single microspheres was demonstrated by Je and Kim's group, who prepared organic crystal nanowires composed of an azobenzene-containing chromophore, tris(4-((*E*)-phenyldiazenyl)phenyl)benzene-1,3,5-tricarboxamide (Azo-1), using a meniscus-guided solidification method.[299] The nanowires showed photomechanical bending and unbending with large displacement upon irradiation with UV and visible light, respectively. Photomechanical nanowire tweezers were created with an Azo-1 nanowire arm that moved against a fixed polystyrene (PS) nanowire arm (Fig. 20G). The photomechanical tweezers can pick up, move and release the sphere, providing a way to manipulate micro-objects without wires or electrodes.

4. Computational methods for studying and predicting mechanical properties and effects in molecular crystals

4.1. From rationalizing to predicting mechanical effects

Computational methods are indispensable in understanding the chemical reactivity[301,302] and physical properties[303,304] of a wide range of materials. With the widespread availability of high-performance computing facilities and the increasing

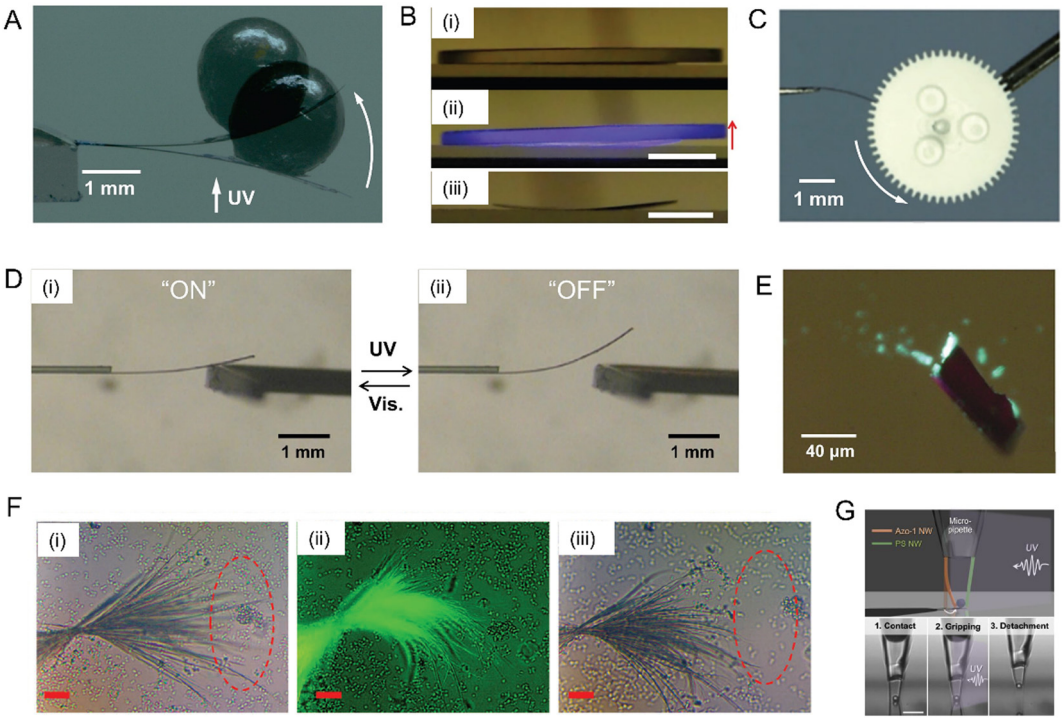

Fig. 20 Simple demonstration of work performed by dynamic molecular crystals. (A) Superimposed photographs of a diarylethene cocrystal cantilever microcrystal lifting a 2 mm lead ball, 46.77 mg; before and after irradiation with UV (365 nm) light, as indicated by the white arrow.[245] Adapted with permission from ref. 245 Copyright 2010, American Chemical Society. (B) Photographs of the 4FCM/AAO composite lifting a mirror (mass, 1.28 g) under UV light irradiation from below, (i) before light, (ii) After UV (365 nm) exposure, and (iii) template remains curved after the mirror is removed. Scale bars, 5 μm.[199] Adapted with permission from ref. 199 Copyright 2020, The Royal Society of Chemistry. (C) Gearwheel rotation activated by rod-like cocrystals containing diarylethene. The microcrystal is actuated by alternate irradiation with visible and UV light.[300] Adapted with permission from ref. 300 Copyright 2016, The Society of Synthetic Organic Chemistry. (D) Photomechanical crystal acts as an on/off current switch upon alternating irradiation with UV and visible light.[298] Adapted with permission from ref. 298 Copyright 2015, The Royal Society of Chemistry. (E) Optical micrograph of 1,2-bis(5-phenyl-2-methyl-4-thiazolyl)perfluorocyclohexene hollow microcrystals containing fluorescent microbeads. These crystals explode upon UV exposure, leading to scattering of fluorescent beads. Scale bars, 20 μm.[222] Adapted with permission from ref. 222 Copyright 2017, Wiley-VCH. (F) Optical micrographs of highly branched microcrystals of 4F-9AC sweeping silica microspheres in suspension (i) before UV light exposure, (ii) during UV (365 nm) light exposure, and (iii) after several exposure cycles. Scale bars, 25 μm.[248] Adapted with permission from ref. 248 Copyright 2017, The Royal Society of Chemistry. (G) Optical microscopy images of Azo-1 and PS nanowire (500 nm (d) × 12.5 mm (l)) arms integrated on the tip of a glass microcapillary tube. The photoinduced tweezers grip a PS microparticle ($d \approx 4$ μm) on a silicon substrate upon irradiation with UV light: 1 (contact) → 2 (gripping) → 3 (detachment). Scale bar, 20 μm.[299] Adapted with permission from ref. 299 Copyright 2015, The Royal Society of Chemistry.

adoption of unsupervised machine learning techniques,[305,306] the volume of information that can now be processed using computer algorithms is significantly larger than was the case 20 years ago. This trend is set to continue in the coming decades, creating new opportunities for the application of computational methods to support the discovery of mechanically responsive molecular crystals.

However, despite this promise, most of the reported discoveries concerning mechanically responsive molecular crystals are currently made with minimal, if any, computational insight. Rather than applying computational methods *a priori* to support the discovery of new mechanically responsive molecular crystals, it is more common to see reports where investigators have applied computational methods after the experimental observation of some mechanical effect, in order to gain a deeper understanding of the mechanistic origins of these phenomena (for example, see ref. 215). This suggests that the promise of true *in silico* design and subsequent experimental discovery of mechanically responsive molecular crystals is yet to be realized. Computational methods that span a range of lengths and timescales (Fig. 21) are already used to understand the mechanical properties of crystalline inorganic[307] and ceramic materials.[308] The commonly used modeling techniques to estimate the mechanical properties in such systems include density functional theory, molecular dynamics, and finite element methods. Although most of the reported studies that use these techniques to understand mechanical effects relate to studies on inorganic and ceramic materials; there is a growing disparity between the increasing amount of mechanical data and effects that experimentalists are reporting on molecular crystals and the scarcity of computational data that can be used to corroborate the emerging theories and hypotheses on the mechanical effects in molecular crystalline materials. This reflects the fact that there are more experimentalists than theoreticians who are currently interested in the mechanical properties and effects of molecular crystalline materials.

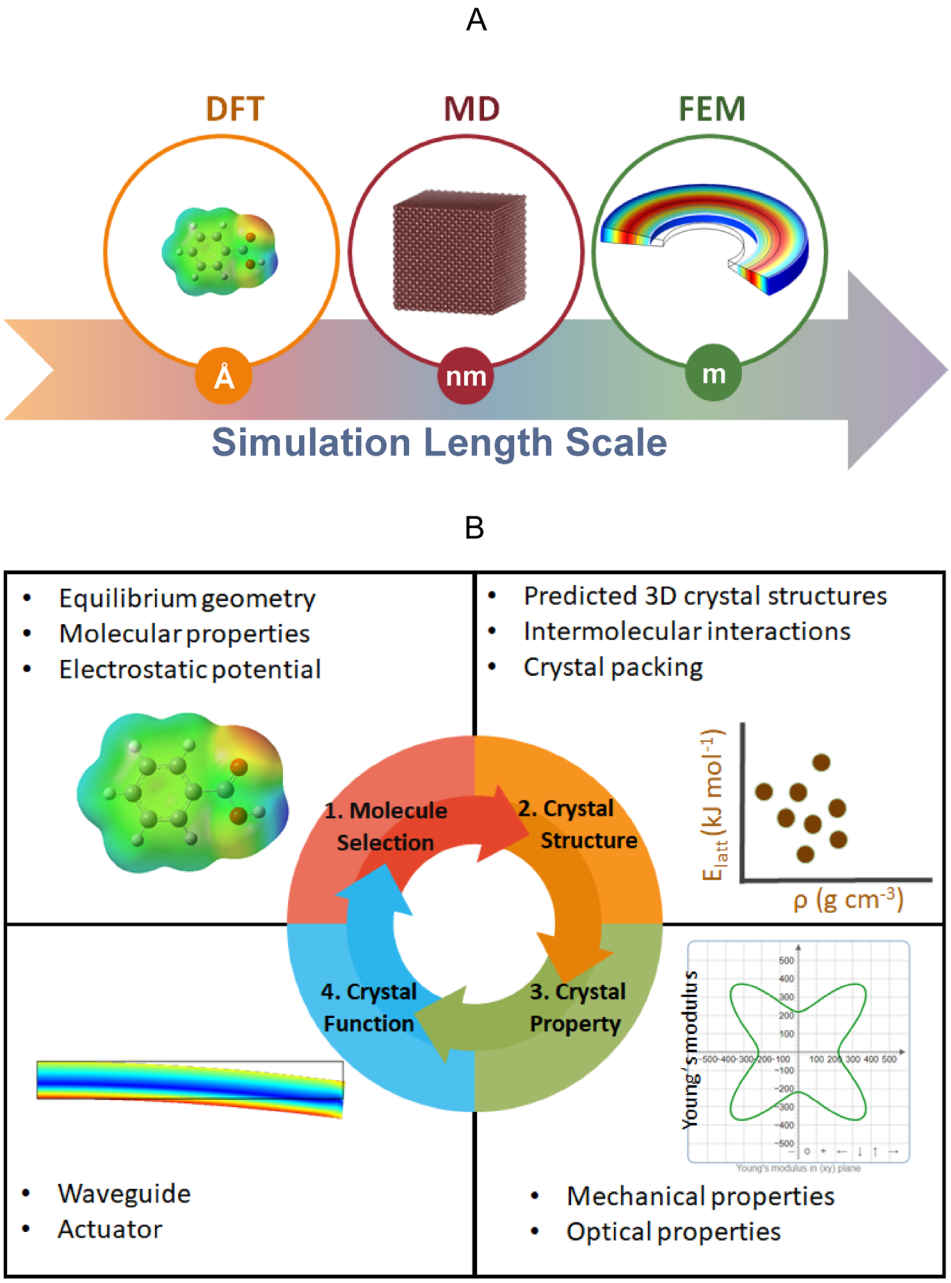

Fig. 21 (a) Most commonly used computational methods for predicting the mechanical properties and effects of crystalline materials. The arrow at the bottom shows the length scale on which each modelling technique applies. DFT = density functional theory, MD = molecular dynamics, and FEM = finite element methods. (b) Proposed steps in the *in silico* discovery of mechanically responsive molecular crystals.

Nevertheless, we anticipate that with the increasing interest in the mechanical properties and effects of molecular crystals, computational methods will play a significant role in correlating not only the structure to the properties but also properties to function in the future.

The increasing body of literature on mechanically responsive molecular crystals has already produced some guiding principles as to what types of molecules may display a particular type of mechanical effect. For example, the photomechanical bending seen in several azobenzene crystals[47,179,309] requires the presence of an azo group that can undergo *trans–cis* isomerization upon irradiation with light. While most organic crystals display relatively low Young's moduli (5–45 GPa),[27] the exceptional mechanical stiffness of amino acid[310] crystals is correlated with the strong charge-assisted hydrogen bonding interactions. This suggests that careful manipulation of the types and strengths of intermolecular interactions observed in molecular crystals may support the optimization of the bulk mechanical properties. Indeed, there have been some successes in the application of the principles of crystal engineering[311] to support the discovery of novel mechanically responsive crystalline materials.[32] For example, the introduction of slip planes in

molecular crystals *via* the careful manipulation of the functional groups in molecules is a viable crystal engineering strategy for the discovery of plastically bendable molecular crystals.[4] Recent work using a combination of nanoindentation and microfocused synchrotron X-ray radiation has validated the accuracy of this slip-plane model in explaining the mechanistic origins of plastic bending in molecular crystals.[74] Despite these successes, it is not yet clear whether we have enough reported examples of mechanically responsive molecular crystals to support the proposal of a set of generally applicable empirical rules for guiding the discovery of such materials.

At present, trial-and-error experiments remain the most common route for the discovery of new mechanically responsive molecular crystals. The process typically starts with the choice of suitable candidate molecules, which is often made by comparing the crystal structures adopted by these molecules with those of related molecules that may either have similar functional groups and/or similar crystal packing. This is followed by the growth of suitable single crystals. Finally, the mechanical properties (*e.g.*, Young's moduli and hardness) are measured on experimentally accessible crystal faces by nanoindentation. Each of these steps either requires a set of underlying assumptions or carries some technical challenges (*e.g.*, crystal growth) that vary for each chemical under investigation. In this section, we discuss: what role can computational methods play in not only rationalizing the experimentally observed mechanical effects but also supporting the discovery of new materials with desirable mechanical effects? We start with a critical assessment of the current applications of computational methods in the field before providing an outlook for the role that computational methods may play in the future.

4.2. Computing the strength of intermolecular interactions and crystal morphologies

Upon the application of a stimulus (stress, light, *etc.*), the mechanical response of a crystal is influenced by the habit (or morphology) and bulk crystal density of the material. At a molecular level, the strength of the intermolecular forces between the molecules is critical in influencing both properties. Most molecular crystals display anisotropic intermolecular interactions due to the uneven charge distribution around the constituent molecules. As such, the observed intermolecular forces are likely to be strong along certain crystallographic axes while they may be weak in others.

The importance of quantifying both the strength and directionality of the intermolecular forces in the study of mechanically responsive materials, has led to the widespread adoption of energy framework (EF) calculations.[312,313] EF calculations provide a quantitative method for correlating the strength of intermolecular interactions to the observed mechanical properties (*e.g.*, hardness or stiffness) along specific crystallographic directions or faces.[77,314,315] This permits the quantitative comparison of the strength of the intermolecular interactions (Fig. 22) as a function of the observed mechanical properties (*e.g.*, brittle, plastic and elastic) of the crystals.[314] EF calculations start by computing the unperturbed molecular wavefunctions at a chosen level of theory, followed by an estimate of the total interaction energy (E_{tot}) in the crystal as the sum of the electrostatic (E_{ele}), polarization (E_{pol}), dispersion (E_{dis}) and exchange-repulsion (E_{rep}) terms according to the following equation:

$$E_{tot} = E_{ele} + E_{pol} + E_{dis} + E_{rep} \quad (5)$$

The energies between molecular pairs are conveniently visualized as cylinders connecting the centers of mass of the molecules, with the radii of the cylinders being proportional to the magnitude of the interaction energies. EF calculations have successfully been applied to provide insight into the mechanism of plastic bending in molecular crystals.[316,317] This is possible because the strength of the interlayer interactions in slip planes can easily be quantified in plastic crystals using EF calculations.[318] The ease with which slip planes can slide past each other upon the application of external stress and a relatively low energy barrier for such sliding has been used to rationalize the mechanism of plastic bending in molecular crystals.[319]

Another important application of the theory of intermolecular forces that can be used to support the discovery of mechanically responsive molecular crystals, is the prediction of crystal morphologies using computational methods.[320,321] Although such calculations are not as widely used as EFs among the growing community of researchers interested in the mechanical effects of molecular crystals; they are integral to the advancement of *in silico* methods for supporting the discovery of mechanically responsive molecular crystals (Fig. 21). Experimentalists working in the field currently perform the face-indexing of crystals using laboratory X-ray diffraction methods before performing nanoindentation experiments. However, if we are to advance the *in silico* discovery of mechanically responsive molecular crystals (Fig. 21), then accurate computational models for predicting crystal morphologies will be necessary since the crystal habit affects its response to mechanical stress.

The simplest computational model for predicting crystal morphologies uses the Bravais–Friedel–Donnay–Harker (BFDH) law.[322] BFDH morphologies are purely geometrical in nature and assume that the growth rate of a given face is inversely proportional to the interplanar distance between the layers parallel to that face. The BFDH morphologies work relatively well for crystals displaying quasi-isotropic intermolecular interactions but are not reliable for predicting morphologies in crystals displaying highly anisotropic intermolecular interactions. In such cases, the attachment energy model[323,324] can be used to estimate the relative growth rates of the crystal faces.

Both EF and morphology calculations rely on an input 3D crystal structure, which is almost always determined using laboratory X-ray diffraction methods. However, for the first-principles discovery of mechanically responsive molecular crystals, one would start with the 2D chemical structure of a candidate molecule and the first step would be to compute the set of energetically accessible 3D crystal structures for the candidate molecule (Fig. 21). Recent advances in computational methods

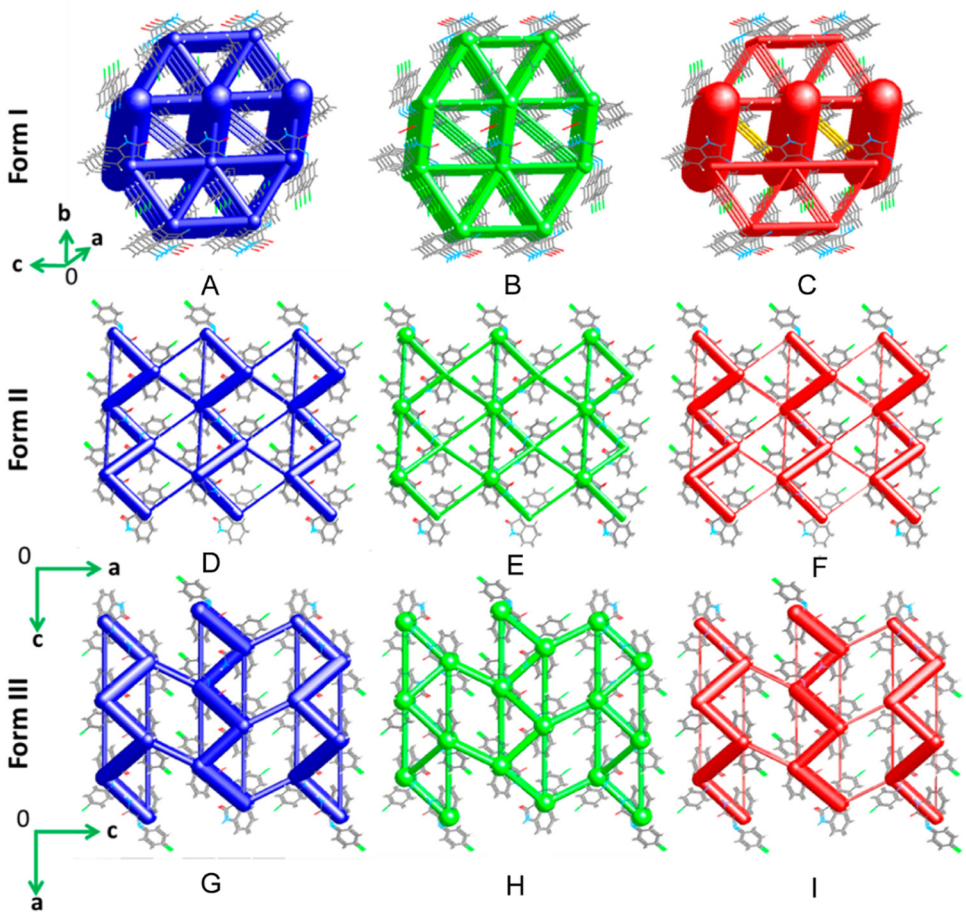

Fig. 22 Energy frameworks (EFs) showing the (A, D and G) total interaction energies (blue), dispersion (B, E and H) contributions (green) and electrostatic (C, F and I) contributions (red) for forms I (brittle), II (plastic) and III (elastic), respectively, for the Schiff base 3-((4-chlorophenyl)imino)indolin-2-one. Adapted with permission from ref. 314 Copyright 2018, American Chemical Society.

of crystal structure prediction (CSP) suggest that this is now feasible for relatively small molecules with limited degrees of freedom.[325] The putative set of predicted crystal structures would then be ranked according to stability and the most stable predicted structures would be subjected to property predictions including but not limited to morphology calculations and the second-order elastic constants (Section 4.3 below). We can therefore envisage a future where several computationally predicted crystal structures will be subjected to theoretical stress–strain tests on specific crystallographic faces using the computed crystal morphologies as a guide for selecting the dominant face(s). This may be supplemented with EF calculations to quantify the strength of the intermolecular interactions along specific crystallographic directions or to identify slip planes in the predicted crystal structures. By comparing the predicted crystal structures and properties from a large pool of candidate molecules, the theoretical data may be used to select and advance the experimental crystallization and mechanical characterization of a limited set of candidate molecules. Such an approach has already been applied successfully for the discovery of porous molecular crystals using energy–structure–function maps (Fig. 23),[326] which relate the predicted polymorphs on the crystal energy landscape to a set of user-specified molecular/crystal descriptors. For research focused on mechanically responsive molecular crystals, the descriptors chosen could be the computed Young's modulus, compressibility or the number of active slip planes present in the predicted crystal structures.

4.3. Computing the second-order elastic constants of molecular crystals

The accurate computation of the second-order elastic constants (SOECs) of molecular crystals provides the opportunity to estimate a range of mechanical properties such as Young's and bulk moduli. The tensorial representation of Hooke's law provides access to the SOECs of a crystal that is deformed within the elastic regime. The relevant equation is

$$\sigma_{ij} = \sum_{kl} C_{ijkl}\varepsilon_{kl} \quad (6)$$

where σ_{ij} is the stress, C_{ijkl} are the SOECs, ε_{kl} is the strain and $i, j, k, l = 1, 2, 3, 4$. There are a total of 21 independent components of the elastic constants but this number may be reduced by symmetry. The above stress–strain relation provides the basis for the computational estimate of the SOECs and, by

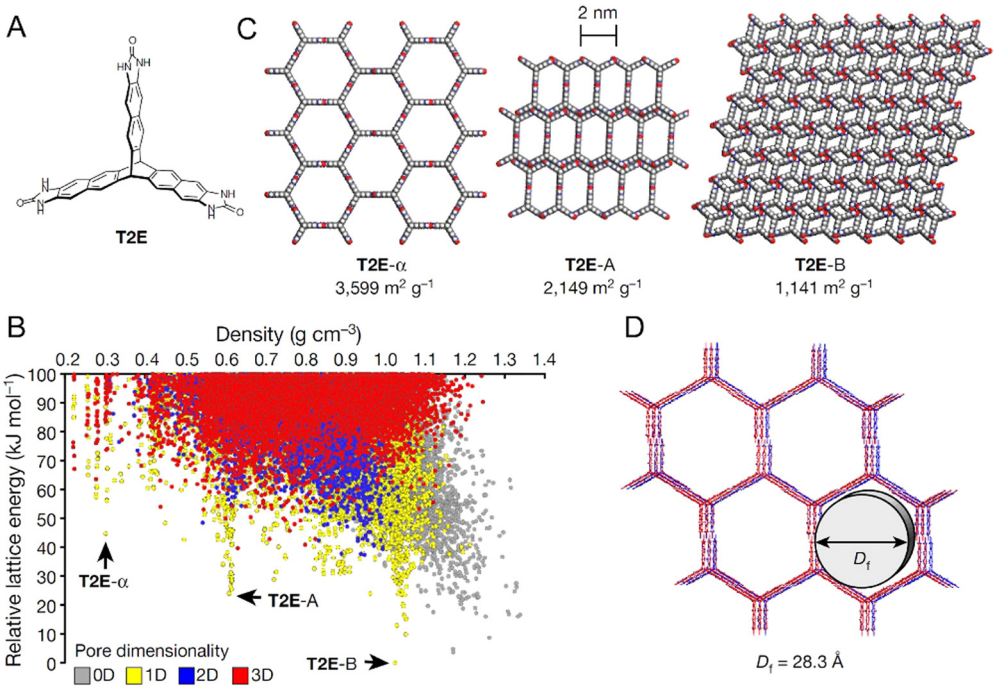

Fig. 23 Comparison of the predicted and experimental structures and properties for molecule T2E whose molecular structure is shown in panel (A). The predicted crystal energy landscape for T2E is shown in panel (B). Selected structures for T2E from the energy-density landscape are shown in panel (C). An overlay of the predicted (red) and experimental (blue) structures for T2E is given in panel (D). Adapted with permission from ref. 326 Copyright 2017, Springer Nature.

extension, the mechanical properties of molecular crystalline materials using molecular mechanics, molecular dynamics or dispersion-corrected density functional theory (DFT-D) methods. At the heart of all these approaches is the accurate calculation of the dependence of the total crystal energy on the strain components according to the following Taylor expansion:

$$E(V,\varepsilon) = E(V_0) + V\sum_{\alpha}\sigma_\alpha\varepsilon_\alpha + \frac{V}{2}\sum_{\alpha\beta}C_{\alpha\beta}\varepsilon_\alpha\varepsilon_\beta + \ldots, \qquad (7)$$

using the Voigt notation (α, β = 1, 2,...6), where V_0 is the equilibrium volume of the crystal. The process starts with the calculation of the stress-free equilibrium crystal structure of the material. The SOECs are then estimated by calculating the second-derivative of the total energy with respect to the applied strain

$$C_{\alpha\beta} = \frac{1}{V}\frac{\partial^2 E}{\partial\varepsilon_\alpha\partial\varepsilon_\beta}\bigg|_0 \qquad (8)$$

The SOECs can be estimated using force fields such as the widely used COMPASSII[327] or Dreiding[328] force fields. However, the assumption of transferability of force fields to the modelling of a range of crystalline materials can lead to significant errors in calculating the equilibrium structure of the material or indeed the second derivatives of the total energy with respect to the applied strain. First principles DFT-D methods are instead a reliable alternative for estimating the SOECs of crystalline materials. Inspection of the literature, however, suggests that such computations are far more common for inorganic crystals (*e.g.*, minerals) compared to molecular crystals. As part of the Materials Project,[329,330] a recent study[331] involving 1181 inorganic compounds has used first-principles DFT methods to estimate the elastic properties of all materials and found that the calculated elastic constants are within 15% of the experimental values. For molecular crystalline materials, the number of reported studies that apply DFT-D methods to estimate the SOECs and by extension the mechanical properties are significantly fewer.[310,332–335] However, for molecular crystals displaying relatively strong hydrogen bonding interactions, work by Kronik *et al.*[310] has shown that the face-specific Young's moduli predicted by DFT-D methods are in excellent agreement with the experimentally observed values from nanoindentation measurements (Fig. 24). However, the relatively strong charge-assisted intermolecular forces in amino acid crystals mean that such agreement between experiments and theory may not be observed in softer crystals with weaker intermolecular forces. Some attempts have already been made[335] to correlate the computed properties (attachment energies, elastic moduli, *etc.*) of molecular crystals with those expected based on the crystal packing, nanoindentation data or the mechanical effect observed in the crystal. However, a systematic survey of the limits of DFT-D methods for predicting the mechanical properties of a wider set of molecular crystals is necessary before we can make

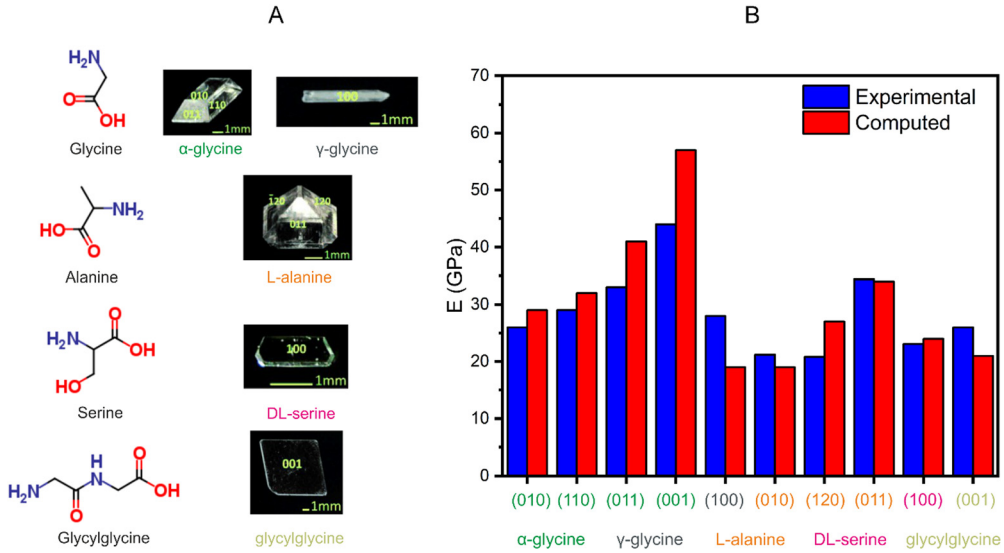

Fig. 24 (A) Chemical structures and photographic images of a number of amino acid crystals. For each photographic image of the crystal, the Miller indices for specific crystallographic faces studied are indicated. (B) Bar graph for comparing the experimental (nanoindentation) and computed Young's moduli (*E* values) for the amino acids shown in panel (A). For each amino acid where the computed and experimental *E* values are compared in the bar graph, the same color is used on the *x* axis to match the name of the amino acid with the Miller index of the crystallographic face studied. The bar graph shown in panel (B) is based on the data reported in ref. 310. The images of the crystals and the data for the bar graph are adapted with permission from ref. 310. Copyright 2015, Wiley-VCH.

progress with the *in silico* design of mechanically responsive molecular crystals.

4.4. Beyond pairwise dispersion-corrected DFT models: many-body dispersion schemes and dynamic effects in mechanically responsive molecular crystals

The bending of a molecular crystal is a dynamic effect that is influenced by a range of factors, such as the applied stress, temperature, crystal defects and crystal morphology. Static computational relaxations of the crystal structure may be used to estimate the change in the energy and bulk crystal packing of a material under an applied strain.[336] However, these simulations neglect thermal effects, and although the implicit errors in the theoretical results are largely canceled when comparing polymorphs of the same material using the same model, serious errors can be introduced when the calculated properties of different materials are compared. The work of O'Reilly and Tkatchenko[337] has shown that the basic pairwise correction to the dispersion energy in static DFT calculations may be improved by using a more expensive many-body dispersion formulism. Such many-body dispersion schemes have shown potential in accurately modelling the anisotropy in the Young's moduli of the polymorphs of aspirin.[338,339] However, such many-body dispersion schemes are expensive. As the field evolves, finding more accurate dispersion schemes for modelling the intermolecular interactions of periodic molecular crystals using DFT-D methods at marginally lower computational costs, will play an important role in the discovery of mechanically responsive molecular crystals. However, given that the bending of a crystal and its response to stress is a dynamic effect, we also anticipate that *ab initio* molecular dynamics (MD) simulations will increasingly be applied to understand the mechanism of bending and the dynamic evolution of the crystal packing under an applied stress. This is because such simulations allow us to monitor the changes in the molecular configurations as a function of time under a defined uniaxial or biaxial strain. Temperature can be implicitly considered in the ensemble as part of the MD simulation. We anticipate that the adoption of *ab initio* MD methods will not be as widespread as that of DFT-D methods given the prohibitively higher computational cost of MD simulations. We, therefore, envisage that such MD simulations will be applied sparingly to understand the mechanism of bending (elastic or plastic) or phase transitions in molecular crystals with interesting mechanical properties and effects. There have already been some examples of the application of MD simulations to understand elastic bending, notably in metals.[340] The stress–strain curves and the response of the material to an applied force provide bounds for the load capacity of such materials. In the context of molecular crystals, MD simulations have also been used[318] to model the stress–strain curves of materials under an applied strain on a particular crystal face. However, there are challenges in comparing the tensile limits of materials from MD simulations with those from three-point bending tests due to the possible role of crystal defects in influencing the empirical data. Such effects cannot be easily modelled on a computer. For the most basic type of MD simulations that employ empirical force fields, there will always be a place for them in the toolkit of the computational chemist. However, such calculations are unlikely to offer the same level of accuracy as DFT-D or *ab initio* MD simulations due to the poor transferability of specific force fields and their associated charge models for modelling the intermolecular interactions in molecular crystals with varying functional groups. As a

consequence, we anticipate that while the modeling of dynamics effects in molecular crystals is critical to propose a set of design rules for the discovery of mechanically compliant molecular crystals, MD simulations will be applied sparingly on a case-by-case basis to probe the mechanical properties and effects of such crystals.

4.5. Outlook for integrating computational methods in the discovery of mechanically responsive molecular crystals

Computational methods for predicting the mechanical properties of crystalline materials are emerging as indispensable tools for rationalizing the observed mechanical effects and, indeed, the underlying mechanisms behind these effects. Machine learning techniques have the potential to play a role in the selection of suitable molecular compounds for targeting a desired mechanical effect. However, before machine learning can support such efforts, there needs to be a community-wide consensus as to which molecular and crystal descriptors are necessary for achieving a desired mechanical effect. This will be important in training a machine learning algorithm for supporting the high-throughput screen of many thousands of candidate chemical and crystal properties. Given the recent advances made in CSP methods, we anticipate the combined application of CSP to predict putative crystal structures, DFT-D methods to rank them and machine learning methods to identify possible candidate crystals for desirable mechanical properties and effects may well be achievable in the coming decade. Another area of significant potential growth is the implicit modelling of dynamic effects in molecular crystals using *ab initio* MD simulations. MD simulations are currently less frequently applied for modelling mechanical effects in molecular crystals when compared to inorganic materials such as metals and minerals. However, we anticipate that with improvements in computing power driven by the Moore's law, MD simulations will be applied sparingly alongside high-throughput static DFT-D methods in order to obtain a more complete picture of the molecular-level response of a crystal to external stress.

5. Confluence of deformable crystals and flexible electronics

5.1. Introduction

The rise of flexible organic crystals offers a unique opportunity in the realm of small-molecule semiconductors to engineer flexible electronics. Flexible molecular crystals combine deformable mechanical properties with the long-range order of single crystals that flexible polymers lack. Moreover, the pursuit of flexible organic semiconductors offers paths to novel electronic devices. Seminal work by Briseno and Bao *et al.*[341] in 2006 reported the flexing of rubrene crystals, which allowed up to 0.74% strain before the observation of reduced mobility. While this is a relatively modest strain applied during bending, performance was recovered upon straightening of the device after applying up to 1.3% strain. On the other hand, concurrent work on pentacene by Someya and Sakurai *et al.*[342] in 2004 took advantage of the decrease in mobility and the threshold voltage of organic field-effect transistors (OFETs) upon bending as a mechanism for pressure sensors. These works highlight two different design strategies harnessing the flexibility of organic semiconductors in devices: preserving performance during bending and stretching for flexible electronics or utilizing electromechanical properties for sensing.

Both elastic and plastic bending modes can be leveraged in organic electronic devices. Elastic bending offers material recoverability and high cyclability, which is ideal for wearable devices that frequently bend with daily activity. On the other hand, plastic deformation preserves shape change. While the difference between elastic and plastic deformation is whether the strain imposed exceeds the yield point, the extent to which molecular crystals may elastically and plastically deform to accommodate strain is determined from parameters such as Young's modulus and crack onset strain.[343] However, these parameters do not necessarily determine how the bending will affect the charge transport through the crystal. Charge transport is highly sensitive to molecular packing in the organic electronic crystals, which in turn is modulated by mechanical deformation.[344] For instance, slight gliding of the pentacene core of 6,13-bis(triisopropylsilylethynyl)pentacene (TIPS-P) along the short and long axes resulted in three orders of magnitude difference in the hole mobility.[345,346] Both the π-stacking distance and π-overlap can result in a dramatically different charge transfer integral, a key parameter for hopping transport in organic semiconductors.[344] For in-depth accounts of the effect of molecular packing on charge transport, we refer the readers to an excellent theoretical investigation by Brédas *et al.*,[344] and a recent review paper by Chung and Diao.[347]

The impact of mechanical deformation on structures depends both on the mechanism of deformation and the direction along which stress is applied. Under both elastic and plastic deformation, where the lattice may deform, local adjustments to the molecular spacing and overlap will be necessary to accommodate the strain.[45] Moreover, this change in molecular packing also modulates the dynamic molecular vibrations, reducing vibration during compression and increasing vibration under tension.[348,349] Through this mechanism, the dynamic disorder in an organic electronic device can be suppressed during elastic compression to attain higher charge carrier mobility. Besides the typical elastic and plastic deformation mechanisms, mechanical stress may induce solid-state phase transitions among different crystal structures (polymorphs[347]), leading to a superelastic effect or deformation-induced twinning which underlies ferroelasticity.[34,97] In contrast to polymorph transitions, deformation twinning preserves the molecular packing before and after deformation everywhere except along the grain boundary.[97] Ultimately, with a diverse set of deformation mechanisms, we observe a substantial variation in the effect on electronic properties. During lattice deformation, charge transport will shift based on both the local change in the intermolecular charge transfer integral and changes in dynamic lattice disorder.[348,350] While

this effect typically occurs smoothly with applied stress until material fracture, coupling deformation with a solid-state phase transition results in property switching between two states, based on the electronic performance of each structure.[50] Alternatively, molecular structure preservation through twin domain formation provides an avenue for maintaining performance without substantial property modulation under high strains.[97] Here, we will explore the underlying features distinguishing these bending mechanisms, the impact on electronic performance, and finally, how they may be harnessed for novel device design.

5.2. Mechanical effects and electronic properties

5.2.1. Effects of elasticity on electronic properties. As discussed above, Briseno and Bao *et al.* fabricated a single-crystal device capable of withstanding up to 0.74% strain reversibly.[341] To achieve this feat, certain engineering aspects must be considered for flexible device design. They showed that extremely thin ($\leq$1 μm thick) crystals are required to achieve good adhesion between the crystal and the dielectric material. Since the device is layered with a flexible substrate, a dielectric, an organic semiconductor and device contacts, the relative placement and thickness of these layers determines whether the organic semiconductor predominantly experiences compression or tension. Moreover, the total thickness determines the resulting maximum strain experienced by the crystal in the bending mode.[351] Notably, this maximum surface strain is not only dependent on the crystal itself but relies on the thickness and properties of both the dielectric layer and the flexible substrate used.

In the case of the rubrene (Fig. 25A), once the crystals were bent beyond 0.74% strain tested by Briseno and Bao *et al.*,[341] the charge carrier mobility decreased by nearly three orders of magnitude before recovering after bending (Fig. 25B). Later, Reyes-Martinez and Briseno *et al.*[352] explored rubrene crystals permanently deformed *via* wrinkling, and they observed that the local charge mobility increased in areas experiencing compression near the dielectric layer and decreased in regions under expansion. Even at local compressive strains as low as 0.2%, the wrinkled rubrene crystals showed a local increase in mobility up to 100%, underscoring the potential for highly strained sensitive devices (Fig. 25C). This change was consistent with alteration in the mobility of devices such as TCDAP (Fig. 25D–F), where the mobility increased by 20% under compression at a 5 mm bending radius, and TIPS-P (Fig. 25G–I), whose mobility increased by 30% at −2% strain.

To understand this underlying effect in TCDAP (Fig. 25D), Ho and Tao *et al.*[353] compared their bending device (Fig. 25E) with the crystallographic direction of TCDAP, showing that the bending occurred along the π-stacking direction. This suggested that the increase in mobility during compression (Fig. 25F) was a result of increased charge transfer integral potentially due to a closer π–π stacking distance or increased π-overlap. Interestingly, while both the rubrene and TCDAP crystals compressed along the π-stacking direction within the crystal, the TIPS-P (Fig. 25G) case was based on films without one alignment direction, suggesting that this trend is not based solely on local changes in the packing. Lai, Mas-Torrent *et al.*[354] showed that bending in both the parallel and orthogonal (Fig. 25H, red and black lines, respectively) directions with respect to printing, affected the strain only slightly, while compression resulted in lower contact resistance. This effect resulted in a cyclable bending device with recoverability even at bending radii down to 0.5 cm (Fig. 25I). This shows that the impact on semiconducting performance during bending is multifaceted with dependencies beyond local structural changes.

To better understand strain on charge carrier mobility, structural studies highlighting changes in the molecular packing during bending have been of fundamental importance. Specifically, applied strain requires distortions in the crystal structure to accommodate expansion or contraction. Although the distortions are typically small, even small changes in packing can lead to large effects on charge transport properties. In many systems, compression and stretching result in changes in the molecular spacing along the charge transport direction, causing changes in the molecular coupling between nearest neighbors.[353] Wu and Frisbie *et al.*[350] investigated the local change in the electronic structure during strain application using scanning Kelvin probe microscopy to measure the change in the work function (ΔWF). By heating crystals of rubrene attached to either PDMS or silicon substrates, the crystals would experience tension or compression, respectively, along the π-stacking direction due to a mismatch in the thermal expansion coefficient (Fig. 26A and B). In a similar fashion to the impact on mobility, the work function was found to decrease up to 100 meV under a compressive strain of −0.1% and increase greater than 200 meV under a tension strain of 0.125% (Fig. 26C). The decrease in the WF under compression was attributed to an increase in coupling of π–π interactions induced by the compressive strain and the opposite under tensile strain. Moreover, during tension, the slope of this work function increased above 0.05% strain. However, no significant morphological changes such as cracks were observed, suggesting an elastic to plastic deformation transition. This effect even manifested through measured hysteresis during compression, shown in Fig. 26D. This switch between elastic and plastic deformation significantly impacted the magnitude of the change in the WF, with the elastic deformation regime only decreasing the WF by 20 meV whereas plastic deformation decreased the WF by 200 meV.

Recently, Choi and Podzorov *et al.*[349] showed that more than simple structural modulation occurs in strained rubrene crystals. Using Raman spectroscopy to investigate the low-frequency vibrational modes, they observed a strong correlation between the applied strain with the phonon mode peak positions. With increasing tensile strain, the low frequency peaks uniformly blueshift by 1 or 2 cm^{-1} under −0.4% uniaxial compressive strain (Fig. 26E and F). This hardening of phonon vibrations followed the mobility measured from both OFET devices and the quantum Hall effect: the mobility increased by a factor of 1.5 with increasing compression (Fig. 26G). These results fit quite nicely with an earlier study by Kubo and Takeya

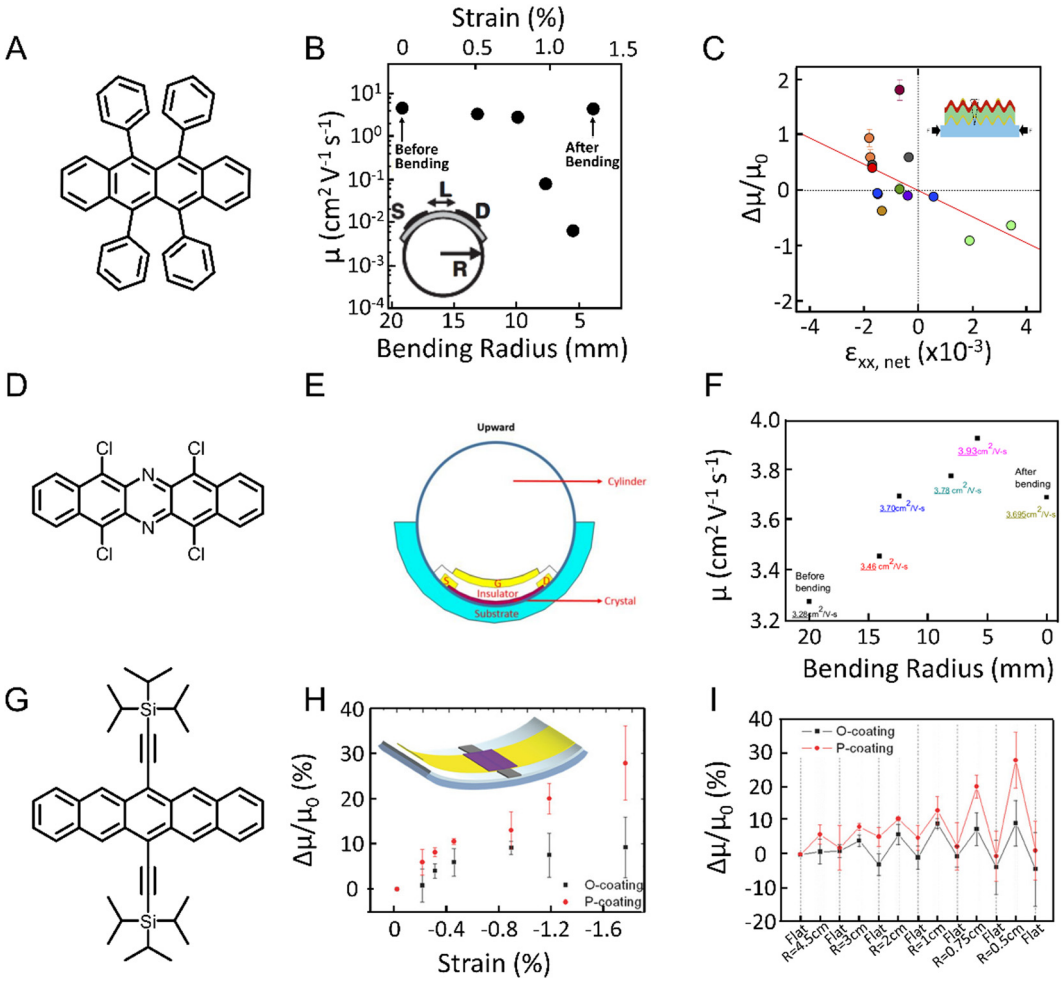

Fig. 25 (A) Crystals of rubrene exhibit (B) stable device performance up to 0.74% strain.[341] Adapted with permission from ref. 341 Copyright 2006, Wiley-VCH. (C) Wrinkled rubrene crystals show mobility changes depending on whether the local strain is tension (decreased mobility) or compression (increased mobility) deformation.[352] Adapted with permission from ref. 352 Copyright 2015, Springer Nature. (D) TCDAP crystals under (E) compression resulting in (F) increasing mobility and partial recoverability of device performance after bending.[353] Adapted with permission from ref. 353 Copyright 2016, Jove. (G) Films of TIPS-P exhibit increasing mobility under compression (H) and reliable recoverability under multiple cycles, systematically decreasing the bending radius (I).[354] Adapted with permission from ref. 354 Copyright 2018, Wiley-VCH.

et al.,[348] who studied the effect of strain on the dynamic disorder in crystals of C_{10}-DNBDT-NW (Fig. 26H). During application of strain *via* compressive bending to a 3% strain, the π–π stacking direction (*c* axis) exhibited a similar 3% decrease in length. At the same time, DFT simulations of this change showed a clear reduction in molecular vibrations under these conditions, decreasing the amplitude of translations in the *c** and *b* directions by 8.7–16% (Fig. 26I, orange and blue arrows) and decreasing rotations around the *a* direction by 7.5% (green arrows). This suggests an overall reduction in the dynamic disorder leading to the substantial 70% increase in mobility (Fig. 26J, red line) under the 3% strain. A decrease in molecular distance along the π–π stacking direction leads to a synergistic decrease in the molecular vibrations, resulting in exceptional strain-responsive devices.

5.2.2. Effects of structural transitions on electronic properties. Recent work has shown that structural transitions arising from cooperative molecular motions can give rise to dynamically modulable or highly deformable single crystal electronics. For instance, Chung and Diao *et al.*[50] found that ditBu-BTBT presented a thermally induced cooperative phase transition (thermoelastic, martensitic transitions) triggered by an order–disorder transition in the *tert*-butyl side chains (Fig. 27A). The phase transition showed only a 2° change in the angle between the molecules; however, the charge transfer integral between the herringbone pairs decreased by 22% (Fig. 27B). As a result, this seemingly inconsequential change in molecular packing produced a 217% modulation in charge carrier mobility between the high-temperature (HT) and low-temperature (LT) forms (Fig. 27C and D). Although the small packing changes of ditBu-BTBT barely affected the crystal size and shape, TIPS-P crystals (Fig. 27E) undergo a thermoelastic cooperative transition accompanied by a remarkable increase in crystal length by more than 10% (along the π–π stacking direction), a strain difficult to achieve *via* elastic bending alone.[50] Despite quite different behaviors compared to ditBu-BTBT, the underlying mechanism was again found to be an order-to-disorder

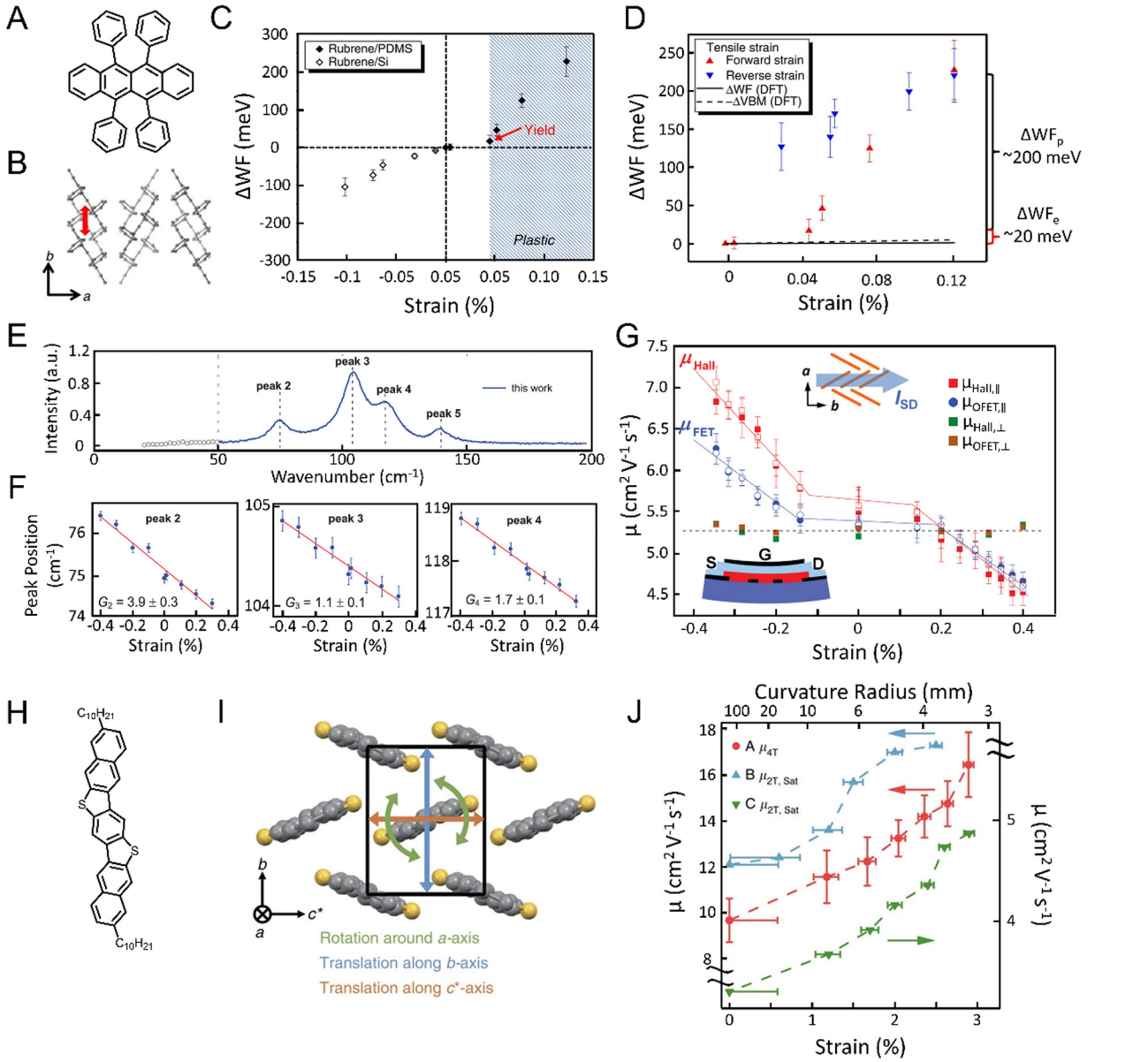

Fig. 26 Rubrene (A) showed strain along the (B) π−π stacking direction caused (C) local change in the work function with strain.[350] Adapted with permission from ref. 350 Copyright 2016, Springer Nature. (D) This effect was more pronounced during plastic deformation and showed hysteresis. Under compression, (E) phonon vibrational modes observed under Raman spectroscopy underwent (F) blue shift, consistent with phonon hardening.[349] Adapted with permission from ref. 349 Copyright 2019, Wiley-VCH. (G) Resulting devices exhibited increased mobility. (H) C_{10}-DNBDT-NW under compression (I) exhibits reduced molecular vibrations. (J) Suppressed vibrations results are correlated with the changes in mobility, increasing (decreasing) upon compression (tension).[348] Adapted with permission from ref. 348 Copyright 2016, Springer Nature. Mobilities were measured along the *c* axis for 3 devices in both 4 terminal (A, red) and 2 terminal (B and C, blue and green, respectively) configurations.

transition in the TIPS groups of the molecule as they begin rotating in the HT form. Like the ditBu-BTBT case, the changes in structure and shape of the TIPS-P crystals also had a profound impact on the electronic properties of OFET devices (Fig. 27F and G), rapidly switching between a higher mobility (high temperature) and lower mobility (low temperature) phases. Reversible shape changes in molecular crystals of organic semiconductors have been proven useful for the creation of thermal-based actuators. Gassensmith *et al.*[355] fabricated a silver-coated naphthalene diimide (NDI) derivative-based crystal. Harnessing the cooperative shape change associated with tilting of the molecular core (Fig. 27H), the crystal operated by switching between an elongated and shortened state (Fig. 27I).[355] By coating the crystal with a conductive material, the transition could successively turn off the current and voltage based on temperature as a thermally activated mechanical actuator (Fig. 27J).

Intriguingly, cooperative, martensitic transitions in molecular crystals of TIPS-P can be triggered by applying a mechanical force, leading to superelasticity and ferroelasticity observed for

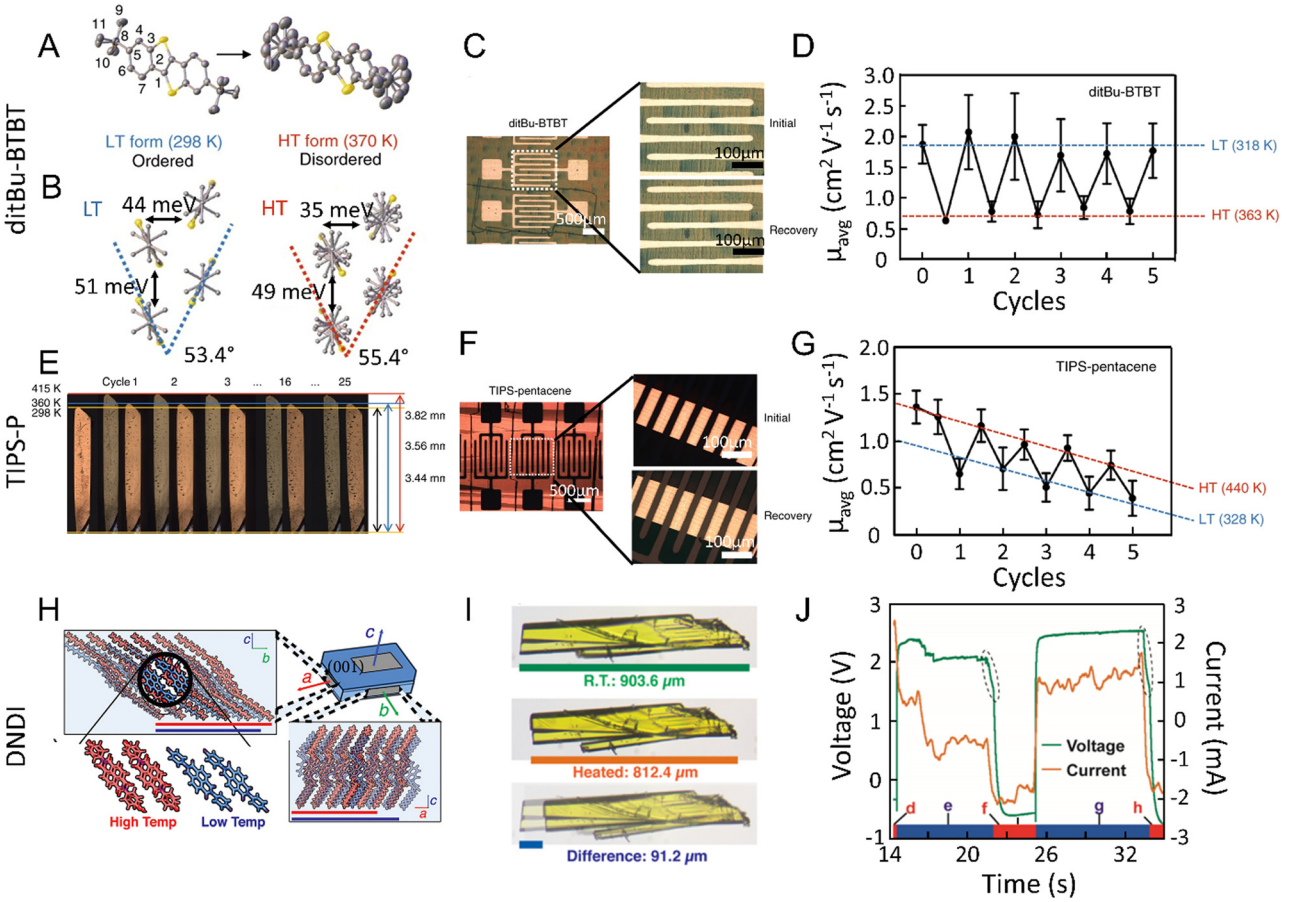

Fig. 27 (A) ditBu-BTBT shows a cooperative phase transition triggered by an order-to-disorder transition in the *tert*-butyl groups. This results in a (B) 2° change in the herringbone angle[50] which, despite the small change, causes the charge transfer integral between neighbors to decrease substantially, and (C) resulting OFET devices (D) show charge carrier mobility modulated by 217% between states over many cycles.[50] (E) TIPS-P shows a similar polymorphic phase transition that is coupled with a 10% elongation of the crystal. (F) Thin film devices exhibited (G) switching of the charge carrier mobility between the high and low temperature phases that evolves with multiple cycles.[50] Adapted with permission from ref. 50 Copyright 2018, Springer Nature. (H) Crystals of NDI derivative also undergo a thermally induced phase transition, as a result of changing molecule tilt, causing a (I) similar length change that was harnessed for (J) a robust actuator device.[355] Adapted with permission from ref. 355 Copyright 2021, American Chemical Society.

the first time in organic semiconductors. Park, Diao *et al.*[97] showed that a TIPS-P crystal held near the phase transition temperature undergoes rapid switching between polymorphs upon application and release of [100]-shear loading (*i.e.*, superelasticity). The mechanical stress was also accompanied by a significant shape change (Fig. 28A and D), previously shown to be thermally triggered.[50] In a similarly cooperative fashion, TIPS-P also exhibited cooperative twinning upon stretching of the crystal or [100] shearing at room temperature. Unlike the previous structural transitions, twinning preserves the same molecular packing in both the mother and daughter crystal (*i.e.*, ferroelasticity), but introduces new domain boundaries which accommodate significant strain (Fig. 28B and E). Remarkably, they demonstrated, in the case of ferroelasticity, that 70% of the charge carrier mobility is preserved under as much as 13% strain (Fig. 28C). Not only does ferroelasticity maintain performance under high strains, but the twinning process is also reversible, showing no signs of degradation even after multiple cycles up to 2.5% strain (Fig. 28F). This work establishes mechanically induced cooperative transitions as a new stress-releasing mechanism for highly deformable single crystal electronic devices.

5.3. Prospects and opportunities

Organic molecular crystals have shown extraordinary mechanical effects that range from elastic and superelastic deformability to self-actuation. The discovery and application of these effects in organic semiconductors in recent work have led the way to the novel electronic design of flexible electronics based on organic crystals. The easy access to deformability in organic semiconducting molecular crystals offers a unique advantage over inorganic counterparts in realizing wearable electronics. Moreover, the discovery of highly sensitive molecular crystals to strain provides a platform to confer additional functionalities for sensor-based devices. The nature of this sensitivity has been elucidated for several systems, suggesting the importance of molecular packing changes occurring during device bending. Coupling structural transitions in recent works have expanded

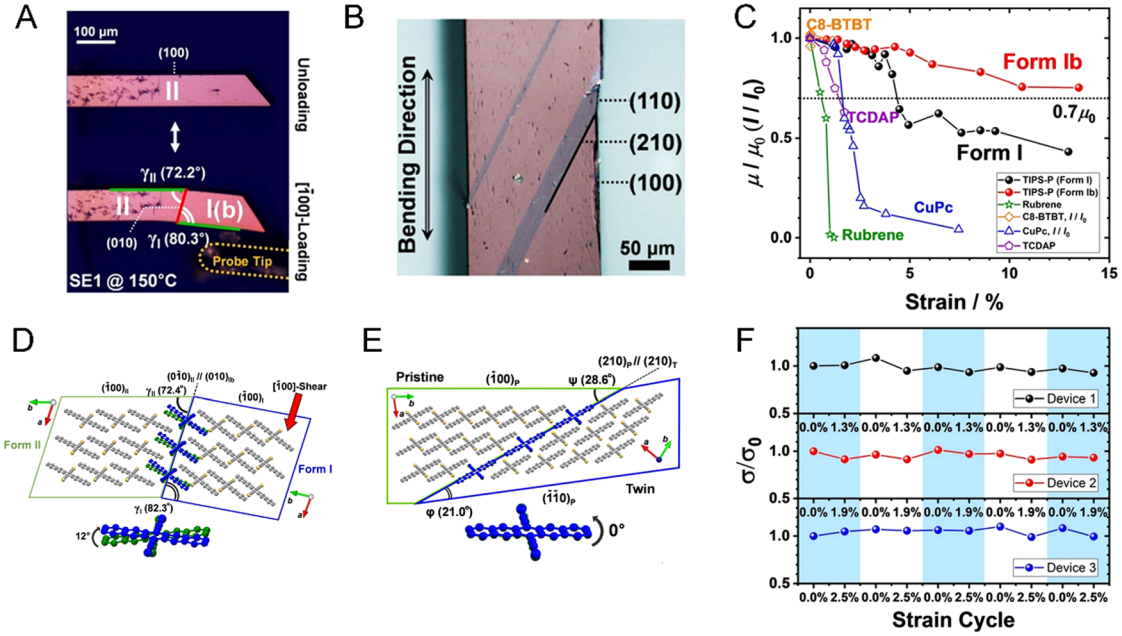

Fig. 28 TIPS-P phase transition coupled with [100] shearing applied to the crystal (A and D) and twinning coupled with stretching (B and E) exhibiting superelasticity and ferroelasticity, respectively. Device performance under stretching showed (C) stable charge carrier mobility in TIPS-P crystals up to 5% strain in form I and even higher strains in form Ib along (F) with high recoverability across 5 cycles.[97] Adapted with permission from ref. 97 Copyright 2020, Wiley-VCH.

the horizons for the functionality of these systems, pushing the limits of strain accommodation past 10% in organic semiconductor crystals. However, intentional access of specific bending modes and tuning their effect on electronic properties still remains elusive.

6. Application of molecular crystals as optical waveguides

6.1. Introduction to single crystal optical waveguides

An optical waveguide, in which light is transmitted internally through total reflection at the interface of an optical medium is a fundamental and pivotal composition of various devices in integrated optical circuits.[356,357] Optical waveguides include both long-distance optical waveguide fibers and short waveguides in centimeters, such as optical waveguides prepared from crystalline materials. Conventional optical waveguides, made of silica or polymers, are the primary media for fast, efficient and long-distance data transmission up to tens of thousands of kilometers. Nevertheless, they are rarely used for short-range micro/nanoscale data transmission. Organic crystals are viable candidates for the next-generation optical waveguides due to their high refractive index, variable chemical composition, uniform morphology, good thermal stability, and high photoluminescence (PL) efficiency.[358–360]

The structure of optical waveguides consists of a waveguide layer with a relatively high refractive index and a substrate and cover layer with a relatively low refractive index. Ideally, light escapes neither to the cover layer nor to the substrate and is completely confined to the waveguide with no attenuation of energy, in which the corresponding transmission mode is called a "guided mode" to describe the distribution of light energy in one-dimensional or multidimensional space. It should be noted that two factors are required to form an optical waveguide: total reflection and a medium with a higher dielectric constant/refractive index than that of the external environment.[361] Total reflection occurs when light propagates from a medium with a higher density to a medium with a lower density, and the incident angle is greater than the critical angle.[362] Therefore, the light field can be well confined in the micro/nanoscale structure. Organic crystals based on small organic molecules have excellent crystallinity and are devoid of grain boundaries, properties that are beneficial to light transmission. In addition, single crystals of π-conjugated organic molecules can be used as high-performance optical waveguides due to their alignment and dense packing.

Devices include passive and active optical waveguides. Passive optical waveguiding refers to the transmission of an unaltered (except for decreased intensity) incident light, while active waveguiding is the transmission of the material's fluorescence obtained *via* excitation with the incident light. In recent years, optical waveguide properties naturally generated from organic molecule crystals have been widely studied to realize both passive and active optical transmission.[363–369] For example, Döbeli *et al.* incorporated H^+ ions in an organic crystal to achieve a refractive index suitable for optical waveguides.[363] This work provides a new prospect for the application of ion implantation to integrated optics, and for the first time, to organic crystals. Fu *et al.* fabricated both perylene 1D

ribbon-like and 2D square-like crystals into waveguides.[364] This excellent example shows that the optical waveguide of an organic crystal can be adjusted by controlling the dimension of the crystal during synthesis. Subsequently, an increasing number of organic crystals with varied structures and morphologies have been synthesized and applied to various optical devices due to their excellent optical waveguide properties.[370–375] These studies have demonstrated broadband signal transmission from visible light to other regions, anisotropic response, and low optical loss (down to about 0.1 dB mm^{-1}) for organic crystals, all of which are promising for optoelectronic applications.

6.2. Flexible organic crystal optical waveguides

The majority of organic crystals are commonly stiff, brittle and tend to crack into pieces or powders under external pressure. This is mainly due to the regular arrangement of atoms, forming an ordered and stable structure. The mechanical properties greatly limit the use of organic crystals in practical applications, and especially in flexible electronic and optical devices. Therefore, organic crystals with exceptional mechanical flexibility[5,29] have attracted extensive attention and emerged as flexible optical media for high-performance waveguides. Flexible organic crystals have been already shown to be favorable waveguides.[370,376–395] In 2018, Zhang *et al.* reported a centimeter-sized elastic crystal of (*E*)-1-(4-(dimethylamino)phenyl)iminomethyl-2-hydroxyl-naphthalene (DPIN).[370] Having a relatively planar donor–acceptor structure, DPIN possesses bright emission and high elasticity in crystalline state. A flexible optical waveguide based on the high elasticity and luminescence of a DPIN crystal was first proposed and implemented (Fig. 29A–I). Subsequently, a self-waveguiding organic crystal with excellent ultralow temperature elasticity was prepared by the same group.[386] The crystal exhibits elasticity and is an excellent optical waveguide even at −196 °C (Fig. 29J–S). These results indicate the application potential of the single-crystal materials in flexible optical/optoelectronic devices in unconventional and extreme environments.

Mechanical deformations can be polymorph-dependent. Zhang *et al.* reported a crystalline molecular material, dimethyl 2,5-bis((thiophen-2-ylmethyl)amino)terephthalate, that has two polymorphs, Cry-**R** and Cry-**O**.[379] Cry-**O** can be elastically bent, almost into a loop, and acts as optical waveguide in both straight and bent state. The other polymorph, Cry-**R**, forms both naturally bent crystals and even forked crystals with optical waveguides as efficient as that of the straight crystal. Naumov *et al.* reported an azo compound, 3′,4′-dimethyl-4-(dimethylamino)azobenzene (DDAB), which combines mechanical response and optical waveguide properties for spatial photocontrol over the optical output.[309] DDAB crystals can be controlled through reversible photoswitching between the *trans* and *cis* isomers on the irradiated crystal surface. The passive optical waveguiding capability of the crystal remains unaffected by its deformation induced by exposure to UV light, which successfully demonstrated that photobendable organic crystals can efficiently transduce light while maintaining their dynamic function. This is the first case of two-dimensional spatial photocontrol of the optical output of an organic crystalline waveguide. In addition, Zhang *et al.* reported a dual stimuli-responsive bendable organic crystal of (*Z*)-4-(1-cyano-2-(4-(dimethylamino)phenyl)vinyl)benzonitrile (CN-DPVB).[385] The crystal is very elastic and bends noticeably when exposed to hydrochloric acid vapors. Millimeter-size crystals of CN-DPVB, in both straight and bent states, were tested as low-loss optical waveguides. This study showed the utility of chemical means to control the shape of crystals. Flexible optical waveguides from plastically bendable organic crystals have also been extensively studied owing to their extraordinarily mechanical compliance.[381,389] For example, Naumov *et al.* prepared an anthracene derivative, 9,10-dicyanoanthracene (DCA) which has both active and passive waveguiding properties in a plastic bent state (Fig. 30).[381] The straight and bent DCA crystals displayed green emission with three bands (530, 570, and 610 nm) upon excitation (365 nm). The excited position emitted green light, while both ends of the crystal emitted orange-red light, which is an evidence of active waveguiding (Fig. 30E and F). When the crystal was excited with 635 nm light, the spectrum of the transmitted light was retained, which is an evidence of passive waveguiding (Fig. 30G and H). Altogether, this and many other examples demonstrate that flexible crystals have excellent optical transmission capability, while they are also flexible. These results have important implications for practical applications, for example, in multiply bent, flexibleor complex optoelectronic devices. In addition, a combination of polymer materials and organic crystals has also been suggested to prepare organic crystals with sustained optical waveguiding properties.[396] The most recent research on hybrid crystal–polymer materials has expanded significantly both the range of stimuli that can be used to control the shape of organic crystals and the kinetics of their operation as dynamic optical waveguides.

The flexible organic crystalline waveguides discussed above typically have dimensions in the centimeter range. Miniaturized devices such as nanophotonic devices require nano-sized optical waveguides as one of their most important components.[397–399] However, due to their small size and brittleness microcrystals are generally difficult to handle. Micromanipulation using an atomic force microscope (AFM) cantilever can be used[80,378,395] to deform microcrystals without damage. Chandrasekar *et al.* proposed a method for precise control of the longitudinal size of self-assembled organic nanotubes.[400] A combination of laser confocal Raman and atomic force microscopes was employed to perform laser ablation/cutting and waveguiding experiments.[80] Recently, the same group in collaboration with others reported microcrystals of dithieno[3,2-*a*:2′,3′-*c*]phenazine (SYN) with mechanical flexibility for wavelength-division multiplexing (WDM) (Fig. 31).[378] When pressed with an AFM cantilever tip, the microcrystals deposited on the glass surface behaved like plastic crystals, due to the strong adhesion between the surface and the crystals. The efficient transmission of optical signals of different fluorescence colors by the flexible crystal waveguides (straight or bent), showed that the SYN crystals are suitable for

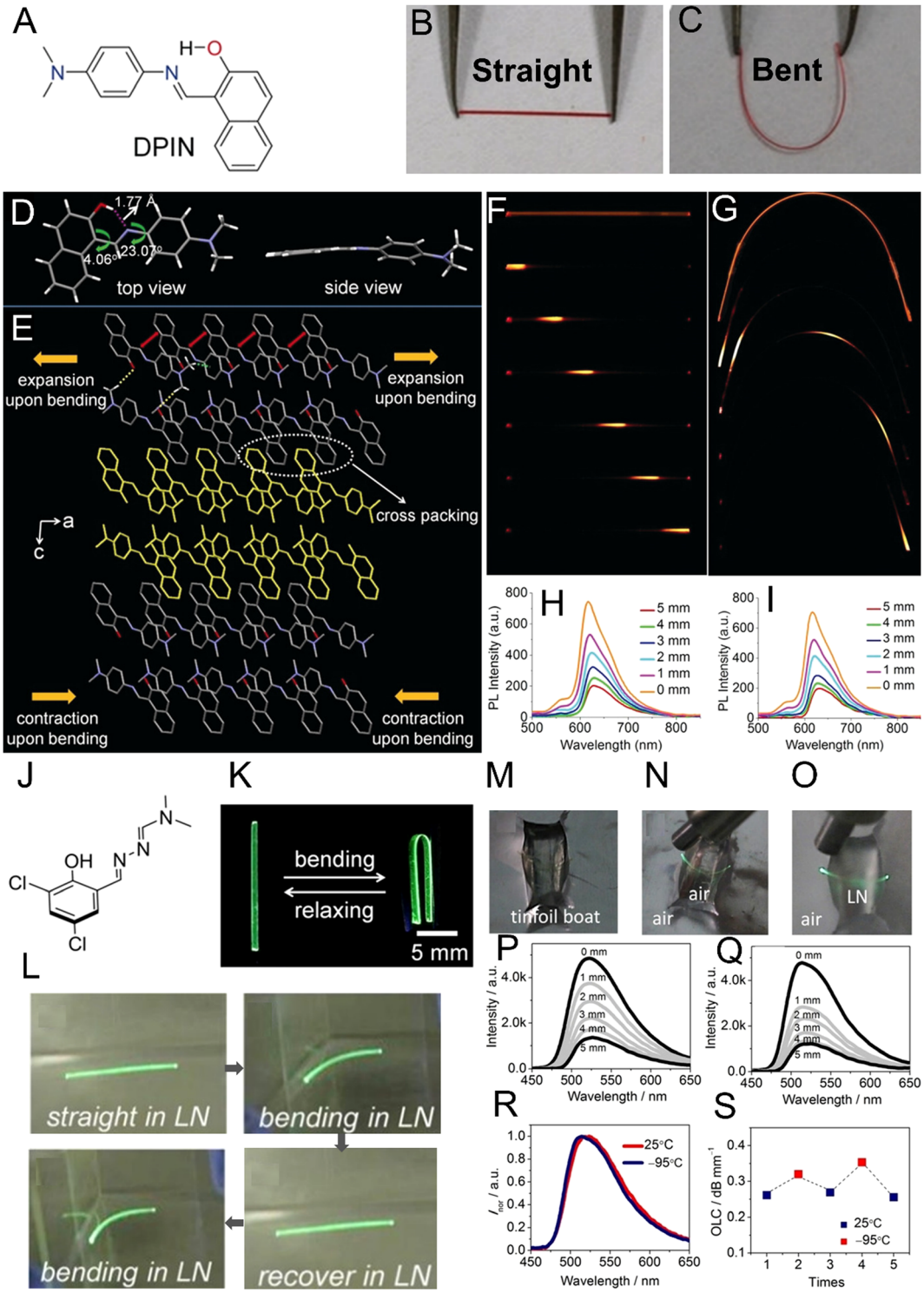

Fig. 29 (A) Chemical structure of DPIN. (B) Straight DPIN crystal and (C) elastically bent DPIN crystal that has been bent by applying mechanical force. (D) Crystal structure of DPIN. (E) Molecular packing in the (010) plane (the red arrows, green dashed lines and yellow lines represent the π–π, C–H···π and C–H···O interactions, respectively). (F and G) Excitation position-dependent fluorescence (FL) images of (F) straight and (G) bent crystals. (H and I) Corresponding fluorescence spectra of (H) straight and (I) bent crystals. Adapted with permission from ref. 370 Copyright 2018, Wiley-VCH. (J) Chemical structure of a compound used to study the temperature dependence. (K) Bending–relaxation (L) images of repeated bending experiments of a single crystal in liquid nitrogen (LN) under UV light. (M–O) Images of (M) tin foil boat, a bent crystal excited using a 355 nm laser from the left of (N) empty boat and (O) boat filled with liquid nitrogen. (P and Q) fluorescence spectra collected at one end of the crystal at (P) 25 °C and (Q) −95 °C. (R) Emission spectra of crystals at 25 °C and −95 °C. (S) Optical loss coefficients (OLC) of the same crystal determined by thermal switching between 25 °C and −95 °C. Adapted with permission from ref. 370 Copyright 2020, Wiley-VCH.

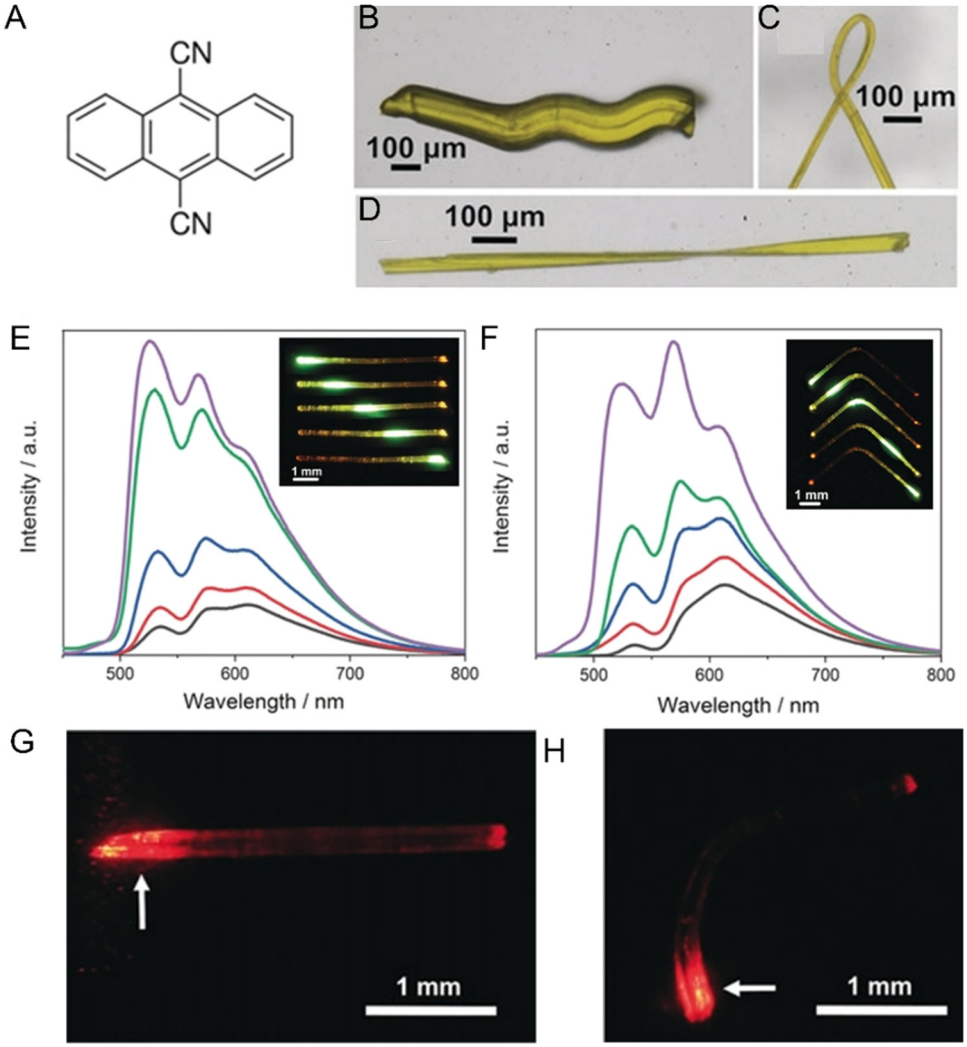

Fig. 30 (A) Chemical structure of 9,10-dicyanoanthracene (DCA). Plastic deformation of DCA crystals, shown as (B) multiple bending, (C) bending over 180°, and (D) twisting. (E and F) Fluorescence spectra recorded at the terminal of the straight (E) and bent (F) DCA crystals when the crystal was excited at different positions. The fluorescence images are shown in the insets. (G and H) Photographs showing the transduction of 635 nm light through the crystal before (G) and after bending (H). Adapted with permission from ref. 381 Copyright 2018, Wiley-VCH.

WDM (Fig. 31A–D). A 2 × 2 directional coupler with two inputs and outputs was constructed from two bent waveguiding crystals that were conjoined by micromanipulation. Optical coupling at either end of the crystal converts fluorescence to the other end of the crystal, and the output intensity of the two signals passing through the two waveguides is related to the optical path length (Fig. 31E–H). This mechanical micromanipulation approach can also be effectively applied to other flexible microcrystals to design and construct complex photonic circuits. Meanwhile, Chandrasekar and Naumov groups have jointly demonstrated an effective and non-destructive method for manipulation of microcrystalline optical waveguides.[80] By using this method, mechanically compliant single microcrystals can be precisely bent, repositioned, and split.

There are still many challenges to be solved towards practical applications of organic crystal waveguides. The speed of information processing is a key parameter and performance index of the future optoelectronic integrated devices. Molecular components of crystals and their photophysical properties, *e.g.* optical band gaps and charge separation, must be properly selected and designed to obtain a reliable high-velocity response. To realize integrated optimization of device geometries, the controllability of crystal shape is a basic requirement. Moreover, it is necessary to improve the control of the optical coupling between the photoconductive medium and the integrated device. Altogether, flexible organic crystals appear as an ideal choice for the fabrication of complex optoelectronic devices.

6.3. Amplified spontaneous emission (ASE) in flexible organic crystals

Compared to ordinary light sources, lasers with conspicuous monochromaticity, directionality and high brightness are widely applied in various fields such as medicine,

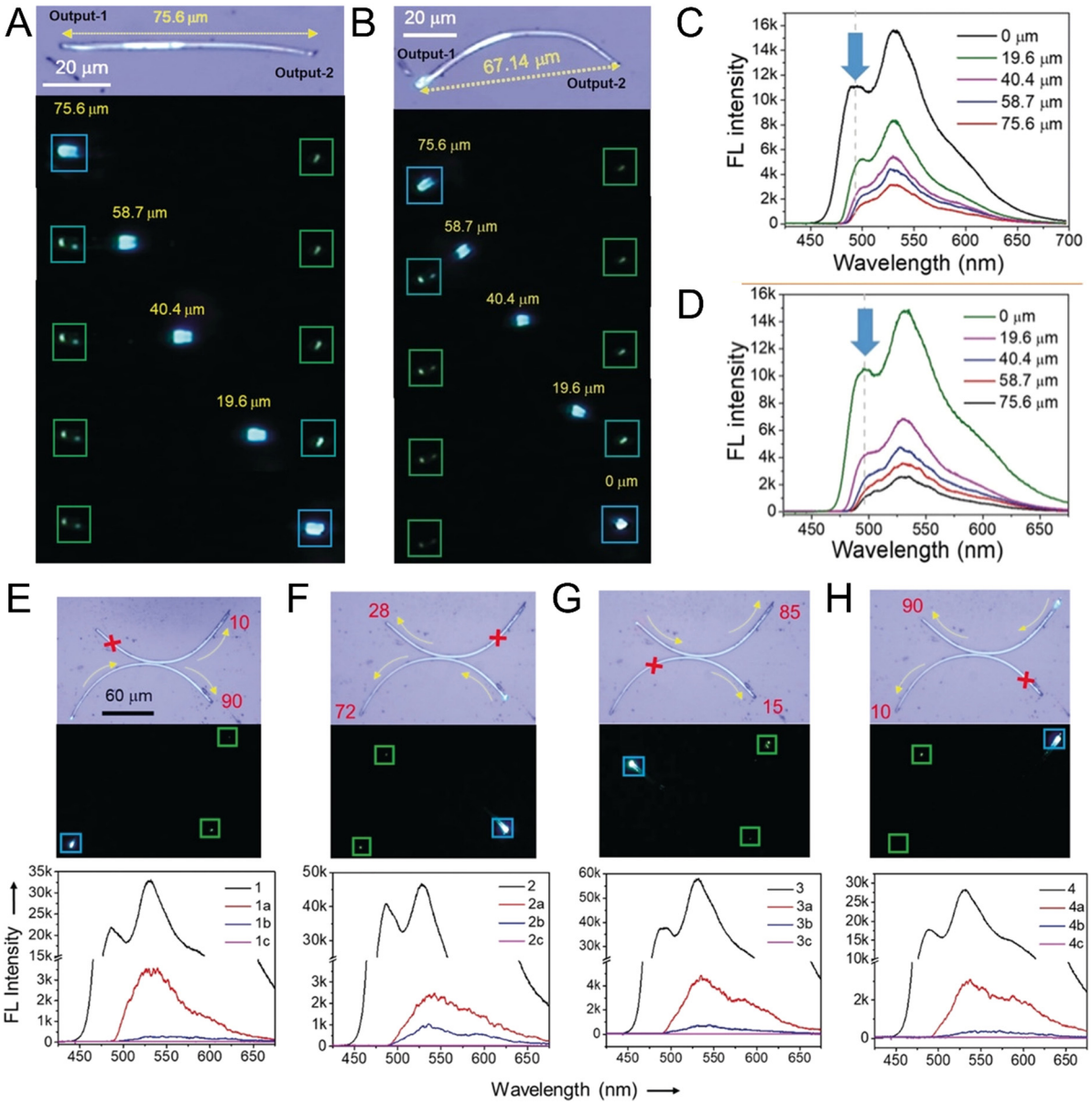

Fig. 31 (A,B) Confocal optical micrographs of (A) nearly straight crystals (B) that were bent into an arc. Fluorescence images of the microcrystals transducing light when excited at different positions are also shown. (C,D) Fluorescence spectra of (C) straight and (D) bent crystals collected at the end of the crystals excited at different positions. (E–H) From top: confocal optical microscopy, fluorescence images and spectra of two coupled crystalline waveguides acting as a 2 × 2 directional coupler when excited at any one of the four termini. The red crosses indicate absence of light output. The yellow arrows show the light propagation paths. The red numbers indicate the path-dependent spectral ratio of the directional coupler. Adapted with permission from ref. 378 Copyright 2020, Wiley-VCH.

telecommunications, and national defense, and even in our daily life, including printers, barcode readers, and video and audio players. The laser generally consists of three parts: a pumping source, an optical gain medium and an optical resonator. The presence of a gain medium that amplifies light is a necessary condition for the generation of laser light.[401] The amplification of light originates from the stimulated radiation process of organic luminescent materials. When the medium is excited with an incident beam of light, the excited particles jump to the ground state and emit photons that have the same phase, frequency, polarization and direction of propagation as the incident photons, which means that the original incident light has been amplified. The amplified light produced by this phenomenon of stimulated emission is laser light.

Organic solid-state lasers (SOLs) that have the advantage of easily adjustable fluorescence, high absorption cross-sectional area, flexibility, and light weight are of interest to laser research.[401] Considering their good processing properties, applicable substrates and wide spectral range, organic luminescent solids hold a great potential for the development of organic lasers. Although

solid organic lasers have been widely used, research on organic crystal-based lasers is still rare due to the difficulty with obtaining high-quality crystals of appropriate size and shape with high fluorescence efficiency. In 1997, Fichou demonstrated the phenomenon of amplified stimulated emission (ASE) of an α-oligothiophene single crystal.[402] Under single-photon pumping, dual-energy dependence of two distinct emission lines and low threshold gain narrowing were observed, which resulted from a net alignment of molecular dipoles in a crystal having the dimensions and optical quality of a resonator. For organic crystals, crystal quality, molecular packing and intermolecular interactions have important effects on the behavior of ASE.[403,404] Until now, ASE properties have been identified in various organic crystals with different molecular structures, including thiophene–phenylene co-oligomers (TPCOs), oligophenylene vinylenes (nPVs), anthracene and chalcone derivatives.[405–418] For instance, Wang *et al*. have reported two new molecules with amplified spontaneous emission.[406,407] Four kinds of crystals with different fluorescence emissions from green to orange were obtained from 4,4′-(thiazole[5,4-*d*]-thiazole-2,5-diyl)bis(*N*,*N*-diphenylaniline) (PTATA) by varying the crystal growing conditions.[406] Only the green-light-emitting PTATA crystal exhibits great potential in organic lasers due to its low threshold ASE character whereas other crystalline phases do not show this phenomenon. Additionally, two polymorphs **1R** and **1O**, with quite different emissions, were prepared based on a very simple organic ESIPT-active molecule, (*E*)-3-(4′-dimethylaminophenyl)-1-(4′-fluoro-2′-hydroxyphenyl)-2-propen-1-one.[407] Crystals **1R** and **1O** display significantly narrowed and amplified emissions, thus providing a rare example of polymorph-dependent ASEs. Recently, a wide-wavelength tuning approach of organic micro/nanolasers was established by Dong *et al.*[410] The output lasing wavelengths of 2,5-bis(4-biphenylyl)thiophene (BP1T), doped with a controllable amount of 5,5″-bis(4-biphenylyl)-2,2′:5′,2″-tetrathiophene (BP3T), were switched across all vibronic bands covering the entire emission spectrum. The results indicate a promising path for rational design of miniaturized lasers and other photonic components with similar performance.

Although organic crystals have drawn immense attention for their attractive applications in laser photonics in recent decades, the future implementation of flexible organic crystals in optical devices, such as crystal lasing devices, remains a formidable challenge.[402,403,419] In 2012, Sun *et al.* fabricated ultra-thin organic single crystals of 1,4-bis(4-methylstyryl)benzene (BSB-Me) that were used as active lasing media in distributed feedback laser devices.[420] The thin single crystals were extended onto bendable poly(ethyleneterephthalate) (PET) substrates and a flexible organic single-crystal distributed feedback (DFB) laser was constructed. The results promise the development of low-cost and flexible crystal lasers. Zhang *et al.* have conducted in-depth studies on flexible ASE crystals in recent years.[379,382,391] In 2018, they reported the elastic organic crystals **1d@2d**, prepared by doping 2,5-dihydro-3,6-bis(octylamino)terephthalate (host **1d**) with 3,6-bis(octylamino)terephthalate (guest **2d**).[382] The potential application of **1d@2d** as flexible crystal lasing medium was revealed by ASE measurements, and the threshold value of bent crystals of **1d@2d** was determined to be 115 kW cm^{-2}, which is comparable to that of a straight crystal (Fig. 32). The doping method combines the advantages of **1d** and **2d** for making doped crystals **1d@2d** with excellent elasticity and strong orange fluorescence. The potential of these doped crystals was evaluated by measuring amplified spontaneous emission in straight and bent states. Crystals of Cry-**O** mentioned in the previous section[379] are also good candidates for flexible crystal lasing media. The results indicate that light was perfectly confined and amplified by stimulated emission inside the highly bent Cry-**O** crystals, and the threshold value was determined to be 107 kW cm^{-2}. Very recently, a diaryl β-diketone with three different emissive organic polymorphs was reported.[391] Cry-**G** and Cry-**Y** exhibit ASE, and Cry-**G** does so when bent. These results could guide the development of crystal flexibility by structure engineering and provide models of flexible organic crystals for multifunctional application in flexible laser devices.

Low ASE thresholds have been demonstrated based on some specific structures, such as fluorene, anthracene and *p*-phenylene vinylene derivatives. However, there is no well established theory to determine whether a particular organic crystal possesses ASE characteristics. The development of effective methods to detect the high gain medium of organic lasers, especially the electrically pumped fiber lasers, remains a great challenge. For the prospective application of electrically pumped organic lasers, there are several critical requirements as to the gain media. An extremely low threshold means that a low current density is required under electrically pumped conditions. A high optical gain coefficient can compensate for the optical loss of the electrically pumped equipment, and high thermal and optical stability is required to ensure long-term operation of the equipment. The mechanical bendability and machinability allow the crystal laser architecture to be flexibly adjusted.[404,421]

6.4. The physics of single-crystal optical micro-microwaveguides, resonators and photonic integrated circuits

Organic crystal-based optical components, *viz.*, optical waveguides,[309,359,370,372,385,400,422–426] resonators,[427–429] modulators,[430] circuits,[378] and lasers[419,431] are essential for construction of future organic nanophotonic devices.[432] Organic optical crystals offer high exciton (electron-hole) binding energy, room temperature-stable exciton-polariton (EP),[433,434] optical bandwidth tunability (from UV to NIR), high refractive index ($n = \sqrt{\varepsilon_r}$; where ε_r is the dielectric constant), optical nonlinearity ($\chi^{(2 \text{ or } 3)}$ where χ is electric susceptibility and the superscript denotes the order),[427–429] responsiveness to stimuli,[309,430,435] and mechanical flexibility.[80,370,422,426]

An optical waveguide can be classified as either active[309,370,372,422,424,425] or passive.[359,423] The first active type flexible microwaveguide based on 3-ethyl-2-[(3-ethyl-2(3*H*)-benzothiazolylidene)methyl] benzothiazolium iodide (thiacyanine, TC) was reported by Takazawa *et al.* in 2015.[424] Later, the first flexible, passive type crystal waveguide based on

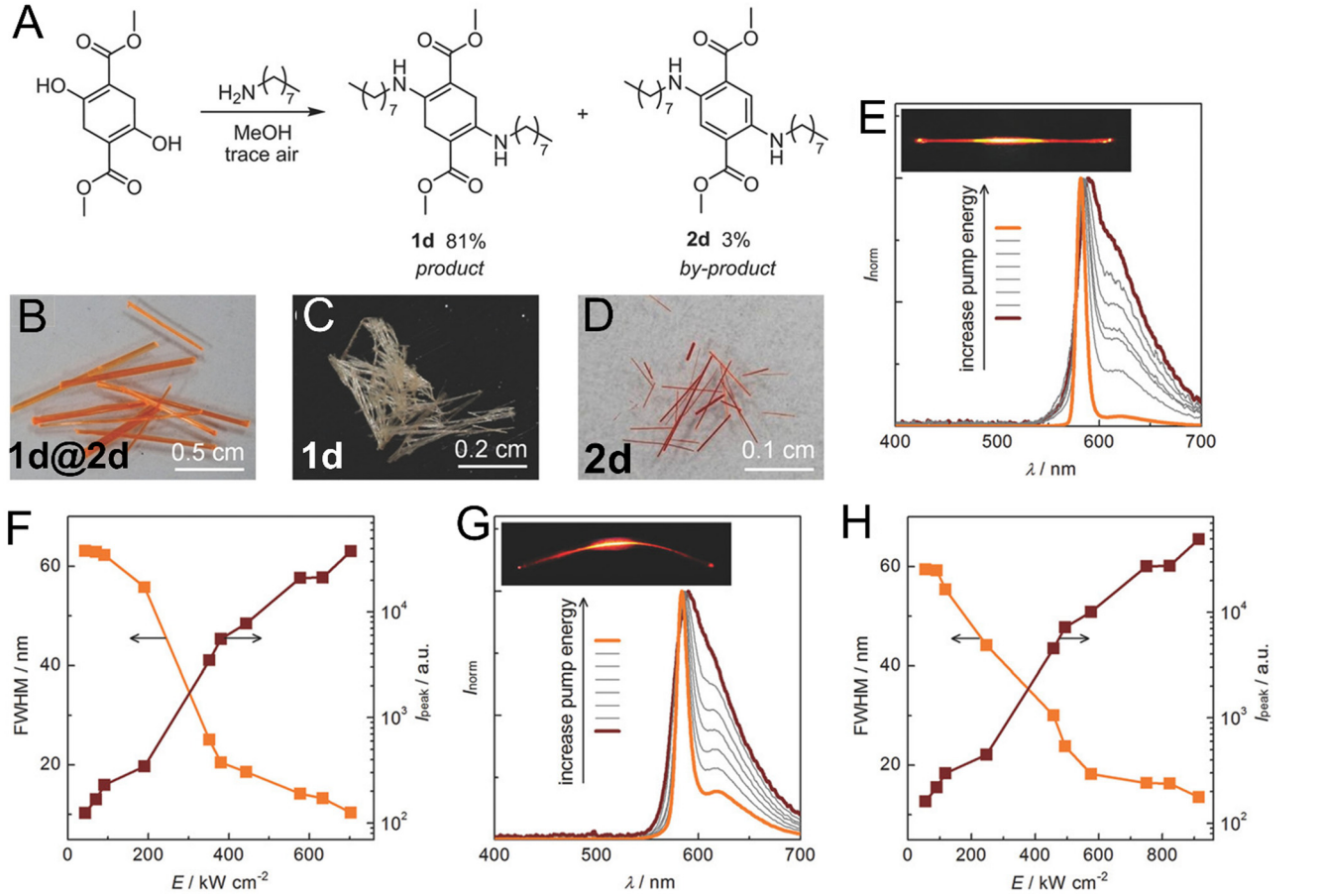

Fig. 32 (A) Synthesis of crude **1d** containing **2d** as an oxidized byproduct. (B–D) Photographs of crystals **1d** containing **2d** (**1d@2d**), **1d** and **2d**. (E and G) Emission spectra of straight (E) and bent (G) crystals as a function of the pump laser energy. Photographs of the crystal under the excitation of a pump laser are shown in the inset. (F and H) Dependencies of the fluorescence intensity and full-width half-maximum (FWHM) on the pump laser energy for straight (F) and bent (H) crystals. Adapted with permission from ref. 382 Copyright 2018, Wiley-VCH.

4,4′-bis(2,6-di(1*H*-pyrazol-1-yridinedin-4-yl)biphenyl that transduces light at any acute angle was reported by Chandrasekar *et al.* in 2013.[426] Both types of waveguides are important for organic integrated photonic circuits (OPICs). Typically, the input light couples to a high refractive index optical waveguide after meeting the total internal reflection (TIR) condition (Fig. 33A), *i.e.*, when the angle of the incident light (θ_1) is greater than the critical angle (θ_c). An example of light transmission within an organic crystal waveguide (n_2) *via* TIR is shown in Fig. 33A. An evanescent field penetrates towards the low-refractive medium (n_1) during the light reflection, and it decays exponentially from the interface. The evanescent field couples the two optical waveguides, excites a resonator, near field interaction, and powers a device wirelessly.

In waveguides, light propagates as modes in finite numbers. Depending upon the diameter of the guiding medium, it can transduce single-mode or multimodal light. By assuming the transverse magnetic (TM) modes of light (in the *x*,*y* plane), the number (m) of propagating optical modes in a rectangular waveguide with uniaxial dielectric parallel and perpendicular components can be determined by using the following relation:[419]

$$m < \frac{2w}{\lambda} \cdot \frac{\varepsilon_{\perp}}{\varepsilon_{\parallel}} \sqrt{\varepsilon_{\parallel} - \varepsilon_S} \tag{9}$$

where λ is the light wavelength, w is the width of the waveguide, and S is the substrate dielectric constant. By considering that the waveguide is optically isotropic ($\varepsilon_{iso} = \varepsilon_{\perp} = \varepsilon_{\parallel}$), the cutoff wavelength (λ_{cutoff}) of a propagation mode (when $m < 1$) is given as

$$\lambda_{cutoff} = 2w\sqrt{\varepsilon_{iso} - \varepsilon_S} \tag{10}$$

Recently, propagation of light down to a subwavelength scale through the EP mechanism was reported.[436] The crystal waveguide's optical loss coefficient (α) can be estimated by fitting the plot of the intensity ratio (I_{tip}/I_{body}) *versus* propagation distance (d) using the following equation:

$$I_{tip} = I_{body}e^{-\alpha d} \tag{11}$$

Optical resonators or cavities trap the light after meeting the TIR conditions. Depending upon the resonator's geometry, the

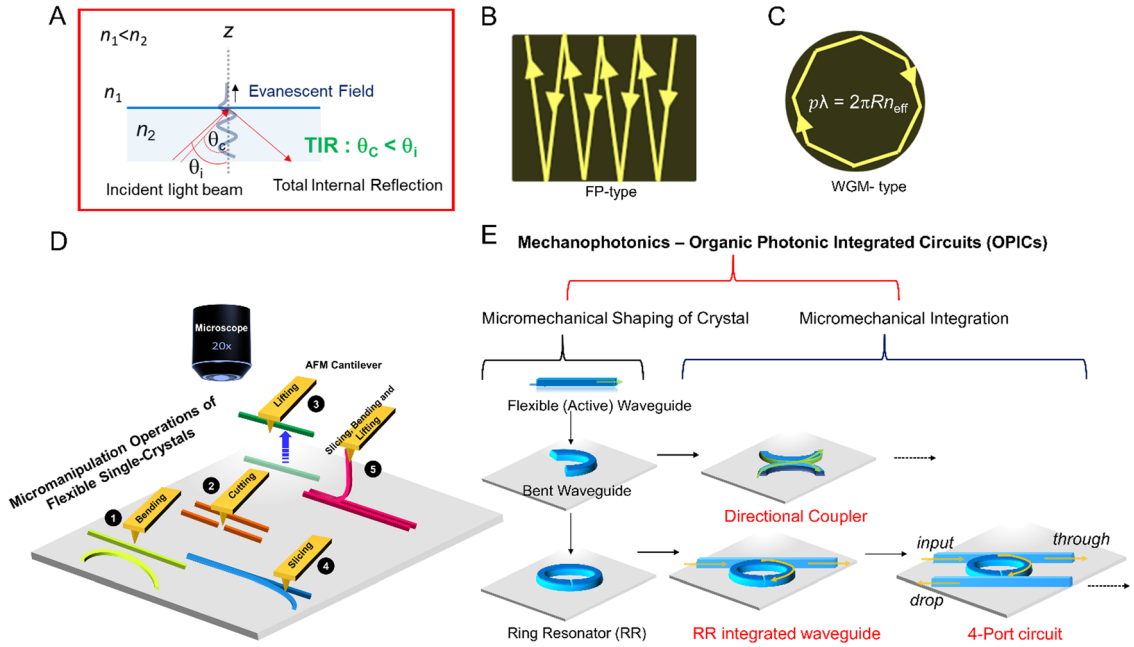

Fig. 33 (A) Total internal reflection condition and exponentially decaying evanescent field formation. (B) Light reflection in Fabry–Pérot (FP) resonators, and (C) circulation in whispering–gallery–mode (WGM) resonators. The inset shows the equation for the resonance condition. (D) Schematic representation of micromechanical operations involved in the AFM-based micromanipulation under a confocal microscope. (E) The proposed mechanophotonics approach towards the fabrication of single-crystal-based OPICs. Adapted with permission from ref. 80 Copyright 2020, Wiley-VCH, adapted with permission from ref. 378 Copyright 2020, Wiley-VCH and ref. 400 Copyright 2014, The Royal Society of Chemistry.

light can be shuttled or circulated, creating two different types of resonance, namely, Fabry–Pérot (FP) or whispering–gallery–mode (WGM), respectively.[419,427] In crystal-based FP resonators, the light is reflected between two parallel mirror-like surfaces (Fig. 33B). In WGM resonators, recurrent light circulations occur *via* multiple light reflections at mirror-like circularly arranged facets, such as crystals with hexagonal, square, or octahedral geometries (Fig. 33C).[427] The light which meets the phase-matching condition or resonance criterion, $p\lambda = 2\pi R n_{eff}$ is self-reinforced, and this corresponds to constructive interference. In contrast, phase-mismatched light is removed, corresponding to destructive interference (in this equation, n_{eff} is the effective refractive index of the resonant mode, R is the cavity radius, λ is the light wavelength, and p is an integer number associated with the angular momentum of a circulating photon). The constructively interfered optical modes appear in the fluorescence spectrum as sharp peaks. The separation between the modes is called the free spectral range (FSR). The FSR value is inversely related to the resonator size.

In optical resonators, an evanescent field is essential to couple two photonic elements (*e.g.*, two waveguides or a waveguide and resonator) optically when they are in physical contact (typically with their separation not longer than $\lambda/2$). An excellent example of a device based on evanescent field coupling is the directional coupler.[437] This evanescent field can be also used to construct crystal-based OPICs.[438–440] Microscale optical waveguides (straight and bent) and resonators are essential components of miniature OPICs. In this context, mechanically flexible (bendable) microcrystal waveguides are important because the circuit demands manipulation of photons in different directions and at various angles. Splitting, modulating (phase/intensity), filtering, lasing, coupling and detecting light are some of the functions that can be realized in OPICs by integrating flexible crystal waveguides (passive/active), resonators, and modulators.[439,440] The high thermo-optic coefficient (temperature dependence of n) of silicon-based PICs[441] makes them sensitive to slight deviations from circuit geometry; therefore, OPICs could be a good substitute for silicon-based circuits.[442]

6.5. Mechanophotonics

6.5.1. Mechanical micromanipulation operations of crystals using AFM. The mechanical fabrication of microscale OPICs hinges on the precise shaping of crystal waveguides and cavities in various geometries on the substrate surface, their alignment at a desirable place, and subsequent physical integration—a method known as mechanophotonics.[80,378,383,400,422,438–440] For the manipulation of flexible crystals, AFM has been recognized as a very convenient tool. Micromanipulation operations such as (i) moving, (ii) lifting, (iii) bending, (iv) slicing, (v) cutting, (vi) transferring (from one substrate to another) and aligning/integration of crystals are required for OPIC fabrication (Fig. 33D).[439,440] Light transport mechanisms such as passive, active, re-absorbance and energy transfer (crystal-to-crystal) can be employed to design OPICs using rigid, elastic, and plastic crystals.

6.5.1.1. Crystal moving and lifting. The lifting of a crystal from the substrate is a vital micromanipulation operation.

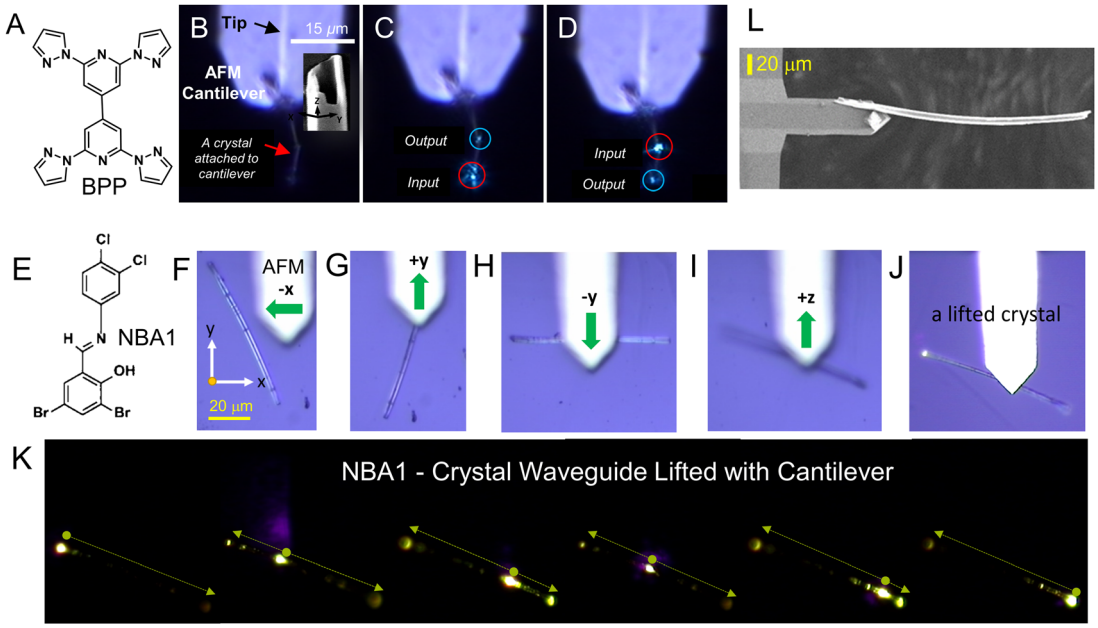

Fig. 34 (A and E) Molecular structure of **BPP** and **NBA1**. Optical micrographs of a (B) bent crystal attached to an inverted AFM cantilever (the inset shows the FESEM image of a tubular crystal tip) and (C and D) passive optical waveguiding behavior of the bent crystal. Optical micrographs of a (F) crystal on the substrate, (G) movement of the cantilever towards the crystal, (H) crystal being pulled by the cantilever in the backward direction and (I) then pushed forward to connect it to the tip, and (J) finally being lifted. (K) Fluorescence images of a single crystal lifted using the cantilever, excited at different positions. The broken yellow arrows show the direction of light propagation. (L) FESEM image of the crystal attached to the cantilever. Adapted with permission from ref. 80 Copyright 2020, Wiley-VCH and ref. 400 Copyright 2014, The Royal Society of Chemistry.

This operation helps to move the selected crystal to the substrate's desired location and to transfer a crystal from one substrate to another for integration. The first example of mechanical manipulation of a microcrystal waveguide was performed using a BPP microcrystal waveguide in 2014 (Fig. 34A).[400] The crystal was lifted from the substrate using an AFM cantilever tip (Fig. 34B–D). The experiment was initially intended to demonstrate the efficient passive waveguiding ability of a crystal even when it is lifted from the substrate and surrounded by air (n = 1).

In 2020, the same experiment was performed with a flexible crystal of *N*-benzylideneaniline derivative, abbreviated **NBA1** (Fig. 34E).[80] The optical images displaying steps that are involved in lifting a single crystal from the substrate using an AFM cantilever are presented in Fig. 34F–J. The first step was attaching the crystal to the tip using tip-crystal attractive forces. The cantilever was then moved back and forth over the crystal, attaching the crystal to the tip (in this particular case, $-x$, $+y$ and $-y$ directions). The cantilever carrying the crystal was slowly lifted ($+z$ direction), as shown in Fig. 34F, G and L. The lifted crystal also efficiently transduced the fluorescence to its tips, confirming the retention of its optical waveguiding properties (Fig. 34K).

6.5.1.2. Crystal cutting and bending. Another essential micromechanical operation is crystal cutting, as it is useful for making optical waveguides of defined lengths suitable for precise OPIC fabrication. The first cutting operation of a DCM dye-based FP crystal to alter the cavity length was also performed with an AFM cantilever (Fig. 35A–D).[443] **NBA2** crystals obtained from a derivative of *N*-benzylideneanilines also exhibit mechanical flexibility (Fig. 35E–G). It was expected that tilting of the π–π stacked (4.464 Å) molecules along with the sliding neighboring molecules drives the compression (concave side) and expansion (convex side) of the bent section of the crystal (Fig. 35G). The Young's modulus of **NBA2** is 0.53–0.61 GPa on the (010) face, as measured by performing the three-point bending test. Applying a force perpendicular to the crystal's longest axis separated the crystal into two pieces (Fig. 35H–J).[80] One of the straight crystals ($L \approx 163$ μm) was bent to an angle $\alpha \approx 12^\circ$ by pushing its right side by using an AFM tip (Fig. 35L). Remarkably, the bent (elastic) crystal retained its bent shape due to surface adhesion (Fig. 35M). Both the left and right ends of the crystal were then bent to angles of $\alpha \approx 34^\circ$ and 43°, respectively, to realize an arc-shaped crystal (Fig. 35M–P). The FESEM examination of another **NBA2** bent crystal's (chord ≈ 115 μm) body and termini showed no visible defects (Fig. 35Q). Single-particle microspectroscopy revealed the microcrystal's optical waveguiding properties before and after bending (Fig. 35R and S). To estimate the optical loss coefficients of waveguides before and after mechanical bending, the excitation-position-dependent fluorescence spectra were collected by varying the optical path length. Subsequent analysis of the spectral data using eqn (3) showed only a slight variation of 0.00207 dB μm^{-1} in the estimated α, indicating a very small bending-induced optical loss (Fig. 35T).

6.5.1.3. Crystal slicing and double bending. Crystal slicing is a vital micromanipulation operation that detaches single crystals from microcrystalline aggregates. This operation was

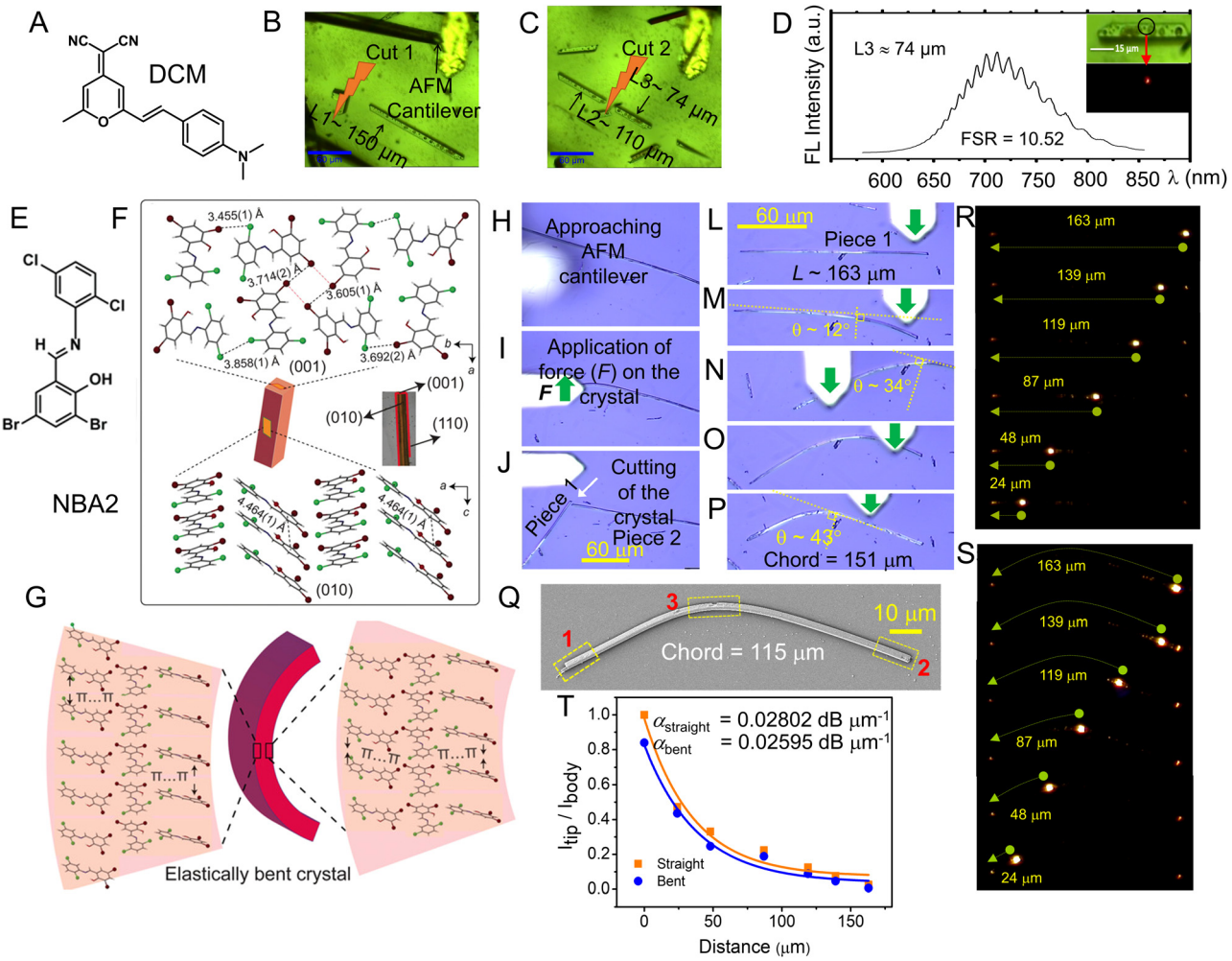

Fig. 35 (A and E) Molecular structures of **DCM** and **NBA2**. (B and C) Cutting of a long microrod into three different lengths using an AFM cantilever tip. (D) FP resonances from a microrod of length ~74 μm. The insets show their corresponding bright and fluorescence field images before and after laser excitation, respectively. (F) Molecular packing in a crystal of **NBA2** viewed perpendicular to their (010) and (001) faces. (G) Schematic diagram showing the mechanism of elastic bending of a **NBA2** crystal. Confocal optical micrographs of (H) an AFM tip approaching the crystal, (I) application of force at the middle of the crystal, which results (J) in breaking of the crystal into two pieces, and (L–P) bending of one of the pieces of length $L \approx 163$ μm by alternative applications of force at both ends of the crystal. (Q) FESEM images of a bent single crystal. (R and S) Fluorescence images of straight and bent crystals of **NBA2** transducing light when they are excited at different positions. (T) Plot of the intensity ratio at the tip and the body of the crystal (I_{tip}/I_{body}) *versus* the distance of light propagation used to estimate the optical loss coefficient (α). Adapted with permissions from ref. 80 Copyright 2020, Wiley-VCH and ref. 443 Copyright 2016, Wiley-VCH.

demonstrated by taking three bundled **NBA2** crystals (Fig. 36A).[80] The crystals' left side was segregated by pressing the AFM cantilever tip against the troughs between the crystals on the left side and moving back and forth perpendicular to the crystal axis (Fig. 36B). Due to their flexibility, the crystals bent and partially separated on the bundle's left side while they remained attached to its right side. Each crystal could be bent further by the AFM tip (Fig. 36C), and the crystals transduced fluorescence in different directions (Fig. 36B and C). Sliding the cantilever along the long axis from the left to the right end of the bundle completely separated one of the bent crystals (Fig. 36D). The separated bent crystal regained its straight shape, confirming the crystal's elasticity when there is no contact with the substrate. Furthermore, the remaining attached crystals could be manipulated to create a doubly bent crystal (Fig. 36E). Schematic representation of the steps involved in the operation is shown in Fig. 36F.

6.5.1.4. Crystal lifting, transfer, and alignment/integration. Transferring crystals from one substrate to another is an essential micromechanical operation for fabricating hybrid OPICs with two or more chemically (electronically) or mechanically different crystals.[438] For example, DPIN crystals (Fig. 37A) are mechanically flexible to an extent that extremely curved geometries, almost circular, can be prepared. The flexibility of DPIN and BPIN crystals presumably arises from the expansion and contraction of crisscross-type weakly interacting molecular chains. Both DPIN and BPIN emit green and orange fluorescence, respectively. To create a hybrid μ-OPIC, the DPIN crystal waveguide was bent to a truncated ring shape on substrate-1 (see Fig. 37C). Later, to

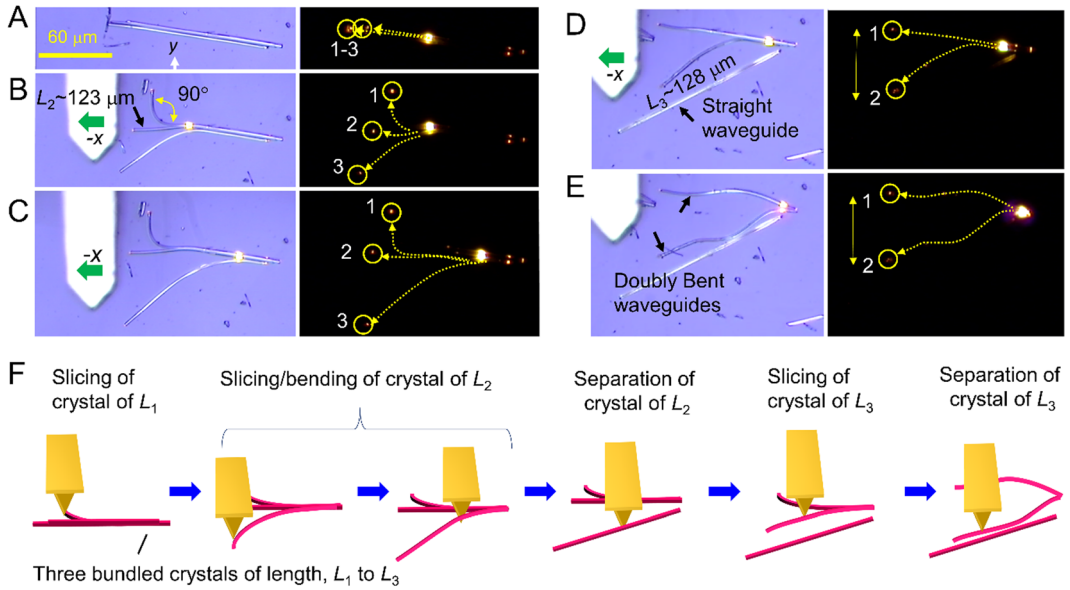

Fig. 36 (A–E) Confocal optical micrographs (left) and the respective fluorescence images (right) of three bundled crystals that were later partially or completely separated by slicing, cutting and bending operations. (B and C) Partial separation of crystals by means of slicing and (D) separation of a crystal from the bundle. (E) Mechanical bending at multiple points to obtain a crystal with an undulated shape. The broken yellow arrows in all fluorescence images indicate the direction of light propagation. (F) Cartoon representation of slicing and bending operations. Adapted with permission from ref. 80 Copyright 2020, Wiley-VCH.

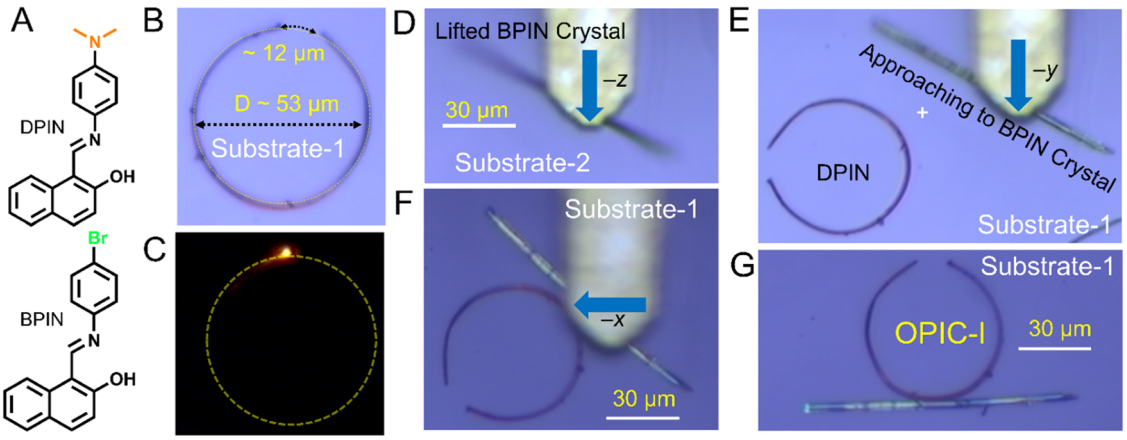

Fig. 37 (A) Molecular structures of **DPIN** and **BPIN**. Confocal micrographs portraying AFM-based, (B and C) mechanically bent truncated circular **DPIN** crystal, (D) mechanical lifting, (E and F) transferring and (G) moving (with positioning) to integrate a straight **BPIN** crystal with a truncated circular **DPIN** crystal to create μ-OPIC-I. Adapted with permission from ref. 438 Copyright 2020, Wiley-VCH.

integrate a straight BPIN optical waveguide with a truncated ring-shaped DPIN crystal, the BPIN waveguide was lifted from one of the substrates by attaching it with an AFM cantilever. This lifted BPIN crystal was carefully moved and aligned close to the DPIN crystal and dropped onto the other substrate. Finally, the BPIN crystal was physically integrated with the DPIN crystal by carefully moving it with the cantilever, forming a micro-OPIC.

6.6. Micro-organic photonic integrated circuit (μ-OPIC) components

6.6.1. Flexible single-crystal monolithic organic directional coupler. Needle-shaped single microcrystals of dithieno[3,2-*a*:2′,3′-*c*]phenazine (**DTP**) are mechanically flexible (Fig. 38A), and can be bent into optical waveguides.[378] These crystal waveguides grow along [100] with two pairs of side faces, $(0\bar{1}1)/(01\bar{1})$ and $(0\bar{1}\bar{1})/(011)$. The molecules stack along [100], forming columns. The crystal's most dominant interactions result from aromatic stacking. During mechanical crystal bending, the molecular rotation towards planarity enables compression of the inner arc (concave) in a herringbone structure. In contrast, rotation in the opposite direction facilitates elongation of the crystal's outer arc (convex).

To fabricate a 2 × 2 directional coupler with four termini, two straight DTP crystals (crystal-1 and crystal-2) were bent into arc-shapes using AFM cantilever tip force. The microcrystal's apparent pseudoplasticity suggests that the crystal–substrate

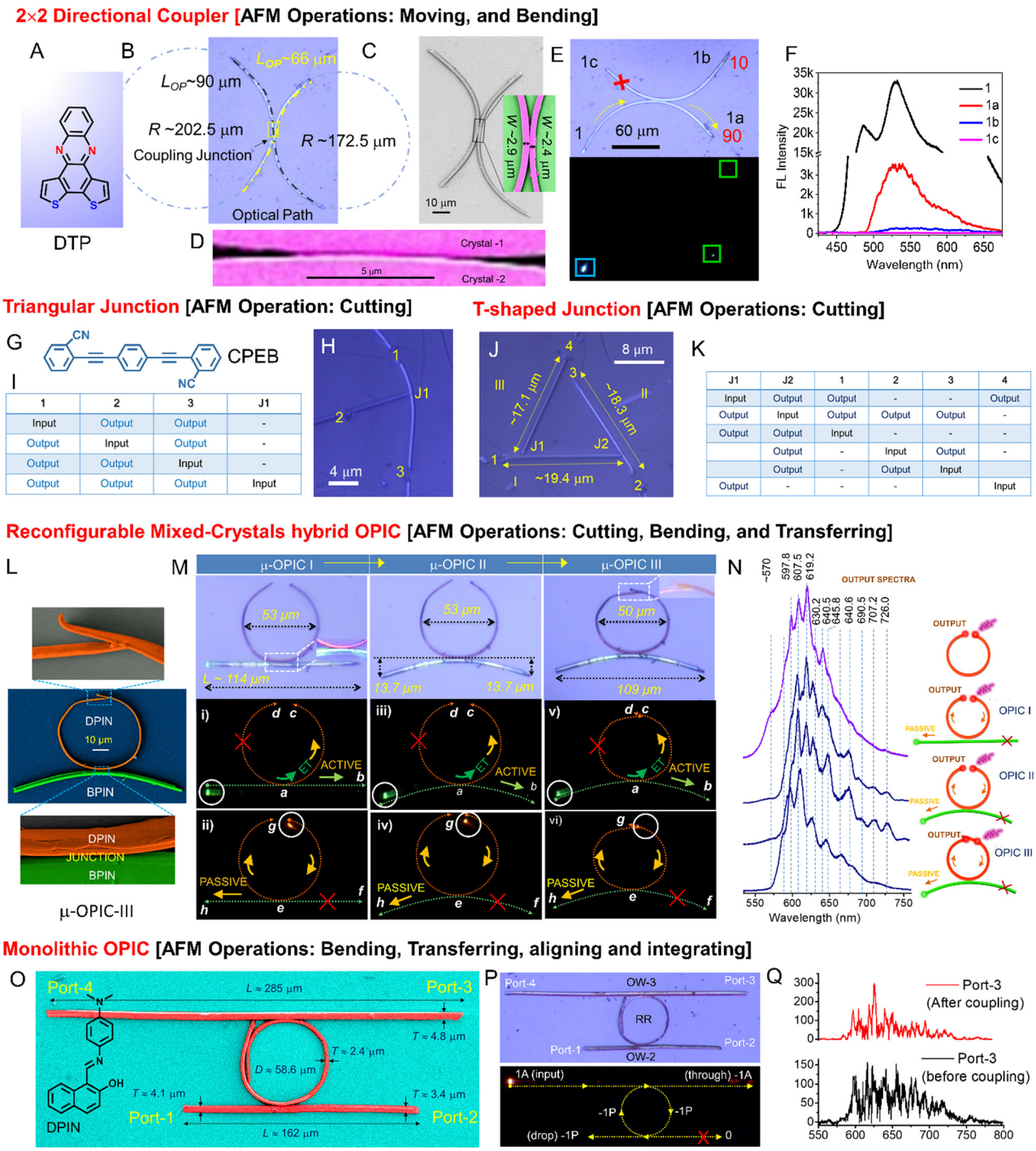

1	2	3	J1
Input	Output	Output	-
Output	Input	Output	-
Output	Output	Input	-
Output	Output	Output	Input

J1	J2	1	2	3	4
Input	Output	Output	-	-	Output
Output	Input	Output	Output	Output	-
Output	Output	Input	-	-	-
	Output	-	Input	Output	-
	Output	-	Output	Input	
Output	-	-	-		Input

Fig. 38 (A and G) Molecular structures of DTP, and CPEB. (B) Micromechanically fabricated two-coupled crystal waveguides (2 × 2 directional coupler) showing optical path length (L_{OP}) between two coupled waveguides and (D) close-up view of the junction. (C) FESEM image of a directional coupler. (E) Confocal optical microscopy and fluorescence images of two coupled crystalline waveguides acting as a directional coupler when excited at one of the four termini and (F) fluorescence spectra. Confocal optical micrographs of (H) T-shaped and (J) triangular junction along with tables (I and K) summarizing input-position-dependent outputs. (L) FESEM image of μ-OPIC III. (M) Confocal optical and fluorescence images of reconfigurable μ-OPICs depicting excitation-position-dependent, directional-specific and mechanism-selective optical outputs. (N) Modulation of the optical modes at output g, due to geometrical reconfiguration of the circuit. (O) False-colored FESEM image of a monolithic micro-add-on/drop filter fabricated using DPIN microcrystals. (P) Optical and fluorescence images of the filter. (Q) Optical modes (fluorescence background-subtracted spectra) recorded at P-3 before and after coupling of OW3 with the circuit. Adapted with permissions from ref. 378 Copyright 2020, Wiley-VCH, ref. 438 Copyright 2020, Wiley-VCH, ref. 383 Copyright 2020, Wiley-VCH, ref. 444 Copyright 2021, Wiley-VCH.

adhesive force is higher than the force that drives the recovery of the crystal shape. The radius (R) of curvature/width of two-coupled crystal-1 and crystal-2 waveguides is 202.5/2.9 and 172.5/2.4 μm, respectively (Fig. 38B–D). The curved junction facilitates light entry from one waveguide to another *via* an evanescent field coupling in the tapered region. Optical excitation of one of the terminals (left) of crystal-1 (Fig. 38E, see input-1), transduces the blue fluorescence signal towards the coupling junction which evanescently couples it with crystal-2. At the junction, the fluorescence signal (after reabsorption) splits into two and outcouples as green fluorescence at termini-1a and -1b in ratio 90 : 10. No fluorescence signal was identified at terminal 1c, confirming the circuit's directional coupling nature. Likewise, excitation of terminals 2, 3 and 4 also shows outputs only at the opposite crystal termini. The output signal ratio also varies inversely with the optical path length ($L_{OP} \approx 90$ and 66 μm).

6.6.2. Single-crystal-based organic integrated waveguides and junctions. Two or more crystals forming an interconnected optical junction of various geometries are useful in OPICs.[383] π-Conjugated 1,4-bis(2-cyanophenylethynyl)benzene (CPEB, Fig. 38G) affords blue-emitting naturally bent crystal waveguides forming various junctions during vapor-phase growth technique. The solid-state analysis shows that bent crystals' formation occurs through the fusion of two crystals growing against each other with variable intersection angles. By crystal-cutting operation, the junctions were separated from their connecting point. For example, a triangular T-shaped geometry with a junction (J1) and three termini (1–3) was isolated by this manipulation (Fig. 38H and I). Optical excitation of any terminal produces two optical outputs in the other two terminals (Fig. 38N–P). Excitation at J1 produces outputs at all three terminals. The input-position-dependent outputs are summarized in Fig. 38L.[383] Similarly, a triangular-shaped junction from three joined bent crystals with two junctions (J1 and J2) and four termini (1–4) was fabricated (Fig. 38J and K). The triangular junction is not a closed-loop structure. Excitation at junctions J1 or J2 produces fluorescence outputs at 1, 4, and J2 or 1, 2, 3, and J1, respectively. Excitation at terminal 1 or 2 or 3 produces fluorescence outputs to J1/J2, J2/3, and J2/2, respectively (Fig. 38K).

6.6.3. Mixed flexible crystals for hybrid OPICs. Using two or more electronically different flexible crystals is necessary to impart complex optical functions in OPICs *via* active, passive and energy-transfer (ET) mechanisms.[438] However, fabrication of such hybrid crystal OPICs is a challenging task. It requires careful transfer of microcrystal-A from substrate-1 to substrate-2, where it has to be integrated with microcrystal-B, as shown in Fig. 37. DPIN[370] and BPIN crystals are suitable for such OPICs as the latter molecule transfers fluorescence energy to the former. The μ-OPIC-I fabricated using DPIN/BPIN crystals and its reconfigurability into geometrically different μ-OPIC-II and -III are shown in Fig. 38M. μ-OPIC-I comprises a DPIN truncated-ring-shape waveguide ($D \approx 53$ μm) integrated with a straight BPIN waveguide ($L \approx 114$ μm). Reconfiguration of μ-OPIC-I into μ-OPIC-II by bending the BPIN waveguide into an arc-shape enables better evanescent coupling at the DPIN-BPIN-junction (Fig. 38L). Finally, manipulation of the truncated-ring-shape of DPIN crystal termini into a closed-loop ($D \approx 50$ μm) produced μ-OPIC-III. These OPICs could be operated by giving an optical input at either the BPIB or DPIN terminal.

When the input light (excitation) was applied at the right terminal of the BPIN crystal, the green fluorescence actively propagated to its opposite terminal b (Fig. 38M, i, iii and v). During fluorescence propagation, part of it evanescently coupled to the DPIN crystal and partly excited it *via* energy transfer. The generated orange fluorescence (active) along with green fluorescence (passive) propagated to terminal c (Fig. 38M, i, iii and v). Here, the OPICs could split the input signal into two different light signals and deliver them to the output termini b and c, but not d. Similarly, when the light input was given at DPIN terminal c, the orange fluorescence propagated in a circular path towards terminal d (Fig. 38M, ii, iv and vi). Furthermore, part of the fluorescence coupled to the BPIN crystal at the junction and was passively outcoupled at terminal h, without any output at terminal f (Fig. 38M, ii, iv and vi). As expected, the fluorescence spectra of OPICs recorded at terminal g of the BPIN (input at terminal c) reveal modulation of the optical modes (Fig. 38N). This modulation demonstrates that the variation of OPIC geometries affects the light electric-field distribution.

6.6.4. Monolithic add-on and drop filters. Analogous to silicon photonics, a monolithic add-on drop filter using three flexible molecular crystals of DPIN, namely, OW1–OW3 was fabricated recently (Fig. 38O, inset).[444] The DPIN crystal waveguide-cavity transduces a long pass filtered (reabsorbed) fluorescence in the 525–580 nm region. At first, a ring resonator (RR) with a diameter 58.6 μm was fabricated by joining the terminals of the crystal, OW1. Later, two optical waveguide-cavities (OW2 and OW3) were micromechanically aligned parallel and integrated with the RR. The ensuing circuit (Fig. 38O) possesses four ports (P1–P4). The fluorescence (signal 1A; 'A' stands for active) produced at either of the OW-3 crystal terminals (for example, P-4) actively propagates and outcouples the (long pass) filtered signal with optical modes at P-3 (signal-1A). Due to evanescent coupling of propagating fluorescence with RR, the signal passively takes a clockwise turn, and enters OW2 and finally outcouples at P-1 as -1P signal (Fig. 38P). Unlike the isolated OW-3 waveguide-cavity, the intensity and wavelength of these modes (at P-3) were different for the same terminal. This result demonstrates the mode-filtering effect of the circuit (Fig. 38Q). Also, these altered modes can be routed either clockwise or counter-clockwise, depending upon the excitation port.[444]

7. Crystals as actuators

7.1. Overview of crystal actuation

Mechanically responsive materials that can move macroscopically by application of external stimuli, such as light, heat,

electricity, and chemical reactions have been studied extensively in materials chemistry over the past two decades. Such mechanically responsive materials have the potential for applications in sensors, switches, actuators, and soft robotics.[104] Although research on mechanically responsive molecular crystals spans only about a decade, many mechanical crystals displaying bending,[220] twisting,[249] rotation,[109] jumping,[60] and locomotion[106] have been reported. However, devices incorporating these crystals have not yet been realized. In contrast, the much more extensive research on mechanical polymers has led to the development of artificial muscles[445] and soft actuators.[446] Most mechanical crystals developed to date are based on photoisomerizations (including reversible photochemical reactions) or phase transitions. However, the number of crystals that undergo photoisomerization is limited. High speed is required for practical applications, but the photoisomerization actuation speed is relatively slow, in the range of seconds to minutes. Furthermore, only thin crystals of 20 μm or less can bend *via* a photoisomerization mechanism. Most of the crystals actuate with ultraviolet (UV) light; only a few actuate with visible or infrared light. In addition, crystals that undergo thermal phase transitions are less common than crystals that undergo photoisomerization. At present, it remains challenging to identify new phase transition crystals; these can only be found serendipitously, or by searching the literature.

Thick crystals that bent quickly upon irradiation with UV or visible light due to the photothermal effect were reported recently.[447] In the past, although numerous photothermally driven actuators of liquid crystal polymers have been reported,[448,449] not much attention has been paid to crystal actuation by photothermal effects. The photothermal effect is a phenomenon by which thermal energy (heat) is generated by nonradiative deactivation of the photoexcited state during a photophysical process. Most of the crystals that absorb light display their own photothermal effects, which suggests that almost any crystal could be actuated by this mechanism. In this section, mechanical crystals that have been used as actuators over the past decade are reviewed. These are based on photoisomerizations, phase transitions, and photothermal effects.

7.2. Actuation by photoisomerization

Dynamic crystals altered by photoisomerization are largely restricted to typical photochromic crystals, such as diarylethenes, azobenzenes, salicylideneanilines, and anthracenes. In this section, we summarize the photomechanical actuation of crystals of azobenzenes, salicylideneanilines, fulgides, and other compounds. The photomechanical effects of diarylethene and anthracene crystals are presented in the other sections.

7.2.1. Azobenzenes. The azobenzenes are typical T-type (thermally and photochemically reversible) photochromic compounds that undergo *trans–cis* photoisomerization. Many photoresponsive polymers, elastomers, and gels cross-linked with azobenzenes have been reported.[445,446] Koshima *et al.* observed bending motion of azobenzene crystals based on *trans–cis* photoisomerization.[82,179,181] A thin (5 μm) plate-like crystal of *trans*-4-(dimethylamino)azobenzene (*trans*-**1**) bent quickly (within 0.5 s) away from a UV light (365 nm) source, forming a curved shape (Fig. 39A).[179] After turning off the UV light, the crystal returned to its initial flat shape within 30 s. This bending motion was reversible for at least 100 cycles, indicating high durability. This first observation was followed by an attempt to generate twisting motion with a molecular crystal. The focus was on chiral crystals made from chiral molecules which may macroscopically deform in a specific direction (*i.e.*, by twisting). Thus, the photomechanical bending of chiral crystals of *trans*-(*S*)-**2** with an (*S*)-phenylethylamide group was studied. When the front face of a thin (2 μm) crystal was irradiated with UV light, the crystal bent away from the light source with a left-handed twist (Fig. 39B).[181] After terminating the UV irradiation, the crystal gradually returned to its original straight shape. The optimized molecular geometry of *cis*-(*S*)-**2** revealed that photoisomerization led to an expansion of the *b* axis (corresponding to the long direction of the crystal) and contraction of the *a* axis (corresponding to the width of the crystal), resulting in elongation of the top surface along the diagonal direction, and bending away with a twist. Crystals of azo dyes, such as methyl red, in which a strong electron-withdrawing group is combined with a strong donor, also bend with visible light.[177] These bending motions are attributed to a gradient in the extent of UV-induced *trans–cis* photoisomerization as a function of light penetration. The photoisomerization causes the surface of the irradiated crystal to expand, which leads to the formation of a bent shape.

7.2.2. Salicylideneanilines and analogs. Salicylideneanilines and salicylideneamines (Schiff bases) are well-known T-type photochromic compounds that exhibit enol–keto photoisomerization in the crystalline state.[450] These compounds are of particular interest because the keto-to-enol back-isomerization proceeds thermally and photochemically, and many kinds of derivatives are readily synthesized and crystallized. A thin (1 μm) plate-like crystal of a salicylideneaniline derivative having a *meta*-nitro substituent in the enol form (enol-**3**) bent away from a UV light (365 nm) source within 5 s of exposure (Fig. 39C).[268] The bending motion was accompanied by a color change from pale yellow to reddish-orange due to enol-to-keto photoisomerization. The recovery took as long as 1400 s in the absence of visible light due to the slow keto-to-enol thermal back-isomerization (τ = 42 days), whereas the straightening was accelerated to 43 s due to the fast photochemical back-isomerization (τ = 63 s). The bending motion was observed over 200 cycles, indicating excellent durability. X-ray crystallographic analyses revealed that after UV light irradiation, the length of the *a* axis (longitudinal direction of the single crystal) increased by 0.42% due to the formation of a *trans*-keto form (Fig. 39C), which resulted in bending away from the light source.

Solid-state photoreactivity in chiral crystals usually differs from that in achiral crystals because the motion of molecules is restricted in the crystal lattice, and the chiral environment is retained during reactions.[451] The photomechanics and physical properties of chiral crystals of the *S*-enantiomer of a salicylideneamine derivative in the enol form (enol-(*S*)-**4**) were compared to those of achiral crystals (enol-(*rac*)-**4**) composed of a racemic

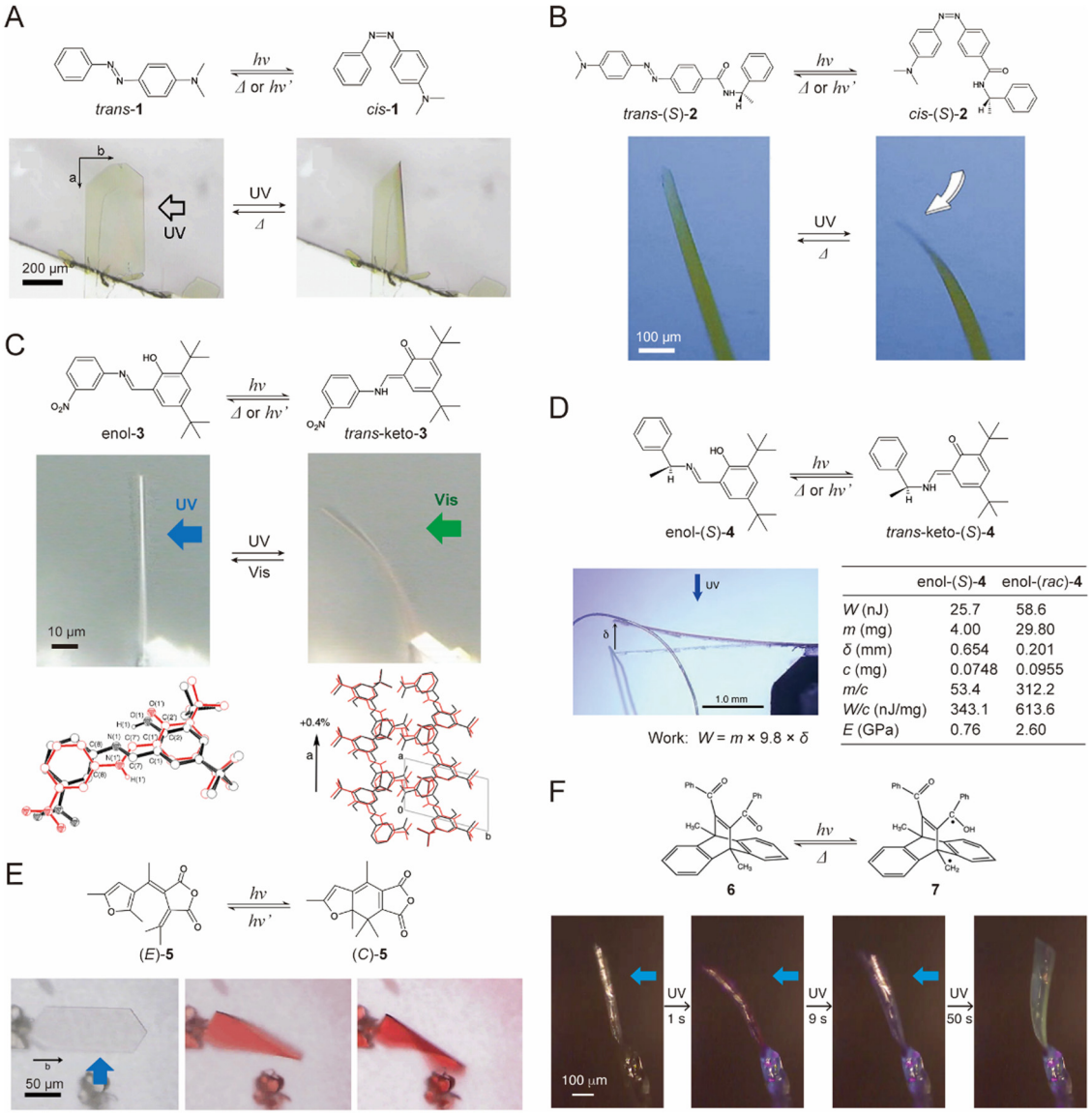

Fig. 39 Photomechanical motions of the crystals driven by photoisomerization that occurs upon UV light irradiation. (A) Bending of a plate-like crystal of azobenzene *trans*-**1** by *trans*–*cis* photoisomerization.[179] Adapted with permission from ref. 179 Copyright 2009, American Chemical Society. (B) Bending with a twist of a plate-like crystal of chiral azobenzene *trans*-**2**.[181] Adapted with permission from ref. 181 Copyright 2016, Wiley-VCH. (C) Bending and photoinduced change in the crystal structure of a plate-like crystal of salicylideneaniline enol-**3** by enol–keto photoisomerization.[268] Adapted with permission from ref. 268 Copyright 2011, The Royal Society of Chemistry. (D) Photomechanical lifting work of a crystal cantilever of enol-(*S*)-**4** by enol–keto photoisomerization.[452] Adapted with permission from ref. 452 Copyright 2013, American Chemical Society. (E) Curling of a thin hexagonal crystal of furylfulgide (*E*)-**5** by photo-electrocyclization.[223] Adapted with permission from ref. 223 Copyright 2012, The Chemical Society of Japan. (F) Two-step bending of a plate-like crystal of dibenzobarrelene **6**.[458] Adapted with permission from ref. 458 Copyright 2018, The Royal Society of Chemistry.

mixture of *S*- and *R*-enantiomers (Fig. 39D).[452] Both the chiral and achiral crystals bent reversibly toward the light source under UV light irradiation due to contraction along the long crystal direction by photoisomerization. The measured Young's modulus of enol-(*S*)-**4** was 0.8 GPa, which is smaller than the modulus of enol-(*rac*)-**4** (2.6 GPa). Under UV light irradiation, the crystal cantilevers lifted metal rings that were 50 and 300 times heavier than the cantilevers themselves for chiral and achiral crystals, respectively, which demonstrated that the achiral enol-(*rac*)-**4** crystal was better than the chiral enol-(*S*)-**4** crystal as a photomechanical material.

7.2.3. Fulgides. Fulgides are classified as P-type (thermally irreversible but photochemically reversible) photochromic compounds that undergo reversible photo-electrocyclic ring-closure and ring-opening reactions.[453] A furylfulgide in its *E* form ((*E*)-**5**) displayed reversible photoisomerization to the closed form ((*C*)-**5**) in the crystalline state.[454] Thin (2 μm) hexagonal crystal of (*E*)-**5** curled upon exposure to UV light (365 nm) from the upper right corner toward the light, reaching maximum deflection after 2 s. This was accompanied by a color change from pale yellow to red due to the formation of the (*C*)-**5** form (Fig. 39E).[223] The bending motion was repeatable over

200 cycles with alternating exposures to UV and visible light. X-ray crystallographic analyses revealed that after two-photon excitation at 742 nm, the *b* axis length of the unit cell, which corresponds to the longitudinal direction of the single crystals, decreased by 0.13% due to the formation of (*C*)-**5** isomers that have a nearly planar conformation.[455] Hence, accumulation of the photoproduct (*C*)-**5** contracted the crystal length near the irradiated area, leading to bending toward the light source.

7.2.4. Dibenzobarrelenes. Dibenzobarrelenes are well-known compounds that undergo various photochemical reactions in crystalline state and solution. These reactions include tri-π-methane rearrangement, di-π-methane rearrangement, Norrish type II reactions, and [2+2] cycloaddition.[456] Photochromism of the dibenzobarrelene derivative (**6**) in the crystal is caused by a long-lived triplet biradical (**7**), formed by Norrish type II intramolecular hydrogen abstraction under UV light irradiation.[457] A thin (9 μm) plate-like crystal of **6** exhibited two-step bending upon exposure to UV light (Fig. 39F).[458] In the first step, the crystal quickly bent away from the direction of illumination after 1 s, with a color change from colorless to purple due to triplet biradical formation. In the second step, the crystal gradually returned to its initial straight shape and then bent in the opposite direction, with an additional color change to light yellow after 50 s due to the formation of a mixture of stable photoproducts under continuous UV exposure.

7.3. Actuation by phase transitions

7.3.1. Thermal phase transitions. Thermal single-crystal-to-single-crystal (SCSC) phase transitions of crystals cause crystal bending,[459] expansion/contraction,[460] and jumping.[461] However, locomotion of crystals rarely has been reported. As described above, thin plate-like crystals of chiral azobenzene *trans*-(*S*)-**2** bend with twisting under UV light irradiation (Fig. 39B).[181] The *trans*-(*S*)-**2** crystal also exhibits a reversible SCSC phase transition at 145 °C. The length of the crystal is shortened above the transition temperature, which induces bending due to the temperature gradient across the depth of the crystal. Walking and rolling locomotion of the crystal caused by this thermal phase transition has been demonstrated.[106] Long plate-like crystals with a thickness gradient in the longitudinal direction walked slowly, like an inchworm, by repeated bending and straightening under heating and cooling cycles near the transition temperature (Fig. 40A). Furthermore, thinner and longer plate-like crystals with a width gradient rolled much faster by tilted bending and then flipping under only one heating or cooling process (Fig. 40B). The bending motion was necessarily converted to walking and rolling locomotion due to the asymmetric shape of the crystal. This finding of crystal locomotion could lead to the development of a new research field of crystal robotics.

7.3.2. Phototriggered phase transitions. The phototriggered phase transitions provide opportunity to induce large structural change using light.[462] Crystalline chiral salicylideneamine in the enol form (enol-(*S*)-**8**) undergoes enol–keto photoisomerization (Fig. 41A). The crystal also exhibits a reversible thermal SCSC phase transition at 40 °C upon heating and cooling. The crystal transforms to an identical phase upon

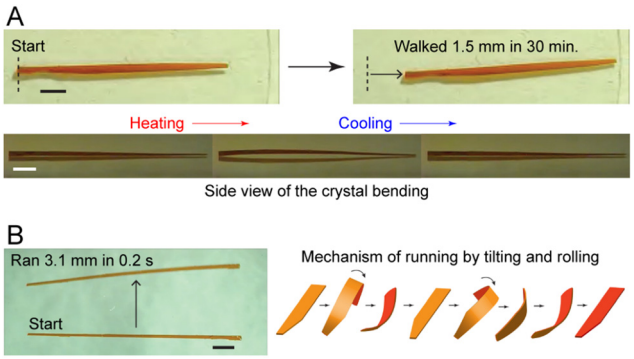

Fig. 40 Locomotion of crystals of chiral azobenzene *trans*-(*S*)-**2**. (A) Inchworm-like walking of a long plate-like crystal with a thickness gradient under repeated heating and cooling cycles. (B) Fast rolling locomotion and the mechanism of a long, thin plate-like crystal with a width gradient under only one process of heating or cooling. The scale bars in (A and B) are 1 mm.[106] Adapted with permission from ref. 106 Copyright 2018, Springer Nature.

photoirradiation over the wide temperature range of −50 to 20 °C, which is lower than the thermal transition temperature (Fig. 41B). The phototriggered phase transition is induced by strain in the *trans*-keto molecules generated by enol–keto photoisomerization and propagates *via* a domino-like effect through the entire crystal due to the presence of a small energy barrier (Fig. 41C). The phototriggered phase is metastable and returns to the initial stable phase *via* back-isomerization from the *trans*-keto to the enol form. The phototriggered phase transition differs from the well-known photoinduced phase transition, which occurs *via* the excited state within femtoseconds or picoseconds.[463] Stepwise bending with and without twisting of a plate-like crystal of enol-(*S*)-**8** was achieved by combining the phototriggered phase transition and enol–keto photoisomerization during and after illumination with UV light (Fig. 41D). The phototriggered phase transition is a new approach to the diversification of the mechanical actuation of photoresponsive crystals.

7.4. Actuation by photothermal effects

A thick (240 μm) plate-like crystal of a salicylideneaniline derivative having a *p*-benzoyl substituent in the enol form (enol-**9**) bent quickly and reversibly due to a photothermal effect upon UV light irradiation (Fig. 42A and B).[447] In contrast, a thin (5 μm) crystal did not exhibit significant bending, likely due to a very low degree of enol–keto photoisomerization. The photothermally driven bending, which occurred even during exposure to visible light, is caused by a temperature gradient in the thickness direction arising due to the heat conduction of photothermal energy generated near the crystal surface (Fig. 42C). High-frequency bending actuation (25 Hz) was achieved using pulsed UV irradiation (Fig. 42D). The photothermal effect is a phenomenon by which thermal energy (heat) is generated very quickly (picoseconds) by nonradiative deactivation of a photoexcited state of a photophysical process. Most crystals that absorb light display their own photothermal effects. Actuation of most

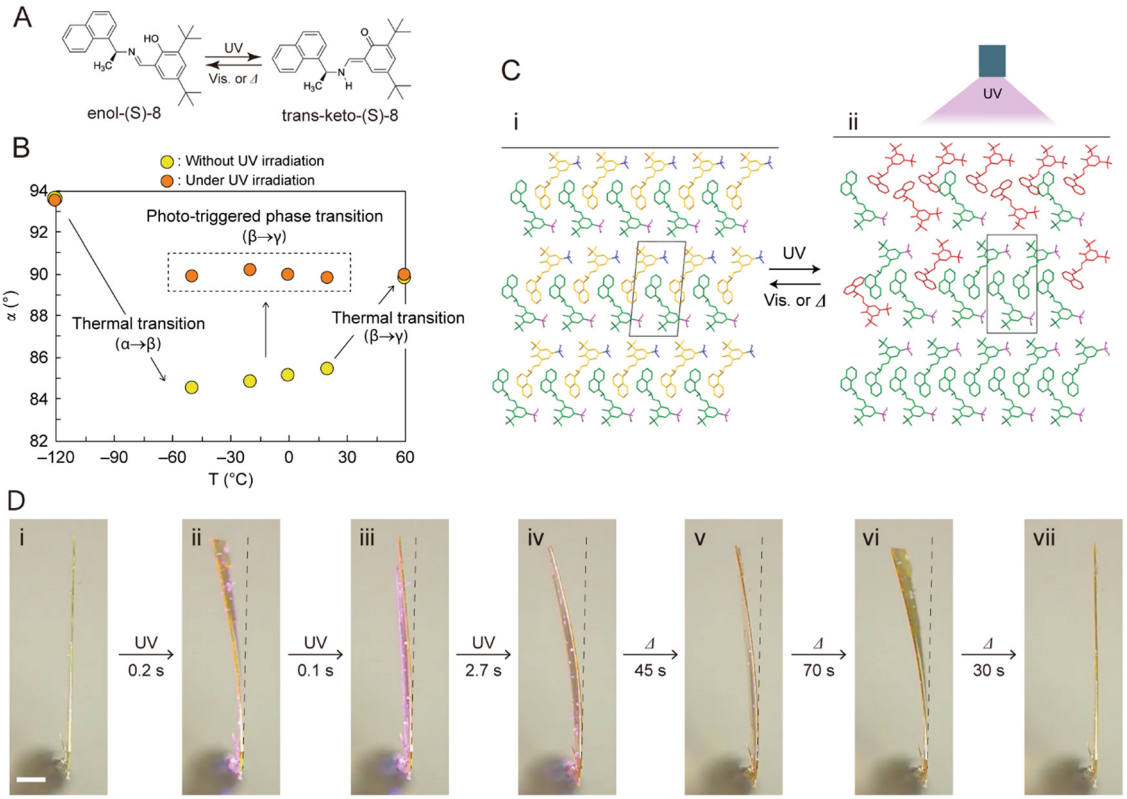

Fig. 41 (A) Enol–keto photoisomerization of a chiral salicylideneamine, (*S*)-**8**. (B) Phototriggered phase transition based on the change of angle α. (C) Mechanism of the phototriggered phase transition. (D) Stepwise bending of a thin plate-like crystal of enol-(*S*)-**8** upon UV irradiation. Scale bar, 500 μm.[462] Adapted with permission from ref. 462 Copyright 2019, Springer Nature.

crystals *via* a photothermal effect is conceivable; such actuation cannot be realized by photoisomerization or phase transition. The versatility and potential of crystals as actuation materials will certainly increase in the near future.

7.5. Outlook

Crystal actuation has been accomplished based on photoisomerization, phase transitions, and photothermal effects. It is important to develop and discover new principles (mechanisms) of crystal actuation. An essential requirement for the dynamic crystals is reversibility, which enables repeated actuation; crystals that irreversibly actuate by external stimuli during only one cycle are of little use. The number of crystals that undergo photoisomerization and phase transitions is limited, which is a significant disadvantage for the development of novel actuators. In contrast, most crystals that absorb light exhibit their own photothermal effects. Hence, the photothermal effect has great potential for crystal actuation, however, the crystal deformations are too small (typically, less than 1°) for practical applications.

Molecular crystals, having regular, three-dimensional structures, can actuate faster, and with greater output force than polymers. Sensors, switches, actuators, and soft robots are some of the promising applications for mechanical crystals that can be moved autonomously by external stimuli. However, it may be impractical or difficult to apply a single crystal as an actuator for soft robotics. Hybridization of single crystals with polymers provides an opportunity to create actuators with more realistic movements. Indeed, light-driven crystal–polymer hybrid actuators, in which photomechanical crystals are aligned in polymer films by application of a magnetic field or rubbing, bent reversibly under photoirradiation and demonstrate the advantages of combining molecular crystals (fast response time) and polymers (large size).[464,465] Extensive basic research on mechanical polymers has already led to the development of artificial muscles and soft actuators.[104] Although current research on mechanical crystals is mostly limited to fundamental studies, future practical application in sensors, switches, actuators, and soft robots is envisioned.

8. Mechanical properties of molecular crystals for pharmaceutical applications

8.1. Relevance to pharmaceutical manufacturing

Molecular crystals are ubiquitous in the manufacturing of pharmaceutical products of small-molecule active pharmaceutical ingredients (APIs) since crystallization is a major means for isolating and purifying APIs. Because of their higher physical and chemical stability, the crystalline solids are still preferred before the final dosage form is manufactured even for drugs given

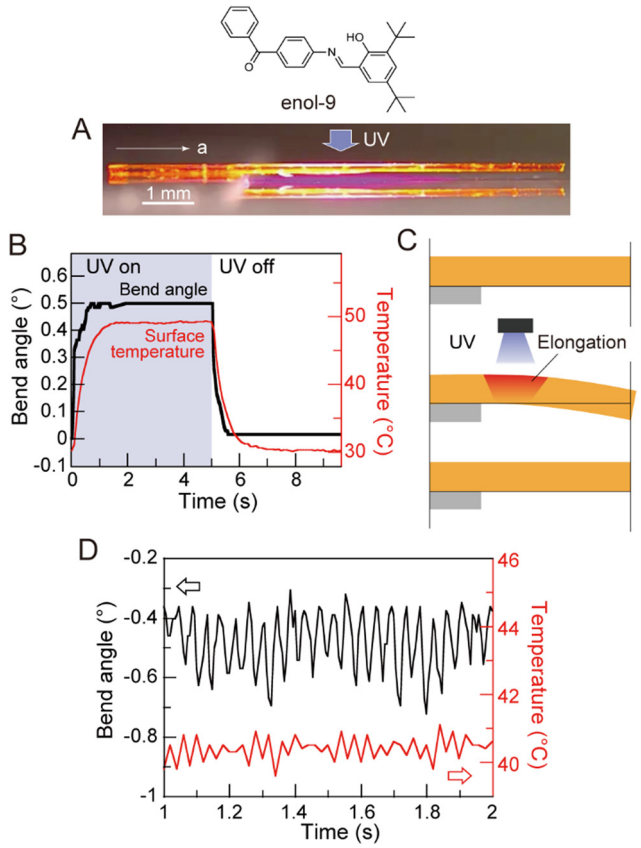

Fig. 42 Fast bending of a crystal of enol-**9** by the photothermal effect. (A) Thick plate-like crystal viewed from the side under UV irradiation. (B) Time dependence of the bending angle and the irradiated surface temperature. (C) Schematic diagram of the possible mechanism of crystal bending caused by the photothermal effect. (D) High-frequency photothermally driven bending (25 Hz) of the crystal by pulsed UV laser irradiation.[447] Adapted with permission from ref. 447 Copyright 2020, The Royal Society of Chemistry.

to patients as a liquid or amorphous solid. As such, the mechanical properties of pharmaceutical crystals have a critical role in the manufacturing of most drugs. This is important to recognize as the mechanical properties of molecular crystals can vary over a wide range (Fig. 43).[27]

8.2. Importance of size reduction by milling

API crystals often need to be milled to reduce the size and achieve more uniform distribution in drug products, especially for potent APIs that are delivered at low doses.[466,467] Efficient delivery of APIs to the deep lung by inhalation requires particles with aerodynamic diameters less than 5 μm.[468] For parenteral delivery, API crystals need to be sufficiently small to avoid ischemia.[469] The dissolution rates of smaller API crystals are higher because of their larger surface area.[470] For poorly soluble APIs, which account for approximately 40% of the marketed drugs and 80% of the new chemical entities in the development pipeline,[471,472] the nanosized API crystals have the added advantage of enhanced solubility.[473]

For a fixed milling process, the size distribution of the resulting powder depends on the mechanical properties,

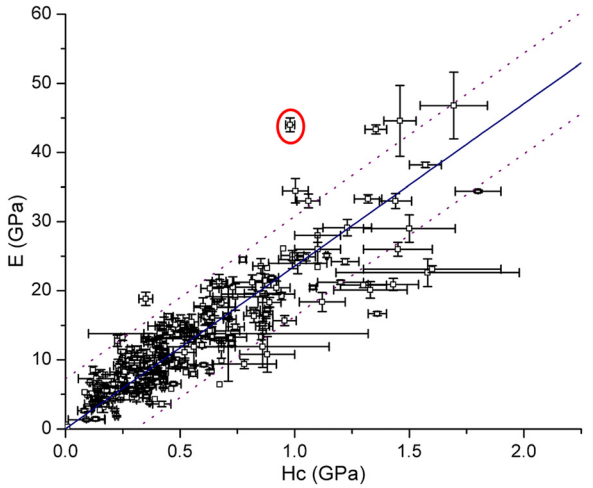

Fig. 43 Elastic modulus (E) and indentation hardness (H_c) of molecular crystals vary over a wide range. Adapted from ref. 27. Copyright 2020, The Royal Society of Chemistry.

including yield strength (Y), hardness (H), Young's modulus (E), and fracture toughness (K_{IC}) or fracture energy (R), as they affect the breakage by influencing the formation and propagation of cracks in crystals.[474–478] In fact, sufficiently small particles undergo plastic deformation instead of brittle fracture when they are subjected to mechanical impact. The critical size corresponding to the plastic yielding–brittle fracture transition, d_{crit}, can be calculated using eqn (12) from E, Y, and R of the crystals.[477]

$$d_{crit} = \frac{32ER}{3Y^2} \quad (12)$$

The plastic yielding–brittle fracture behavior was experimentally demonstrated and the predicted d_{crit} was confirmed by experiments using polystyrene (Fig. 44).[477] However, it is applicable to crystals because the model only depends on mechanical properties and surface energy.

This is supported by the common observation that size reduction by milling tends to be inefficient for a highly plastic API crystal, because of the large d_{crit}, corresponding to a low Y. A brittleness index, defined as the ratio of H to K_{IC}, has been used to predict the milling performance of pharmaceutical crystals.[479,480] As expected, the fracture of anisotropic molecular crystals during milling is also anisotropic because cracks can propagate more easily along the weaker cleavage planes.[475,481] It should be mentioned that, along with the size reduction, milling can potentially cause a loss of crystallinity or polymorph change. Thus, milled API powders need to be carefully characterized for possible phase change, and milling parameters should be optimized to minimize or even eliminate phase changes. This is important for avoiding unexpected changes in stability and dissolution performance of the API.[482,483] In this regard, harder API crystals tend to be more resistant to the generation of structural disorders.[484]

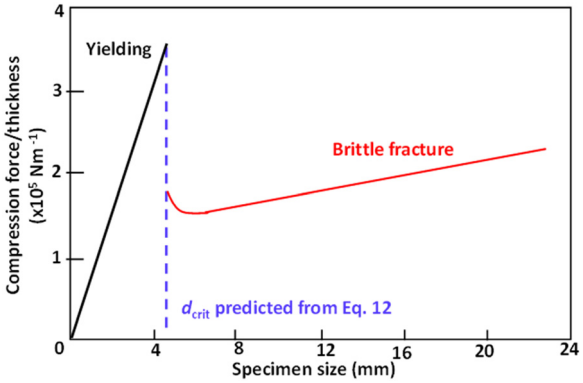

Fig. 44 Normalized force required to cause the brittle fracture of a large particle (red line) or yield of a small particle (black line) of polystyrene. The vertical dashed line signifies the value of d_{crit} predicted from eqn (12). Adapted with permission from ref. 477 Copyright 1978, Nature Publishing Group.

8.3. Importance for tableting

Mechanical properties also have a major role in the success or failure of the pharmaceutical tableting process by affecting the transmission of stress through the powder bed (Fig. 45A)[485] and deformation of crystals during die compaction (Fig. 45B).[486] A powder consisting of more plastic crystals transmits axial compaction stresses in the radial direction (die wall stress) more effectively during loading but the residual die wall stress is usually lower.[487] This explains why tablets of softer materials can be more easily ejected out of the die after compression.

According to the bonding area and bonding strength interplay model, the mechanical strength of a compressed tablet positively correlates with the total inter-particulate bonding area in the tablet.[488,489] Under a given set of compression conditions, the bonding area is determined from mechanical properties, where permanent plastic deformation and fragmentation contribute to the development of the bonding area, while reversible elastic deformation does not (Fig. 45B).[486,489] Therefore, the poor tableting performance of an API is generally caused by the fracture and elastic deformation being energetically preferred over crystal slip (plasticity). This problem can be effectively overcome by engineering crystals to access the API crystalline forms with higher plasticity for use in tablet formulation.[490–493] It is useful to point out that, while elastic deformation is detrimental to tableting performance, 1D or 2D elastically bending molecular crystals should not be rejected on the grounds of expected poor tabletability. This is because the one-dimensional stress applied to bend a crystal is fundamentally different from the pseudohydrostatic stress during die compression. Plastic deformation of crystals, through a slip among crystallographic planes, along even one direction, is sufficient for developing a large bonding area between API crystals, because of their random orientation in the powder bed.[494]

8.4. Importance for punch sticking

While enhancing API crystal plasticity is effective in solving the poor tabletability problem, higher plasticity also correlates with a higher tendency of punch sticking during tableting.[495] When punch sticking occurs, the tableting process must be stopped as the contaminated punch causes a change in tablet weight and defective tablet surfaces. If not resolved, these issues can lead to the rejection of an entire batch.[496] The higher punch sticking propensity of more plastic crystals arises from the development of a larger area of contact with the punch surface during compression, which makes it more difficult to separate the API crystals from the punch surface (Fig. 46).[497] Therefore, to avoid the punch sticking problem of an API, a crystal form of the API with lower plasticity may be designed through crystal engineering to mitigate or eliminate the problem.[333,498] Such an effort can be significantly facilitated by engaging available computational tools to predict crystal plasticity.[333]

8.5. The current status of this research field and future perspective

Temperature rises during prolonged milling or compaction because of the high energy input inherent to these processes. A temperature rise may affect the mechanical properties of an API, which can consequently cause unexpected problems during large-scale manufacturing. It has been shown that the API crystals become softer at higher temperatures.[159,499] This would explain the common observation that punch sticking problems

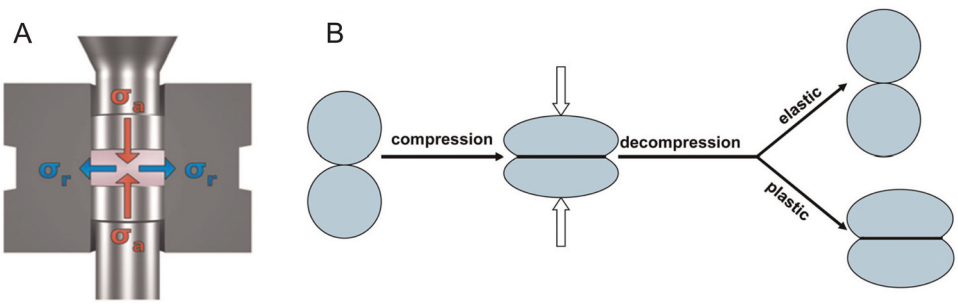

Fig. 45 (A) Transmission of an axial stress (σ_a) to the radial die wall (σ_r) during die compression of a powder, creating a pseudohydrostatic stress environment and (B) effects of particle mechanical properties on bonding area formation during a powder compression cycle. More plastic particles can undergo more permanent plastic deformation than less plastic particles. Pure elastic deformation does not contribute to bonding area. Adapted with permission from ref. 485 and 507 Copyright 2009, 2022, Elsevier.

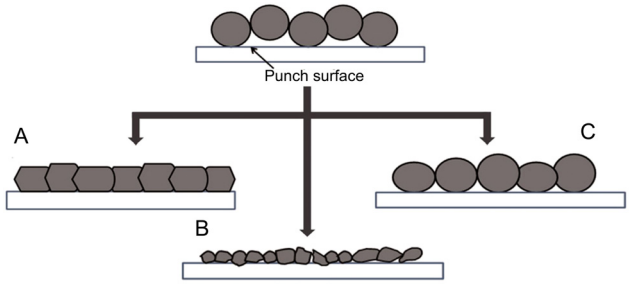

Fig. 46 Effects of mechanical behaviors of API crystals on punch sticking propensity. (A) Plastic crystals undergo extensive deformation so that larger areas of contact with the punch surface are developed, leading to severe sticking; (B) brittle and (C) elastic API crystals only develop small areas of contact with the punch surface at the end of the compression cycle so that they can easily detach from the punch surface after compression, leading to low sticking propensity. Adapted with permission from ref. 495. Copyright 2017, Elsevier.

can either become aggravated over time or unexpectedly appear during large-scale tablet manufacturing.

It was also shown that more plastic polymorphs of curcumin and sulfathiazole exhibit higher solubility.[500] A globally positive trend between plasticity and solubility of polymorphs is reasonable because they both correlate with weaker intermolecular interactions and lower lattice energy. If broadly applicable, this relationship offers a way to rank-order the solubility of API polymorphs based on their mechanical properties. When the amount of an API is insufficient for conducting solubility experiments or when the solubility of a polymorph cannot be easily measured due to a facile phase conversion during the solubility experiment, their solubilities can still be rank ordered based on the mechanical properties attained through nanoindentation. However, a predictive model to reliably predict solubility from hardness of drug crystals must incorporate the factor of hardness anisotropy. To this end, more systems must be thoroughly investigated to provide sufficient data for developing such a model. It may also be useful to incorporate mechanical properties calculated from their crystal structures.

Similar to metallic crystals, the mechanical properties of molecular crystals can be modified by dislocations. For example, omeprazole crystals are hardened when the percentage of a tautomer in the crystals increases.[501] The incorporation of molecular impurities at a low concentration initially lowers the elastic modulus of uric acid crystals by creating dislocations to promote plastic deformation through slip. However, the crystals become harder when the impurity level surpasses a specific threshold.[502] This line of research deserves more attention because it may give us the ability to fine-tune mechanical properties for optimal performance in pharmaceutical manufacturing.

The mechanical responses of pharmaceutical crystals are diverse, from being highly elastic[319,503–505] to highly plastic.[308,506] Therefore, it is possible to effectively solve several pharmaceutical problems through the modulation of crystal mechanical properties by applying various crystal engineering approaches. Such efforts are most effective when they are based on a clear understanding of the crystal structure, mechanical properties, and performance relationship.[507] However, despite the significant recent progress, a broadly applicable theoretical framework for reliably predicting mechanical properties of molecular crystals from their structures remains elusive. Therefore, continued research in this direction is strongly encouraged. The first step towards achieving this goal is to expand the list of molecular crystals for which the mechanical properties have been carefully characterized and structural origin has been understood. The analysis of a high-quality database containing a large number of crystals, aided by machine learning and other techniques, will then enable the development of a theoretical framework that can be used to accurately predict the properties and performance of interest from their crystal structures.

9. Final remarks

The deformations of solid bodies are grounded in their characteristic mechanical properties. If the center of mass or the rotational inertia of a body changes over time, deformations become translations and rotations, *i.e.*, motion. In crystals made from molecules, the aforementioned dynamic processes can be controlled or even programmed into the component compounds but this control can only be realized once we reckon systematically with the scarcity of data on the fundamental mechanical properties of organic crystals. Our poor intuition with regard to the mechanical properties of, and mechanical effects displayed by, molecular crystals is likely a result of the compartmentalization of research communities whose common interests are only now coming into focus. The solid-state chemistry research community has traditionally emphasized X-ray crystal structure elucidation of monoliths from which correlations with solid-state reactivity and crystal growth (crystal engineering) were drawn. The broader mechanical engineering community, on the other hand, has hardly considered molecular crystals as a viable class of engineering materials, quoting their small size, pronounced softness, and proneness to wear and tear as some of their drawbacks. It is encouraging to see that the cross-talk between these two communities has been already initiated at multiple levels, and it already underpins some notable progress in understanding of molecular crystals, tying fundamental structural studies with applications in photonics, electronics, and soft robotics.

The key to the understanding of the mechanical effects of crystals is the relationship between structural details such as the strength, abundance, and directionality (anisotropy) of intermolecular interactions, rigidity and conformational flexibility of molecules, material symmetries and the mechanical property profile. This particular aspect requires reliable high-throughput experimental methods that can provide data from a suite of crystal samples with varying chemical and crystal structures. The experimental techniques used to characterize mechanical effects should be complementary—structural, spectroscopic, microscopic, and thermal—to provide sufficient supporting evidence in conjunction with mechanical characterization.

As the amount of data increases, so does the necessity for systematic investigations that would establish molecular crystals in the global material property space. As in many contemporary scientific endeavors of scientific exploration, computational methods will play an increasingly important role in gaining deeper understanding of mechanical properties and effects of molecular crystals. Modeling is particularly important for the emerging dynamic properties of molecular crystals. Once reliable theoretical protocols have been established, computational methods could be used to not only explain the experimental data, but also to predict mechanical properties and even dynamic mechanical effects in molecular crystals. This latter goal would necessarily require combined simulation approaches, where phenomena that occur on very different scales—both in length and time—are tackled by atomistic classical and quantum chemical methods as well as by coarse-grained modelling. The results from such concerted research efforts, based on experimental data and supplemented by robust computational techniques, will accelerate the application of molecular crystals. In these efforts, one needs to think outside the chemistry–physics dichotomy that has entrenched science and engineering training, and be cognizant of the virtues of modes of analysis—as well as of their limitations—that each complementary community has developed in isolation.

Concurrent with these developments, there are efforts aimed to demonstrate that molecular crystals can act as simple devices that are able to move objects, progress through space, transmit light, reshape, self-heal, conduct electricity, or transmit information. These examples should go beyond mere replication of engineering devices analogous to those that are available with other materials; they should instead capitalize on the true assets of molecular crystals being anisotropic, light, ordered materials and provide realistic quantifiable parameters to assess their performance.

Couplings between the molecular-scale changes that occur under the effect of external stimuli and their translation and amplification to macroscopic scales are multifaceted phenomena. Researchers thus resort to either the 'molecular approach' or to the general mechanical theory, which in most cases suffices to explain simple observations and to make correlations with physical data. Going beyond those semiempirical and increasingly quantitative approaches, however, requires concerted efforts from researchers working on various aspects of mechanical properties and effects of molecular crystals, as is the exemplary case of this review article which combines contributions from various experts. Such collaborative efforts will likely enhance the understanding of the underlying phenomena, provide realistic performance parameters for assessment of various assets of molecular crystals, and will eventually facilitate the translation of these exciting materials from the crystallographic laboratory to the prototyping stage and finally to real-world implementations and applications.

Molecular crystals, typically monocomponent, uniform structures, are not obviously like multicomponent hierarchical machines whether evolved as in biology or constructed in the machine lab. Nevertheless, they embody sufficient complexity that they can sometimes mimic the functions of those objects designed to be animated. Once we learn to 'pull the levers' of molecular crystalline machines with greater fidelity through the cooperative studies outlined here, the greater will be the mimicry that emerges in the near future.

Author contributions

Conceptualization, P. N.; data curation, W. M. A., D. W. D., D. K., J. M. H., M. B. A.-H., I. T., F. T., G. C.-A., A. G. S., T. A., Y. H., M. A., L. L., S. H., D. P. K., S. M., H. K., S. K., Y. D., R. C., H. Z., C. C. S., C. B., R. O. A., B. K., and P. N.; funding acquisition, P. N.; project administration, W. M. A., J. M. H., M. B. A.-H., I. T., and P. N.; resources, P. N.; supervision, P. N.; writing – original draft, W. M. A., J. M. H., M. B. A.-H., I. T., and P. N. (abstract, Sections 1.1., 1.2., 3.1, and final remarks); D. P. K. retrieved and compiled the information used to prepare Fig. 1.; M. B. A.-H. prepared the graphics; I. T. and D. P. K. consolidated the reference list and citations based on the contributions from all the authors; A. S. G., and B. K. (Sections 2.1, 2.2, 2.3, 2.4, and 2.5); S. K., D. K., F. T. R. O. A., and C. B. (Sections 3.2, 3.3, 3.4 and 3.5); T. A., M. A., and S. M. (Sections 4.1, 4.2, 4.3, 4.4 and 4.5); D. W. D., G. C.-A., and Y. D. (Sections 5.1, 5.2 and 5.3); L. L., and H. Z. (Sections 6.1, 6.2 and 6.3); R. C. (Sections 6.4, 6.5, and 6.6); Y. H., S. H., and H. K. (Sections 7.1, 7.2, 7.3, 7.4 and 7.5); C. C. S. (Sections 8.1 and 8.2); and writing, review, compilation and editing, W. M. A., and P. N.

Conflicts of interest

The authors declare there is no financial or other conflict of interest.

Acknowledgements

P. N. thanks New York University Abu Dhabi for the financial support of the research performed in the Smart Materials Lab over the past ten years (2012–2022). This material is based upon works supported by Tamkeen under NYUAD RRC Grant No. CG011 (Center for Smart Engineering Materials).

References

1 R. O. Ritchie, *Nat. Mater.*, 2011, **10**, 817–822.
2 S. Varughese, M. S. R. N. Kiran, U. Ramamurty and G. R. Desiraju, *Angew. Chem., Int. Ed.*, 2013, **52**, 2701–2712.
3 A. Mondal, B. Bhattacharya, S. Das, S. Bhunia, R. Chowdhury, S. Dey and C. M. Reddy, *Angew. Chem., Int. Ed.*, 2020, **59**, 10971–10980.
4 G. R. Krishna, R. Devarapalli, G. Lal and C. M. Reddy, *J. Am. Chem. Soc.*, 2016, **138**, 13561–13567.
5 P. Commins, D. P. Karothu and P. Naumov, *Angew. Chem., Int. Ed.*, 2019, **58**, 10052–10060.
6 P. Gupta, S. A. Rather, B. K. Saha, T. Panda, D. P. Karothu and N. K. Nath, *Cryst. Growth Des.*, 2020, **20**, 2847–2852.
7 J. Gilman, *Chemistry and Physics of Mechanical Hardness*, Wiley, 2009.

8 *Functional Materials: Preparation, Processing and Applications*, ed. S. Banerjee and A. K. Tyagi, Elsevier, Amsterdam, 2011.
9 B. R. Lawn and D. B. Marshall, *J. Am. Ceram. Soc.*, 1979, **62**, 347–350.
10 J. J. Vlassak and W. D. Nix, *J. Mech. Phys. Solids*, 1994, **42**, 1223–1245.
11 W. Lu, Y. Shi, X. Li and Y. Lei, *J. Mater. Eng. Perform.*, 2013, **22**, 1694–1700.
12 P. Zhang, S. X. Li and Z. F. Zhang, *Mater. Sci. Eng., A*, 2011, **529**, 62–73.
13 C. M. Reddy, G. R. Krishna and S. Ghosh, *CrystEngComm*, 2010, **12**, 2296–2314.
14 W. C. Oliver and G. M. Pharr, *J. Mater. Res.*, 2004, **19**, 3–20.
15 N. R. Moody, W. W. Gerberich, N. Burnham and S. P. Baker, *Fundamentals of Nanoindentation and Nanotribology (No. CONF-980405-)*, Materials Research Society, Warrendale, PA (United States), 1998.
16 K. I. Schiffmann, *Int. J. Mater. Res.*, 2007, **98**, 424–429.
17 A. L. M. Costa, D. J. Shuman, R. R. Machado and M. S. Andrade, *Determination of the Compliance of an Instrumented Indentation Testing Machine, HARDMEKO 2004*, Washington DC, USA, November 2–5, 2004.
18 W. C. Oliver and G. M. Pharr, *J. Mater. Res.*, 1992, **7**, 1564–1583.
19 J. J. Vlassak, M. Ciavarella, J. R. Barber and X. Wang, *J. Mech. Phys. Solids*, 2003, **51**, 1701–1721.
20 W. J. Meng and G. L. Eesley, *Thin Solid Films*, 1995, **271**, 108–116.
21 W. Wang and K. Lu, *J. Mater. Res.*, 2002, **17**, 2314–2320.
22 T. Nakamura and Y. Gu, *Mech. Mater.*, 2007, **39**, 340–356.
23 J. G. Swadener, J. Y. Rho and G. M. Pharr, *J. Biomed. Mater. Res.*, 2001, **57**, 108–112.
24 R. Hill, *The Mathematical Theory of Plasticity*, Oxford University Press, London, 1950.
25 D. Labonte, A.-K. Lenz and M. L. Oyen, *Acta Biomater.*, 2017, **57**, 373–383.
26 M. Sakai, *J. Mater. Res.*, 1999, **14**, 3630–3639.
27 C. Wang and C. C. Sun, *CrystEngComm*, 2020, **22**, 1149–1153.
28 M. F. Ashby, *Materials Selection in Mechanical Design*, Elsevier, 2011.
29 P. Naumov, S. Chizhik, M. K. Panda, N. K. Nath and E. Boldyreva, *Chem. Rev.*, 2015, **115**, 12440–12490.
30 P. Naumov, D. P. Karothu, E. Ahmed, L. Catalano, P. Commins, J. Mahmoud Halabi, M. B. Al-Handawi and L. Li, *J. Am. Chem. Soc.*, 2020, **142**, 13256–13272.
31 P. Commins, I. T. Desta, D. P. Karothu, M. K. Panda and P. Naumov, *Chem. Commun.*, 2016, **52**, 13941–13954.
32 S. Saha, M. K. Mishra, C. M. Reddy and G. R. Desiraju, *Acc. Chem. Res.*, 2018, **51**, 2957–2967.
33 E. Ahmed, D. P. Karothu and P. Naumov, *Angew. Chem., Int. Ed.*, 2018, **57**, 8837–8846.
34 S. K. Park and Y. Diao, *Chem. Soc. Rev.*, 2020, **49**, 8287–8314.
35 S. Das, A. Mondal and C. M. Reddy, *Chem. Soc. Rev.*, 2020, **49**, 8878–8896.
36 A. Basile, M. Hilder, F. Makhlooghiazad, C. Pozo-Gonzalo, D. R. MacFarlane, P. C. Howlett and M. Forsyth, *Adv. Energy Mater.*, 2018, **8**, 1703491.
37 N. K. Nath, M. K. Panda, S. C. Sahoo and P. Naumov, *CrystEngComm*, 2014, **16**, 1850–1858.
38 A. G. Shtukenberg, Y. O. Punin, A. Gujral and B. Kahr, *Angew. Chem., Int. Ed.*, 2014, **53**, 672–699.
39 O. Sato, *Nat. Chem.*, 2016, **8**, 644–656.
40 D. Kitagawa, T. Okuyama, R. Tanaka and S. Kobatake, *Chem. Mater.*, 2016, **28**, 4889–4892.
41 A. Ravi and K. M. Sureshan, *Angew. Chem., Int. Ed.*, 2018, **57**, 9362–9366.
42 G. A. R. Nobes, R. H. Marchessault, H. Chanzy, B. H. Briese and D. Jendrossek, *Macromolecules*, 1996, **29**, 8330–8333.
43 M. K. Mishra, A. Mukherjee, U. Ramamurty and G. R. Desiraju, *IUCrJ*, 2015, **2**, 653–660.
44 T. Seki, T. Mashimo and H. Ito, *Chem. Sci.*, 2019, **10**, 4185–4191.
45 M. K. Panda, S. Ghosh, N. Yasuda, T. Moriwaki, G. D. Mukherjee, C. M. Reddy and P. Naumov, *Nat. Chem.*, 2015, **7**, 65–72.
46 F. Tong, M. Al-Haidar, L. Zhu, R. O. Al-Kaysi and C. J. Bardeen, *Chem. Commun.*, 2019, **55**, 3709–3712.
47 O. S. Bushuyev, A. Tomberg, T. Friščić and C. J. Barrett, *J. Am. Chem. Soc.*, 2013, **135**, 12556–12559.
48 S. Saha and G. R. Desiraju, *Chem. Commun.*, 2017, **53**, 6371–6374.
49 T. Kim, M. K. Al-Muhanna, S. D. Al-Suwaidan, R. O. Al-Kaysi and C. J. Bardeen, *Angew. Chem., Int. Ed.*, 2013, **52**, 6889–6893.
50 H. Chung, D. Dudenko, F. Zhang, G. D'Avino, C. Ruzié, A. Richard, G. Schweicher, J. Cornil, D. Beljonne, Y. Geerts and Y. Diao, *Nat. Commun.*, 2018, **9**, 278.
51 T. Sasaki, S. Sakamoto and S. Takamizawa, *Cryst. Growth Des.*, 2019, **19**, 5491–5493.
52 S. Takamizawa, Y. Takasaki, T. Sasaki and N. Ozaki, *Nat. Commun.*, 2018, **9**, 3984.
53 T. Sasaki and S. Takamizawa, *Cryst. Growth Des.*, 2020, **20**, 6990–6994.
54 S. Takamizawa and Y. Takasaki, *Cryst. Growth Des.*, 2019, **19**, 1912–1920.
55 M. C. Etter and A. R. Siedle, *J. Am. Chem. Soc.*, 1983, **105**, 641–643.
56 M. K. Panda, R. Centore, M. Causà, A. Tuzi, F. Borbone and P. Naumov, *Sci. Rep.*, 2016, **6**, 29610.
57 M. Lusi and J. Bernstein, *Chem. Commun.*, 2013, **49**, 9293–9295.
58 D. P. Karothu and P. Naumov, *Isr. J. Chem.*, 2021, **61**, 557–562.
59 M. I. Tamboli, D. P. Karothu, M. S. Shashidhar, R. G. Gonnade and P. Naumov, *Chem. – Eur. J.*, 2018, **24**, 4133–4139.
60 P. Naumov, S. C. Sahoo, B. A. Zakharov and E. V. Boldyreva, *Angew. Chem., Int. Ed.*, 2013, **52**, 9990–9995.
61 F. Tong, M. P. Hanson and C. J. Bardeen, *Phys. Chem. Chem. Phys.*, 2016, **18**, 31936–31945.
62 D. P. Karothu, J. Weston, I. T. Desta and P. Naumov, *J. Am. Chem. Soc.*, 2016, **138**, 13298–13306.

63 K. Yadava, G. Gallo, S. Bette, C. E. Mulijanto, D. P. Karothu, I.-H. Park, R. Medishetty, P. Naumov, R. E. Dinnebier and J. J. Vittal, *IUCrJ*, 2020, **7**, 83–89.
64 S. Takahashi, H. Miura, H. Kasai, S. Okada, H. Oikawa and H. Nakanishi, *J. Am. Chem. Soc.*, 2002, **124**, 10944–10945.
65 O. Bolton, L. R. Simke, P. F. Pagoria and A. J. Matzger, *Cryst. Growth Des.*, 2012, **12**, 4311–4314.
66 K. B. Landenberger and A. J. Matzger, *Cryst. Growth Des.*, 2010, **10**, 5341–5347.
67 G. Liu, R. Gou, H. Li and C. Zhang, *Cryst. Growth Des.*, 2018, **18**, 4174–4186.
68 K. Numata, P. Cebe and D. L. Kaplan, *Biomaterials*, 2010, **31**, 2926–2933.
69 R. H. Marchessault and J. Kawada, *Macromolecules*, 2004, **37**, 7418–7420.
70 T. Kim, L. Zhu, L. J. Mueller and C. J. Bardeen, *CrystEngComm*, 2012, **14**, 7792–7799.
71 K. Omoto, T. Nakae, M. Nishio, Y. Yamanoi, H. Kasai, E. Nishibori, T. Mashimo, T. Seki, H. Ito, K. Nakamura, N. Kobayashi, N. Nakayama, H. Goto and H. Nishihara, *J. Am. Chem. Soc.*, 2020, **142**, 12651–12657.
72 S. C. Sahoo, S. B. Sinha, M. S. R. N. Kiran, U. Ramamurty, A. F. Dericioglu, C. M. Reddy and P. Naumov, *J. Am. Chem. Soc.*, 2013, **135**, 13843–13850.
73 S. Mannepalli and K. S. R. N. Mangalampalli, *Crystals*, 2017, **7**, 324.
74 S. Bhandary, A. J. Thompson, J. C. McMurtrie, J. K. Clegg, P. Ghosh, S. R. N. K. Mangalampalli, S. Takamizawa and D. Chopra, *Chem. Commun.*, 2020, **56**, 12841–12844.
75 E. Ahmed, D. P. Karothu, M. Warren and P. Naumov, *Nat. Commun.*, 2019, **10**, 3723.
76 Y. Zhang, C. Peng, Z. Zhou, R. Duan, H. Ji, Y. Che and J. Zhao, *Adv. Mater.*, 2015, **27**, 320–325.
77 D. J. Shields, D. P. Karothu, K. Sambath, R. A. A. U. Ranaweera, S. Schramm, A. Duncan, B. Duncan, J. A. Krause, A. D. Gudmundsdottir and P. Naumov, *J. Am. Chem. Soc.*, 2020, **142**, 18565–18575.
78 J. M. Cole, J. de, J. Velazquez-Garcia, D. J. Gosztola, S. G. Wang and Y.-S. Chen, *Chem. Mater.*, 2019, **31**, 4927–4935.
79 E. Ahmed, D. P. Karothu, L. Pejov, P. Commins, Q. Hu and P. Naumov, *J. Am. Chem. Soc.*, 2020, **142**, 11219–11231.
80 M. Annadhasan, D. P. Karothu, R. Chinnasamy, L. Catalano, E. Ahmed, S. Ghosh, P. Naumov and R. Chandrasekar, *Angew. Chem., Int. Ed.*, 2020, **59**, 13821–13830.
81 P. Gupta, S. Allu, D. P. Karothu, T. Panda and N. K. Nath, *Cryst. Growth Des.*, 2021, **21**, 1931–1938.
82 H. Koshima and N. Ojima, *Dyes Pigm.*, 2012, **92**, 798–801.
83 J. Peng, K. Ye, C. Liu, J. Sun and R. Lu, *J. Mater. Chem. C*, 2019, **7**, 5433–5441.
84 Y. Sun, Y. Lei, H. Dong, Y. Zhen and W. Hu, *J. Am. Chem. Soc.*, 2018, **140**, 6186–6189.
85 A. Worthy, A. Grosjean, M. C. Pfrunder, Y. Xu, C. Yan, G. Edwards, J. K. Clegg and J. C. McMurtrie, *Nat. Chem.*, 2018, **10**, 65–69.
86 F. Bernauer, *"Gedrillte" Kristalle; Verbreitung, Entstehungsweise und Beziehungen zu optischer Aktivität und Molekülasymmetrie*, Gebrüder Borntraeger, Berlin, 1929.
87 S. Saha and G. R. Desiraju, *J. Am. Chem. Soc.*, 2017, **139**, 1975–1983.
88 G. Campillo-Alvarado, C. Li, Z. Feng, K. M. Hutchins, D. C. Swenson, H. Höpfl, H. Morales-Rojas and L. R. MacGillivray, *Organometallics*, 2020, **39**, 2197–2201.
89 L. Zhu, R. O. Al-Kaysi and C. J. Bardeen, *J. Am. Chem. Soc.*, 2011, **133**, 12569–12575.
90 R. Rai, B. P. Krishnan and K. M. Sureshan, *Proc. Natl. Acad. Sci. U. S. A.*, 2018, **115**, 2896–2901.
91 P. Gupta, D. P. Karothu, E. Ahmed, P. Naumov and N. K. Nath, *Angew. Chem., Int. Ed.*, 2018, **57**, 8498–8502.
92 P. Commins, M. B. Al-Handawi, D. P. Karothu, G. Raj and P. Naumov, *Chem. Sci.*, 2020, **11**, 2606–2613.
93 S. Hayashi and T. Koizumi, *Angew. Chem.*, 2016, **128**, 2751–2754.
94 R. O. Al-Kaysi, L. Zhu, M. Al-Haidar, M. K. Al-Muhannah, K. El-Boubbou, T. M. Hamdan and C. J. Bardeen, *CrystEngComm*, 2015, **17**, 8835–8842.
95 L. Li, P. Commins, M. B. Al-Handawi, D. P. Karothu, J. M. Halabi, S. Schramm, J. Weston, R. Rezgui and P. Naumov, *Chem. Sci.*, 2019, **10**, 7327–7332.
96 A. Colin-Molina, D. P. Karothu, M. J. Jellen, R. A. Toscano, M. A. Garcia-Garibay, P. Naumov and B. Rodríguez-Molina, *Matter*, 2019, **1**, 1033–1046.
97 S. K. Park, H. Sun, H. Chung, B. B. Patel, F. Zhang, D. W. Davies, T. J. Woods, K. Zhao and Y. Diao, *Angew. Chem., Int. Ed.*, 2020, **59**, 13004–13012.
98 I. Ohkata and K. Otsuka, *J. Robot. Soc. Jpn.*, 1995, **13**, 189–192.
99 S. Takamizawa and Y. Miyamoto, *Angew. Chem., Int. Ed.*, 2014, **53**, 6970–6973.
100 S. Takamizawa and Y. Takasaki, *Angew. Chem., Int. Ed.*, 2015, **54**, 4815–4817.
101 T. Mutai, T. Sasaki, S. Sakamoto, I. Yoshikawa, H. Houjou and S. Takamizawa, *Nat. Commun.*, 2020, **11**, 1824.
102 T. Sasaki, S. Sakamoto, Y. Takasaki and S. Takamizawa, *Angew. Chem., Int. Ed.*, 2020, **59**, 4340–4343.
103 S. Takamizawa and Y. Takasaki, *Chem. Sci.*, 2016, **7**, 1527–1534.
104 H. Koshima, *Mechanically Responsive Materials for Soft Robotics*, Wiley-VCH Verlag, Weinheim, Germany, 2020.
105 H. Wang, P. Chen, Z. Wu, J. Zhao, J. Sun and R. Lu, *Angew. Chem., Int. Ed.*, 2017, **56**, 9463–9467.
106 T. Taniguchi, H. Sugiyama, H. Uekusa, M. Shiro, T. Asahi and H. Koshima, *Nat. Commun.*, 2018, **9**, 538.
107 Y. Norikane, S. Tanaka and E. Uchida, *CrystEngComm*, 2016, **18**, 7225–7228.
108 E. Uchida, R. Azumi and Y. Norikane, *Nat. Commun.*, 2015, **6**, 7310.
109 L. Zhu, R. O. Al-Kaysi and C. J. Bardeen, *Angew. Chem., Int. Ed.*, 2016, **55**, 7073–7076.
110 B. Kahr and A. G. Shtukenberg, *Isr. J. Chem.*, 2017, **57**, 31–38.

111 A. Shtukenberg, E. Gunn, M. Gazzano, J. Freudenthal, E. Camp, R. Sours, E. Rosseeva and B. Kahr, *ChemPhysChem*, 2011, **12**, 1558–1571.
112 A. G. Shtukenberg, X. Zhu, Y. Yang and B. Kahr, *Cryst. Growth Des.*, 2020, **20**, 6186–6197.
113 B. Kahr, M. Tan, H.-M. Ye and A. G. Shtukenberg, *Cryst. Growth Des.*, 2019, **19**, 5999–6003.
114 Y. Yang, Y. Zhang, C. T. Hu, M. Sun, S. Jeong, S. S. Lee, A. G. Shtukenberg and B. Kahr, *Chem. Mater.*, 2022, **34**, 1778–1788.
115 A. G. Shtukenberg, M. Tan, L. Vogt-Maranto, E. J. Chan, W. Xu, J. Yang, M. E. Tuckerman, C. T. Hu and B. Kahr, *Cryst. Growth Des.*, 2019, **19**, 4070–4080.
116 J. Yang, C. T. Hu, X. Zhu, Q. Zhu, M. D. Ward and B. Kahr, *Angew. Chem., Int. Ed.*, 2017, **56**, 10165–10169.
117 A. G. Shtukenberg, Q. Zhu, D. J. Carter, L. Vogt, J. Hoja, E. Schneider, H. Song, B. Pokroy, I. Polishchuk, A. Tkatchenko, A. R. Oganov, A. L. Rohl, M. E. Tuckerman and B. Kahr, *Chem. Sci.*, 2017, **8**, 4926–4940.
118 M. Tan, A. G. Shtukenberg, S. Zhu, W. Xu, E. Dooryhee, S. M. Nichols, M. D. Ward, B. Kahr and Q. Zhu, *Faraday Discuss.*, 2018, **211**, 477–491.
119 X. Cui, A. L. Rohl, A. Shtukenberg and B. Kahr, *J. Am. Chem. Soc.*, 2013, **135**, 3395–3398.
120 A. G. Shtukenberg, R. Drori, E. V. Sturm, N. Vidavsky, A. Haddad, J. Zheng, L. A. Estroff, H. Weissman, S. G. Wolf, E. Shimoni, C. Li, N. Fellah, E. Efrati and B. Kahr, *Angew. Chem.*, 2020, **132**, 14701–14709.
121 A. G. Shtukenberg, A. Gujral, E. Rosseeva, X. Cui and B. Kahr, *CrystEngComm*, 2015, **17**, 8817–8824.
122 A. G. Shtukenberg, Y. O. Punin, E. Gunn and B. Kahr, *Chem. Rev.*, 2012, **112**, 1805–1838.
123 B. Kahr, J. Freudenthal and E. Gunn, *Acc. Chem. Res.*, 2010, **43**, 684–692.
124 O. Arteaga and B. Kahr, *J. Opt. Soc. Am. B*, 2019, **36**, F72–F83.
125 E. Gunn, R. Sours, J. B. Benedict and B. Kahr, *J. Am. Chem. Soc.*, 2006, **128**, 14234–14235.
126 X. Cui, A. G. Shtukenberg, J. Freudenthal, S. Nichols and B. Kahr, *J. Am. Chem. Soc.*, 2014, **136**, 5481–5490.
127 X. Cui, S. M. Nichols, O. Arteaga, J. Freudenthal, F. Paula, A. G. Shtukenberg and B. Kahr, *J. Am. Chem. Soc.*, 2016, **138**, 12211–12218.
128 J. H. Freudenthal, E. Hollis and B. Kahr, *Chirality*, 2009, **21**, E20–E27.
129 H.-M. Ye, J. Xu, J. Freudenthal and B. Kahr, *J. Am. Chem. Soc.*, 2011, **133**, 13848–13851.
130 M. Tan, W. Jiang, A. T. Martin, A. G. Shtukenberg, M. D. McKee and B. Kahr, *Chem. Commun.*, 2020, **56**, 7353–7356.
131 H.-M. Ye, J. H. Freudenthal, M. Tan, J. Yang and B. Kahr, *Macromolecules*, 2019, **52**, 8514–8520.
132 A. G. Shtukenberg, X. Cui, J. Freudenthal, E. Gunn, E. Camp and B. Kahr, *J. Am. Chem. Soc.*, 2012, **134**, 6354–6364.
133 B. Kahr, A. Shtukenberg, E. Gunn, D. J. Carter and A. L. Rohl, *Cryst. Growth Des.*, 2011, **11**, 2070–2073.
134 A. G. Shtukenberg, J. Freudenthal and B. Kahr, *J. Am. Chem. Soc.*, 2010, **132**, 9341–9349.
135 M. Rosenthal, M. Burghammer, G. Bar, E. T. Samulski and D. A. Ivanov, *Macromolecules*, 2014, **47**, 8295–8304.
136 E. Efrati and W. T. M. Irvine, *Phys. Rev. X*, 2014, **4**, 011003.
137 Q. Zhu, A. G. Shtukenberg, D. J. Carter, T.-Q. Yu, J. Yang, M. Chen, P. Raiteri, A. R. Oganov, B. Pokroy, I. Polishchuk, P. J. Bygrave, G. M. Day, A. L. Rohl, M. E. Tuckerman and B. Kahr, *J. Am. Chem. Soc.*, 2016, **138**, 4881–4889.
138 J. Yang, C. T. Hu, A. G. Shtukenberg, Q. Yin and B. Kahr, *CrystEngComm*, 2018, **20**, 1383–1389.
139 A. Shtukenberg, J. Freundenthal, E. Gunn, L. Yu and B. Kahr, *Cryst. Growth Des.*, 2011, **11**, 4458–4462.
140 J. M. Schultz, *Polymer*, 2003, **44**, 433–441.
141 B. Crist and J. M. Schultz, *Prog. Polym. Sci.*, 2016, **56**, 1–63.
142 A. Toda, M. Okamura, K. Taguchi, M. Hikosaka and H. Kajioka, *Macromolecules*, 2008, **41**, 2484–2493.
143 A. Toda, K. Taguchi and H. Kajioka, *Macromolecules*, 2008, **41**, 7505–7512.
144 A. Toda, K. Taguchi, M. Hikosaka and H. Kajioka, *Polym. J.*, 2008, **40**, 905–909.
145 F. Meng, S. A. Morin, A. Forticaux and S. Jin, *Acc. Chem. Res.*, 2013, **46**, 1616–1626.
146 C. Li, A. G. Shtukenberg, D. J. Carter, X. Cui, I. Olson, A. L. Rohl, J. D. Gale, P. Raiteri and B. Kahr, *J. Phys. Chem. C*, 2018, **122**, 25085–25091.
147 I. A. Olson, A. G. Shtukenberg, G. Hakobyan, A. L. Rohl, P. Raiteri, M. D. Ward and B. Kahr, *J. Phys. Chem. Lett.*, 2016, **7**, 3112–3117.
148 X. Zhong, H. Zhou, C. Li, A. G. Shtukenberg, M. D. Ward and B. Kahr, *Chem. Commun.*, 2021, **57**, 5538–5541.
149 J. M. Schultz and D. R. Kinloch, *Polymer*, 1969, **10**, 271–278.
150 A. J. Lovinger, *Macromolecules*, 2020, **53**, 741–745.
151 M. Rosenthal, G. Portale, M. Burghammer, G. Bar, E. T. Samulski and D. A. Ivanov, *Macromolecules*, 2012, **45**, 7454–7460.
152 D. A. Ivanov and M. Rosenthal, Microstructure of Banded Polymer Spherulites: New Insights from Synchrotron Nanofocus X-Ray Scattering, in *Polymer Crystallization II*, Springer International Publishing, Cham, 2016, pp. 95–126.
153 Y. O. Punin and A. G. Shtukenberg, *Autodeformation Defects in Crystals*, University Press, St. Petersburg, 2008.
154 C. Li, A. G. Shtukenberg, L. Vogt-Maranto, E. Efrati, P. Raiteri, J. D. Gale, A. L. Rohl and B. Kahr, *J. Phys. Chem. C*, 2020, **124**, 15616–15624.
155 E. Efrati, *Isr. J. Chem.*, 2020, **60**, 1185–1189.
156 A. Haddad, H. Aharoni, E. Sharon, A. G. Shtukenberg, B. Kahr and E. Efrati, *Soft Matter*, 2019, **15**, 116–126.
157 S. Armon, E. Efrati, R. Kupferman and E. Sharon, *Science*, 2011, **333**, 1726–1730.
158 Y. Liu, J. Wang, S. Kim, H. Sun, F. Yang, Z. Fang, N. Tamura, R. Zhang, X. Song, J. Wen, B. Z. Xu, M. Wang, S. Lin, Q. Yu, K. B. Tom, Y. Deng, J. Turner, E. Chan, D. Jin, R. O. Ritchie, A. M. Minor, D. C. Chrzan, M. C. Scott and J. Yao, *Nature*, 2019, **570**, 358–362.

159 R. M. Mohamed, M. K. Mishra, L. M. AL-Harbi, M. S. Al-Ghamdi, A. M. Asiri, C. M. Reddy and U. Ramamurty, *Cryst. Growth Des.*, 2015, **15**, 2474–2479.
160 H. Frost and M. F. Ashby, *Deformation-Mechanism Maps: The Plasticity and Creep of Metals and Ceramics*, Pergamon Press, Oxford, 1982, vol. 175.
161 H. K. Bisoyi and Q. Li, *Chem. Rev.*, 2016, **116**, 15089–15166.
162 M. A. Garcia-Garibay, *Angew. Chem., Int. Ed.*, 2007, **46**, 8945–8947.
163 C. Huang, R. Huang, S. Zhang, H. Sun, H. Wang, B. Du, Y. Xiao, T. Yu and W. Huang, *Research*, 2021, **2021**, 9816535.
164 H. Koshima, S. Hasebe, Y. Hagiwara and T. Asahi, *Isr. J. Chem.*, 2021, **61**, 683–696.
165 B. Zhou and D. Yan, *Appl. Phys. Rev.*, 2021, **8**, 041310.
166 T. Kim, L. Zhu, R. O. Al-Kaysi and C. J. Bardeen, *ChemPhysChem*, 2014, **15**, 400–414.
167 D. Kitagawa, C. J. Bardeen and S. Kobatake, *Symmetry*, 2020, **12**, 1478.
168 A. Perrot, E. Moulin and N. Giuseppone, *Trends Chem.*, 2021, **3**, 926–942.
169 D. P. Karothu, J. M. Halabi, E. Ahmed, R. Ferreira, P. R. Spackman, M. A. Spackman and P. Naumov, *Angew. Chem., Int. Ed.*, 2022, **61**, e202113988.
170 F. Terao, M. Morimoto and M. Irie, *Angew. Chem., Int. Ed.*, 2012, **51**, 901–904.
171 M. K. Panda, M. Etter, R. E. Dinnebier and P. Naumov, *Angew. Chem., Int. Ed.*, 2017, **56**, 8104–8109.
172 H. Chiba, M. Morimoto and M. Irie, *Chem. Lett.*, 2021, **50**, 84–86.
173 L. Lan, X. Yang, B. Tang, X. Yu, X. Liu, L. Li, P. Naumov and H. Zhang, *Angew. Chem., Int. Ed.*, 2022, **61**, e202200196.
174 R. O. Al-Kaysi, R. J. Dillon, L. Zhu and C. J. Bardeen, *J. Colloid Interface Sci.*, 2008, **327**, 102–107.
175 P. Xu, Q. Yu, Y. Chen, P. Cheng and Z. Zhang, *CCS Chem.*, 2022, **4**, 205–213.
176 T. Taniguchi, T. Asahi and H. Koshima, *Crystals*, 2019, **9**, 437.
177 O. S. Bushuyev, T. A. Singleton and C. J. Barrett, *Adv. Mater.*, 2013, **25**, 1796–1800.
178 Y. Hao, S. Huang, Y. Guo, L. Zhou, H. Hao, C. J. Barrett and H. Yu, *J. Mater. Chem. C*, 2019, **7**, 503–508.
179 H. Koshima, N. Ojima and H. Uchimoto, *J. Am. Chem. Soc.*, 2009, **131**, 6890–6891.
180 E. Merino, *Chem. Soc. Rev.*, 2011, **40**, 3835–3853.
181 T. Taniguchi, J. Fujisawa, M. Shiro, H. Koshima and T. Asahi, *Chem. – Eur. J.*, 2016, **22**, 7950–7958.
182 O. S. Bushuyev, A. Tomberg, J. R. Vinden, N. Moitessier, C. J. Barrett and T. Friščić, *Chem. Commun.*, 2016, **52**, 2103–2106.
183 O. S. Bushuyev, T. C. Corkery, C. J. Barrett and T. Friščić, *Chem. Sci.*, 2014, **5**, 3158–3164.
184 S.-C. Cheng, K.-J. Chen, Y. Suzaki, Y. Tsuchido, T.-S. Kuo, K. Osakada and M. Horie, *J. Am. Chem. Soc.*, 2018, **140**, 90–93.
185 Z. Mahimwalla, K. G. Yager, J.-I. Mamiya, A. Shishido, A. Priimagi and C. J. Barrett, *Polym. Bull.*, 2012, **69**, 967–1006.
186 J. Peng, J. Zhao, K. Ye, H. Gao, J. Sun and R. Lu, *Chem. – Asian J.*, 2018, **13**, 1719–1724.
187 L. Zhu, F. Tong, N. Zaghloul, O. Baz, C. J. Bardeen and R. O. Al-Kaysi, *J. Mater. Chem. C*, 2016, **4**, 8245–8252.
188 F. Tong, M. Liu, R. O. Al-Kaysi and C. J. Bardeen, *Langmuir*, 2018, **34**, 1627–1634.
189 F. Tong, S. Chen, Z. Li, M. Liu, R. O. Al-Kaysi, U. Mohideen, Y. Yin and C. J. Bardeen, *Angew. Chem., Int. Ed.*, 2019, **58**, 15429–15434.
190 F. Tong, D. Kitagawa, I. Bushnak, R. O. Al-Kaysi and C. J. Bardeen, *Angew. Chem., Int. Ed.*, 2021, **60**, 2414–2423.
191 G. M. J. Schmidt, *Pure Appl. Chem.*, 1971, **27**, 647–678.
192 S. Khan, Akhtaruzzaman, R. Medishetty, A. Ekka and M. H. Mir, *Chem. – Asian J.*, 2021, **16**, 2806–2816.
193 Y. Shu, K. Ye, Y. Yue, J. Sun, H. Wang, J. Zhong, X. Yang, H. Gao and R. Lu, *CrystEngComm*, 2021, **23**, 5856–5868.
194 N. K. Nath, T. Runčevski, C.-Y. Lai, M. Chiesa, R. E. Dinnebier and P. Naumov, *J. Am. Chem. Soc.*, 2015, **137**, 13866–13875.
195 H. Wang, J. Liu, K. Ye, Q. Li, J. Zhang, H. Xing, P. Wei, J. Sun, F. Ciucci, J. W. Y. Lam, R. Lu and B. Z. Tang, *CCS Chem.*, 2021, **3**, 1491–1500.
196 J. Liu, K. Ye, Y. Shen, J. Peng, J. Sun and R. Lu, *J. Mater. Chem. C*, 2020, **8**, 3165–3175.
197 Y. Shu, K. Ye, J. Sun, Y. Yue, C. Liu, H. Wang and R. Lu, *Chem. – Eur. J.*, 2021, **27**, 17960–17969.
198 B. B. Rath and J. J. Vittal, *J. Am. Chem. Soc.*, 2020, **142**, 20117–20123.
199 F. Tong, W. Xu, T. Guo, B. F. Lui, R. C. Hayward, P. Palffy-Muhoray, R. O. Al-Kaysi and C. J. Bardeen, *J. Mater. Chem. C*, 2020, **8**, 5036–5044.
200 J.-K. Sun, W. Li, C. Chen, C.-X. Ren, D.-M. Pan and J. Zhang, *Angew. Chem., Int. Ed.*, 2013, **52**, 6653–6657.
201 R. Klajn, *Chem. Soc. Rev.*, 2014, **43**, 148–184.
202 G. Kaupp, Organic Solid-State Reactions, *Encyclopedia of Physical Organic Chemistry*, 2016, 1–80.
203 L. Zhu, A. Agarwal, J. Lai, R. O. Al-Kaysi, F. S. Tham, T. Ghaddar, L. Mueller and C. J. Bardeen, *J. Mater. Chem.*, 2011, **21**, 6258–6268.
204 R. O. Al-Kaysi, A. M. Müller and C. J. Bardeen, *J. Am. Chem. Soc.*, 2006, **128**, 15938–15939.
205 C. Yang, L. Zhu, R. A. Kudla, J. D. Hartman, R. O. Al-Kaysi, S. Monaco, B. Schatschneider, A. Magalhães, G. J. O. Beran, C. J. Bardeen and L. J. Mueller, *CrystEngComm*, 2016, **18**, 7319–7329.
206 R. O. Al-Kaysi, R. J. Dillon, J. M. Kaiser, L. J. Mueller, G. Guirado and C. J. Bardeen, *Macromolecules*, 2007, **40**, 9040–9044.
207 T. Kim, L. Zhu, L. J. Mueller and C. J. Bardeen, *J. Am. Chem. Soc.*, 2014, **136**, 6617–6625.
208 F. Tong, W. Xu, M. Al-Haidar, D. Kitagawa, R. O. Al-Kaysi and C. J. Bardeen, *Angew. Chem., Int. Ed.*, 2018, **57**, 7080–7084.
209 M. D. Cohen, Z. Ludmer, J. M. Thomas and J. O. Williams, *Proc. R. Soc. London*, 1971, **324**, 459–468.

210 B. Stevens, T. Dickinson and R. R. Sharpe, *Nature*, 1964, **204**, 876–877.
211 K. Chen, J. Wang, Y. Feng, H. Liu, X. Zhang, Y. Hao, T. Wang, X. Huang and H. Hao, *J. Mater. Chem. C*, 2021, **9**, 16762–16770.
212 H. Koshima, H. Uchimoto, T. Taniguchi, J. Nakamura, T. Asahi and T. Asahi, *CrystEngComm*, 2016, **18**, 7305–7310.
213 L. Zhu, R. O. Al-Kaysi, R. J. Dillon, F. S. Tham and C. J. Bardeen, *Cryst. Growth Des.*, 2011, **11**, 4975–4983.
214 L. Zhu, F. Tong, C. Salinas, M. K. Al-Muhanna, F. S. Tham, D. Kisailus, R. O. Al-Kaysi and C. J. Bardeen, *Chem. Mater.*, 2014, **26**, 6007–6015.
215 T. J. Gately, W. Sontising, C. J. Easley, I. Islam, R. O. Al-Kaysi, G. J. O. Beran and C. J. Bardeen, *CrystEngComm*, 2021, **23**, 5931–5943.
216 C. W. Lange, M. Foldeaki, V. I. Nevodchikov, K. Cherkasov, G. A. Abakumov and C. G. Pierpont, *J. Am. Chem. Soc.*, 1992, **114**, 4220–4222.
217 S. Chizhik, A. Sidelnikov, B. Zakharov, P. Naumov and E. Boldyreva, *Chem. Sci.*, 2018, **9**, 2319–2335.
218 K. Kato, T. Seki and H. Ito, *Inorg. Chem.*, 2021, **60**, 10849–10856.
219 M. Irie, T. Fukaminato, K. Matsuda and S. Kobatake, *Chem. Rev.*, 2014, **114**, 12174–12277.
220 S. Kobatake, S. Takami, H. Muto, T. Ishikawa and M. Irie, *Nature*, 2007, **446**, 778–781.
221 D. Kitagawa, H. Tsujioka, F. Tong, X. Dong, C. J. Bardeen and S. Kobatake, *J. Am. Chem. Soc.*, 2018, **140**, 4208–4212.
222 E. Hatano, M. Morimoto, T. Imai, K. Hyodo, A. Fujimoto, R. Nishimura, A. Sekine, N. Yasuda, S. Yokojima, S. Nakamura and K. Uchida, *Angew. Chem.*, 2017, **129**, 12750–12754.
223 H. Koshima, H. Nakaya, H. Uchimoto and N. Ojima, *Chem. Lett.*, 2012, 107–109.
224 L. Ma, Z. Yuan, Z. Huang, J. Jin, D. Cao, R. Guan, Q. Chen and X. Sun, *Chem. Commun.*, 2017, **53**, 12630–12633.
225 B. Shao, H. Qian, Q. Li and I. Aprahamian, *J. Am. Chem. Soc.*, 2019, **141**, 8364–8371.
226 B. Shao and I. Aprahamian, *Chem*, 2020, **6**, 2162–2173.
227 T. Suzuki, Y. Kaneko and T. Arai, *Chem. Lett.*, 2000, 756–757.
228 M. S. M. Rawat, S. Mal and P. Singh, *Open Chem. J.*, 2015, **2**, 7–19.
229 A. Takanabe, M. Tanaka, K. Johmoto, H. Uekusa, T. Mori, H. Koshima and T. Asahi, *J. Am. Chem. Soc.*, 2016, **138**, 15066–15077.
230 G. Kuzmanich, M. N. Gard and M. A. Garcia-Garibay, *J. Am. Chem. Soc.*, 2009, **131**, 11606–11614.
231 M. J. E. Resendiz, J. Taing and M. A. Garcia-Garibay, *Org. Lett.*, 2007, **9**, 4351–4354.
232 G. Kuzmanich, A. Natarajan, K. K. Chin, M. Veerman, C. J. Mortko and M. A. Garcia-Garibay, *J. Am. Chem. Soc.*, 2008, **130**, 1140–1141.
233 M.-L. Tsao and M. S. Platz, *J. Phys. Chem. A*, 2004, **108**, 1169–1176.
234 Ž. Skoko, S. Zamir, P. Naumov and J. Bernstein, *J. Am. Chem. Soc.*, 2010, **132**, 14191–14202.
235 R. Medishetty, S. C. Sahoo, C. E. Mulijanto, P. Naumov and J. J. Vittal, *Chem. Mater.*, 2015, **27**, 1821–1829.
236 Y. Nakagawa, M. Morimoto, N. Yasuda, K. Hyodo, S. Yokojima, S. Nakamura and K. Uchida, *Chem. – Eur. J.*, 2019, **25**, 7874–7880.
237 E. Hatano, M. Morimoto, K. Hyodo, N. Yasuda, S. Yokojima, S. Nakamura and K. Uchida, *Chem. – Eur. J.*, 2016, **22**, 12680–12683.
238 B. Dutta, C. Sinha and M. H. Mir, *Chem. Commun.*, 2019, **55**, 11049–11051.
239 K. Yadava and J. J. Vittal, *Cryst. Growth Des.*, 2019, **19**, 2542–2547.
240 S. C. Sahoo, N. K. Nath, L. Zhang, M. H. Semreen, T. H. Al-Tel and P. Naumov, *RSC Adv.*, 2014, **4**, 7640–7647.
241 I. T. Desta, S. A. Chizhik, A. A. Sidelnikov, D. P. Karothu, E. V. Boldyreva and P. Naumov, *J. Phys. Chem. A*, 2020, **124**, 300–310.
242 A. Hirano, T. Hashimoto, D. Kitagawa, K. Kono and S. Kobatake, *Cryst. Growth Des.*, 2017, **17**, 4819–4825.
243 D. Kitagawa and S. Kobatake, *J. Phys. Chem. C*, 2013, **117**, 20887–20892.
244 N. K. Nath, L. Pejov, S. M. Nichols, C. Hu, N. Saleh, B. Kahr and P. Naumov, *J. Am. Chem. Soc.*, 2014, **136**, 2757–2766.
245 M. Morimoto and M. Irie, *J. Am. Chem. Soc.*, 2010, **132**, 14172–14178.
246 F. Tong, D. Kitagawa, X. Dong, S. Kobatake and C. J. Bardeen, *Nanoscale*, 2018, **10**, 3393–3398.
247 R. O. Al-Kaysi and C. J. Bardeen, *Adv. Mater.*, 2007, **19**, 1276–1280.
248 R. O. Al-Kaysi, F. Tong, M. Al-Haidar, L. Zhu and C. J. Bardeen, *Chem. Commun.*, 2017, **53**, 2622–2625.
249 D. Kitagawa, H. Nishi and S. Kobatake, *Angew. Chem., Int. Ed.*, 2013, **52**, 9320–9322.
250 Y. Zhang, Y. Gong, B. Li, R.-M. Ma, Y. Che and J. Zhao, *Small*, 2019, **15**, 1804102.
251 M. Tamaoki, D. Kitagawa and S. Kobatake, *Cryst. Growth Des.*, 2021, **21**, 3093–3099.
252 C. Ahn, K. Li and S. Cai, *ACS Appl. Mater. Interfaces*, 2018, **10**, 25689–25696.
253 J. J. Wie, M. R. Shankar and T. J. White, *Nat. Commun.*, 2016, **7**, 13260.
254 H. Zeng, P. Wasylczyk, D. S. Wiersma and A. Priimagi, *Adv. Mater.*, 2018, **30**, 1703554.
255 H. Shahsavan, A. Aghakhani, H. Zeng, Y. Guo, Z. S. Davidson, A. Priimagi and M. Sitti, *Proc. Natl. Acad. Sci. U. S. A.*, 2020, **117**, 5125–5133.
256 J. De, Q. Liao, X. Xiao, H. Liu, W. Chen, L. Chen, H. Geng, Y. Liao and H. Fu, *ACS Appl. Mater. Interfaces*, 2020, **12**, 27493–27498.
257 Y. Gong, Y. Guo, F. Ge, W. Xiong, J. Su, Y. Sun, C. Zhang, A.-M. Cao, Y. Zhang, J. Zhao and Y. Che, *Angew. Chem.*, 2020, **132**, 10423–10428.
258 K. Saito, M. Ohnuma and Y. Norikane, *Chem. Commun.*, 2019, **55**, 9303–9306.

259 Y. Norikane, E. Uchida, S. Tanaka, K. Fujiwara, E. Koyama, R. Azumi, H. Akiyama, H. Kihara and M. Yoshida, *Org. Lett.*, 2014, **16**, 5012–5015.
260 W.-C. Xu, S. Sun and S. Wu, *Angew. Chem., Int. Ed.*, 2019, **58**, 9712–9740.
261 S. Saito, S. Nobusue, E. Tsuzaka, C. Yuan, C. Mori, M. Hara, T. Seki, C. Camacho, S. Irle and S. Yamaguchi, *Nat. Commun.*, 2016, **7**, 12094.
262 R. O. Al-Kaysi, T. H. Ghaddar and G. Guirado, *J. Nanomater.*, 2009, **2009**, 1–14.
263 R. O. Al-Kaysi and C. J. Bardeen, *Chem. Commun.*, 2006, 1224–1226.
264 K. R. Chalek, X. Dong, F. Tong, R. A. Kudla, L. Zhu, A. D. Gill, W. Xu, C. Yang, J. D. Hartman, A. Magalhães, R. O. Al-Kaysi, R. C. Hayward, R. J. Hooley, G. J. O. Beran, C. J. Bardeen and L. J. Mueller, *Chem. Sci.*, 2020, **12**, 453–463.
265 K. Morimoto, D. Kitagawa, F. Tong, K. Chalek, L. J. Mueller, C. J. Bardeen and S. Kobatake, *Angew. Chem., Int. Ed.*, 2022, **61**, e202114089.
266 M. Irie, T. Lifka, S. Kobatake and N. Kato, *J. Am. Chem. Soc.*, 2000, **122**, 4871–4876.
267 T. Yamada, K. Muto, S. Kobatake and M. Irie, *J. Org. Chem.*, 2001, **66**, 6164–6168.
268 H. Koshima, K. Takechi, H. Uchimoto, M. Shiro and D. Hashizume, *Chem. Commun.*, 2011, **47**, 11423–11425.
269 R. A. Laudise, C. Kloc, P. G. Simpkins and T. Siegrist, *J. Cryst. Growth*, 1998, **187**, 449–454.
270 C. Kloc, P. G. Simpkins, T. Siegrist and R. A. Laudise, *J. Cryst. Growth*, 1997, **182**, 416–427.
271 J. Yang, H.-H. Fang, R. Ding, S.-Y. Lu, Y.-L. Zhang, Q.-D. Chen and H.-B. Sun, *J. Phys. Chem. C*, 2011, **115**, 9171–9175.
272 D.-K. Bucar and L. R. Macgillivray, *J. Am. Chem. Soc.*, 2007, **129**, 32–33.
273 D. Mattia and H. Leese, *Nanoscale*, 2014, **6**, 13952–13957.
274 L. Zhi, J. Wu, J. Li, U. Kolb and K. Müllen, *Angew. Chem., Int. Ed.*, 2005, **44**, 2120–2123.
275 L. Zhi, T. Gorelik, J. Wu, U. Kolb and K. Müllen, *J. Am. Chem. Soc.*, 2005, **127**, 12792–12793.
276 M. H. Abumaree, L. Zhu, C. J. Bardeen, S. D. Al-Suwaidan and R. O. Al-Kaysi, *RSC Adv.*, 2011, **1**, 884–892.
277 M. H. Abumaree, S. Al-Suwaidan and R. O. Al-Kaysi, *J. Nanomater.*, 2012, **2012**, 1–9.
278 J. T. Good, J. J. Burdett and C. J. Bardeen, *Small*, 2009, **5**, 2902–2909.
279 K. Balakrishnan, A. Datar, T. Naddo, J. Huang, R. Oitker, M. Yen, J. Zhao and L. Zang, *J. Am. Chem. Soc.*, 2006, **128**, 7390–7398.
280 K. Balakrishnan, A. Datar, R. Oitker, H. Chen, J. Zuo and L. Zang, *J. Am. Chem. Soc.*, 2005, **127**, 10496–10497.
281 R. Matthews, J. Swisher, K. M. Hutchins and E. B. Pentzer, *Chem. Mater.*, 2018, **30**, 3571–3577.
282 M. Campione, R. Ruggerone, S. Tavazzi and M. Moret, *J. Mater. Chem.*, 2005, **15**, 2437–2443.
283 Q. Wang, F. Yang, Y. Zhang, M. Chen, X. Zhang, S. Lei, R. Li and W. Hu, *J. Am. Chem. Soc.*, 2018, **140**, 5339–5342.
284 J. Qian, S. Jiang, S. Li, X. Wang, Y. Shi and Y. Li, *Adv. Mater. Technol.*, 2019, **4**, 1800182.
285 H. Fu, D. Xiao, J. Yao and G. Yang, *Angew. Chem., Int. Ed.*, 2003, **42**, 2883–2886.
286 X. Zhang, C. Dong, J. Zapien, S. Ismathullakhan, Z. Kang, J. Jie, X. Zhang, J. Chang, C.-S. Lee and S.-T. Lee, *Angew. Chem., Int. Ed.*, 2009, **48**, 9121–9123.
287 Z.-Q. Lin, P.-J. Sun, Y.-Y. Tay, J. Liang, Y. Liu, N.-E. Shi, L.-H. Xie, M.-D. Yi, Y. Qian, Q.-L. Fan, H. Zhang, H. H. Hng, J. Ma, Q. Zhang and W. Huang, *ACS Nano*, 2012, **6**, 5309–5319.
288 J. Zhang, W. Xu, P. Sheng, G. Zhao and D. Zhu, *Acc. Chem. Res.*, 2017, **50**, 1654–1662.
289 L. R. MacGillivray, G. S. Papaefstathiou, T. Friščić, T. D. Hamilton, D.-K. Bučar, Q. Chu, D. B. Varshney and I. G. Georgiev, *Acc. Chem. Res.*, 2008, **41**, 280–291.
290 C. Wang, H. Dong, L. Jiang and W. Hu, *Chem. Soc. Rev.*, 2018, **47**, 422–500.
291 Y. Huang, Z. Wang, Z. Chen and Q. Zhang, *Angew. Chem., Int. Ed.*, 2019, **58**, 9696–9711.
292 Y. Ye, L. Gao, H. Hao, Q. Yin and C. Xie, *CrystEngComm*, 2020, **22**, 8045–8053.
293 S. Li and D. Yan, *ACS Appl. Mater. Interfaces*, 2018, **10**, 22703–22710.
294 F. Tong, W. Li, Z. Li, I. Islam, R. O. Al-Kaysi and C. J. Bardeen, *Angew. Chem., Int. Ed.*, 2020, **59**, 23035–23039.
295 X. Dong, F. Tong, K. M. Hanson, R. O. Al-Kaysi, D. Kitagawa, S. Kobatake and C. J. Bardeen, *Chem. Mater.*, 2019, **31**, 1016–1022.
296 X. Dong, T. Guo, D. Kitagawa, S. Kobatake, P. Palffy-Muhoray and C. J. Bardeen, *Adv. Funct. Mater.*, 2020, **30**, 1902396.
297 J. M. Abendroth, O. S. Bushuyev, P. S. Weiss and C. J. Barrett, *ACS Nano*, 2015, **9**, 7746–7768.
298 D. Kitagawa and S. Kobatake, *Chem. Commun.*, 2015, **51**, 4421–4424.
299 J. Lee, S. Oh, J. Pyo, J.-M. Kim and J. H. Je, *Nanoscale*, 2015, **7**, 6457–6461.
300 M. Morimoto and M. Irie, *J. Synth. Org. Chem. Jpn.*, 2016, **74**, 1217–1224.
301 J. B. Siegel, A. Zanghellini, H. M. Lovick, G. Kiss, A. R. Lambert, J. L. St Clair, J. L. Gallaher, D. Hilvert, M. H. Gelb, B. L. Stoddard, K. N. Houk, F. E. Michael and D. Baker, *Science*, 2010, **329**, 309–313.
302 M. Pastore and F. De Angelis, *Phys. Chem. Chem. Phys.*, 2012, **14**, 920–928.
303 S. Curtarolo, G. L. W. Hart, M. B. Nardelli, N. Mingo, S. Sanvito and O. Levy, *Nat. Mater.*, 2013, **12**, 191–201.
304 K. T. Butler, J. M. Frost, J. M. Skelton, K. L. Svane and A. Walsh, *Chem. Soc. Rev.*, 2016, **45**, 6138–6146.
305 V. L. Deringer, M. A. Caro and G. Csányi, *Adv. Mater.*, 2019, **31**, e1902765.
306 F. Musil, S. De, J. Yang, J. E. Campbell, G. M. Day and M. Ceriotti, *Chem. Sci.*, 2018, **9**, 1289–1300.
307 J. D. Evans and F.-X. Coudert, *Chem. Mater.*, 2017, **29**, 7833–7839.

308 P. Kroll, *J. Eur. Ceram. Soc.*, 2005, **25**, 163–174.
309 J. M. Halabi, E. Ahmed, L. Catalano, D. P. Karothu, R. Rezgui and P. Naumov, *J. Am. Chem. Soc.*, 2019, **141**, 14966–14970.
310 I. Azuri, E. Meirzadeh, D. Ehre, S. R. Cohen, A. M. Rappe, M. Lahav, I. Lubomirsky and L. Kronik, *Angew. Chem., Int. Ed.*, 2015, **54**, 13566–13570.
311 G. R. Desiraju, *Angew. Chem., Int. Ed.*, 1995, **34**, 2311–2327.
312 M. J. Turner, S. Grabowsky, D. Jayatilaka and M. A. Spackman, *J. Phys. Chem. Lett.*, 2014, **5**, 4249–4255.
313 M. J. Turner, S. P. Thomas, M. W. Shi, D. Jayatilaka and M. A. Spackman, *Chem. Commun.*, 2015, **51**, 3735–3738.
314 K. B. Raju, S. Ranjan, V. S. Vishnu, M. Bhattacharya, B. Bhattacharya, A. K. Mukhopadhyay and C. M. Reddy, *Cryst. Growth Des.*, 2018, **18**, 3927–3937.
315 J. P. Yadav, R. N. Yadav, P. Sihota, H. Chen, C. Wang, C. C. Sun, N. Kumar, A. Bansal and S. Jain, *Cryst. Growth Des.*, 2019, **19**, 4465–4475.
316 S. P. Thomas, M. W. Shi, G. A. Koutsantonis, D. Jayatilaka, A. J. Edwards and M. A. Spackman, *Angew. Chem., Int. Ed.*, 2017, **56**, 8468–8472.
317 C. Wang and C. C. Sun, *Cryst. Growth Des.*, 2018, **18**, 1909–1916.
318 R. Devarapalli, S. B. Kadambi, C.-T. Chen, G. R. Krishna, B. R. Kammari, M. J. Buehler, U. Ramamurty and C. M. Reddy, *Chem. Mater.*, 2019, **31**, 1391–1402.
319 K. Zhang, C. C. Sun, Y. Liu, C. Wang, P. Shi, J. Xu, S. Wu and J. Gong, *Chem. Mater.*, 2021, **33**, 1053–1060.
320 M. Zhang, Z. Liang, F. Wu, J.-F. Chen, C. Xue and H. Zhao, *J. Cryst. Growth*, 2017, **467**, 47–53.
321 Y. Liu, S. Niu, W. Lai, T. Yu, Y. Ma, H. Gao, F. Zhao and Z. Ge, *CrystEngComm*, 2019, **21**, 4910–4917.
322 J. D. H. Donnay and D. Harker, *American Mineralogist*, 1937, **22**, 446–467.
323 P. Hartman and W. G. Perdok, *Acta Crystallogr.*, 1955, **8**, 49–52.
324 P. Hartman and P. Bennema, *J. Cryst. Growth*, 1980, **49**, 145–156.
325 A. M. Reilly, R. I. Cooper, C. S. Adjiman, S. Bhattacharya, A. D. Boese, J. G. Brandenburg, P. J. Bygrave, R. Bylsma, J. E. Campbell, R. Car, D. H. Case, R. Chadha, J. C. Cole, K. Cosburn, H. M. Cuppen, F. Curtis, G. M. Day, R. A. Jr. DiStasio, A. Dzyabchenko, B. P. van Eijck, D. M. Elking, J. A. van den Ende, J. C. Facelli, M. B. Ferraro, L. Fusti-Molnar, C. A. Gatsiou, T. S. Gee, R. de Gelder, L. M. Ghiringhelli, H. Goto, S. Grimme, R. Guo, D. W. M. Hofmann, J. Hoja, R. K. Hylton, L. Iuzzolino, W. Jankiewicz, D. T. de Jong, J. Kendrick, N. J. J. de Klerk, H. Y. Ko, L. N. Kuleshova, X. Li, S. Lohani, F. J. J. Leusen, A. M. Lund, J. Lv, Y. Ma, N. Marom, A. E. Masunov, P. McCabe, D. P. McMahon, H. Meekes, M. P. Metz, A. J. Misquitta, S. Mohamed, B. Monserrat, R. J. Needs, M. A. Neumann, J. Nyman, S. Obata, H. Oberhofer, A. R. Oganov, A. M. Orendt, G. I. Pagola, C. C. Pantelides, C. J. Pickard, R. Podeszwa, L. S. Price, S. L. Price, A. Pulido, M. G. Read, K. Reuter, E. Schneider, C. Schober, G. P. Shields, P. Singh, I. J. Sugden, K. Szalewicz, C. R. Taylor, A. Tkatchenko, M. E. Tuckerman, F. Vacarro, M. Vasileiadis, A. Vazquez-Mayagoitia, L. Vogt, Y. Wang, R. E. Watson, G. A. de Wijs, J. Yang, Q. Zhu and C. R. Groom, *Acta Crystallogr., Sect. B: Struct. Sci., Cryst. Eng. Mater.*, 2016, **72**, 439–459.
326 A. Pulido, L. Chen, T. Kaczorowski, D. Holden, M. A. Little, S. Y. Chong, B. J. Slater, D. P. McMahon, B. Bonillo, C. J. Stackhouse, A. Stephenson, C. M. Kane, R. Clowes, T. Hasell, A. I. Cooper and G. M. Day, *Nature*, 2017, **543**, 657–664.
327 H. Sun, Z. Jin, C. Yang, R. L. C. Akkermans, S. H. Robertson, N. A. Spenley, S. Miller and S. M. Todd, *J. Mol. Model.*, 2016, **22**, 47.
328 S. L. Mayo, B. D. Olafson and W. A. Goddard, *J. Phys. Chem.*, 1990, **94**, 8897–8909.
329 A. Jain, S. P. Ong, G. Hautier, W. Chen, W. D. Richards, S. Dacek, S. Cholia, D. Gunter, D. Skinner, G. Ceder and K. A. Persson, *APL Mater.*, 2013, **1**, 011002.
330 The Materials Project. **www.materialsproject.org** (accessed: 2022-06-14).
331 M. de Jong, W. Chen, T. Angsten, A. Jain, R. Notestine, A. Gamst, M. Sluiter, C. Krishna Ande, S. van der Zwaag, J. J. Plata, C. Toher, S. Curtarolo, G. Ceder, K. A. Persson and M. Asta, *Sci. Data*, 2015, **2**, 150009.
332 F. Colmenero, Organic Acids under Pressure: Elastic Properties, *Mater. Adv.*, 2020, **1**, 1399–1426.
333 C. Wang, S. Paul, D. J. Sun, S. O. Nilsson Lill and C. C. Sun, *Cryst. Growth Des.*, 2020, **20**, 4217–4223.
334 V. Basavalingappa, S. Bera, B. Xue, I. Azuri, Y. Tang, K. Tao, L. J. W. Shimon, M. R. Sawaya, S. Kolusheva, D. S. Eisenberg, L. Kronik, Y. Cao, G. Wei and E. Gazit, *Nat. Commun.*, 2019, **10**, 5256.
335 C. Wang and C. C. Sun, *Mol. Pharm.*, 2019, **16**, 1732–1741.
336 A. E. Masunov, M. Wiratmo, A. A. Dyakov, Y. V. Matveychuk and E. V. Bartashevich, *Cryst. Growth Des.*, 2020, **20**, 6093–6100.
337 A. M. Reilly and A. Tkatchenko, *J. Chem. Phys.*, 2013, **139**, 024705.
338 A. M. Reilly and A. Tkatchenko, *Phys. Rev. Lett.*, 2014, **113**, 055701.
339 E. Kiely, R. Zwane, R. Fox, A. M. Reilly and S. Guerin, *CrystEngComm*, 2021, **23**, 5697–5710.
340 H. A. Wu, *Comput. Mater. Sci.*, 2004, **31**, 287–291.
341 A. L. Briseno, R. J. Tseng, M.-M. Ling, E. H. L. Falcao, Y. Yang, F. Wudl and Z. Bao, *Adv. Mater.*, 2006, **18**, 2320–2324.
342 T. Someya, T. Sekitani, S. Iba, Y. Kato, H. Kawaguchi, T. Sakurai and A. Large-Area, *Proc. Natl. Acad. Sci. U. S. A.*, 2004, **101**, 9966–9970.
343 W. D. Callister and D. G. Rethwisch, *Materials Science and Engineering: An Introduction*, Wiley, 10th edn, 2020.
344 J. L. Brédas, J. P. Calbert, D. A. da Silva Filho and J. Cornil, *Proc. Natl. Acad. Sci. U. S. A.*, 2002, **99**, 5804–5809.
345 Y. Diao, K. M. Lenn, W.-Y. Lee, M. A. Blood-Forsythe, J. Xu, Y. Mao, Y. Kim, J. A. Reinspach, S. Park, A. Aspuru-Guzik, G. Xue, P. Clancy, Z. Bao and S. C. B. Mannsfeld, *J. Am. Chem. Soc.*, 2014, **136**, 17046–17057.

346 J. Xu, Y. Diao, D. Zhou, Y. Mao, G. Giri, W. Chen, N. Liu, S. C. B. Mannsfeld, G. Xue and Z. Bao, *J. Mater. Chem. C*, 2014, **2**, 2985–2991.
347 H. Chung and Y. Diao, *J. Mater. Chem. C*, 2016, **4**, 3915–3933.
348 T. Kubo, R. Häusermann, J. Tsurumi, J. Soeda, Y. Okada, Y. Yamashita, N. Akamatsu, A. Shishido, C. Mitsui, T. Okamoto, S. Yanagisawa, H. Matsui and J. Takeya, *Nat. Commun.*, 2016, **7**, 11156.
349 H. H. Choi, H. T. Yi, J. Tsurumi, J. J. Kim, A. L. Briseno, S. Watanabe, J. Takeya, K. Cho and V. Podzorov, *Adv. Sci.*, 2020, **7**, 1901824.
350 Y. Wu, A. R. Chew, G. A. Rojas, G. Sini, G. Haugstad, A. Belianinov, S. V. Kalinin, H. Li, C. Risko, J.-L. Brédas, A. Salleo and C. D. Frisbie, *Nat. Commun.*, 2016, **7**, 10270.
351 R. Taguchi, N. Akamatsu, K. Kuwahara, K. Tokumitsu, Y. Kobayashi, M. Kishino, K. Yaegashi, J. Takeya and A. Shishido, *Adv. Mater. Interfaces*, 2021, **8**, 2001662.
352 M. A. Reyes-Martinez, A. J. Crosby and A. L. Briseno, *Nat. Commun.*, 2015, **6**, 6948.
353 M.-T. Ho and Y.-T. Tao, *J. Visualized Exp.*, 2016, **118**, e54651.
354 S. Lai, I. Temiño, T. Cramer, F. G. del Pozo, B. Fraboni, P. Cosseddu, A. Bonfiglio and M. Mas-Torrent, *Adv. Electron. Mater.*, 2018, **4**, 1700271.
355 M. Dharmarwardana, S. Pakhira, R. P. Welch, C. Caicedo-Narvaez, M. A. Luzuriaga, B. S. Arimilli, G. T. McCandless, B. Fahimi, J. L. Mendoza-Cortes and J. J. Gassensmith, *J. Am. Chem. Soc.*, 2021, **143**, 5951–5957.
356 *Integrated Optics*, ed. T. Tamir, Springer Berlin Heidelberg, Berlin, Heidelberg, 1975.
357 R. G. Hunsperger, *Integrated Optics: Theory and Technology*, Springer, New York, NY, 2009.
358 H. Jiang and W. Hu, *Angew. Chem., Int. Ed.*, 2020, **59**, 1408–1428.
359 R. Chandrasekar, *Phys. Chem. Chem. Phys.*, 2014, **16**, 7173–7183.
360 C. Zhang, Y. S. Zhao and J. Yao, *Phys. Chem. Chem. Phys.*, 2011, **13**, 9060–9073.
361 S. Min, A. Dhamsaniya, L. Zhang, G. Hou, Z. Huang, K. Pambhar, A. K. Shah, V. P. Mehta, Z. Liu and B. Song, *J. Phys. Chem. Lett.*, 2019, **10**, 5997–6002.
362 S. Wu, B. Zhou and D. Yan, *Adv. Opt. Mater.*, 2021, **9**, 2001768.
363 L. Mutter, A. Guarino, M. Jazbinsek, M. Zgonik, P. Günter and M. Döbeli, *Opt. Express*, 2007, **15**, 629–638.
364 Q. Liao, H. Zhang, W. Zhu, K. Hu and H. Fu, *J. Mater. Chem. C*, 2014, **2**, 9695–9700.
365 W. Ji, B. Xue, S. Bera, S. Guerin, Y. Liu, H. Yuan, Q. Li, C. Yuan, L. J. W. Shimon, Q. Ma, E. Kiely, S. A. M. Tofail, M. Si, X. Yan, Y. Cao, W. Wang, R. Yang, D. Thompson, J. Li and E. Gazit, *ACS Nano*, 2020, **14**, 10704–10715.
366 Y.-L. Shi, M.-P. Zhuo, X.-D. Wang and L.-S. Liao, *ACS Appl. Nano Mater.*, 2020, **3**, 1080–1097.
367 D. P. Karothu, G. Dushaq, E. Ahmed, L. Catalano, S. Polavaram, R. Ferreira, L. Li, S. Mohamed, M. Rasras and P. Naumov, *Nat. Commun.*, 2021, **12**, 1326.
368 M.-P. Zhuo, Y.-X. Zhang, Z.-Z. Li, Y.-L. Shi, X.-D. Wang and L.-S. Liao, *Nanoscale*, 2018, **10**, 5140–5147.
369 D. P. Karothu, G. Dushaq, E. Ahmed, L. Catalano, M. Rasras and P. Naumov, *Angew. Chem., Int. Ed.*, 2021, **60**, 26151–26157.
370 H. Liu, Z. Lu, Z. Zhang, Y. Wang and H. Zhang, *Angew. Chem., Int. Ed.*, 2018, **57**, 8448–8452.
371 J. Y. Zheng, Y. Yan, X. Wang, Y. S. Zhao, J. Huang and J. Yao, *J. Am. Chem. Soc.*, 2012, **134**, 2880–2883.
372 M.-P. Zhuo, J.-J. Wu, X.-D. Wang, Y.-C. Tao, Y. Yuan and L.-S. Liao, *Nat. Commun.*, 2019, **10**, 3839.
373 D. Tian and Y. Chen, *Adv. Opt. Mater.*, 2021, **9**, 2002264.
374 Y. Ma, Y. Zong, H. Yin, H. Lin, S. Chen and X.-D. Wang, *Adv. Opt. Mater.*, 2021, **9**, 2101481.
375 S. Chen, M. P. Zhuo, X. D. Wang, G. Q. Wei and L. S. Liao, *PhotoniX*, 2021, **2**, 1–24.
376 S. Hayashi, S. Yamamoto, D. Takeuchi, Y. Ie and K. Takagi, *Angew. Chem.*, 2018, **130**, 17248–17254.
377 R. Huang, B. Tang, K. Ye, C. Wang and H. Zhang, *Adv. Opt. Mater.*, 2019, **7**, 1900927.
378 M. Annadhasan, A. R. Agrawal, S. Bhunia, V. V. Pradeep, S. S. Zade, C. M. Reddy and R. Chandrasekar, *Angew. Chem., Int. Ed.*, 2020, **59**, 13852–13858.
379 B. Tang, B. Liu, H. Liu and H. Zhang, *Adv. Funct. Mater.*, 2020, **30**, 2004116.
380 H. Liu, Z. Bian, Q. Cheng, L. Lan, Y. Wang and H. Zhang, *Chem. Sci.*, 2019, **10**, 227–232.
381 L. Catalano, D. P. Karothu, S. Schramm, E. Ahmed, R. Rezgui, T. J. Barber, A. Famulari and P. Naumov, *Angew. Chem., Int. Ed.*, 2018, **57**, 17254–17258.
382 R. Huang, C. Wang, Y. Wang and H. Zhang, *Adv. Mater.*, 2018, **30**, e1800814.
383 V. V. Pradeep, C. Tardío, I. Torres-Moya, A. M. Rodríguez, A. V. Kumar, M. Annadhasan, A. de la Hoz, P. Prieto and R. Chandrasekar, *Small*, 2021, **17**, e2006795.
384 J. Kjelstrup-Hansen, C. Simbrunner and H.-G. Rubahn, *Rep. Prog. Phys.*, 2013, **76**, 126502.
385 Z. Lu, Y. Zhang, H. Liu, K. Ye, W. Liu and H. Zhang, *Angew. Chem.*, 2020, **132**, 4329–4333.
386 B. Liu, Z. Lu, B. Tang, H. Liu, H. Liu, Z. Zhang, K. Ye and H. Zhang, *Angew. Chem., Int. Ed.*, 2020, **59**, 23117–23121.
387 B. Liu, Q. Di, W. Liu, C. Wang, Y. Wang and H. Zhang, *J. Phys. Chem. Lett.*, 2019, **10**, 1437–1442.
388 J. Cao, H. Liu and H. Zhang, *CCS Chem.*, 2021, **3**, 2569–2575.
389 K. Naim, M. Singh, S. Sharma, R. V. Nair, P. Venugopalan, S. C. Sahoo and P. P. Neelakandan, *Chem. – Eur. J.*, 2020, **26**, 11979–11984.
390 B. Liu, H. Liu, H. Zhang, Q. Di and H. Zhang, *J. Phys. Chem. Lett.*, 2020, **11**, 9178–9183.
391 X. Chu, Z. Lu, B. Tang, B. Liu, K. Ye and H. Zhang, *J. Phys. Chem. Lett.*, 2020, **11**, 5433–5438.
392 S. Zhao, H. Yamagishi, O. Oki, Y. Ihara, N. Ichiji, A. Kubo, S. Hayashi and Y. Yamamoto, *Adv. Opt. Mater.*, 2022, **10**, 2101808.
393 J. Peng, J. Bai, X. Cao, J. He, W. Xu and J. Jia, *Chem. – Eur. J.*, 2021, **27**, 16036–16042.

394 B. Tang, X. Yu, K. Ye and H. Zhang, *Adv. Opt. Mater.*, 2022, **10**, 2101335.
395 J. Ravi, A. Vinod Kumar, D. P. Karothu, M. Annadhasan, P. Naumov and R. Chandrasekar, *Adv. Funct. Mater.*, 2021, **31**, 2105415.
396 L. Lan, H. Liu, X. Yu, X. Liu and H. Zhang, *Angew. Chem., Int. Ed.*, 2021, **60**, 11283–11287.
397 S. I. Bozhevolnyi, V. S. Volkov, E. Devaux, J.-Y. Laluet and T. W. Ebbesen, *Nature*, 2006, **440**, 508–511.
398 *Nanophotonics and Nanofabrication*, ed. M. Ohtsu, Wiley-VCH Verlag, Weinheim, Germany, 2009.
399 S. A. Maier, P. G. Kik, H. A. Atwater, S. Meltzer, E. Harel, B. E. Koel and A. A. G. Requicha, *Nat. Mater.*, 2003, **2**, 229–232.
400 S. Basak and R. Chandrasekar, *J. Mater. Chem. C*, 2014, **2**, 1404–1408.
401 I. D. W. Samuel and G. A. Turnbull, *Chem. Rev.*, 2007, **107**, 1272–1295.
402 D. Fichou, S. Delysse and J. M. Nunzi, *Adv. Mater.*, 1997, **9**, 1178–1181.
403 J. Gierschner, S. Varghese and S. Y. Park, *Adv. Opt. Mater.*, 2016, **4**, 348–364.
404 Y. Jiang, Y.-Y. Liu, X. Liu, H. Lin, K. Gao, W.-Y. Lai and W. Huang, *Chem. Soc. Rev.*, 2020, **49**, 5885–5944.
405 G. Kreiza, P. Baronas, E. Radiunas, P. Adomėnas, O. Adomėnienė, K. Kazlauskas, J.-C. Ribierre, C. Adachi and S. Juršėnas, *Adv. Opt. Mater.*, 2017, **5**, 1600823.
406 K. Wang, H. Zhang, S. Chen, G. Yang, J. Zhang and W. Tian, *Adv. Mater.*, 2014, **26**, 6168–6173.
407 X. Cheng, Y. Zhang, S. Han, F. Li, H. Zhang and Y. Wang, *Chem. – Eur. J.*, 2016, **22**, 4899–4903.
408 B. Tang, C. Wang, Y. Wang and H. Zhang, *Angew. Chem.*, 2017, **129**, 12717–12721.
409 H. Dong, C. Zhang, X. Lin, Z. Zhou, J. Yao and Y. S. Zhao, *Nano Lett.*, 2017, **17**, 91–96.
410 H. Dong, C. Zhang, Y. Liu, Y. Yan, F. Hu and Y. S. Zhao, *Angew. Chem.*, 2018, **130**, 3162–3166.
411 X. Cheng, Z. Wang, B. Tang, H. Zhang, A. Qin, J. Z. Sun and B. Z. Tang, *Adv. Funct. Mater.*, 2018, **28**, 1706506.
412 B. Tang, Z. Zhang, H. Liu and H. Zhang, *Chin. Chem. Lett.*, 2017, **28**, 2129–2132.
413 X. Cheng, K. Wang, S. Huang, H. Zhang, H. Zhang and Y. Wang, *Angew. Chem., Int. Ed.*, 2015, **54**, 8369–8373.
414 L. Wang, Z. Zhang, X. Cheng, K. Ye, F. Li, Y. Wang and H. Zhang, *J. Mater. Chem. C*, 2015, **3**, 499–505.
415 B. Tang, H. Liu, F. Li, Y. Wang and H. Zhang, *Chem. Commun.*, 2016, **52**, 6577–6580.
416 B. Tang, H. Zhang, X. Cheng, K. Ye and H. Zhang, *ChemPlusChem*, 2016, **1**, 1320–1325.
417 Z. Zhang, X. Song, S. Wang, F. Li, H. Zhang, K. Ye and Y. Wang, *J. Phys. Chem. Lett.*, 2016, **7**, 1697–1702.
418 H. Liu, Z. Lu, B. Tang, Z. Zhang, Y. Wang and H. Zhang, *Dyes Pigm.*, 2018, **149**, 284–289.
419 W. Zhang, J. Yao and Y. S. Zhao, *Acc. Chem. Res.*, 2016, **49**, 1691–1700.
420 H.-H. Fang, R. Ding, S.-Y. Lu, X.-L. Zhang, J. Feng, Q.-D. Chen and H.-B. Sun, *J. Mater. Chem.*, 2012, **22**, 24139–24144.
421 S. Z. Bisri, T. Takenobu and Y. Iwasa, *J. Mater. Chem. C*, 2014, **2**, 2827–2836.
422 M. Annadhasan, S. Basak, N. Chandrasekhar and R. Chandrasekar, *Adv. Opt. Mater.*, 2020, **8**, 2000959.
423 P. Hui and R. Chandrasekar, *Adv. Mater.*, 2013, **25**, 2963–2967.
424 K. Takazawa, Y. Kitahama, Y. Kimura and G. Kido, *Nano Lett.*, 2005, **5**, 1293–1296.
425 L. Catalano, P. Commins, S. Schramm, D. P. Karothu, R. Rezgui, K. Hadef and P. Naumov, *Chem. Commun.*, 2019, **55**, 4921–4924.
426 N. Chandrasekhar, Md. A. Mohiddon and R. Chandrasekar, *Adv. Opt. Mater.*, 2013, **1**, 305–311.
427 D. Venkatakrishnarao, E. A. Mamonov, T. V. Murzina and R. Chandrasekar, *Adv. Opt. Mater.*, 2018, **6**, 1800343.
428 V. V. Pradeep, N. Mitetelo, M. Annadhasan, E. Mamonov, T. V. Murzina and R. Chandrasekar, *Adv. Opt. Mater.*, 2020, **8**, 1901317.
429 J. Ravi, D. Venkatakrishnarao, C. Sahoo, S. R. G. Naraharisetty, N. Mitetelo, A. A. Ezhov, E. Mamonov, T. Murzina and R. Chandrasekar, *ChemNanoMat*, 2018, **4**, 764–768.
430 D. Venkatakrishnarao, M. A. Mohiddon, N. Chandrasekhar and R. Chandrasekar, *Adv. Opt. Mater.*, 2015, **3**, 1035–1040.
431 D. Venkatakrishnarao, Y. S. L. V. Narayana, M. A. Mohaiddon, E. A. Mamonov, N. Mitetelo, I. A. Kolmychek, A. I. Maydykovskiy, V. B. Novikov, T. V. Murzina and R. Chandrasekar, *Adv. Mater.*, 2017, **29**, 1605260.
432 Y. S. Zhao, *Organic Nanophotonics: Fundamentals and Applications*, Springer, Berlin Heidelberg, 2014.
433 D. Pile, *Nat. Photonics*, 2010, **4**, 402.
434 K. Takazawa, J.-I. Inoue, K. Mitsuishi and T. Takamasu, *Adv. Mater.*, 2011, **23**, 3659–3663.
435 M. Irie, Photomechanical Response of Diarylethene Single Crystals, in *New Frontiers in Photochromism*, ed. M. Irie, Y. Yokoyama and T. Seki, Springer, Tokyo, 2013, pp. 3–19.
436 F. Balzer, V. G. Bordo, A. C. Simonsen and H.-G. Rubahn, *Phys. Rev. B: Condens. Matter Mater. Phys.*, 2003, **67**, 115408.
437 M. K. Barnoski, Optical Directional Couplers, in *Introduction to Integrated Optics*, ed. S. Somekh, Springer, Boston, 1974.
438 J. Ravi, M. Annadhasan, A. V. Kumar and R. Chandrasekar, *Adv. Funct. Mater.*, 2021, **31**, 2100642.
439 R. Chandrasekar, *Small*, 2021, **17**, 2100277.
440 R. Chandrasekar, *Chem. Commun.*, 2022, **58**, 3415–3428.
441 B. Jalali and S. Fathpour, *J. Lightwave Technol.*, 2006, **24**, 4600–4615.
442 D.-X. Xu, J. H. Schmid, G. T. Reed, G. Z. Mashanovich, D. J. Thomson, M. Nedeljkovic, X. Chen, D. Van Thourhout, S. Keyvaninia and S. K. Selvaraja, *IEEE J. Sel. Top. Quantum Electron.*, 2014, **20**, 189–205.
443 D. Venkatakrishnarao and R. Chandrasekar, *Adv. Opt. Mater.*, 2016, **4**, 112–119.
444 J. Ravi and R. Chandrasekar, *Adv. Opt. Mater.*, 2021, **9**, 2100550.

445 K. Iwaso, Y. Takashima and A. Harada, *Nat. Chem.*, 2016, **8**, 625–632.
446 O. M. Wani, H. Zeng and A. Priimagi, *Nat. Commun.*, 2017, **8**, 15546.
447 Y. Hagiwara, T. Taniguchi, T. Asahi and H. Koshima, *J. Mater. Chem. C*, 2020, **8**, 4876–4884.
448 L. Liu, M.-H. Liu, L.-L. Deng, B.-P. Lin and H. Yang, *J. Am. Chem. Soc.*, 2017, **139**, 11333–11336.
449 L. Dong and Y. Zhao, *Mater. Chem. Front.*, 2018, **2**, 1932–1943.
450 K. Amimoto and T. Kawato, *J. Photochem. Photobiol., C*, 2005, **6**, 207–226.
451 *Chiral Photochemistry*, ed. Y. Inoue and V. Ramamurthy, CRC Press, Boca Raton, FL, 2004.
452 H. Koshima, R. Matsuo, M. Matsudomi, Y. Uemura and M. Shiro, *Cryst. Growth Des.*, 2013, **13**, 4330–4337.
453 Y. Yokoyama, *Chem. Rev.*, 2000, **100**, 1717–1740.
454 L. Khedhiri, A. Corval, R. Casalegno and M. Rzaigui, *J. Phys. Chem. A*, 2004, **108**, 7473–7478.
455 J. Harada, R. Nakajima and K. Ogawa, *J. Am. Chem. Soc.*, 2008, **130**, 7085–7091.
456 J. Chen, J. R. Scheffer and J. Trotter, *Tetrahedron*, 1992, **48**, 3251–3274.
457 M. C. Sajimon, D. Ramaiah, C. H. Suresh, W. Adam, F. D. Lewis and M. V. George, *J. Am. Chem. Soc.*, 2007, **129**, 9439–9445.
458 T. Taniguchi, A. Kubota, T. Moritoki, T. Asahi and H. Koshima, *RSC Adv.*, 2018, **8**, 34314–34320.
459 T. Shima, T. Muraoka, N. Hoshino, T. Akutagawa, Y. Kobayashi and K. Kinbara, *Angew. Chem., Int. Ed.*, 2014, **53**, 7173–7178.
460 Z.-S. Yao, M. Mito, T. Kamachi, Y. Shiota, K. Yoshizawa, N. Azuma, Y. Miyazaki, K. Takahashi, K. Zhang, T. Nakanishi, S. Kang, S. Kanegawa and O. Sato, *Nat. Chem.*, 2014, **6**, 1079–1083.
461 M. K. Panda, T. Runčevski, S. C. Sahoo, A. A. Belik, N. K. Nath, R. E. Dinnebier and P. Naumov, *Nat. Commun.*, 2014, **5**, 4811.
462 T. Taniguchi, H. Sato, Y. Hagiwara, T. Asahi and H. Koshima, *Commun. Chem.*, 2019, **2**, 19.
463 S. Koshihara, Y. Tokura, K. Takeda and T. Koda, *Phys. Rev. Lett.*, 1992, **68**, 1148–1151.
464 H. Koshima, M. Matsudomi, Y. Uemura, F. Kimura and T. Kimura, *Chem. Lett.*, 2013, **42**, 1517–1519.
465 S. Hasebe, D. Matsuura, T. Mizukawa, T. Asahi and H. Koshima, *Front. Robot. AI*, 2021, **8**, 684287.
466 B. R. Rohrs, G. E. Amidon, R. H. Meury, P. J. Secreast, H. M. King and C. J. Skoug, *J. Pharm. Sci.*, 2006, **95**, 1049–1059.
467 M. C. Johnson, *Pharm. Acta Helv.*, 1972, **47**, 546–559.
468 C. Jacobs and R. H. Müller, *Pharm. Res.*, 2002, **19**, 189–194.
469 E. Merisko-Liversidge and G. G. Liversidge, *Adv. Drug Delivery Rev.*, 2011, **63**, 427–440.
470 A. A. Noyes and W. R. Whitney, *J. Am. Chem. Soc.*, 1897, **19**, 930–934.
471 T. Takagi, C. Ramachandran, M. Bermejo, S. Yamashita, L. X. Yu and G. L. Amidon, *Mol. Pharm.*, 2006, **3**, 631–643.
472 A. M. Thayer, *Chem. Eng. News Archive*, 2010, **88**, 13–18.
473 V. B. Patravale, A. A. Date and R. M. Kulkarni, *J. Pharm. Pharmacol.*, 2004, **56**, 827–840.
474 A. C. Bentham, C. C. Kwan, R. Boerefijn and M. Ghadiri, *Powder Technol.*, 2004, **141**, 233–238.
475 X. Kou, L. W. Chan, C. C. Sun and P. W. S. Heng, *Asian J. Pharm. Sci.*, 2017, **12**, 59–65.
476 A. Halme, M. J. Quayle, S. O. Nilsson Lill, A. Pettersen, M. Fransson and C. Boissier, *Cryst. Growth Des.*, 2019, **19**, 3670–3680.
477 K. Kendall, *Nature*, 1978, **272**, 710–711.
478 S. Zügner, K. Marquardt and I. Zimmermann, *Eur. J. Pharm. Biopharm.*, 2006, **62**, 194–201.
479 M. Meier, E. John, D. Wieckhusen, W. Wirth and W. Peukert, *Powder Technol.*, 2009, **188**, 301–313.
480 L. J. Taylor, D. G. Papadopoulos, P. J. Dunn, A. C. Bentham, N. J. Dawson, J. C. Mitchell and M. J. Snowden, *Org. Process Res. Dev.*, 2004, **8**, 674–679.
481 D. Olusanmi, K. J. Roberts, M. Ghadiri and Y. Ding, *Int. J. Pharm.*, 2011, **411**, 49–63.
482 H. Abouhakim, M. J. Quayle, S. T. Norberg, S. O. Nilsson Lill, M. Asachi, S. L. M. Schroeder, F. L. Muller and A. Hassanpour, *Cryst. Growth Des.*, 2020, **20**, 6057–6068.
483 M. Descamps and J. F. Willart, *Adv. Drug Delivery Rev.*, 2016, **100**, 51–66.
484 S. Chen, A. Y. Sheikh and R. Ho, *J. Pharm. Sci.*, 2014, **103**, 3879–3890.
485 G. Vreeman and C. C. Sun, *Powder Technol.*, 2022, **398**, 117066.
486 E. N. Hiestand, *J. Pharm. Sci.*, 1997, **86**, 985–990.
487 C. C. Sun, *Powder Technol.*, 2015, **279**, 123–126.
488 F. Osei-Yeboah, S.-Y. Chang and C. C. Sun, *Pharm. Res.*, 2016, **33**, 1126–1132.
489 C. C. Sun, *J. Adhes. Sci. Technol.*, 2011, **25**, 483–499.
490 P. P. Bag, M. Chen, C. C. Sun and C. M. Reddy, *CrystEngComm*, 2012, **14**, 3865–3867.
491 S.-Y. Chang and C. C. Sun, *Mol. Pharm.*, 2017, **14**, 2047–2055.
492 C. C. Sun and H. Hou, *Cryst. Growth Des.*, 2008, **8**, 1575–1579.
493 C. Wang, S. Paul, K. Wang, S. Hu and C. C. Sun, *Cryst. Growth Des.*, 2017, **17**, 6030–6040.
494 G. Vreeman, C. Wang, C. M. Reddy and C. C. Sun, *Cryst. Growth Des.*, 2021, **12**, 6655–6659.
495 S. Paul, K. Wang, L. J. Taylor, B. Murphy, J. Krzyzaniak, N. Dawson, M. P. Mullarney, P. Meenan and C. C. Sun, *J. Pharm. Sci.*, 2017, **106**, 2060–2067.
496 S. Chattoraj, P. Daugherity, T. McDermott, A. Olsofsky, W. J. Roth and M. Tobyn, *J. Pharm. Sci.*, 2018, **107**, 2267–2282.
497 S. Paul, L. J. Taylor, B. Murphy, J. Krzyzaniak, N. Dawson, M. P. Mullarney, P. Meenan and C. C. Sun, *J. Pharm. Sci.*, 2017, **106**, 151–158.
498 S. Paul, C. Wang, K. Wang and C. C. Sun, *Mol. Pharm.*, 2019, **16**, 2700–2707.
499 R. M. Mohamed, M. K. Mishra, L. M. AL-Harbi, M. S. Al-Ghamdi and U. Ramamurty, *RSC Adv.*, 2015, **5**, 64156–64162.
500 M. K. Mishra, P. Sanphui, U. Ramamurty and G. R. Desiraju, *Cryst. Growth Des.*, 2014, **14**, 3054–3061.

501 M. K. Mishra, U. Ramamurty and G. R. Desiraju, *J. Am. Chem. Soc.*, 2015, **137**, 1794–1797.
502 F. Liu, D. E. Hooks, N. Li, J. F. Rubinson, J. N. Wacker and J. A. Swift, *Chem. Mater.*, 2020, **32**, 3952–3959.
503 A. J. Thompson, A. I. Chamorro Orué, A. J. Nair, J. R. Price, J. McMurtrie and J. K. Clegg, *Chem. Soc. Rev.*, 2021, **50**, 11725–11740.
504 K. Wang, M. K. Mishra and C. C. Sun, *Chem. Mater.*, 2019, **31**, 1794–1799.
505 M. K. Mishra and C. C. Sun, *Cryst. Growth Des.*, 2020, **20**, 4764–4769.
506 S. Hu, M. K. Mishra and C. C. Sun, *Chem. Mater.*, 2019, **31**, 3818–3822.
507 C. C. Sun, *J. Pharm. Sci.*, 2009, **98**, 1671–1687.